Preparation and Performance of Nanostructured Iron Oxide Thin Films for Solar Hydrogen Generation

---

by

Sina Saremi Yarahmadi

A doctoral thesis
submitted in partial fulfilment of the requirements
for the reward of

Doctor of Philosophy of Loughborough University

December 2010

To:

Goli & My Parents

Acknowledgments

I would like to thank and admire the support, guidance, and patience of my supervisors, Dr. Bala Vaidhyanathan and Dr. Upul Wijayantha, throughout this study. I value being given the opportunity to undertake this work and I thank the staff of Departments of Materials and Chemistry for providing me with an excellent environment to perform research and study. I am also thankful to Materials Research School (MRS), Loughborough University and Prof. Rachel Thomson, Director of MRS, for the financial support. I would like to thank my Directors of Research, initially Dr Houzheng Wu and subsequently Prof Jon Binner.

I must also thank Dr Asif A. Tahir for his unlimited help and advice in this work. I must also express my special thanks to Mr J. Bates, Dr. G. West and Mr. D Hall for their help in SEM, FIBSEM and XPS measurements. Also, I would like to thank Dinesh Asogan for ICP-MS measurements.

My very special thanks to my wife, Goli, who deserves more than what I could ever express, for her unwavering help and support throughout my studies, for everything. Sincere thanks to my family who supported me all the time: mum, dad, sister Setare, auntie Ziba, my lovely cousins, Donia, Nika, Nava, Farnaz and Siavash, Uncles Ahmad, Essi, Alesh, and Hamid, Pari, Faranak, Termeh, and my grandparents. And finally, thanks to my wonderful friends; Hossein, Parysa, Asif, Ruvini, Asri, Senthil, Tom, Henry, Guilan, Victor, Florentinos, Kiki, Vinu, Anish, Khosrow, for moral support, tea breaks, dinners and other necessary or un-necessary distractions.

Abstract

Nowadays, energy and its resources are of prime importance at the global level. During the last few decades there have been several driving forces for the investigation of new sources of energy. Hydrogen has long been identified as one of the most promising carriers of energy. Photoelectrochemical (PEC) water splitting is one of the most promising means of producing hydrogen through a renewable source. Hematite (α-Fe_2O_3) is a strong candidate material as photoelectrode for PEC water splitting as it fulfils most of the selection criteria of a suitable photocatalyst material for hydrogen generation such as bandgap, chemical and photelectrochemical stability, and importantly ease of fabrication.

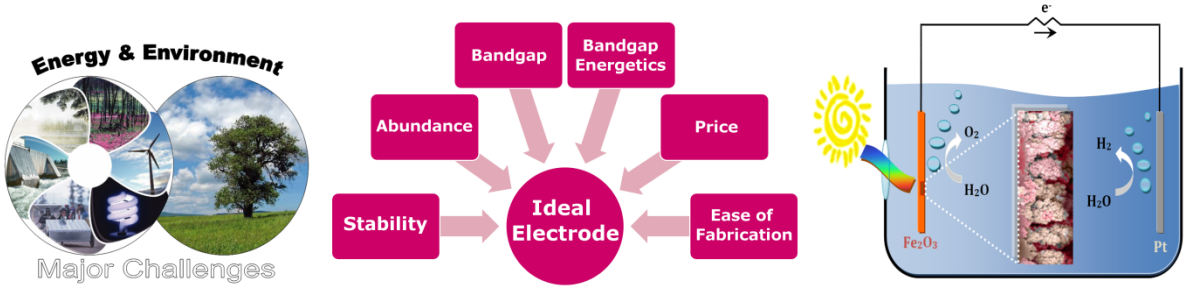

This work has explored different preparation techniques for undoped and Si-doped iron oxide thin films using microwave-assisted and conventional preparation methods. Two distinct strategies towards improving PEC performance of hematite photoelectrodes were examined: retaining a finer nanostructure and enhancing the photocatalytic behaviour through doping.

By depositing thin films using atmospheric pressure chemical vapour deposition (APCVD) and aerosol-assisted CVD (AACVD) at high temperature, it was shown that a combination of different factors (such as silicon incorporation into the hematite structure and formation of lattice defects, along with a nanostructure of small agglomerate/cluster enhancing hole transportation to the surface) were the contributing factors in improving the PEC performance in hematite films. The role of the Si-containing precursors and their consecutive effect on nanostructure of the hematite films were investigated. Further work is needed to study the decomposition pattern of precursors and consequent effects of Si additives as well as co-dopants on fundamental physical and electrical properties of hematite electrodes.

In addition, the feasibility of using microwave annealing for the fabrication of iron oxide thin films prepared by electrodeposition at low temperature was also investigated. Hematite films showed improved PEC performance when microwave assisted annealing was used. Microwave heating decreased the annealing temperature by ~40% while the PEC performance was increased by two-fold. The improved performance is attributed to the lower processing temperatures and rapidity of the microwave method that help to retain the nanostructure of the thin films whilst restricting the grain coalescence to a minimum. Around 60% of the energy can be saved using this low carbon foot-print approach compared to conventional annealing procedures for the lab-scale preparation of hematite films – a trait that will have significant implications for scale-up production. The lower processing temperature requirements of the microwave process can also open up the possibility of fabricating hematite thin films on conducting, flexible, plastic electronic substrates.

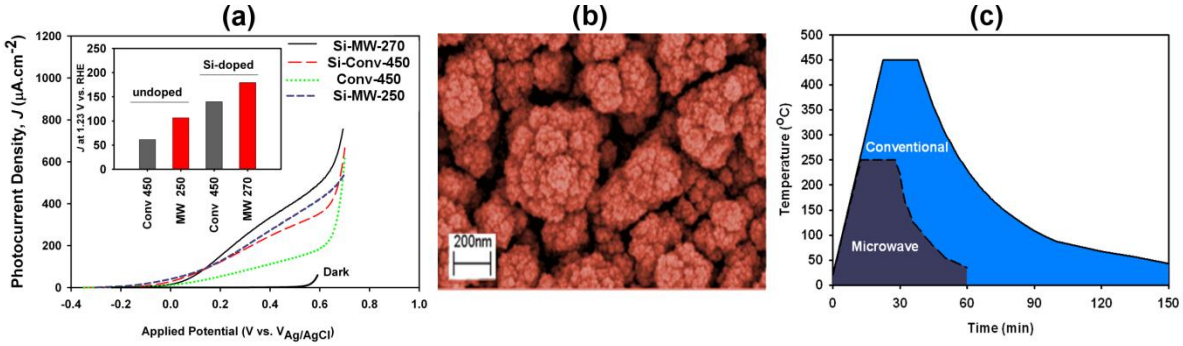

(a) Photocurrent performance plot of undoped and Si-doped samples of electrodeposited films. (b) Surface morphology of Si-doped hematite electrode prepared by APCVD (the primary size of the hematite grains is of the order of 20 nm). (c) Temperature-Time profile of microwave and conventional annealing of electrodeposited samples.

Table of Contents

List of Figures

List of Tables

Chapter 1

1 Introduction

1.1 Energy challenge in the 21st century

Nowadays, energy and its resources are of prime importance at global levels. During the last few decades there have been several driving forces for the investigation of new sources of energy. For example, a tremendous increase in worldwide energy consumption together with the threat of depletion of fossil fuel energy resources has encouraged many researchers to explore alternative energies. Although the price of fossil energy per watt is cheap comparing to renewable energy sources, concerns of climate change and global warming as well as renewed fears of an impending energy crisis have pushed policy makers to shift their focus to the development of renewable energy technologies.[1]

Figure 1-1 shows 2001 global primary* energy use, including both commercial and non-commercial sources of energy. Fossil fuels (oil, natural gas, and coal) represent nearly 80 percent of the total. Nuclear power contributes approximately 7 percent; however, because nuclear power plants have only one third of thermal efficiency, the final total electricity generated for consumption is basically the same as that generated by large hydropower. Large hydropower and "new" renewable energies (which include modern uses of biomass and small hydropower, geothermal, wind, solar, and marine energy) each contribute slightly more than 2 percent; the percentage contribution of "new renewable energy sources" has changed little in recent years.[2]

If the global growth rate of about 1.5 percent per year in primary energy use continues, total energy use will double between 2000 and 2040, and triple by 2060.[2] Fossil fuels, supplying 80% of all energy consumed worldwide, are facing rapid resource depletion.

* Primary energy includes all types of energy resources before their conversion to energy carriers. The other type of energy is classified as final energy which is the energy that is suitable for end use. An oil well is a primary energy source while diesel fuel is considered as final energy.

Careful analysis of the long-term availability of energy resources, starting with conventional and unconventional oil and gas, indicates that these resources could last another 50 to 100 years – and possibly much longer – with known exploration and extraction technologies and anticipated technical progress in upstream operations. Coal and unconventional oil resources, and nuclear materials, are so abundant that they could, respectively, last for centuries or millennia.[2] However, there are serious issues concerning each of them. The most obvious challenge is the high environmental risks associated with these routes. Very recently, in 2010, the oil spill resulted from an explosion in an offshore oil rig owned by BP caused catastrophic damages to the ecosystem of the Gulf of Mexico in the US.

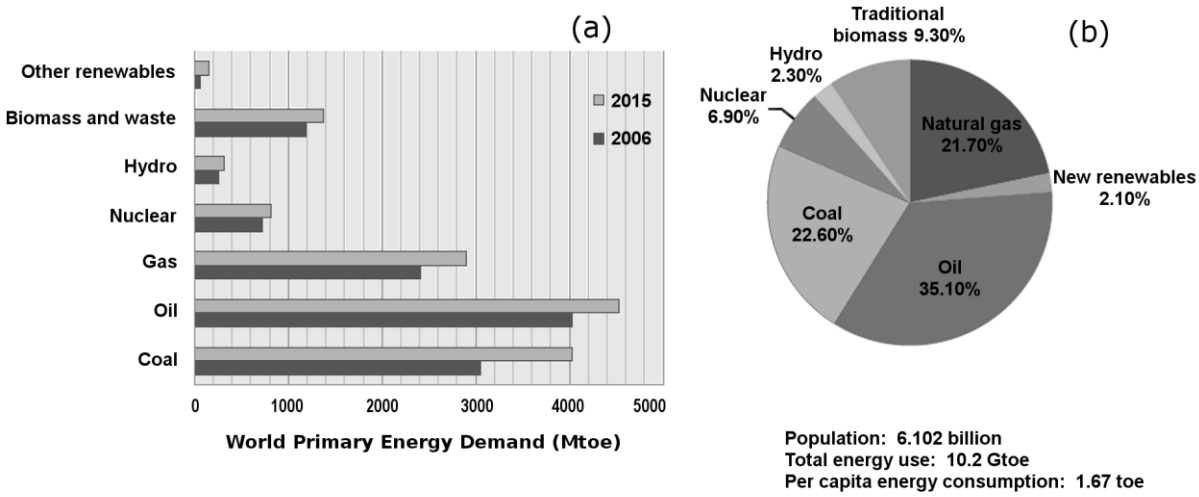

Figure 1-1. (a) World primary energy demand projections in 2006 and 2015[3] (in million tonnes of oil equivalent Mtoe, 1 toe ~ 42 GJ) and (b) world primary energy use, by energy source in 2001.[2]

The other major issue is the CO_2 emissions associated with coal and unconventional oil due to either inefficient burning of the fuel or significant deforestation involved for unconventional oil. Nuclear energy has also got many safety and radioactive waste disposal problems which makes it a less favourable option. In contrast, environmentally-sustainable renewable energy technologies merit energy resources such as radioactive materials in many areas. Minimum green house gas emissions and environmentally-benign waste are only some examples.

1.2 Sustainable energy pathways

Because of a growing demand for energy, combined with the depletion of fossil resources, global warming and its associated climate change, there is an urgent need for environmentally sustainable energy technologies.[4] Fossil fuel combustion produces more carbon dioxide (CO_2) than any other human activity.[2] It accounts for nearly 75 % of the CO_2 flow to the atmosphere while second most harmful human activity for CO_2 emissions, deforestation for land clearing only reaches a 15 % mark.[2] This is the biggest source of the anthropogenic greenhouse gas emissions that are changing the composition of the atmosphere and could alter the global climate system, including the amount and pattern of rainfall.[2] Stabilising CO_2 at close to the present concentration would require reducing emissions to half of current levels within the next few decades.[2] It clearly indicates the importance of the development of environmentally-sustainable technologies. Such technologies would enable us to satisfy our energy requirements through non-CO_2 emission pathways.

1.3 Hydrogen - the fuel of the future

Hydrogen has long been identified as one of the most promising energy carriers. Although it is the most abundant element in the universe and is present in stars and in the Sun, it is only present in the world as a constituent of a compound such as water (H_2O). The biggest challenge is to produce hydrogen at a high rate by a process with no (or minimum) CO_2 emissions. The prospect of the use of hydrogen as an alternative energy source become more significant if one notes the fact that every 1 gram of hydrogen can produce 140 kJ of energy.[5] Thus there is huge scope for hydrogen as an energy carrier to be further exploited. Nowadays, 95% of the hydrogen is produced using a catalytic thermochemical conversion process which reforms natural gas.[6] The catalytic thermochemical conversion causes significant amounts of CO_2 emission. Therefore, if hydrogen generation has only to rely on this process, then, it negates the prospect of hydrogen as an environmentally-friendly fuel. Therefore, generation of hydrogen from clean and environmentally-safe[7] sources such as solar energy should be explored. Among many other methods, solar-driven water splitting has become one of the most promising means of producing hydrogen through a renewable source. In this process, water molecules are broken into hydrogen and oxygen, using

sunlight. There are several driving forces behind the development of this route such as abundance of solar energy, inexpensive materials used for photocatalysis, and adoptability to the needs of individual households.[7,8] In addition, solar energy enables the production of sufficient enough hydrogen to satisfy the fast growing demands[9] without the expensive infrastructure needed for hydrogen economy.

1.4 Photoelectrochemical water splitting (solar-driven water splitting)

There are two general routes for the conversion of solar energy into useful energy forms; solar thermal and solar photonic processes.[10] In the solar thermal process, solar energy is converted into heat which can be used either directly or through a medium such as water which is then used for running a steam turbine and generation of electricity. In a solar photonic process, photons are absorbed by an absorber and then converted into different forms of energy such as electricity. A simple example of such a process occurs in photovoltaic cells where absorbed photons are converted directly into electricity. Absorbed photons can also be converted into chemical energy instead of electricity. The stored chemical energy is then used to facilitate chemical reactions such as water dissociation into hydrogen and oxygen.[10] This process is generally known as photoelectrochemical (PEC) water splitting. The final products, hydrogen and oxygen, can be utilised as alternative sources of energy.

In 1972, Fujishima and Honda[11] reported photo-dissociation of water into hydrogen and oxygen using a single crystal TiO_2 electrode. Since then there has been significant interest in developing an efficient device for the production of hydrogen using PEC cells. In a PEC cell, water molecules are broken into hydrogen and oxygen at the surface of a semiconductor; photon absorption leads to the formation of charge carriers (electrons and holes) in the conduction and valence band of the semiconductor. The generated electrons can then reduce hydrogen ions to hydrogen atoms. It must be noted that the exact mechanism through which water oxidation is occurred is still not clear. However, Somorjai and Turner[12] in 1984 proposed the following mechanism for light-induced water oxidation. Hydrogen gas is formed if two hydrogen ions are combined with each other (Equation 1.1):[12]

$$2H^+ + 2e^- \rightarrow H_2 \qquad (1.1)$$

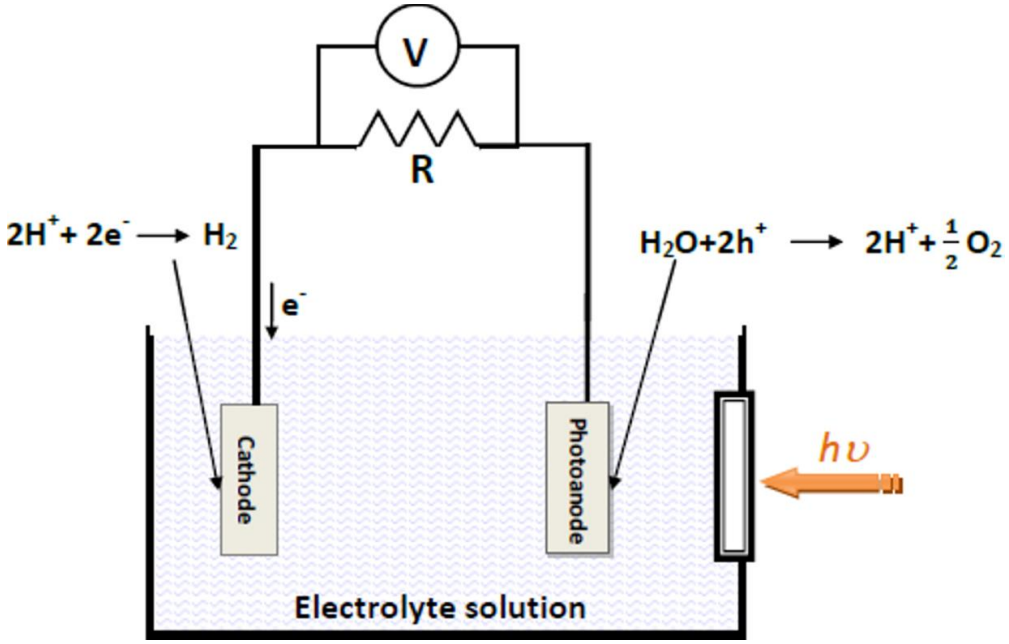

Figure 1-2. Schematic structure of a PEC cell. Hydrogen is generated at the surface of the cathode while oxygen evolution happens at the surface of the photoanode which is a semiconductor.[11]

On the other hand, hole captures the negative charge from a hydroxyl ion forming an unstable OH radical, which will form a peroxide molecule H_2O_2 through subsequent dimerization.[12] Finally, peroxide molecule decomposes and oxygen is released. Equation 1.2 shows the oxygen evolution reaction that occurs at the semiconductor surface:

$$H_2O + 2h^+ \rightarrow 2H^+ + \frac{1}{2}O_2 \qquad (1.2)$$

This process is shown schematically in Figure 1-2. In summary, light-induced PEC water splitting occurs following a sequence of different processes; incident photon is absorbed by the anodic semiconductor and charge carriers are generated. Photo-generated electron-hole pairs are then separated; electrons are transferred towards the metal electrode where hydrogen reduction is occurred while oxidation of water takes place at the semiconductor/electrolyte interface. In effect, light has the potential to provide the energy required to break water molecules into hydrogen and oxygen (Equation 1.3):

$$H_2O + h\nu \rightarrow \frac{1}{2}O_2 + H_2 \qquad (1.3)$$

1.4.1 Advantages and drawbacks

There are number of advantages in PEC water splitting. Most importantly, it is a method that exploits two of the most readily available sources of energy; water and sunlight. In this process, water molecules are broken into hydrogen and oxygen, using sunlight. Although there have been significant advances in the development of PEC water splitting it is still a long way from an industrial scale hydrogen production. The efficiencies of the devices have not yet reached their full potential and further research is needed to obtain an efficient operating device which has the capability of providing sufficient energy at reasonable cost. Another barrier is the difficulties in handling and storage of hydrogen gas. Generation of hydrogen is not the only challenge today; there are also few obstacles in storage and handling of it. Hydrogen is extremely difficult to transport and highly flammable which causes health and safety concerns in development of hydrogen-powered applications. However, the automotive industry which is the forefront in developing hydrogen fuel cell-powered vehicles appears to be addressing these safety issues. PEM fuel cell community is working actively to overcome the safety issues related with hydrogen as it is a vital step in their efforts to push fuel cells in short term applications in automobile and other industries. The application of fuel cells is a promising way of harnessing the hydrogen gas and producing electricity as a more accessible form of energy.

1.4.2 Materials-related issues - Requirements for an ideal photoanode

The semiconductor materials suitable for PEC water splitting electrodes must satisfy several requirements. However, it is very difficult to fabricate an ideal electrode as the configuration of final device depends on the material processing techniques. In this section, most important functional properties of a suitable electrode are discussed.

1.4.2.1 Bandgap and position of band edges

Before explaining the bandgap requirements, it is important to become familiar with the concept of reference electrode since all potentials are measured with respect to a specific reference electrode. The vacuum level is commonly used as the reference energy. When studying the electrochemical properties of materials several different energy scales are likely

to be used. Therefore, the electrical potentials are reversed with respect to the vacuum level as it is the potential of the electrode of interest. Different energy scales of reference electrodes are depicted in Figure 1-3 and water oxidation potentials (H^+/H_2 and O_2/H_2O) are also shown on the electrochemical energy scales. The normal hydrogen electrode (NHE) potential is the potential of a platinum electrode at 298 K at pH=0 (in equilibrium with 1 atm of H_2). The potential of reversible hydrogen electrode (RHE) diverges from the NHE potential by +59.2 mV/pH at 25 °C. The saturated calomel electrode (SCE) and silver/silver chloride (Ag/AgCl) electrode are the most commonly used reference electrodes in three-electrode configuration PEC cells.

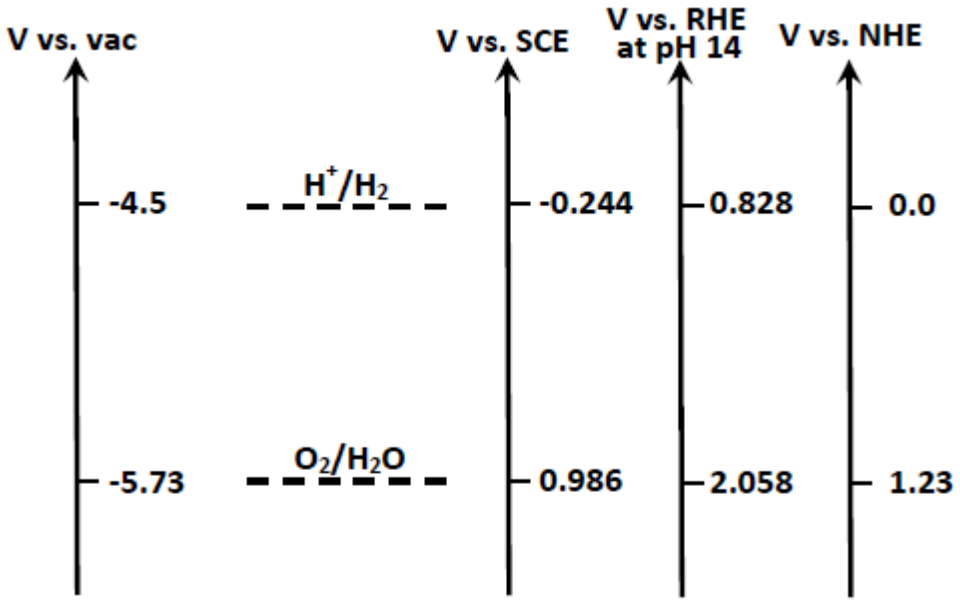

Figure 1-3. Schematic showing the relations between different reference electrodes with respect to the vacuum level. Electrochemical potentials of water oxidation are also mentioned in the scheme.

A basic requirement of the semiconductor electrode material is that its bandgap must not be, at least, less than that of the potential required for breaking a water molecule into hydrogen and oxygen which is 1.23 V vs. reversible hydrogen electrode (V_{RHE}) at standard conditions. However, it has been shown that a semiconductor material with a bandgap of approximately 2 eV is the best photoanode material. Bolton[10] showed that in an ideal system, the actual energy loss (U_{loss}) per hydrogen molecule (H_2) in the overall PEC process is ~0.3-

0.4 eV while U_{loss} of ~0.8 eV could be regarded as a good estimate in a practical system. He described that U_{loss} cannot be zero because the energy of the ensemble of photo-generated electron-hole pairs is thermodynamically the internal energy and not Gibbs energy, therefore, entropic considerations dictate a minimum energy loss in the order of 0.3-0.4 eV.

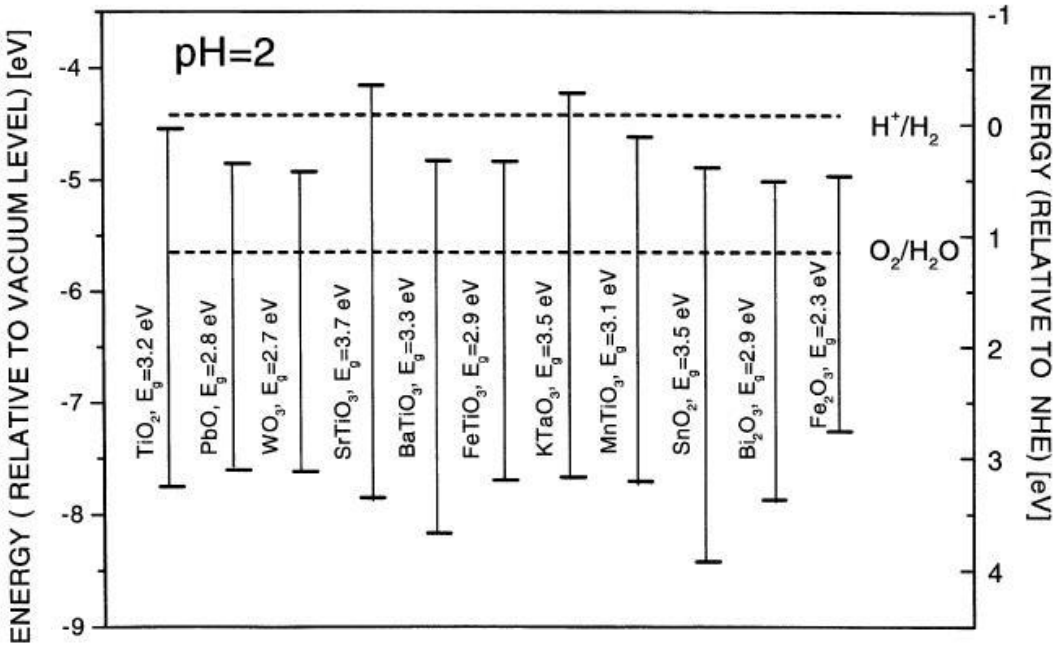

Figure 1-4. Schematic showing the bandgap of some semiconductor materials and the position of the band edges with respect to the redox potentials of hydrogen and oxygen evolution reactions.[16]

Another important parameter is the position of conduction and valence band edges of the semiconductor. The ideal material should have a bandgap of ~2 eV while its band edges straddle the redox potentials of water dissociation. For example, as shown in Figure 1-4, the band edges of $SrTiO_3$ satisfy this requirement, however, it is a large bandgap material and therefore only ~4% of visible solar spectrum is absorbed. On the other hand, Fe_2O_3 has the near ideal bandgap. However, its conduction band edge is situated too positively to the hydrogen evolution potential hence, a bias potential is needed to drive the reduction reaction.

In n-type and p-type semiconductors the flat-band potential can be used as an indicator for conduction and valence band edge positions. PEC water splitting may take place, without the imposition of a bias, if flat-band potential of an n-type semiconductor lies above the redox potential of H^+/H_2 reaction. In other words, photoanodes with negative flat-band potentials relative to the redox potential of H^+/H_2 reaction do not need a bias potential to decompose water. Figure 1-5 illustrates the flat-band potential of several oxide materials against the bandgap compared to the vacuum level and NHE.

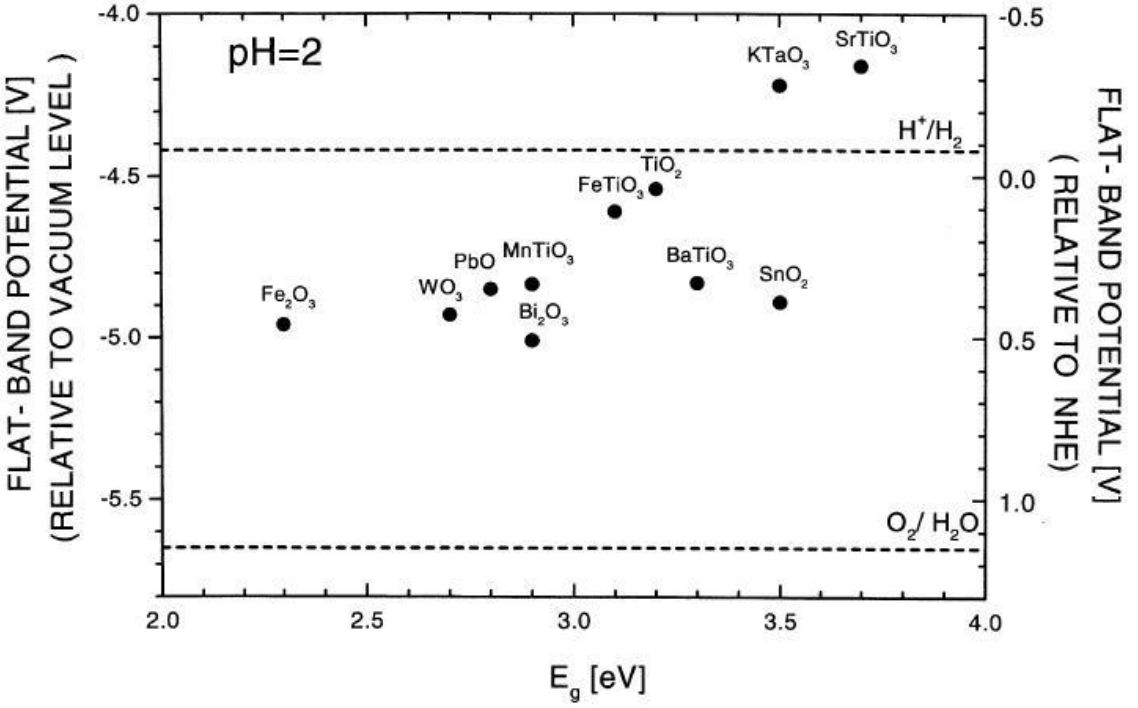

Figure 1-5. Flat-band potential of several oxide materials against the bandgap compared to the vacuum level and NHE.[14]

1.4.2.2 Stability

When the semiconductor electrode is illuminated, electron-hole pairs are generated. These electrons and holes have strong oxidizing and reducing potentials, respectively.[13] If they are not injected into electrolyte or transferred to the conducting substrate, under certain circumstances, they can oxidize or reduce the semiconductor itself. However, this is only one side of the problem. An ideal semiconductor electrode must not only be resistant to corrosion associated with photo-generated electron and holes, but it also needs to be

resistant to electrochemical corrosion and dissolution. Most oxide materials are generally stable under these conditions and, therefore, good candidate photoelectrode materials in aqueous electrolytes in PEC cells.

1.4.2.3 Electrical properties

When a semiconductor electrode is illuminated, photo-generated charge carriers need to be transported efficiently. Generally, the electrical conductivity of a semiconductor is smaller than that of a metal by several orders of magnitude. The electrical conductivity of a semiconductor (σ) is described in Equation 1.4:

$$\sigma = en\mu_n + ep\mu_p + Z_i ei\mu_i \qquad (1.4)$$

where n is the concentration of electrons, p is the concentration of holes, i is the concentration of ions, Z_i is the charge number of ions, μ_n, μ_p, and μ_i are the mobilities of electrons, holes and ions, respectively. It has to be noted that at room temperature, ionic component of the above equation may be ignored.

As the concentration of charge carriers increases, as a result of coulombic interaction between electrons and holes, the mobility of carriers decreases. Therefore, an optimal conductivity is achieved if there is a balance between charge carriers' concentration and their mobility. Introduction of defect disorders in the semiconductor can improve the electrical conductivity. It is achieved by incorporating donor or acceptor cations into the semiconductor structure and controlling oxygen partial pressure during the preparation of semiconductor material.[14]

The mechanism of charge carrier transport in nanostructured electrode is thought to be generally dominated by diffusion (see 2.3.2.1, p.27). Therefore, the electron and hole diffusion length is an important parameter for a semiconductor. It can be optimised by the modification of the chemical composition.[15] Moreover, a modified nanostructure may allow for a better charge transport, for example, if the size of the nanostructure building blocks, e.g. nanoparticles, is smaller than the diffusion length of the carrier, it will lead to relatively low bulk recombination. However, it may also be disadvantageous as it could increase the recombination at interparticle necks/boundaries.

1.4.3 Efficiency of PEC water splitting

Efficiency is of prime importance in any energy conversion process as the more efficient the conversion process, the lower the cost of energy generated. The free energy required to break water reversibly into hydrogen and oxygen gases at room temperature is approximately 1.23 eV. Although a large portion of solar radiant energy is larger than 1.23 eV, efficiencies achieved by PEC water splitting are not reasonably high. It is attributed to the thermodynamic and kinetic losses present during the conversion process.

In a PEC cell, solar energy is absorbed by the semiconductor. The characteristic of the semiconductor is that it does not absorb light at wavelengths larger than the wavelength of its absorption edge (λ_g). The maximum energy that can be absorbed by the semiconductor is described by its bandgap energy E_g (Equation 1.5):

$$E_g = \frac{hc}{\lambda_g} \qquad (1.5)$$

where h is the Planck's constant and c is the speed of light. Bandgap of the semiconductor plays an important role in the efficiency of the PEC cell as it determines the amount of energy that can be absorbed by the semiconductor. The efficiency of a PEC cell is mainly limited by the charge carrier excitation and transfer processes within the semiconductor electrode. In a PEC cell, energy is lost through 4 major processes.[10] Firstly, solar photons with $\lambda \geq \lambda_g$ cannot be absorbed and therefore, cannot be used in the conversion process. Secondly, although solar photons with $\lambda \leq \lambda_g$ are absorbed, the excess energy ($E - E_g$) is lost as heat through relaxation of the excited states (E is the incident energy absorbed by the semiconductor). The third energy loss occurs during the conversion of the solar energy to chemical energy. The energy of the excited states, photo-generated electron-hole pairs, is internal energy not Gibbs energy.[10] It means that during the conversion process, some part of energy is lost as a result of the changes in the entropy of the system. The last process contributing to the overall loss is fluorescence. In a PEC water splitting device, solar energy is stored as chemical energy in an energy-rich product P (e.g. hydrogen).[10] The efficiency η_c of this process is described as in Equation 1.6:[10]

$$\eta_C = \frac{\Delta G_p^0 R_p}{E_s A} \qquad (1.6)$$

where ΔG_p^0 is the standard Gibbs energy for the energy storage reaction generating product P, R_p is the rate of generation of the product, E_s is the incident solar irradiance (W.m^{-2}) and A is the irradiated area (m^2). This equation shows the importance of the light source used in the characterisation of PEC cells which has been studied in detail in the literature.[16]

It is widely believed that PEC water splitting will not be a commercially viable technology unless it shows a photo-conversion efficiency of at least 10%.[17] Weber and Dignam[18] derived upper limit photo-conversion efficiencies for three different types of PEC cells. Their results showed the efficiency of 18% could be achieved only if a tandem cell, a PEC cell coupled with a photovoltaic cell, was used. However, the upper limit conversion efficiency of a simple PEC cell comprising of one semiconductor electrode decreased to only 7%.

1.4.3.1 Incident photon to electron conversion efficiency (IPCE)

The IPCE is the accepted measure to calculate the conversion efficiency of incident photons on a PEC cell to photocurrent flowing between the working and counter electrodes.[16] An IPCE of 100% indicates the generation of one photoelectron per each incident photon.

However, IPCE of 100% cannot be achieved as there are losses due to the reflection of incident photons, imperfect photon absorption by the photoelectrode and recombination.[16,19] IPCE is also called the external quantum efficiency and can be calculated using Equation 1.7:

$$IPCE = 1240\frac{I_p(\lambda)}{P(\lambda)\lambda} \qquad (1.7)$$

where $I_p(\lambda)$ and $P(\lambda)$ are the photocurrent density and incident light intensity at wavelength λ, respectively.[19]

Another way of understanding the effectiveness of the photon to electron conversion process in a photoelectrode is by measuring the absorbed photon to electron conversion efficiency (APCE) or the internal quantum efficiency. It basically shows the number of charge carriers collected per absorbed photon. The advantage of this method is that, unlike

IPCE, it considers the losses in the conversion process. Knowing the absorbance of the photoelectrode (A), APCE can be calculated using Equation 1.8:

$$APCE = \frac{IPCE}{1 - 10^{-A}} \qquad (1.8)$$

The efficient PEC performance of photoelectrodes is greatly influenced by the preparation methods and the parameters involved during the fabrication. This work investigates the effects of two distinct preparation methods and examines different approaches towards fabrication of more efficient α-Fe_2O_3 photoelectrodes. Chapter 2 provides an overview on the fundamentals of semiconductor materials and physical and chemical aspects of semiconductor/electrolyte interface. It also reviews the reported preparation methodologies of α-Fe_2O_3 photoelectrodes with the view of focusing on high temperature chemical vapour deposition (CVD) and low temperature techniques for the production of such photoelectrodes. In the latter part of this chapter, a review of the concept of microwave processing of semiconductor materials is presented and reports on microwave assisted preparation of α-Fe_2O_3 are summarised. Chapter 3 explains the fabrication methodologies, film preparation conditions and characterisation methods used in this work. The results obtained are discussed in detail in Chapter 4 with the first part focused on high temperature preparation (CVD) and the second part is dedicated to the low temperature microwave assisted method. The next chapters present a summary of the findings of this work (Chapter 5) and suggestions for future work (Chapter 6).

Chapter 2

2 Literature Review

2.1 Semiconductor materials

A semiconductor is simply a material with electrical conductivity found between an insulator and a conductor. An insulator exhibits very low conductivity whereas a conductor shows high conductivity. Charge carriers are situated at different energy levels with a material. The highest occupied energy level is known as the valence band and the lowest unoccupied energy level is known as the conduction band. In a conductor, the two bands overlap and hence electron movement occurs readily. In insulators, the two bands are too far apart and electrons cannot be promoted. In semiconductors, there is a forbidden energy gap in which no energy states can exist: this is known as the band gap. Energy states are only allowed in the conduction band or the valence band. Therefore, given enough energy, electrons are able to be promoted. The band gap values of interest are measured between 0.5 and 3.5 eV. When sufficient energy has been supplied and the electrons are promoted, leaving positively charged 'holes' in the valance band.

There are two types of semiconductors: p-type and n-type. A p-type semiconductor occurs when the charge is carried by holes. An n-type semiconductor occurs when the charge is carried by electrons. Electrochemical processes at semiconductor electrodes under both irradiation and dark conditions are understood by considering the fundamental properties of semiconductors. By combining the classical approaches with quantum mechanical methods, a free electron in space can be characterised. The relationship between the wavelength of a free electron (λ) and its momentum (p) is described as in Equation 2.1:[20]

$$\lambda = \frac{h}{p} = \frac{h}{mv} \qquad (2.1)$$

where h is the Planck constant, m is the electron mass and v is the electron velocity. By solving the equations of kinetic energy of free electron a parabolic relation between kinetic energy of free electron (E_k) and electron wave vector (k) is obtained (Figure 2-1):

$$k = \frac{2\pi}{\lambda} \qquad (2.2)$$

$$E_k = \frac{1}{2}mv^2 = \frac{h^2}{8\pi^2 m}k^2 \qquad (2.3)$$

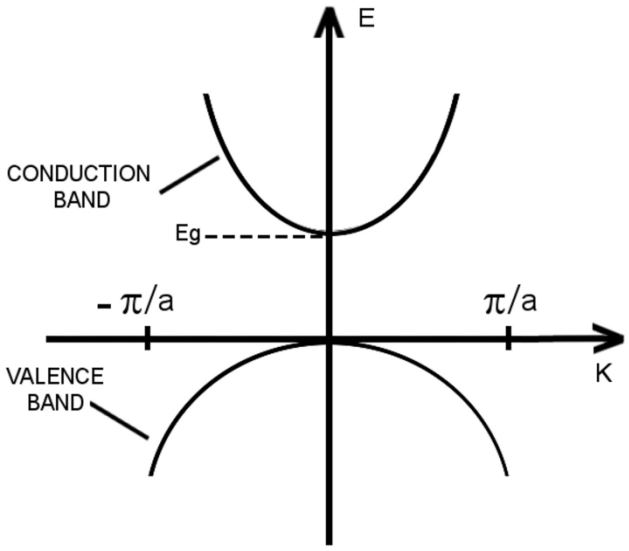

Figure 2-1. Electron energy and wave vector in semiconductor materials.

In metals, electrons are not completely free and can only obtain certain values but the relationship still remains parabolic. However, in semiconductors and insulators, while no free electrons are present,[20] there is a periodic potential energy profile with the periodicity of the lattice of crystal. Mathematical calculations have shown that in semiconductors, unlike metals, two energy bands exist which are separated by an energy gap. As shown in Figure 2-2, charge carriers are situated at different energy levels within an intrinsic semiconductor material. The highest occupied energy level is known as the valence band and the lowest unoccupied energy level is known as the conduction band.[21] In insulators, the two bands are

too far apart and electrons cannot be promoted. Semiconductors are a group of materials that their conductivity falls between conductors and insulators.

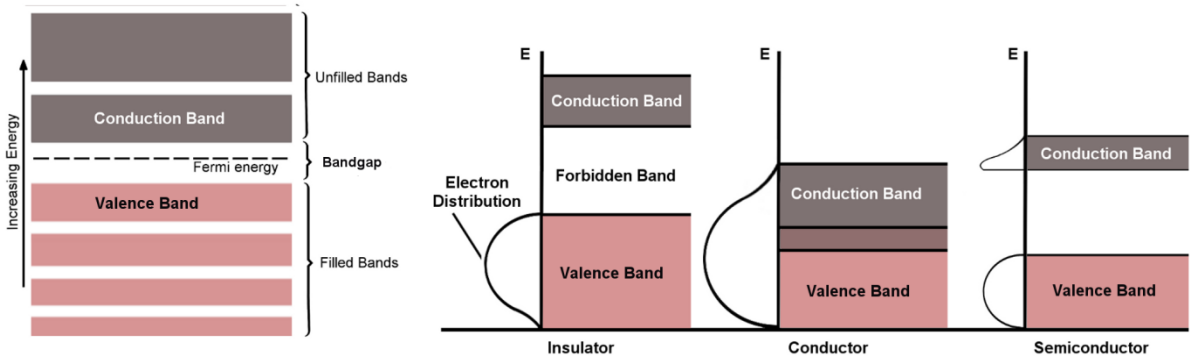

Figure 2-2. The semiconductor band structure in an intrinsic semiconductor.

Semiconductor materials are usually categorised in two main groups; direct bandgap and indirect bandgap semiconductors. This distinction occurs due to the difference in the position of the lowest minimum of the conduction band with respect to that of the maximum of the valence band. In direct bandgap semiconductors both the conduction band minimum and the valence band maximum occur at k=0 (Figure 2-1). However, if the lowest conduction band minimum is situated at k≠0, the semiconductor is known as indirect bandgap.

2.1.1 Optical absorption

Light is simply a form of energy and energy is intangible, apprehended only on its interaction with matter, which acts as an origin or as a detector of energy.[22] According to quantum theory, photons which are a form of energy packets resulting from absorption or emission of radiation have discrete values of energy (Equation 2.4) in quanta:

$$E = h\upsilon = \frac{hc}{\lambda} \qquad (2.4)$$

where h is Planck constant, υ is frequency, c is the speed of light, and λ is wavelength. As radiation interacts with solids an energy exchange occurs. Due to the different levels of

energy present, the system can make a transition from one state of energy to another state with either a lower or higher energy level.

Many photoelectric phenomena are described in terms of a set of basic concepts including optical absorption by which free carriers are created, electrical transport by which free carriers contribute to the electrical conductivity of the material, and the capture of free carriers leading to recombination.

A way of describing optical absorption by a semiconductor is explained by Frenkel.[23] This model includes the excitation of a molecule to a neutral, mobile localized excited state called an exciton. This neutral state is considered as a tight electron/hole (e^-/h^+) pair held together by a strong coulombic interaction. This model is applicable in organic materials which generally possess low dielectric constant and large coulombic interaction.[23] Excitons can move and transport energy a certain distance from where they are formed.[22] Optical absorption also offers a simple way of measuring the bandgap of semiconductors. Absorption coefficient (α) of a semiconductor can be calculated using the following equation (Equation 2.5):

$$\alpha = \frac{1}{d} \ln \frac{I_0}{I} \qquad (2.5)$$

where d, I and I_0 are thickness of the material, incident and transmitted light intensities, respectively. The fundamental absorption is considered as a band-to-band excitation which is seen as a steep rise in absorption as the incident photon energy approaches this range.[23]

However, the determination of the bandgap from absorption measurements has some complications due to the presence of certain selection rules in optical transitions. The relationship between the absorption coefficient near the absorption edge and the optical bandgap (E_g) can be obtained according to following equation (Equation 2.6):[24]

$$\alpha h\upsilon = A_0(h\upsilon - E_g)^n \qquad (2.6)$$

where $h\upsilon$ is the incident photon energy, n depends on the nature of band transition; $n = 1/2$ or $3/2$ for direct allowed and direct forbidden transitions, and $n = 2$ or 3 for indirect allowed and indirect forbidden transitions and A_0 is a constant given by:

$$A_0 = \left(\frac{e^2}{nch^2 m_e^*}\right)(2m_r)^{\frac{3}{2}} \qquad (2.7)$$

where m_e^* and m_r are the effective and reduced masses of majority charge carriers, respectively. The intercept of the extrapolated linear fit to the experimental data of a plot of $(\alpha h\upsilon)^2$ versus photon energy, $h\upsilon$ is determined as the optical bandgap. This plot is commonly known as the Tauc plot.

2.2 Semiconductor/electrolyte interface

2.2.1 Charge and potential distribution at the interface

PEC cells function on the basis of the well-known Becquerel effect. According to Nozik,[13] Edmund Becquerel in 1839, for the first time, demonstrated a photoelectrochemical experiment. He immersed a silver chloride electrode in an electrolyte solution and connected it to a counter electrode. He showed that a voltage and electric current can be produced if a silver chloride electrode is illuminated. Further studies showed that Becquerel effect was due to the presence of a semiconductor at the semiconductor-electrolyte interface; in other words, it was the formation of a semiconductor-electrolyte junction which caused the Becquerel effect.[13]

When a semiconductor becomes in contact with an electrolyte, a junction is formed at the semiconductor-electrolyte interface.[25] The formation of the junction is a result of the difference between chemical potential of electrons across the interface. An important concept in semiconductor physics is the Fermi level. As mentioned, semiconductors are characterised by their two separated energy band levels; filled low energy valence band with the Fermi level at the top and empty high energy conduction band.[26] Chemical potential of electrons is defined as Fermi level in semiconductors while for liquid electrolytes, it is determined by the redox potential of the redox couples present in the electrolyte.[13] A better explanation is that Fermi level is the electron energy where the probability of occupation of a single state at statistical-mechanical equilibrium is 50%.[27]

In an n-type semiconductor Fermi level lies just below the conduction band while it is slightly above the valence band for a p-type semiconductor. Electronic and thermodynamic

equilibrium across the junction requires the Fermi energy of electrons (E_F) in the semiconductor to be equal to the redox potential of the electrolyte (E°_{redox}). In order to reach the equilibrium majority charge carriers (electrons in n-type semiconductor and holes in p-type semiconductors) are transferred to the electrolyte and a band bending ensues within the semiconductor. The position of the band edges and band bending before and after the formation of the junction is illustrated in Figure 2-3.

When two materials with two different Fermi levels are brought into contact, free carriers will flow from one material into the other until an equilibrium condition is established, that is, until the Fermi levels of both materials are aligned, meaning that the Fermi levels for electrons in both materials are equal at the contact.[22] This net carrier flow will set up a positive space charge on one side and a negative space charge on the other side of the interface, forming an electric double layer (Hemholtz layer). This double layer is generally referred to as the potential barrier, and the potential across it is called the contact potential.[22] The internal field created by the potential fluctuations of the band edges due to high concentration of both types of carriers tend to separate electrons and holes, causing dissociation of excitons.[22]

As illustrated in Figure 2-3, the transfer of charge carriers creates a region in which the charge distribution is different from the bulk material. If the initial Fermi level of the semiconductor is above the initial Fermi level (redox potential) of the electrolyte, for example, in an n-type semiconductor, majority charge carriers flow from the semiconductor to the electrolyte. This charge transfer creates a positive space charge layer in the semiconductor. This region is also called depletion layer as it is depleted of electrons. Therefore, band bending in the semiconductor occurs in such a way that a potential barrier is formed which inhibits further charge transfer from the semiconductor to the electrolyte.

For a p-type semiconductor with Fermi energy lower than that of the electrolyte the analogous but inverse process happens where holes are transferred to the electrolyte, which results in the formation of a negative space charge layer in the semiconductor. Valence and conduction bands in the p-type semiconductor are bent to establish a potential barrier against further hole transfer into the electrolyte.

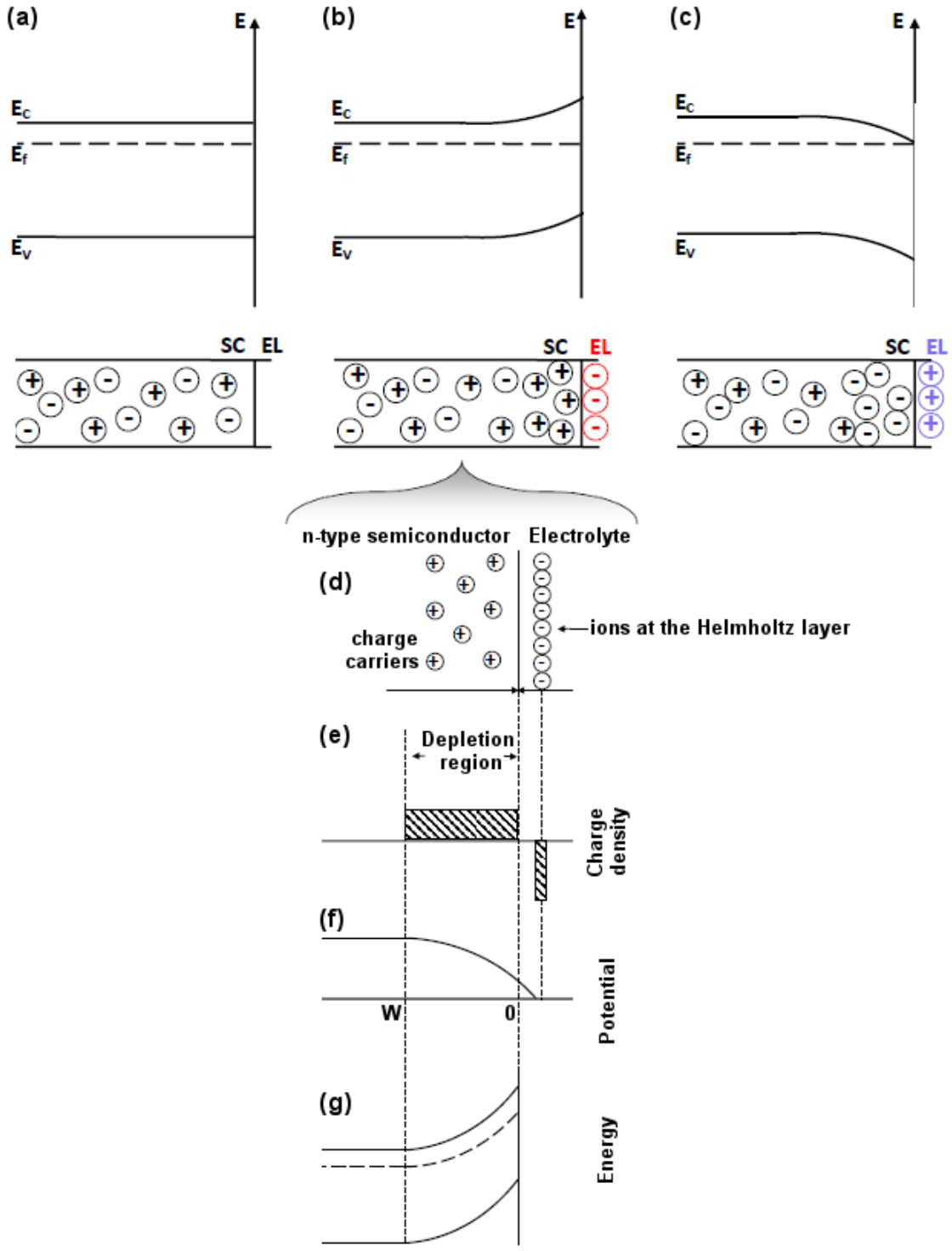

Figure 2-3. The position of the band edges and band bending (a) before and (b and c) after the formation of the semiconductor-electrolyte junction. Schematic shows the variations in (d) charge distribution, (e) charge density distribution, (f) potential distribution, and (g) the band bending at the junction, assuming no surface charge nor surface dipole is present.[28]

2.2.2 Flat-band potential

Flat-band potential (V_{fb}) is a very important parameter in the characterisation of a semiconductor electrode. It is defined as the electrode potential when the semiconductor bands are flat (when space charge layer is zero) (Equation 2.8):

$$V_B = V - V_{fb} \qquad (2.8)$$

In the above equation, V_B is the band bending and V is the semiconductor electrode potential (Fermi level). When the semiconductor is at equilibrium with the electrolyte and in the dark, Fermi level of the semiconductor is equal to the Fermi level of the electrolyte (redox potential).

Flat-band potential is usually measured with respect to a reference electrode potential, for example, the normal H^+/H_2 redox potential (NHE) at standard conditions which is measured as -4.5 eV with respect to vacuum energy. As shown in Figure 2-4, the flat-band potential can be calculated using Equation 2.9:[13]

$$V_{fb} = (\chi + \Delta E_F + V_H) - 4.5 = (\phi_{sc} + V_H) - 4.5 \qquad (2.9)$$

where χ is the electron affinity of the semiconductor, ϕ_{sc} is the work function of the semiconductor, ΔE_F is the energy difference between Fermi level and conduction band edge of the semiconductor, and V_H is the potential drop across the Helmholtz layer. This equation clearly shows the determining effect of the Helmholtz layer on the band bending of the semiconductor. It also indicates that the flat-band potential is dependent on the nature of the semiconductor as well as the electrolyte.

Similar to the space charge layer in the semiconductor side of the interface, there is a charged layer in the electrolyte at the semiconductor-electrolyte interface. It is known as Helmholtz layer and consists of charged electrolyte ions which are adsorbed on the surface of the semiconductor.[13] Existence of this layer is significant in the amount of net band bending that occurs in the semiconductor as shown in Figure 2-4. Without the potential drop across the Helmholtz layer, the band bending would be equal to the difference in initial Fermi levels between semiconductor and electrolyte (the difference between corresponding work functions).[13]

Currently, there are two different methods for determining the flat-band potential of a semiconductor in equilibrium with an electrolyte; capacitance-voltage and photocurrent-voltage methods. The capacitance method is based on the Mott-Schottky relation (Equation 2.10):

$$\frac{1}{C_{sc}^2} = \frac{2}{N_D e \varepsilon_o \varepsilon_s}\left[(V - V_{fb}) - \frac{kT}{e}\right] \qquad (2.10)$$

where C_{sc} is the capacitance of the space charge layer, N_D is the charge carrier density, e is the elementary electronic charge, ε_o is the permittivity of vacuum, ε_s is the static dielectric constant of the semiconductor, k is the Boltzman constant and T is the temperature. If differential capacitance of the semiconductor is measured as a function of electrode potentials, then, for an ideal system, the intercept of the plot of $\frac{1}{C^2}$ versus electrode potential (V) at $\frac{1}{C^2}$=0 will be equal to the flat-band potential.

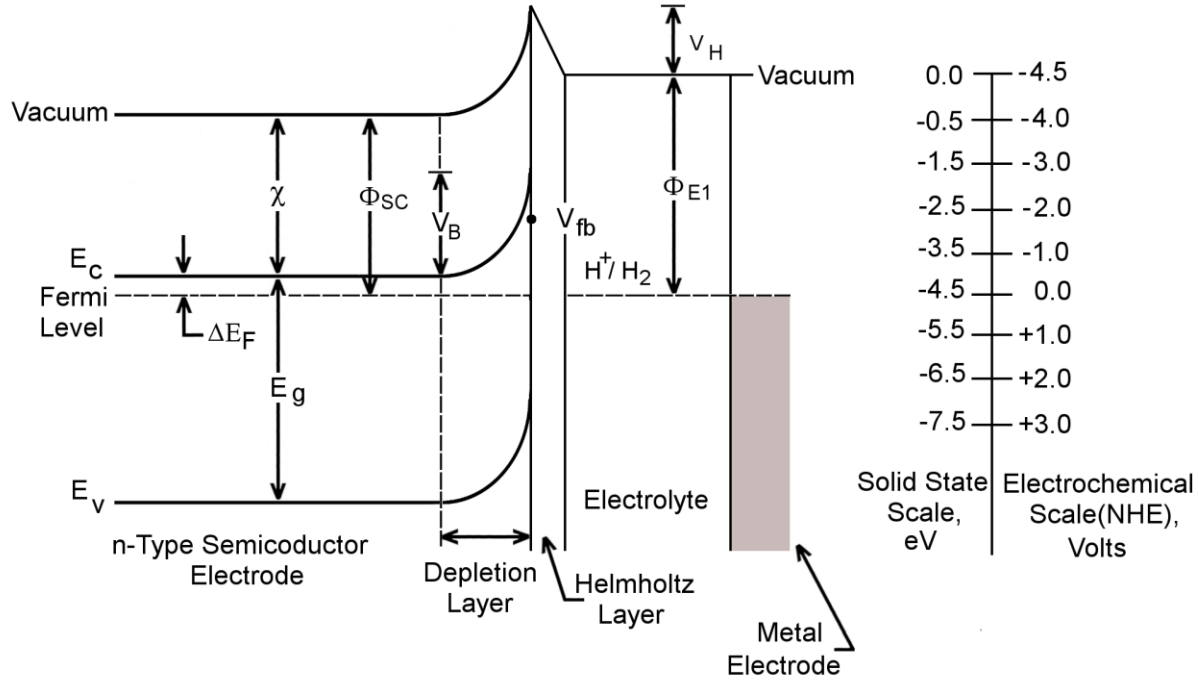

Figure 2-4. Energy level diagram for semiconductor-electrolyte junction showing the relationships between the electrolyte redox couple (H^+/H_2), the Helmholtz layer potential drop (V_H) , and the semiconductor bandgap (Eg), electron affinity (χ), work function (ϕ_{sc}), bending (V_B), and flat-band potential (V_{fb}). The electrochemical and solid state energy scales are shown for comparison. ϕ_{E1} is the electrolyte work function.[13]

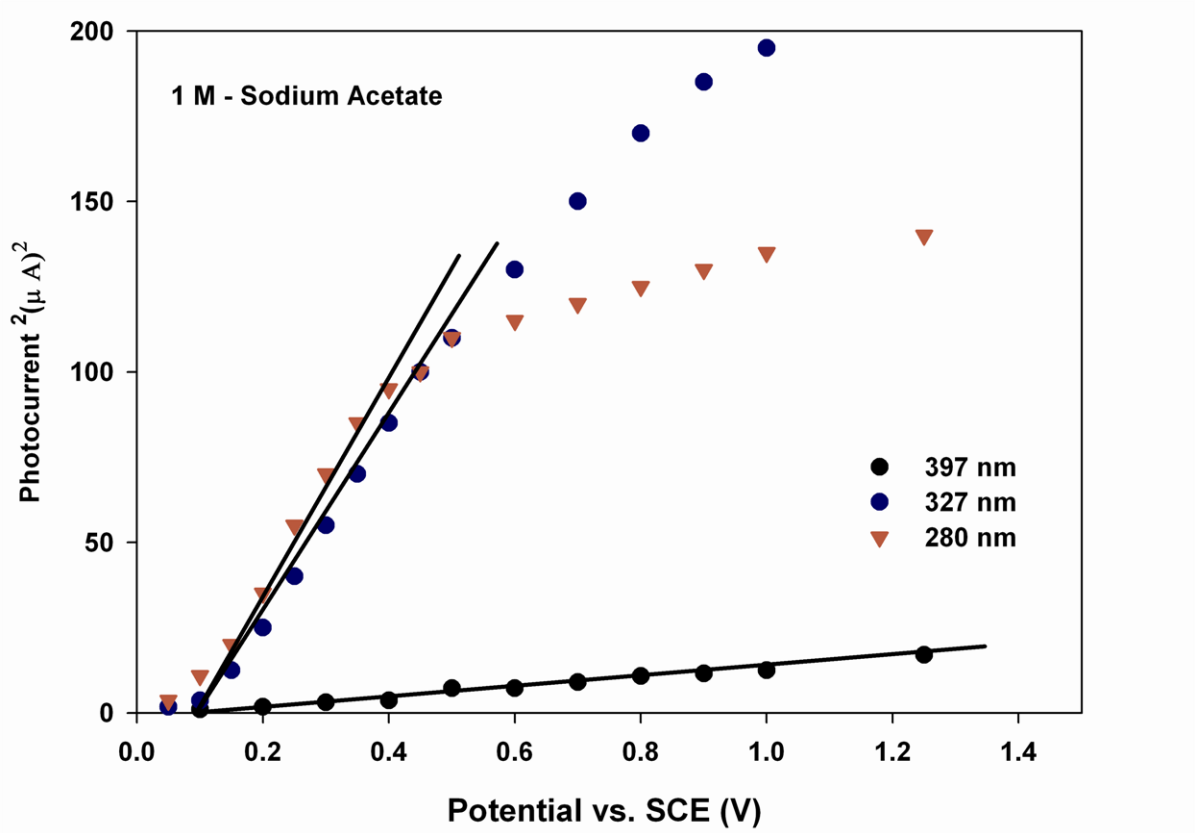

Figure 2-5. Plot of J^2-V for WO_3 electrode. Flat-band potential can be calculated from the intercept of the linear part of the plot at $J^2=0$. (Reproduced from ref. 29)

The second method which was proposed by M. A. Butler in 1977[29] measures the flat-band potential from photocurrent density-voltage (J-V) plots. He calculated that the relation between applied potential and photocurrent density could be described as in Equation 2.11:

$$V - V_{fb} \sim \left(\frac{J}{\alpha W_0 q \varphi_0}\right)^2 \qquad (2.11)$$

where α is the optical absorption coefficient, W_0 is the width of the depletion layer for a potential of 1 V across it, q is the charge transferred per ion and φ_0 is the photon flux. Flat-band potential can be calculated from the intercept of the linear part of the J^2-V plot at $J^2=0$ (Figure 2-5). This model has to be treated carefully at small applied potentials and where band bending is relatively small.[13,29] It should also be noted that this method is only applicable if $\alpha L_p \ll 1$, where L_p is hole diffusion length.

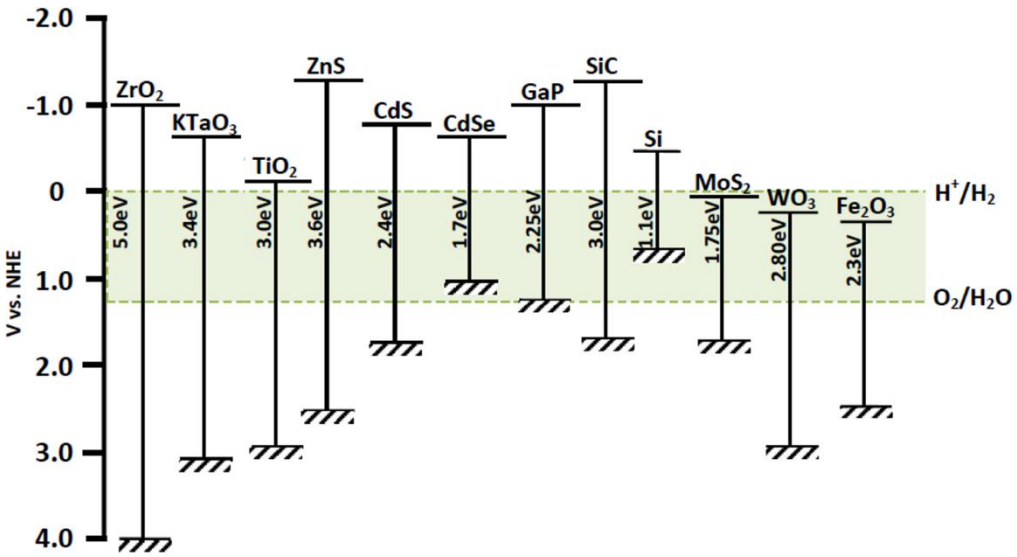

Figure 2-6. The band edge positions of some of the common semiconductors in equilibrium with an aqueous electrolyte (pH=0).[30] The redox potentials of water are highlighted in the figure.

Once the flat-band potential is known and if it is assumed that flat-band potential is equal to the conduction band potential of the semiconductor, it is easy to determine the conduction and valence band edges of a semiconductor with respect to the standard redox scale. The bandgap can be deduced from the optical absorption measurements and also more accurately from external quantum efficiency measurements.[31] Figure 2-6 illustrates the band edge positions of some of the commonly known semiconductors in equilibrium with an aqueous electrolyte. It should be noted that bend edge positions measured from flat-band potential calculations are only valid for a set of given conditions (pH, redox concentration, adsorbed ion concentrations, etc.) and changes in the condition will affect the flat-band potential and consequently band edges of the semiconductor.[25]

2.3 Processes at illuminated semiconductor/electrolyte junctions

Electrical conduction and photo-conduction are essentially governed by the manner of generating charge carriers, their transport in the material and various recombination processes. If the carriers are generated by any means other than optical excitation, the

conduction is referred to as dark electrical conduction or simply electrical conduction.[22] Photo-conduction is the conduction in which the carriers are generated primarily by optical excitation. In the following section, different processes involved in the charge generation, transport and recombination are discussed.

2.3.1 Charge generation

When a semiconductor is illuminated by photons with energies greater than that of its bandgap, the photons are absorbed by the semiconductor and the electrons are excited to higher energy levels at the conduction band and create photo-excited holes in the valence band. The photo-excited electron/hole pairs play a major part in subsequent charge transfer and recombination processes. In general, the effect of photo-excitation on the concentration of the charge carriers is more substantial on minority charge carriers than the majority charge carriers.[32] For example, in n-type semiconductors, where electrons are majority charge carriers, photo-excitation greatly influences the concentration of holes (minority charge carriers) while its effect on electron concentration in the conduction band is minimal. This is due to the fact that under dark conditions the number of majority charge carriers present in the conduction band of an n-type semiconductor is much larger than the number of minority charge carriers at the valence band. Under equilibrium condition,

$$np = n_i^2 \qquad (2.12)$$

where n is electron density, p is hole density and n_i is the intrinsic carrier density which is dependent on bandgap and temperature.[33] When the semiconductor is illuminated, this equilibrium is perturbed. However, if the excited electron/hole pairs are separated they can be transferred and collected.

2.3.2 Charge separation and transfer

Photo-excited electron/hole pairs can be separated under the influence of space charge layer. The collection of photo-generated charge carriers separated by the electric field associated with the space charge layer will lead to photocurrent. Charge transport and

relaxation mechanisms are normally described with the help of the continuity and current density relations.[33] For example, for one dimensional charge injection:

$$\frac{\partial n}{\partial t} = G_e - \frac{\Delta n}{\tau_e} + n u_e \frac{\partial \varepsilon}{\partial x} + u_e E \frac{\partial n}{\partial x} + D_e \frac{\partial^2 n}{\partial x^2} \qquad (2.13)$$

where G_e is electron generation rate, Δn is the excess carrier density, τ_e is the lifetime of the excess electrons, E is electric field, u_e electron mobility, D_e the electron diffusion coefficient, t is time and x is penetration depth from the surface. For uniform optical excitation:

$$G_e(x,t) = J_{abs}(x,t) = J_0(t)(1 - e^{-\alpha x}) \qquad (2.14)$$

where α is absorption coefficient, J_{abs} and J_0 are absorbed photon flux and incident light intensity, respectively. Total photocurrent (i_{ph}) can then be calculated by integration of above equation:

$$i_{ph} = eJ_0 \left(1 - \frac{\exp(-\alpha w_d)}{1 + \alpha L}\right) \qquad (2.15)$$

where w_d is the width of the space charge layer and L is the diffusion length of minority carriers. This equation shows that if αw_d is much larger than 1, all photo-excited minority carriers may be collected and subsequently transferred at the interface and photocurrent will remain constant ($i_{ph} = eJ_0$) at potentials larger than the flat band potential. However, if αw_d <1 then the photocurrent is controlled by diffusion as shown in Figure 2-7.

An important area in studying PEC properties of semiconductor electrodes is to understand the formation of space charge layer within the semiconductor electrode. Under dark conditions, the net charge is redistributed in such a way that an electrochemical potential equilibrium is established at the interface between semiconductor and electrolyte.[33] At the interface, there is an abrupt redistribution of charges due to the mobilisation of ions in the solution.

The formation of a junction at the interface leads to the development of a field in the space charge layer. The charge in the space charge layer per unit area of surface (Q_{sc}) can be calculated using the following equations (Equation 2.16 and 2.17):

$$Q_{sc} = qN_D w_d \qquad (2.16)$$

$$w_d = \sqrt{\frac{2\varepsilon_0 \varepsilon_r}{qN_D}(V_{bi} - V - \frac{kT}{q})} \qquad (2.17)$$

where q is the primary charge of an electron, N_D is the donor density, w_d is the width of the space charge layer, ε_0 is the permittivity of free space, ε_r is the dielectric constant of the material, V_{bi} is the built-in potential drop, V is the applied potential, k is the Boltzmann constant and T is the absolute temperature.

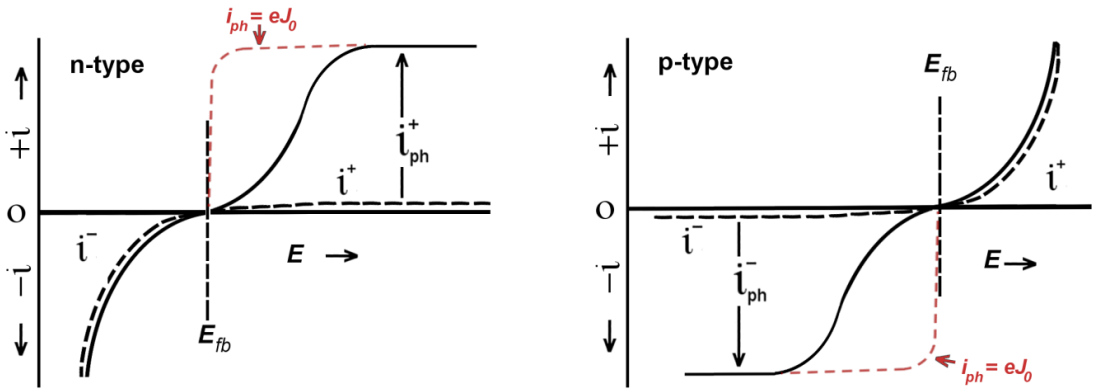

Figure 2-7. Photocurrent-potential graphs of n-type and p-type semiconductor.[20]

2.3.2.1 Electrochemistry of nanostructured semiconductor electrodes

So far, the discussion in this thesis has been generally focused on the basis of solid state semiconductor physics. When a nanostructured semiconductor electrode, which consists of interconnected nanometre size particles, is used the conditions for charge separation and charge transport become very complicated. Nanostructured electrodes have completely different properties comparing to single crystal electrodes in contact with electrolyte. The electrolyte penetrates into the porous structure of the electrode and reaches the surface of the substrate and, therefore, a semiconductor-electrolyte junction occurs at each nanoparticle.[34] The small size of the particles diminishes the presence of an effective depletion layer[35] and increases the importance of kinetics of the reactions at the interface of semiconductor-electrolyte.[36] In a bulk single crystal (classic case), electron-hole pairs are separated by the electrical field present in the semiconductor depletion layer while in a

nanostructured electrode electron-hole separation takes place due to the capture of the photo-generated holes by reduced species in the electrolyte interpenetrated in the matrix of nanopores (Figure 2-8).[37]

Södergren et. al.[38] proposed a model assuming the photo-generated electrons in the conduction band of an n-type nanostructured semiconductor were driven by diffusion due to the concentration gradient of electrons in the film. They introduced a diffusion length for majority charge carriers, which remains constant throughout the whole film and dependent on the rate of recombination losses; the shorter the diffusion length the higher the probability of recombination. Since then, this model has been used to describe the transport properties of nanostructured electrodes.

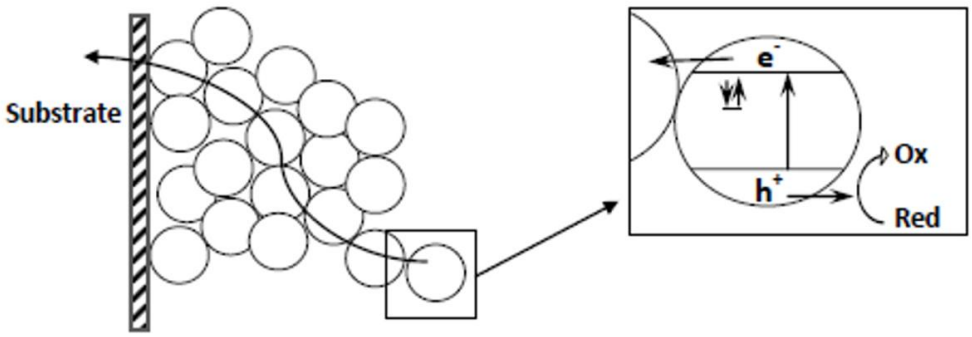

Figure 2-8. A photoelectrode consisting of a nanostructured network contacting a conducting substrate. Electron-hole separation occurs due to the capture of the photo-generated holes by reduced species in the electrolyte interpenetrated in the matrix of nanopores.[37]

Vanmaekelberg and de Jongh[37] also proposed that there was a light-induced electrical field which, together with concentration gradient of electrons, attributed to the electron transport in a porous nanostructured electrode. They showed that the negative charge due to electrons trapped in interfacial bandgap states may shift the band edges to higher energies resulting in an electric field component in the driving force for the transport of electrons. They also found that in an illuminated nanostructured semiconductor electrode the driving force for electron transport was independent of light intensity and in the order of (kT/d), where d is the thickness of the film.[37]

2.3.2.2 Charge transport

Charge transport in a semiconductor material is carried out by different processes. Tunnelling process occurs if an excited electron at a higher energy level tunnels through a potential barrier to an unoccupied state in a neighbouring molecule.[22] The charge carrier moves from site to site through a tunnelling mechanism with a probability of occurrence related to the shape, the height, and the width of potential barrier between the sites.[23]

Another electrical transport mechanism is the hopping process. In this process a localized electron can drift through a solid specimen by hopping from one molecule (or atom) to an unoccupied state of neighbouring molecule if it acquires the energy necessary to overcome the potential barrier.[22] The concept of hopping transport has been applied for electrons, particularly for electronic conduction in amorphous and disordered non-metallic solids.[23]

2.3.3 Charge recombination

2.3.3.1 Recombination in the bulk

When an electron or hole has been excited to a higher energy state, there are three relaxation and recombination pathways by which the energy can be given up when the carrier returns to its thermal equilibrium.[39] For example, the excited electrons can recombine with holes. In general, the excess energy can be given up by

- Emitting photons, a radiative recombination commonly called luminescence,
- Emitting phonons (lattice vibrations) either simultaneously or sequentially, a non-radiative process,
- Raising other free carriers, either electrons or holes, to higher energy states in their bands, another non-radiative recombination process called Auger recombination, after which they may relax by the emissions of phonons.[39]

Radiative processes are mainly involved in the direct electron-hole recombination which is the dominant process in direct bandgap semiconductors. In such recombination processes, the recombination rate and also the halftime of the band-band recombination strongly

depends on the charge carrier density.[20] In case of indirect bandgap semiconductors, such as Fe_2O_3, the dominant bulk recombination process is via deep traps. In this process, the recombination is generally consisted of two steps; firstly, an electron (or a hole in p-type semiconductor) is captured by a trap and then the trapped electron is recombined with a hole. The trapping rate (R_t) depends on the concentration of free charge carriers in the conduction band as well as the number of empty traps.[20] It is best described by Equation 2.18, considering N_t is the trap density in an anodic semiconductor and f_t is the fraction of traps occupied by electrons:

$$R_t = C_n(1 - f_t)N_t n \qquad (2.18)$$

$$C_n = \gamma_n \nu_{th} \qquad (2.19)$$

$$\nu_{th} = \sqrt{\frac{3kT}{m^*}} \qquad (2.20)$$

where m^* is effective carrier mass, γ_n and ν_{th} are electron capture cross section and carrier thermal velocity, respectively. The generalised equation for the recombination via traps under stationary illumination is known as Shockley-Read equation[20] (Equation 2.21), which is also used to explain the recombination at the surface states of semiconductor/electrolyte interface:

$$R = \frac{\gamma_n \gamma_p \vartheta_{th}(np - n_i^2)N_t}{\gamma_n(n + n_1) + \gamma_p(p + p_1)} \qquad (2.21)$$

where γ_p is hole capture cross section, n and p are the electron and hole density, n_i is the intrinsic carrier density and n_1 and p_1 are electron and hole density for Fermi levels located just above and below the trap level.

2.3.3.2 Recombination at the surface

Impurities and defects (such as crystal disorders or dopant ions) would result in the formation of traps which play a major role in the charge transfer and recombination processes in semiconductors. Defects in crystal structure create breaks in the bonding patterns within the semiconductor and distort the electronic coupling, which could

eventually lead to the formation of midgap states (traps). The rate of the surface recombination is described by Equation 2.22, following Shockley-Read equation, if considering that the surface states are associated with single charged centres with single and discrete energy level within the bandgap:

$$R = \frac{\gamma_n \gamma_p v_{th}(n_s p_s - n_i^2)N_t}{\gamma_n(n_s + n_1) + \gamma_p(p_s + p_1)} \qquad (2.22)$$

where n_s and p_s are carrier densities at the surface. The presence of surface states indicates that two processes can take place at the surface states; recombination and charge transfer. If only recombination is considered, then the total flux must be comprised of two components; faradic (J_{ct}) and recombination component (J_s^R):

$$J = J_{ct} + J_s^R \qquad (2.23)$$

However, this is not the case and charge transfer also occurs at the surface states. Therefore, the flux equation for electron and hole capture at the surface can be formulated as shown in Equation. 2.24 and 2.25:

$$J_n^R = n_s N_t \gamma_n v_{th}(1 - f_t) \qquad (2.24)$$

$$J_p^R = p_s N_t \gamma_p v_{th} f_t \qquad (2.25)$$

Several studies of iron oxide photoelectrodes have resulted in the conclusion that poor photo-response of hematite electrodes is due to the presence of surface states which could facilitate recombination.[40,41,42] Dare-Edwards et. al.[42] investigated the surface properties of hematite electrodes comprehensively and showed that anodic shift of photocurrent onset and reduced efficiency of hematite PEC electrodes was due to a large fraction of recombination sites at the surface in form of Fe_3O_4 surface species.

2.4 Fe_2O_3 as a photoanodic material for PEC water splitting

In the last few decades a wide range of materials such as metal oxides, metal nitrides and sulphides has been used as photoelectrodes. As the first reports on PEC water splitting emerged in early 1970s, different research groups started looking for a suitable

semiconductor material to be used as the photoelectrode. The first investigations involved wide bandgap semiconductors such as TiO_2[11], $SrTiO_3$[43] and SnO_2[44]. As discussed previously (see Figure 2-6), TiO_2 and $SrTiO_3$ possess the ideal band edge positions as the conduction and valence band edges straddles the redox potentials of H_2 and O_2 evolution. However, unfortunately these materials only absorb a small amount of solar energy (about 3-4%) as their absorption edge lies in the range of wavelengths of ~360-410 nm. Materials with lower bandgap will absorb a higher portion of solar spectrum raising the hope of efficient solar energy conversion.

Metal sulphides are another group of materials which have attracted considerable interest in the preparation of PEC photoelectrodes. CdS is one of the metal sulphides which has been studied extensively.[45,46] CdS has the bandgap of ~2.4 eV which is a suitable bandgap for PEC photoelectrode. The energy positions of the conduction and valence band edges of CdS allow for photo-dissociation of water without any need for an external bias potential. However, it has the tendency to photo-corrosion under prolonged irradiation as it converts into Cd^{2+} and sulphate (in the presence of oxygen).[47]

Most of the new environmentally-sustainable energy technologies are usually very expensive either due to the cost of the starting material or expensive manufacturing technologies. Therefore, they are in a constant battle with well-established existing technologies. Therefore, production cost and ease of fabrication are the determining factors in the selection process of materials used in PEC water splitting.

Hematite (α-Fe_2O_3) is a strong candidate material as photoelectrodes in PEC water splitting as it fulfils most of the selection criteria of a suitable photocatalyst material for water splitting such as bandgap, chemical and photelectrochemical stability, and ease of fabrication. Although hematite has an ideal bandgap of ~2.1-2.3 eV its conduction band edge is positioned below the hydrogen redox potential hence requiring an external bias to initiate the water splitting reaction. Moreover, photocurrent efficiencies reported for hematite were mostly well below the expected levels. Poor performance of hematite electrodes has been attributed to its relatively slow charge transfer kinetics and a high rate of hole-electron recombination due to its short hole diffusion length.

2.4.1 Crystal Structure of hematite

α-Fe_2O_3 is a common mineral widely known as hematite and is widespread in soil and rocks. Its name "hematite" comes from the Greek name "haima = blood" due to its red colour. However, if it is formed of large and coarse crystalline grains it appears as black or sparkling gray.[48] Hematite is a major source in inorganic pigment industry as a red pigment. As it is a major product of the iron and steel corrosion it has been studied extensively.

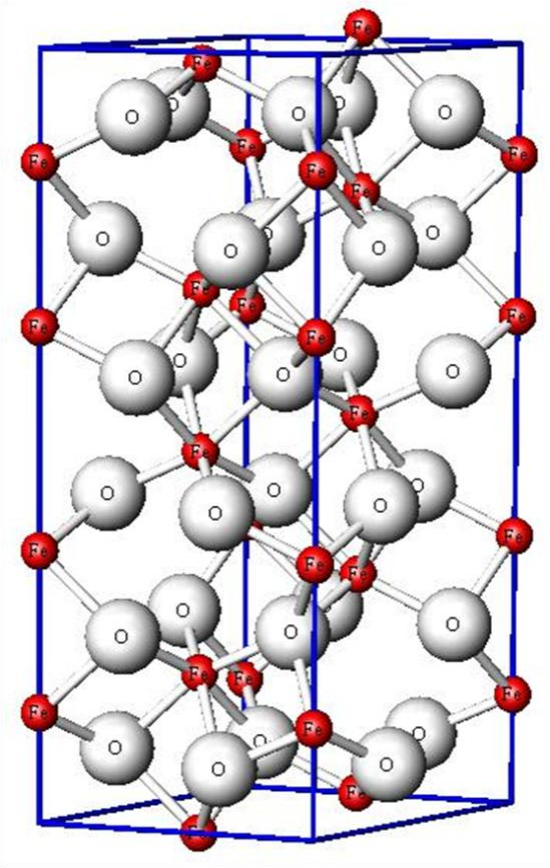

Figure 2-9. Schematic representation of the structure of hematite. Red circles show iron atoms while grey circles denote oxygen atoms.[49]

Hematite is isostructural to corundum (Al_2O_3). Its structure consists of distorted hexagonal (hcp) close-packing of (001) layers of oxygen atoms with Fe (III) ions occupying 2/3 of the octahedral interstices (Figure 2-9).[15,50] Therefore, each oxygen atom is surrounded by four irons and each iron has six oxygen neighbours. This arrangement leads to the formation of pairs of $Fe(O)_6$ octahedra each of which shares edges with three neighbouring octahedral in the same plane and one edge and one face with the octahedron situated at the

adjacent plane.[48] Hematite is usually indexed in hexagonal symmetry, i.e. (hkil), where h + k = -i and i is usually omitted. There are six formula units per hexagonal unit cell (a=0.5034 nm and c=1.375 nm).[48]

2.4.2 Electronic and electrical properties of hematite

Understanding the electronic configuration and electrical properties of iron oxides, especially hematite, is crucial in successful application of α-Fe_2O_3 as water splitting electrodes. Fe^{3+} has the electronic configuration of $1s^2$ $2s^2$ $2p^6$ $3s^2$ $3p^6$ $3d^5$ while Fe^{2+} is $1s^2$ $2s^2$ $2p^6$ $3s^2$ $3p^6$ $3d^6$. Therefore, the electrons in the d orbital and their characteristics are the ones which define the electrical properties of iron oxides.

An orbital is a region in space occupied by either one single electron or a pair of electrons. If two electrons occupy one orbital then they will have opposite spins. There are 5 different d orbitals which are oriented at 5 different orientations in space. The regions within orbitals where the electron density is at maximum are called orbital's lobes. The 5 orbitals are categorised into two set of orbitals according to the direction of their lobes. Three orbitals (t_{2g}), namely d_{xy}, d_{yz}, d_{xz}, each have four lobes which are directed between the coordinate axes of the nucleus. The second set of orbitals (e_g), dx^2-y^2 and dz^2, have their lobes oriented along the axis.[48] In iron oxides and hydroxides, Fe ions are coordinated to negatively charged O^{2-}/OH^- ions. Therefore, due to the electrostatic field of the coordination, the Fe d orbitals do not show equal energies unlike as in their ground state.

d orbitals can be filled in different ways. The general rule of showing the filling of d orbitals is described as $(t_{2g})^n(e_g)^m$ where m and n shows the number of electrons situated at each sets of orbitals. For example, the ground state configuration of tetrahedral coordination for Fe^{3+} is $(e_g)^2(t_{2g})^3$. It means that the first two electrons enter e_g orbitals and the other 3 enter t_{2g}. Tanabe-Sugano diagrams (Figure 2-10) depict the energies of different multi-electronic states (multiplets), formed as the results of electrostatic field splitting caused by the ligands, as a function of crystal field stabilisation energy. This diagram is useful for the interpretation of optical behaviour of iron oxides and provides a useful tool in predicting the electronic transitions between different states.[48]

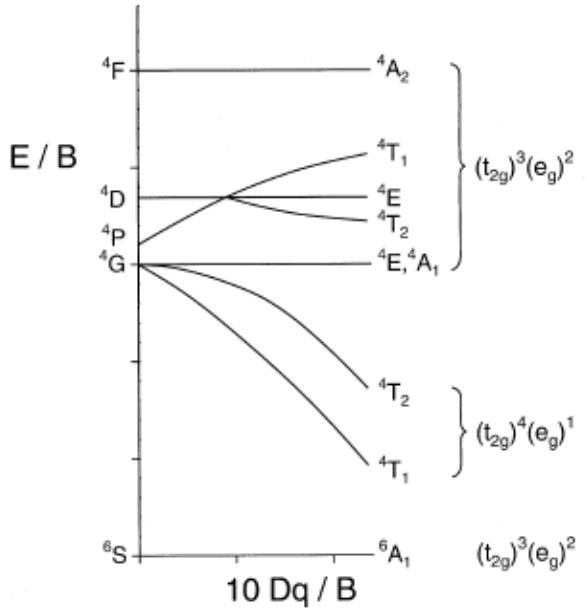

Figure 2-10 . Tanabe-Sugano diagram of high spin Fe^{III}.[48]

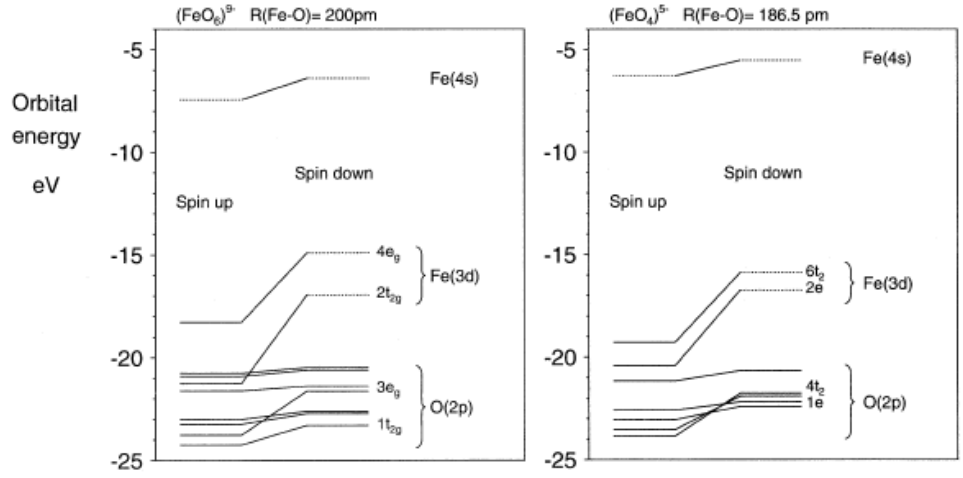

Figure 2-11. Molecular orbital diagram of FeO_6^{9-} and FeO_4^{5-}.[48]

The electronic structure of iron oxide can be simplified by smaller structural entities which resemble similar properties as to of actual oxides. For example, FeO_6^{9-} represents Fe^{3+} in octahedral coordination, i.e. hematite, and FeO_4^{5-} is used for tetrahedral coordination of Fe^{3+} in magnetite (Fe_3O_4). The molecular orbital diagrams of these two types are shown in Figure 2-11. Hematite is an extrinsic semiconductor with a bandgap of ~2.1-2.3 eV.[15] Both n-type and p-type behaviour can be induced in the hematite structure; however, it is more

difficult to induce p-type conductivity. In n-type hematite, the conduction band comprises of empty Fe^{3+} d orbitals while the valence band is composed of full $2t_{2g}$ Fe 3d ligand field orbitals and some admixture from the oxygen antibonding 2p orbitals.[48]

2.5 Fabrication processes of Fe_2O_3 photoelectrodes

A variety of fabrication methods such as sol-gel[51] has been used previously for the preparation of hematite photoelectrodes. Two different types of photoelectrodes have also been fabricated; pellets and films. In the following, the major fabrication techniques for the preparation of both types of hematite photoelectrodes are briefly discussed.

2.5.1 Powder Processing

Preparation of hematite electrodes using the conventional powder processing techniques was one of the first methods used to fabricate pellets of hematite photoelectrodes.[52] In this method α-Fe_2O_3 powders with different purities are used as the starting materials. These powders are then mixed together, pressed and sintered to form the desired photoelectrodes. Doped hematite samples can also be prepared if the starting hematite powders are mixed with the powders of doping agents prior to the sintering. There are disadvantages associated with this method. For example, the electrodes consist of large hematite particles which result in electrodes with small surface areas. The samples produced are very thick and the recombination rate is generally very high. In addition, the process also comprises long and energy-consuming mixing and sintering procedures. As a result of these drawbacks powder processing has only been used in the early stages of the development of hematite photoelectrodes and is not regarded as a suitable method for the fabrication of photoelectrodes anymore.

2.5.2 Spray pyrolysis

Spray pyrolysis is a common process for the preparation of hematite photoelectrodes which has been used extensively by research groups throughout the world. In this method, an iron-containing solution is used as the precursor. The precursor is then converted into

small droplets using an atomiser and is transferred onto a heated substrate. As the precursor sits on the substrate, it undergoes chemical reactions which lead to the decomposition of the precursor and a film is formed.

A wide range of iron precursors can be used in this method. Different concentrations of doping agents can also be added to either the starting precursor or used as a separate precursor. The films produced by this method are fine in microstructure and provide a high internal surface area for the penetration of the electrolyte into the porous hematite photoelectrode. As the deposition is carried out at temperatures around 450 °C there is no need for a further annealing step. Spray pyrolysis is a very fast and versatile technique and it allows for the deposition of translucent films onto various substrates. However, one of the common problems of this method is the clogging of the atomiser jet which increases the maintenance costs of the deposition apparatus.

2.5.3 Chemical vapour deposition (CVD)

Chemical vapour deposition was the first method used in the preparation of hematite photoelectrodes by Hardee and Bard[53,54] in 1976 and 1977. It is very similar to spray pyrolysis in many respects but their fundamental difference is that the reactions in CVD take place in the gas phase; the precursor undergoes decomposition before reaching the substrate and the particles of the desired film material are deposited onto the substrate.

Spray pyrolysis has been the preferred deposition method for the production of hematite photoelectrodes due to the simplicity of the deposition apparatus and availability of starting materials. However, the unprecedented results reported by Cesar et al.[55] have renewed the interest in the fabrication of hematite photoelectrodes using atmospheric pressure CVD (APCVD). One of the reasons behind the recent improvement in the PEC performance is believed to be the unique dendrite nanostructure of the hematite films prepared by this technique. The main advantage of this method is that the apparatus is even simpler than that of spray pyrolysis technique.

A major drawback of APCVD of hematite films is the limited number of iron precursors suitable for this technique as it requires a material with high enough vapour pressure at room temperature. However, other types of CVD such as aerosol-assisted CVD (AACVD) provide

a great degree of flexibility in the selection of starting materials whilst preserving the advantages of APCVD such as simplicity.

2.6 Preparation techniques at high temperature

2.6.1 APCVD

The CVD processes carried out at atmospheric pressure are generally known as APCVD. In this method, the starting material must possess a high enough vapour pressure at the atmospheric pressure to provide a satisfactory deposition rate. Some APCVD precursors are heated to temperatures higher than the room temperature in order to achieve the desired vapour pressure for the deposition. Some reactants in atmospheric-pressure reactors must be highly diluted with inert gases to prevent vapour phase precipitation. Atmospheric pressure reactors are reasonably simple and inexpensive.

2.6.2 AACVD

The AACVD method involves the atomization of a precursor solution into fine, sub-micrometer sized aerosol droplets which are delivered to a heated reaction zone and undergo evaporation, decomposition, and homogeneous and/or heterogeneous chemical reactions to form the desired products. In conventional CVD techniques, the problems of selection and delivery of chemical precursors are often considerable, especially for multi-component products.[56] The lack of proper volatile precursors and the difficulties in achieving the controlled stoichiometry of the final products are the major challenges in the development of CVD processes for new and complex compounds.[57,58] AACVD addresses the availability and delivery issues that are generally encountered in other CVD processes. A wide range of precursors can be used since volatility is no longer crucial, offering more possibilities to produce high quality CVD products at low cost.

In AACVD, precursor's volatility is not a requirement, but the precursor needs to be merely soluble in a solvent from which the aerosol can be generated. Metalorganic compounds as well as metal salts (e.g., nitrates, chlorides, or acetates) can be used as

precursors. In some cases, nanocomposite coatings can also be deposited by generating an aerosol precursor from a colloid or suspension.

AACVD offers better capability and flexibility than the conventional CVD process, especially for the fabrication of multi-component compounds with well-controlled stoichiometry. Inexpensive and environmentally-friendly chemicals can be used as precursors, which is important for large-scale or mass production. Furthermore, AACVD has generally higher deposition rate and a lower overall cost than the conventional CVD method. Compared to the conventional CVD methods, the AACVD technique presents the following key advantages:[59,60]

i. A wider choice and availability of precursors for high quality CVD products at low cost, which is a critical issue for mass production.

ii. Simplification of the delivery and vaporization of precursors via the generation of a precursor aerosol.

iii. High deposition rate, which may be obtained from a high mass transport rate of the precursor and the possible improvement of precursor selection.

iv. A more flexible reaction environment (AACVD can be operated under low pressure, atmospheric pressure, or even in an open atmosphere).

v. Simplification of the synthesis of multi-component products with precise stoichiometric control.

Ultrasonic aerosol generation is the most common method in the AACVD process. An ultrasonic aerosol generator has a piezoelectric transducer placed underneath the precursor solution. When a high-frequency electric field is applied, the transducer vibrates and instigates the formation of fine droplets.[61] The average atomized or nebulised particle size (d_h) is related to the surface tension (T), density (ρ) and the frequency (f). The following formula is used in determining the droplet size:[62]

$$d_h = 0.73\sqrt[3]{\frac{T}{\rho f^2}} \qquad (2.26)$$

Equation 2.26 suggests that when the physical characteristics of a precursor liquid are known, the diameter of the aerosol droplets is only an inverse function of the ultrasonic frequency. A higher ultrasonic frequency will be needed to obtain finer droplets. Ultrasonic generation offers advantages in terms of providing a suitable droplet size for AACVD process.[63]

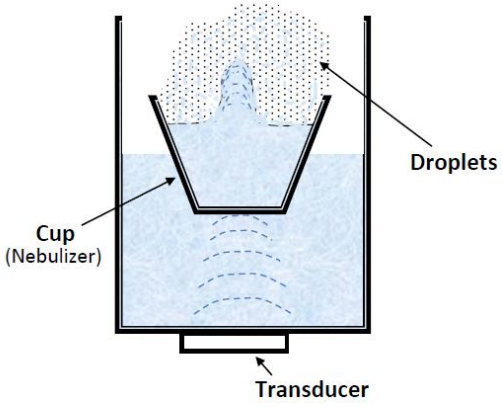

Figure 2-12. Schematic of an ultrasonic aerosol generator.[64]

Carrier gases are used to assist the delivery of the generated aerosol and transport of the aerosol to the reaction zone. Argon and nitrogen are the most commonly used inert carrier gases, while compressed air is also used for the deposition of oxide products. Reactive gases such as H_2 may also be introduced at this stage with other primary carrier gases to aid the subsequent CVD reaction.[65]

2.7 Preparation techniques at low temperature

One approach towards preparation of nanostructured hematite electrode is to fabricate amorphous films at low temperature and then anneal them at higher temperatures to obtain crystalline electrodes. The main advantage of the low temperature methodologies is the better control over the film formation due to the low operating temperatures. These fabrication methods are readily available at industrial scale. The interesting prospect of such methods is the potential to reduce the energy consumption at the post annealing step by the introduction of microwave irradiation. The main goal of this approach is to retain the nanostructure of the amorphous film while increasing the crystallinity of hematite electrodes.

2.7.1 Electrochemical deposition (ED)

Fabrication of thin films of different classes of materials using an electrochemical deposition (ED) route is a well-established method and a wide range of materials has been prepared by this method. ED is considered to be a viable method to prepare hematite (or related compounds such as FeOOH) as thin film electrodes.[66] This solution-based method offers flexibility in tuning compositions and morphologies of thin films through controlling the potential and current, which can have significant implications on improving the intrinsically poor charge transport properties of materials such as hematite. Reports on ED of hematite films, however, have been very scarce[67,68,69] since 2006. The reports published by Zotti et. al.[70] and Kulurani et. al.[71] are among the more recent work on ED of iron oxide. Zotti et al.[70] in 1998 reported ED of amorphous hematite films while the work by Kulkurani et al.[71] involved the preparation of ε-Fe_2O_3 which is an intermediate polymorph between maghemite (γ-Fe_2O_3) and hematite. In 2006, Schrebler et. al.[72] reported an electrochemical route for obtaining hematite. Since then, this method has been extended by McFarland and co-workers[73] at University of California in order to fabricate doped and undoped hematite films as PEC water splitting electrodes and the results have been very promising.

Both anodic and cathodic ED, have been employed to fabricate hematite films. As mentioned earlier, the most typical cathodic deposition method is the one described by Schrebler et. al[72]. In this method, the deposition is based on electrochemical generation of OH^- ions as a result of the reduction of H_2O_2 in a solution containing Fe^{3+} ions. Therefore, the local pH near the working electrodes is increased which would consequently reduce the solubility of Fe^{3+} ions in the solution leading to the precipitation of FeOOH films. The deposited film is then converted to hematite by a subsequent heat treatment step at 500 °C.

In the anodic deposition method, Fe^{2+} undergoes an oxidation step to form Fe^{3+} ions followed by precipitation of FeOOH films. This method, first published by Cohen and co-workers,[67,68] involved the deposition of FeOOH film from a neutral solution (pH 6.6−8.0). As a result, the solubility of Fe^{2+} was limited. Therefore, complexing agents such as ammonium sulfate/ammonium, boric acid/ammonium borate were used to stabilize these ions in solutions. However, the photo-performance of these films was not reported. In a more recent study by Spray and Choi,[66] a new anodic deposition condition in a slightly acidic plating solution (pH 4.1) was reported. This method removed the need to use complexing agents since Fe^{2+} ions were soluble. Deposition in this medium resulted in the formation of

amorphous γ-FeOOH films which were then converted to crystalline hematite by annealing at 520 °C.

2.7.2 Other methods

Low temperature synthesis of hematite nanostructres from chemical solutions is extensively studied and, as a result, methods for the fabrication of a wide range of hematite nanostructures including nanoparticles[74,75], nanocubes[76], nanorods[77] and three-dimensional hierarchical nanostructures[78] are viable. Hydrothermal synthesis as the main solution-based low temperature method is an attractive technique as it provides tailoring of size and morphology, controlled degree of agglomeration, reduced incorporation of impurities, and relatively low processing temperature.

Recently, Tang et. al.[79] reported the fabrication of hollow hematite spindles and microspheres using an $FeCl_3$ solution. Yang et. al.[80] successfully produced hollow sea urchin-like hematite nanostructures and nanocubes using an anions-assisted hydrothermal process with subsequent annealing. Furthermore, Almeida et. al.[81] presented a simple method of producing shape-controllable hematite nanostructures by controlling the concentration of PO_4^{3-} anions under hydrothermal conditions.

Despite all this success, the fabrication of thin films directly from chemical solutions has remained a challenge so far. Hematite, in particular is a difficult material to be fabricated as thin films from chemical solutions since formation of iron hydroxide especially FeOOH is favoured in such systems. In 2000, Pejova et. al.[82] reported the preparation of hematite thin films using a CBD method. The film deposition was basically as a result of the thermal treatment of an aqueous solution of iron (II) chloride containing urea. The overall chemical reaction of the deposition process was suggested to lead to the formation of $Fe_2O_3.H_2O$ through the following reactions:

$$2Fe^{3+} + NH_2CONH_2 + 5H_2O \rightarrow Fe_2O_3 \cdot H_2O + 2NH_4^+ + CO_2 + 4H^+$$

The deposition was performed at 90-100 °C and therefore urea was decomposed to CO_2 and NH_3. As a result of this aging treatment in aqueous medium, $Fe_2O_3.H_2O$ was converted

to FeOOH. In order to obtain hematite, the films were annealed at 300-400 °C. No PEC performance for these films has been reported so far.

2.8 PEC performance of α-Fe_2O_3 photoelectrodes

The first reports on the application of hematite electrodes in PEC cells published by Hardee and Bard[53,54] in 1976 and 1977. They prepared polycrystalline hematite electrodes using CVD and iron acetylacetonate as precursor. Quinn et. al.[83] prepared a single crystal hematite electrode. The behaviour of the single crystal was similar to the polycrystalline electrodes reported by Hardee and Bard reaching the photocurrent density of ~80 $\mu A.cm^{-2}$ at the wavelength of 400 nm and 0.5 V vs. SCE using a 2 M NaOH electrolyte.

Further investigations on the PEC performance of hematite electrodes carried out by Kennedy et. al.[84,85] They used conventional powder processing method of mixing and sintering of hematite powders to prepare electrodes. Their investigations included determination of the flat-band potential and effect of electrolyte and donor density on the solar energy conversion efficiency. They showed that flat-band potential fell into more negative values as the pH of the electrolyte increased. They also calculated the diffusion length in the hematite electrode was around 2-4 nm which was considerably lower than values for TiO_2 (100 nm).

Conductivity of semiconductor electrodes is significantly lower than that of metallic counter electrodes. Pure-phase hematite is a Mott insulator and has poor conductivity which restricts its quantum efficiency in photoelectrochemical processes to very small values.[86] Doping is widely regarded as a solution to this problem. The effect of different doping agents has been studied extensively in the literature. One of the early reports on the effect of doping on the photoactivity of hematite electrodes was published by Shinar and Kennedy[87] in 1982. They studied the effect of different oxides such as ZrO_2, CeO_2, V_2O_5, Nb_2O_5 and also Al_4C_3 on the photoactivity of hematite electrodes prepared using conventional powder processing.

One of their interesting findings was that the best performance achieved was not necessarily for the sample with the lowest doping level as it is expected that low doping levels lead to the formation of a large depletion layer width and consequently, to a higher quantum

efficiency. However, the ideal doping level was different for each doping agent. Addition of Al_4C_3, which is a strong reducing agent, resulted in the formation of FeO and Fe_3O_4 and the doped samples showed the best efficiency. The higher efficiency was contributed to the formation of Fe^{2+} in the structure of hematite which improved the conductivity of the electrode.

Merchant et. al.[88] reported an improved efficiency of the hematite electrode in the presence of Fe_3O_4 on the surface of the hematite films and claimed that it was due to the presence of Fe^{2+} which acted as donor centres which could provide electrons by thermal excitation. However, Fe^{2+} can function as electron trapping centres as the trapped electrons might not be free to conduct and, therefore, would not contribute to photocurrent.[87] The effect of different doping agents will be discussed later.

Khan and Akikusa[89] in 1999 reported a highly efficient hematite photoelectrode prepared using spray pyrolysis method reaching a practical conversion efficiency of 1.84% and the maximum IPCE value of 22.5% at 370 nm. Their results showed a considerable improvement in the apparent donor density of the films, 2.2×10^{20} cm^{-3} at AC frequency of 1000 Hz and in 1M NaOH electrolyte, which was attributed to the preparation method and claimed to be responsible for the improvement in the conversion efficiency. The reported donor density was almost three times higher than that of TiO_2-doped samples previously reported by Kennedy et. al.[85] ($\sim7.3\times10^{19}$ cm^{-3} at 1000Hz and 1M NaOH).

Beermann et. al.[90] studied the effect of nanostructure on the conversion efficiency of hematite electrodes. They prepared electrodes comprising nanorods of hematite parallel and perpendicular to the surface of the substrate and reported IPCE of around 18% at 360 nm and pH=12. The same group studied the effect of light intensity on the conversion efficiency and concluded that IPCE of nanorod electrodes was independent of light intensity.[91]

Photocurrent densities and conversion efficiencies reported for undoped hematite electrodes have not been promising so far. However, significant improvements have been achieved when doping agents have been used. The following section contains a brief summary of the different doping agents and their effect on the conversion efficiency.

2.8.1 Doping (Cation Substitution)

Most of the iron oxides have isostructural equivalents at which other cations such as Al^{3+} replace the Fe^{3+} sites. For example, hematite is isostructural to eskolite (α-Cr_2O_3) and corundum (Al_2O_3). Therefore, it is possible for the Fe^{3+} in hematite to be replaced by trivalent cations such as Al^{3+}, Co^{3+} and Cr^{3+}. The extent of the substitution is determined by the difference in the ionic radii and the valency of the cations.[48] It is worth mentioning that the cation substitution in hematite in not restricted to trivalent cations but other cations such as Si^{4+} and P^{5+} have also been used for this purpose.[48] One of the important implications of the isomorphous cationic substitution in hematite is that it allows for tailoring and improving electrical and semiconducting properties of hematite.

As discussed earlier, doping is believed to increase the conductivity of hematite electrodes and consequently, could lead to an improvement in the PEC performance of hematite electrodes. Several different mechanisms have been suggested to improve the conductivity of hematite by doping. One mechanism is the introduction of lattice strains into the crystal lattice.[92] The substitution of an Fe atom with a cation of smaller size will decrease the Fe-O-metal bond distance. Similar effect is observed when the pressure of ~40-50 GPa is applied on hematite.[93] At this point, hematite experiences a phase transition which induces a breakdown of the d-electron correlation. This breakdown results in the collapse of the magnetic ordering, which consequently leads to the onset of an insulator-to-metal transition due to the closing of the d-d or p-d gap.[94] Small strains to the lattice induced by substitutional doping can effectively reduce the Fe-O-Fe bond distance. Recently, Kleiman-Shwarsctein et. al.[94] showed that the isovalent Al did not contribute to the electronic structure around the band edges of hematite. They suggested that improved PEC performance of Al-doped hematite films was due to the increased conductivity of the hematite as a result of the induced lattice strain by aluminum substitution.

In most cases, however, the improvement in conductivity hence performance has been attributed to preferential ordering of the crystallites and/or lattice distortions. The change in the structural symmetries and easier spin-forbidden transitions has been suggested to contribute to the improved performance of hematite electrodes.[94] Other mechanism suggested for conductivity improvement is the formation of Fe^{2+} sites when tetravalent cation substitution is present. For example, it has been shown that addition of Ti^{4+} increased the conductivity of hematite.[95] The mechanism suggested was that titanium (Ti^{4+}) entered the

hematite lattice substitutionally which led to the formation of Fe^{2+} sites in order to maintain the average charge per cation at three. Fe^{2+} would act as donor centre with respect to the surrounding Fe^{3+} and can provide electrons to Fe^{3+} by thermal excitation; therefore, under the influence of an external electric field, an electric current could be created.

Another explanation is that +4 ions may introduce electrons to the conduction band of the semiconductor and under the influence of a potential gradient the localised electrons can produce electric current.[87] These mechanisms are similar to the mechanism which has been suggested for the improvement of conductivity in thermally-reduced hematite samples.[87] In these samples thermal reduction would result in the production of oxygen vacancies in the hematite lattice. Ionization of the oxygen vacancies would result in either introduction of electrons into the conduction band or formation of electrons which would reduce Fe^{3+} to Fe^{2+}. However, the effect of doping agents is not limited to the improvement of the conductivity. It has been suggested that mechanisms such as improved charge transfer coefficient at the surface of the semiconductor and passivation of the grain boundaries by dopants could be responsible for the improvement of the photocurrent efficiency in doped samples.[96]

2.8.1.1 Niobium (Nb)

Photoelectrochemical performance of an Nb-doped hematite single crystal was the best reported for many years. Sanchez et. al.[97] prepared a Nb-doped Fe_2O_3 single crystal using a chemical vapour transport method, which showed quantum efficiencies of around 40% at 370 nm and +0.5 V vs. SCE in a 1M NaOH electrolyte. It was suggested that Nb entered substitutionally and an improved electron hopping mechanism between Fe^{2+} and Fe^{3+} led to an improvement in the conductivity. Moreover, single crystal hematite did not have any grain boundaries which contribute to a loss in the photocurrent through increased recombination.

2.8.1.2 Titanium (Ti)

Sartoretti et. al.[98] in 2005 presented a comprehensive study on the effect of different dopants on photoelectrochemical performance of hematite electrodes. They prepared doped hematite films using spray pyrolysis method. They studied a wide range of dopants such as

Li, Al, Ni, Cr, and Zn but the best results achieved when Ti was used as the dopant. They observed that a post deposition thermal treatment (annealing in air at 550 °C for 1 hour) of the films increased the performance up to 7-fold. It was attributed to the improvement in the crystallinity of the film. The best results (IPCE of 25% at 400 nm and photocurrent density of 4.08 $mA.cm^{-2}$ at 0.45 V vs. NHE) was obtained when 5% Ti + 1% Al doping was used. It was suggested that the improvement in the conductivity and stabilisation of oxygen vacancies along with an improved crystallinity after annealing were responsible for the increase in the performance of the films.

Glasscock et. al.[96] studied undoped and doped hematite films prepared using reactive magnetron sputtering and Si and Ti as doping agents. They reported that doped samples showed much higher photoelectrochemical performance where Ti-doped hematite exhibited the highest photocurrent of 0.57 $mA.cm^{-2}$ at 0.5 V vs. SCE. The enhanced photocurrent was attributed to reduction of recombination which itself was a result of improved charge-transfer rate coefficient at the surface of the doped-hematite electrode. They also proposed that part of the gain was possibly due to passivation of the grain boundaries by the dopants.

2.8.1.3 Silicon (Si)

One approach to increase the PEC performance of hematite electrode is to modify the nanostructure of the film. High conversion efficiency cannot be achieved unless recombination process is inhibited and photo-generated holes are collected at the semiconductor-electrolyte interface. As mentioned earlier, hole diffusion length of hematite is around 2-4 nm, which will make it even more difficult to prevent or slow down the recombination.

Fabricating a hematite film comprising of small nanoparticles in sizes comparable to the hole diffusion length of hematite is regarded to be a possible answer to this problem. In a series of publications, a group at Swiss Federal Institute of Technology, reported Si-doped hematite films with IPCE values of more than 40%.[99] The improvement was attributed to the structure-directing effects of Si in the hematite films. The first report published in 2005 described the preparation of an un-doped film using both spray pyrolysis and ultrasonic spray methods,[100] however, in a later publication,[55] it was mentioned that films were doped

with Si unintentionally as silicon tubing was used in the preparation setup. They produced hematite films comprising of 100-nm-sized platelets with a thickness of 5-10 nm oriented perpendicularly to the substrate. It was suggested that the leaflet structure allowed for efficient light harvesting while offering a very short distance for the photo-generated holes to reach the electrolyte interface before recombining with the electrons of the conduction band.[100] The formation of the leaflet structure was later attributed to the presence of Si as the dopant.[55]

Although many reports on the effects of silicon doping on PEC performance of hematite films had been published throughout the years[101,102,103] the breakthrough came when Si-doped hematite films where prepared using APCVD. Kay et. al.,[99] in 2006, used iron pentacarbonyl ($FeCO_5$) and tetraethoxysilane (TEOS) as precursors for atmospheric pressure chemical vapour deposition (APCVD) of Si-doped hematite films. These films showed outstanding PEC performance reaching IPCE of 42% at 370 nm and photocurrent density of 2.2 $mA.cm^{-2}$ at 1.23 V vs. V_{RHE}. XRD results confirmed a preferential orientation of [001] planes vertical to the substrate. These planes have the high electric conductivity within these planes (four times higher than that of orthogonal planes to them). It was suggested that this preferential orientation facilitated collection of photo-generated electrons and eventually contributed to the outstanding performance of the films. They also claimed that introduction of a SiO_2 under-layer improved the performance but the reason behind this improvement was not known.

2.8.1.4 Other dopants

So far, the effect of doping agents which result in an n-type semiconductor was discussed. However, if ions such as Mg^{2+} are introduced to the hematite lattice they would induce p-type characteristic to the hematite electrode as they would act as acceptors rather than donors. Quantum efficiency of ~20% in the case of Zn-doped samples has been reported.[104] Table 2-1 summarises the results obtained for different doping agents in preparation and performance of hematite water splitting photoelectrodes.

Table 2-1. Summary of the results obtained for doped hematite photoelectrodes.

Dopant	Preparation Method	Potential (V)	Electrolyte	Light Intensity ($mW.cm^{-2}$)	IPCE (%)	Photocurrent Density ($mA.cm^{-2}$)	Ref.
undoped	Electrodeposition	0.4 vs. Ag/AgCl	1 M NaOH	410	3	0.690	105
Mo					12	2.00	
Cr					6	~1.500	
Undoped	Sputtering	0.5 vs. SCE	1 M NaOH	100	U.A.	Negligible	96
Si					3	0.100	
Ti					15	0.620	
Undoped	Spray Pyrolysis	0.45 vs. NHE	0.1 M NaOH	U.A.	U.A.	0.800	98
Ti						4.000	
Ti-Al						4.000	
Ta						1.000	
Ti-Pt						0.800	
Ni						negligible	
Undoped	Electrodeposition	0.4 vs. Ag/AgCl	1 M NaOH	410	3	0.690	73
Pt					12	1.340	
Undoped	Electrodeposition	0.4 vs. Ag/AgCl	1 M NaOH	410	3	0.690	94
Al					8	~1.000	
Undoped	Spray Pyrolysis	0.5 vs. SCE	1 M NaOH	150	U.A.	Negligible	106
Ti						1.980	
Undoped	Powder Processing	0.7 vs. SCE	5 N NaOH	U.A.	U.A.	Negligible	107
Ta						0.640	
Undoped	Spray Pyrolysis	0.2 vs. SCE	0.5 M H_2SO_4	U.A.	U.A.	U.A.	108
Mg						0.22	
Undoped	Spray Pyrolysis	0 vs. SCE	0.5 M H_2SO_4	40	U.A.	U.A.	104
Zn					20	U.A.	

U.A. = Unavailable

2.8.2 Nanostructure approach

Poor hole transport to the semiconductor/electrolyte interface is one of the limiting factors for the efficient photo-response of hematite photoanodes due to the short hole diffusion length of α-Fe_2O_3. A practical solution to this problem is to fabricate films with high aspect-ratio objects such as nanowires or reduce the size of nanoparticulate features to around 10 nm. As shown in Figure 2-13, it can be concluded that hole recombination can be minimised if the size of the surface features are controlled to be very close to the hole diffusion length of α-Fe_2O_3 (2–4 nm or 20 nm[42]). Another advantage of the fabrication of high aspect ratio films is that the large specific surface area obtained would address the intrinsically slow kinetics of water oxidation by valence band holes.[109]

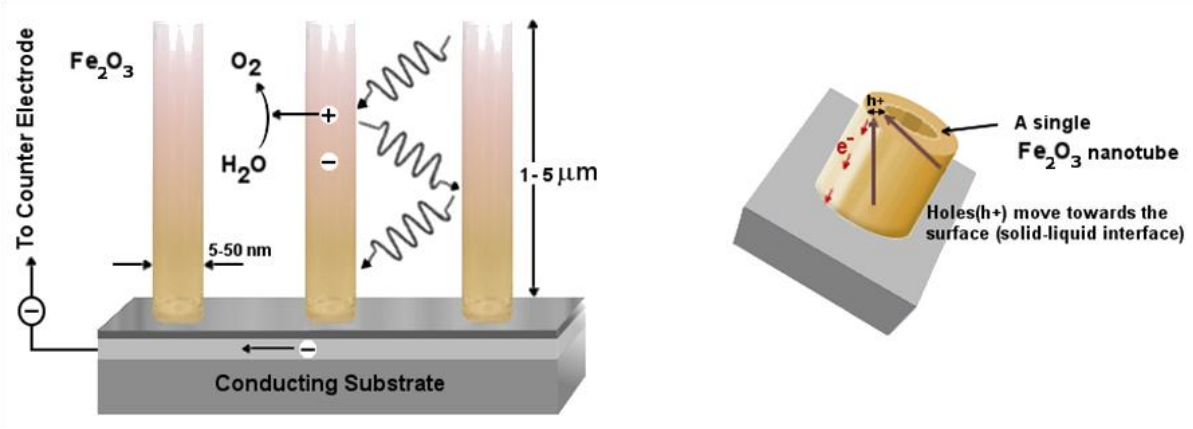

Figure 2-13. Scheme showing the effectiveness of a nanostructured film morphology in charge carrier transport in hematite a film.

It has been shown that recombination at grain boundaries limited the photo-response in nanocrystalline hematite electrodes prepared by particle-based colloidal methods.[110] Therefore, it is essential that high-aspect ratio features such as nanowires consist of only one single crystallite. Vayssieres et. al.[111] observed a blue-shift in hematite nanorod arrays where the primary rod diameter was ~4–5 nm. This phenomenon can have significant implications if the blue-shift is translated as an upward shift of the conduction band, which would lead to the possibility of direct photo-oxidation of water by hematite electrodes without the need for an external bias.

However, if this goal is achieved it will result in the widening of the bandgap of the fabricated hematite. This would lead to the reduced overlap of hematite absorbance spectrum with the solar light visible spectrum. Therefore, a smaller portion of the solar energy would be absorbed and converted into useful forms of energy. Hence, there should be a trade-off between favouring the thermodynamics of the system (i.e. tailoring the energetic of the reactions) and optical absorption. Although results on the fabrication of hematite nanowires and high-aspect ratio features with enhanced PEC performance have been promising[112,113,114] the photo-oxidation of water by using hematite electrodes and without assistance of a bias voltage is yet to be achieved.

2.9 State-of-the-art in preparation and performance

Since the publication of APCVD of hematite with TEOS as dopant by Kay et. al.[99] in 2006 many attempts have been made to match the performance reported by them. Several different approaches have been applied yet the results obtained by Kay et. al.[99] still remain as the highest. It is worth mentioning that all these explorations follow one of the strategies mentioned above; doping or nanostructuring the hematite electrodes.

Spray and Choi[66] reported the fabrication of hematite electrodes through anodic electrodeposition. They performed the deposition in the solution with different pH and tailored the morphology and nanostructure of the deposited film. Their results also confirmed that an important aspect in enhancing the photo-performance of hematite films was the thickness of the films as well as the roughness. They concluded that in order to produce hematite electrodes with enhanced photoactivity the optimum surface area and material loading per unit thickness must be optimised.

As discussed earlier, nanostructures such as nanotubes and nanowires are of great importance in water splitting hematite electrodes. Recently, Mohapatra et. al.[112] reported a sonoelectrochemical anodisation method for the fabrication of ultrathin (5-7 nm) nanotube arrays of hematite on Fe foil. They compared three types of films; nanoporous, nanoparticles and nanotubes. It was shown that 1D nanotube array surpassed the performance of the other two types of the films by an order of minimum 6 times. Despite promising performance, the

maximum solar-to-hydrogen conversion efficiency of 0.84% remained far from the maximum theoretical value of 16.8%.

Thin films of vertically-oriented nanocolumnar structures are thought to be one of the ideal candidate structures for PEC water splitting electrodes. One methodology to produce such nanostructures is glancing angle deposition (GLAD). This technique is also known as reactive ballistic deposition if carried out through the directional evaporation of a metal target under ambient reactive gas. Hahn et. al.[113] prepared nanostructured hematite electrodes by this method and optimised structural and morphological properties of hematite films with the view of improving the performance. They successfully fabricated nanocolumnar structures of hematite at optimised deposition conditions and obtained IPCE values of up to 10% at 420 nm in 1M KOH at 0.5 V vs. $V_{Ag/AgCl}$. However, this efficiency falls below the values reported for hematite films prepared with simpler methods such as electrodeposition.

A novel approach in resolving the problem of short hole diffusion length in hematite is to use ultrathin films of iron oxide in a stacked formation deposited conformal to a nanostructured charge collector. This concept was first suggested by Itoh and Bockeris[115] in 1984. Recently, Sivula et. al.[116] and Le Formal et. al.[117] have applied this approach on hematite electrodes but the results have not been as promising as expected. Sivula et. al.[116] implemented a host-scaffold guest-absorber approach similar to dye sensitised solar cells by using WO_3 as host and hematite as absorber material. Although, the results showed a small improvement in the photo-performance, their claim of the effectiveness of this approach in reducing the recombination in hematite film is highly debatable. The reported 20% improvement in the photocurrent of host/guest design compared with that of hematite only film is likely to have resulted from WO_3 acting as a light absorber itself, since the bandgap of these two materials are very close.

From the practical point of view, any emerging technology such as solar hydrogen generation can only strive in this current global situation if the market price is reasonably low so it can compete with well-established technologies. Therefore, reducing the production costs by minimising preparation steps and energy consumption are of prime importance. Scalable fabrication methods such as screen printing, electrodeposition and CVD are attractive choices. These are highly versatile methods which simplify the fabrication of

nanostructured electrodes while offering suitable control for tailoring structure and properties of thin films. On the other hand, harnessing the microwave energy has a great potential in reducing production costs as it allows significant savings in the energy consumptions during preparation procedures. It could also provide good opportunity to fabricate electrodes with well-defined nanostructures at less demanding conditions.

2.10 Microwave-assisted heating of solid materials

Properties of materials are generally introduced by the preparation processes and the heating procedures used to make them. Time-temperature profiles determine the amount of energy given to the system, which significantly affects the final structure and properties of processed materials. Microwave heating or dielectric heating is one of the alternatives to conventional conductive heating. It utilises the ability of some groups of materials to absorb and convert electromagnetic energy into heat. The use of microwaves in the processing of materials, especially for metals and oxide ceramics, has attracted huge interest in scientific and industrial communities.

Microwave heating offers interesting advantages such as reducing the time and energy thus cost of processing. This would help to develop faster and more reliable routes compared to many other processing techniques. Also microwave heating is an environmentally-benign process with zero carbon emissions. The very first attempts to generate microwaves and their use in industrial scale date back to 1920s-30s. According to Stuerga,[118] the earliest description of the microwave power cavity (magnetron), was published by A.W. Hull in 1921. Just before and during World War II, a great amount of research and technological advances were achieved as microwaves were exploited in the development of radar systems. Microwaves heating of materials was first patented in 1945[118] and the first microwave ovens were introduced in 1952 by Ratheon.[119] Since then, a whole variety of different materials, especially semiconductors,[120-133] has been prepared by microwave-assisted heating (Table 2-2). The application of microwave processing on a commercial scale started in the 1960s by Cryodry Corporation of San Ramon, California, who introduced microwave ovens in conveyer systems.[118] Nowadays, microwave heating is used extensively in both industrial and domestic applications, particularly in food processing.

Table 2-2. Summary of some semiconductor materials processed by microwave irradiation.

Group	Material	Processing Method	Application	Advantage of microwave method	Ref
Semiconductor Materials	CoO	Dispersion of the precursor [$Co(ac)_2$] in benzyl alcohol, followed by heating in a microwave of 2.45 GHz frequency	~	Reaction time only a few mins	120
	CuO	Sample in commercial MW oven	~	Temperature >500^{0}C after 1min	121
	Fe_3O_4	Dispersion of the precursor [$Fe(ac)_2$] or [$Fe(acac)_2$]or [$Fe(acac)_3$] in benzyl alcohol , followed by heating in a MW at 2.45 GHz frequency	~	Reaction time a few mins	120
	Ga_2O_3	Thermal evaporation of raw materials (Ga_2O_3/graphite+charocal 1:3)	Optoelectronics and gas sensors	Fast reaction time (30s)	122
	MnO	Dispersion of the precursor [$Mn(ac)_2$] in benzyl alcohol, followed by heating in a MW at 2.45 GHz frequency	~	Reaction time a few mins	120
	NiO	Sample in commercial MW oven	~	~	123
	SiO_2 nanowires	Thermal evaporation of raw materials (Si/SiO_2 1:1)	Optoelectronic devices	Reaction time 5mins	122
	SnO_2 nanowires	Thermal evaporation of raw materials (SnO_2/ graphite+charcoal 1:3)	Chemical sensor; lithium ion-batteries	Fast reaction time (30s)	124 122 125
	TiO_2 (anatase)	Microwave hydrothermal method: urea and $TiOCl_2$ in MW hydrothermal autoclave	Dye-sensitised solar cell	Single phase anatase produced	126 127
	TiO_2 (rutile)	Microwave Hydrothermal method: $TiOCl_2$ solution placed in teflon double walled vessel MW system (treated temp 160 C for 120mins	Dye-sensitised solar cell	Single phase rutile produced	128 129
	V_2O_5	V_2O_3 oxidised using MW	~	~	130
	BaTiO3	Dispersion of the precursor [Ba + $Ti(OPr)_4$] in benzyl alcohol, followed by heating in a MW at 2.45 GHz	Capacitors	Reaction time a few mins	120
	$BaWO_4$	Synthesised from BaO and WO_3	~	Faster than conventional	131
	CulnSe2	Stoichiometric mixtures of the pure elements by MW irradiation. The reactions were performed in sealed quartz tubes	Solar cells	Reaction time <3mins (conventional method ~48h)	132
	ZnS	Metal powders (Zn) and chalcogen (S) were taken in sealed quartz ampoules evacuated to 10-5 torr, and were exposed to microwaves.	~	Reaction time of only 20mins	133

According to Katz[134] claims of the invention of microwave processing of ceramics dates back to 1984, however, pioneering work carried out by Tinga in 1968 is generally regarded as the real originator in this field. Shortage of natural gas intensified the activity in this field in the mid-1970s.[134] During this period drying and firing of castable alumina ceramics using microwave heating were investigated by several groups.[119,134,135] In the next decades, microwave heating and sintering of uranium oxide,[136] ferrites,[137] and glass-ceramics,[138] among others, were explored (Table 2-1).

Nowadays, microwave heating is used extensively especially in the food industry, ceramic processing and rubber vulcanisation.[139] Rapid heat transfer, volumetric and selective heat transfer, compactness of equipment,[140] and high overall efficiency of high-power magnetrons (85% at 900 MHz and 80% at 2.45 GHz)[139] are among the attractive features of microwave heating systems for industrial applications. However, application of microwaves in processing of materials is limited by the material properties and the changes in the dielectric properties of materials with temperature.

2.10.1 Electromagnetic spectrum and microwaves

Electromagnetic radiation is the energy radiated in the form of a wave travelling at the speed of light.[141] This wave comprises both electric and magnetic fields which oscillate in the direction of propagation and perpendicular to each other (Figure 2-14). Electromagnetic radiation is generally classified by the wavelength (in order of decreasing wavelength and increasing frequency)[141] and electromagnetic spectrum covers the range from a few cycles per second in the radio band to 10^{20} cycles per second for gamma rays (Figure 2-15).[119]

Microwave is the name given to a broad spectrum of frequencies in the electromagnetic spectrum ranging from 300 MHz to 300 GHz which corresponds to 1 m to 1 mm in wavelength. According to Gupta and Leung[141] the term "micro-wave" was first used in a paper by A. G. Clavier in 1931 to describe the propagation of an 18 cm wavelength radio link across the Channel from Dover, UK, to Calais, France.

Most of the microwave frequency band is restricted to government usage and used for communications and defence purposes (e.g. radar). The international table of frequency allocations is provided by The International Telecommunication Union (ITU) operating

within the United Nations System.[141] Different countries utilize this table as a guideline to release specific bands termed as industrial, scientific and medical (ISM) bands for unregulated usage.[141] Most of the common equipments operate at the permitted ISM bands of 915 MHz, 2.45 GHz and 5.8 GHz.

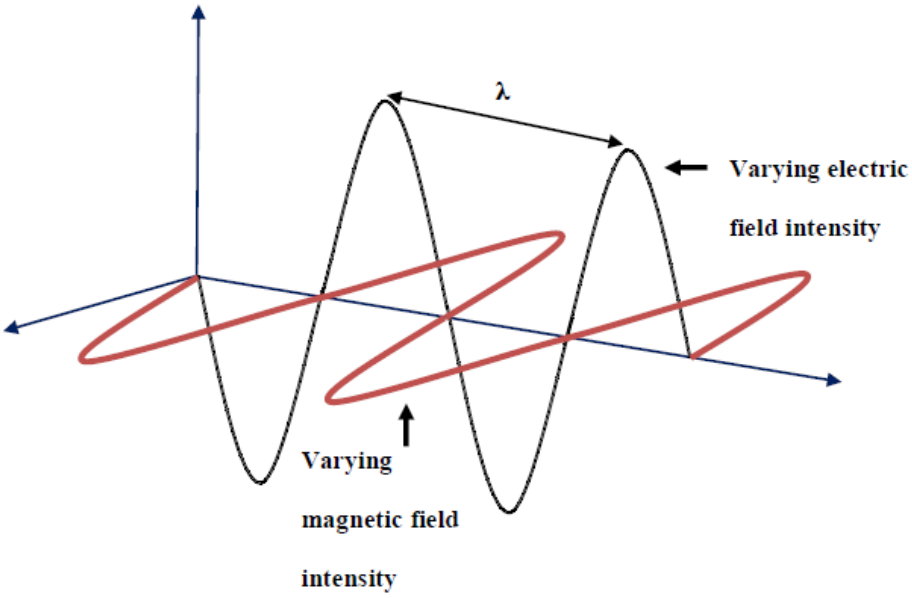

Figure 2-14. Electromagnetic wave propagation.

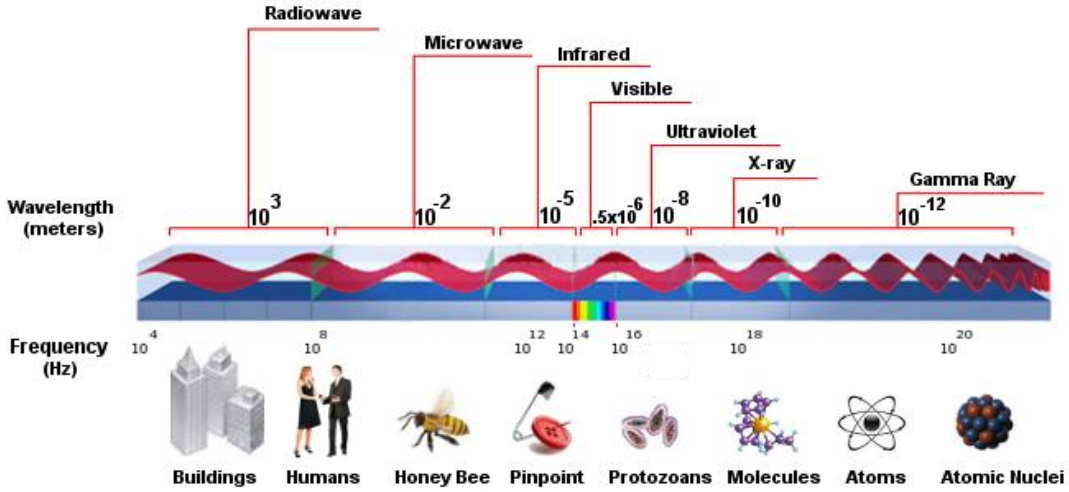

Figure 2-15. Electromagnetic spectrum. The size of the wavelength is compared to different physical objects to highlight the difference across the spectrum.[141]

2.10.2 Microwave generation through magnetrons

The simplest form of a microwave processing system comprises of a microwave source to generate microwaves, an applicator to deliver microwave power to the material/sample and a control system to monitor and maintain the delivery of the power to the material.[141] Different types of microwave generators are available such as power grid tubes, travelling wave tubes, klystron and gyrotron. However, the most common microwave generator is the magnetron which is a highly- efficient, compact size and low cost.

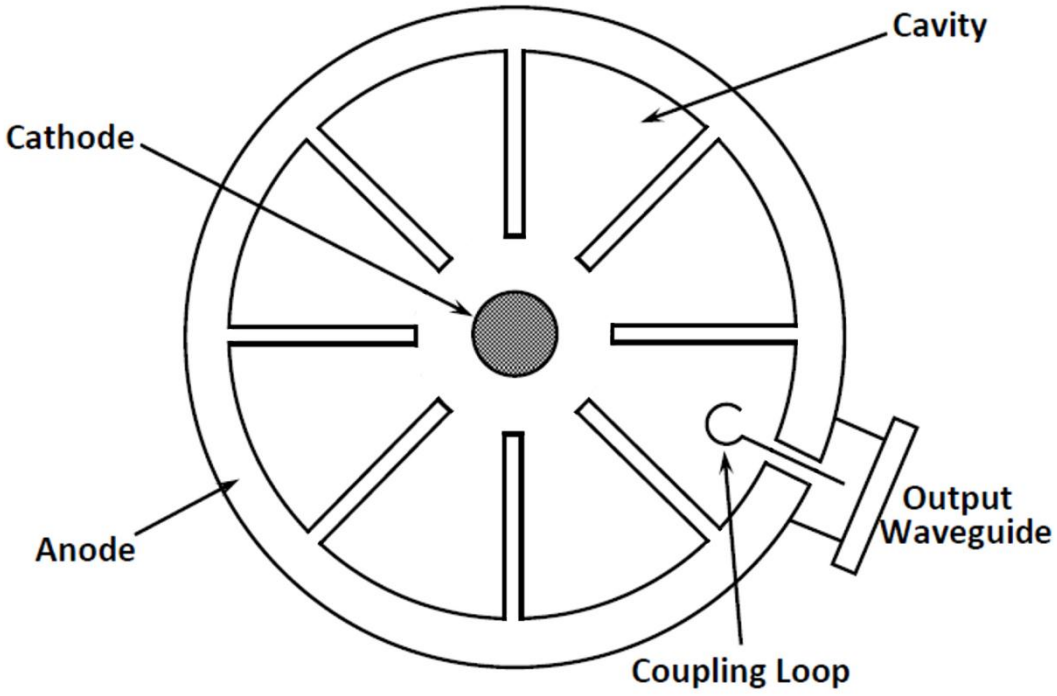

Figure 2-16. Magnetron structure.

Magnetron is essentially a thermionic diode that converts electrical energy to microwave radiation. A typical cross-sectional view of a magnetron cavity is shown Figure 2-16. In the magnetron, heated cathodes act as sources of electrons and electrons are emitted from the cathode. The cathode is surrounded by a circular anode having an array of radial slots acting as resonators tuned to the desired operating frequency.[139] The electric field created by the applied DC voltage draws the electron from the cathode to anode region. However, due to the presence of magnetic field the electrons cannot travel radially outward to the anode but they are forced to rotate circularly in the coaxial space between the cathode and the anode.

Consequently, the bunching of electron cloud occurs and electron cloud would appear as a rotating spoked wheel.[139] In the presence of an electromagnetic field, the electrons entering the positive microwave electric field gradient will accelerate and those entering the negative gradient will deaccelerate.[139,141] The changes in the kinetic energy of the electrons leaving the cathode and arriving at the anode will result in the generation of the microwave power. The transfer of power from the DC power input to the microwave power is extremely efficient. The microwaves are then directed towards a target with the use of microwave guides which are usually made of sheet metals.[142] The output microwave power can be generated in two ways; pulsed or continuous. Pulsed magnetrons produce output power of kilowatts to several megawatts for short durations while continuous magnetrons produce output power of a few watts to kilowatts continousely.[141]

2.10.3 Electromagnetic heating

The fundamental relationship between energy, E, frequency, v, wavelength, λ, can be written as:

$$E = hv = \frac{hc}{\lambda} \qquad (2.27)$$

where c is the speed of light. While X-rays, for example, provide enough energy for the excitation of inner or core electrons in materials, microwaves can only provide sufficient energy to excite molecular rotations.[118]

All materials are formed of charged particles. The fact that these charges can be polarised by an applied electric field and the extent to which this polarisation could follow extremely rapid reversals of the electric field forms the basis of electromagnetic heating. This determines the ability of the material to be heated by electromagnetic radiation at high frequency range.

Generally speaking, materials can be divided into two main groups; conductors and insulator. In conductors, electrons move freely and if an electric field is applied an electric current will be generated. Except in the case of superconductors, it is resistive heating which will heat up conductors as a result of the flow of electrons. In insulators where electrons do

not flow freely, it is the electronic reorientation or the distortions of induced/permanent dipoles, i.e. net polarisation, which cause the heating.[119]

2.10.4 Polarisation

A dielectric material is a material which comprises of either induced or permanent dipoles. When it is placed between two electrodes it acts as a capacitor, i.e. charge is stored. Rotation of dipoles or displacement of charge in an electric field leads to polarisation of the dielectric material. There are several mechanisms - namely electronic, ionic (atomic), molecular (dipolar) and interfacial (space-charge) polarisation - which contribute to the net polarisation of a dielectric material when interacting with microwaves.

A. Electronic polarisation

The origin of the interaction of materials with microwaves stems from the response of the charged particles to the applied electric field. Electronic polarisation is the mechanism that involves the displacement of the electron cloud around the nuclei. As shown in Figure 2-17, when the electric field is applied the electron cloud is shifted from its equilibrium with regards to its nuclei and along the direction of the applied field. This type of polarisation occurs at most of the frequency regimes but drops off at very high frequencies (10^{15} Hz).[143] Electronic polarisation as a result of displacement of valence electrons in covalent solids such as silicon and germanium is responsible for large dielectric constants of covalent crystals (dielectric constant of Si = 11.9).[141]

B. Ionic (atomic) polarisation

When the positive and negative ions or atoms are shifted from their equilibrium lattice sites within their molecules and crystal structures, ionic (atomic) polarisation occurs. The relative displacement of ions or atoms under applied electric field will result in the formation of a net dipole moment which is not zero (Figure 2-17). Ionic polarisation mainly happens at infrared frequency range (10^{12} to 10^{13} Hz).[143] Alkali halides such as potassium fluoride or

sodium chloride and also combination of elements from Groups I and VII of the periodic table are among the materials which undergo ionic polarisation when an electric field is applied.[141]

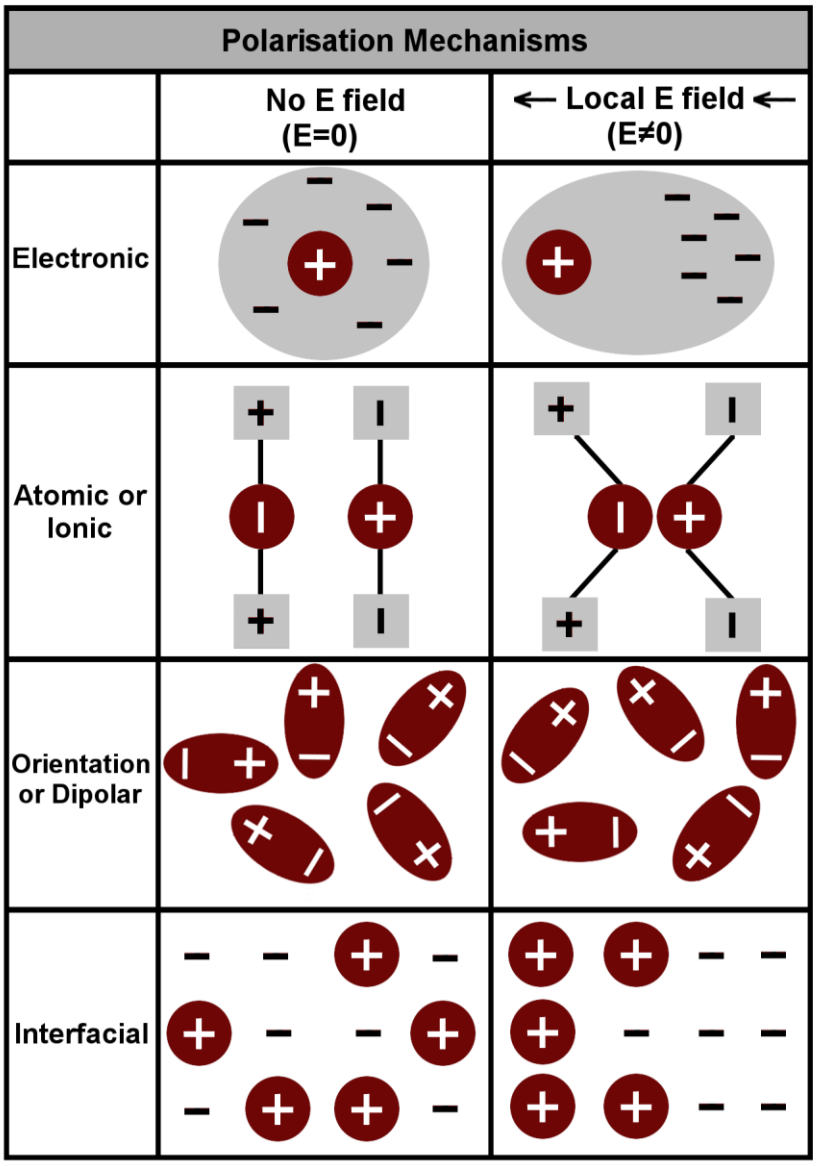

Figure 2-17. Schematic of different polarisation mechanism and the position of charged particles/species within a material under electromagnetic field.[141]

C. Molecular (dipolar) polarisation

A group of materials called polar dielectrics, such as water and hydrogen chloride, are made up of molecules that contain permanent dipoles (dipolar moments). In the absence of

external electric field, the permanent dipoles are distributed randomly in such a way that net dipole moment is zero. Under an applied alternating electric field the asymmetric polar molecules or dipoles attempt to align themselves parallel to the electric field by rotation, leading to molecular (dipolar or orientation) polarisation. At microwave frequencies, the dipoles do not have enough time to respond to the alternating electric field by rotating to align with the field. Therefore, there is a phase difference between the orientations of the electric field with that of the dipoles. This phase difference is responsible for the release of energy from molecules as a result of random collisions between them, leading to dielectric heating. Dipolar polarisation is the mechanism responsible for the majority of microwave heating observed in solvent systems.[143]

D. Interfacial (space-charge) polarisation

Within a material there is equal number of positive and negative charge carriers and ions. These charged species are accelerated under an applied electric field until they are faced by a barrier. The barrier could exist either within the material at grain/phase boundaries and defect regions, or between two materials, for example, at free surfaces. The displacement of the mobile charges and their build up at the barriers dictate the polarisation of the material. This polarisation that occurs in heterogeneous systems is known as interfacial polarisation, also termed as space charge or Maxwell-Wagner polarisation.

2.10.5 Frequency dependence of polarisation mechanisms

Different polarisation mechanisms are frequency dependent and the contribution of each mechanism varies with frequency. Electronic polarisation involves the displacement of electrons around the nuclei. Electrons have little inertia since they are species with small mass, which could follow the alternating electric field up to high frequencies in the electromagnetic spectrum, e.g. visible and ultraviolet region.[141] At these high frequencies, dipoles do not have sufficient time to rotate as they respond to the electric field. Since dipoles do not rotate and no motion is induced in the molecules, thus no energy transfer occurs and no heating is observed.[143] At the other end of the electromagnetic spectrum, at low frequencies around radio frequency range, the dipoles rotate under the influence of

external electric field. However, they have the time they require to align parallel to the electric field as the orientation of the electric field changes. Therefore, the rotation of dipoles occurs almost in phase with the alternating field. As a result, although some energy is gained by the molecule in this process and some is lost due to the collision, the total heating effect is minimal.[143] Dipoles have different rotational motions than that of the vibrations of heavy nuclei or electron clouds around nuclei. The vibrational motions of heavy nuclei (which form chemical bonds) and also vibrational motions of electron clouds around nuclei occur at much faster speeds than the rotational motions of dipoles. This difference in the time scale of different motions generates discrete energy levels within the energy spectrum of matter leading to the formation of small regions associated with electronic, ionic, dipolar and interfacial degrees of freedom.[118] With regards to microwave frequencies (for example ~10^{10} Hz), it is primarily dipolar and interfacial polarisation (together with resistive heating) which are responsible for microwave heating. Microwave frequency is low enough to allow the dipoles sufficient time to respond to the alternating electric field and rotate and does not stop them from responding. However, on the other hand, it does not provide the dipoles with the sufficient time to follow the alternating electric field simultaneously, hence generates a phase difference between dipole rotation and electric field, which causes the energy transfer as a result of random collisions and induces microwave (dielectric) heating.

2.10.6 Loss mechanisms

The mechanisms through which materials interact with microwave and convert microwave energy to heat depend on a variety of parameters such as composition, microstructure, frequency and temperature. This conversion of energy is completed by three main loss mechanisms which contribute to the heating of materials by microwave irradiation; conduction, dielectric and magnetic losses.

A. Conduction loss

Conduction loss is a major contributing factor in microwave heating of metals and semiconductors. Conduction losses are responsible for heating of metals with high conductivity thus low resistivity when a large current density is passed through the material.

Similar type of loss mechanism is present in case of heating liquids and slurries as dissolved salts and inclusions provide ions as charge carriers. It has also been shown that introduction of fine metal powders increased the microwave absorption and the rate of solid-state reactions.[144]

Current research shows that conduction losses as a result of eddy currents induced in highly conductive metals (i.e. magnetic induction) are key in microwave heating of such materials. The interaction of material with magnetic field leads to the formation of eddy currents which force the conducting electrons towards a narrow region near the surface of material. This behaviour is known as skin effect. The depth at which this phenomenon exists within the material is defined by penetration depth (skin depth) which is described in section 2.10.7 (p.66).

B. Dielectric loss

As discussed earlier, dielectric materials interact with microwaves and undergo different polarisation mechanisms. The energy of electromagnetic field is converted into heat if the polarisation lags the time harmonic electric and magnetic fields. The heating of dielectric materials is therefore partly due to the dielectric losses which include the losses generated from inertial, elastic and frictional resistance against the movement of dipoles.

B. i) Complex Dielectric permittivity

The interaction of materials with electromagnetic waves (electromagnetic properties of materials) are characterised by two complex physical properties, dielectric permittivity ε^* and magnetic permeability (susceptibility) μ^*. The storage of electromagnetic energy within the matter and the thermal conversion of electromagnetic energy with regards to the frequency of the electromagnetic irradiation are the two main points of polarisation phenomena resulting from the interaction between electromagnetic waves and dielectric material.

Complex permittivity or dielectric permittivity describes the ability of dielectric material to absorb and store electrical potential energy and is described by the real permittivity or

dielectric constant, ε', representing the penetration of microwaves into the material, and the loss factor, ε'', characterising the ability of the material to store the energy.

$$\varepsilon' = \varepsilon_0 \varepsilon_r' \qquad (2.28)$$

$$\varepsilon^* = \varepsilon' - j\varepsilon'' \qquad (2.29)$$

where ε_0 is the permittivity of free space (ε_0=8.85×10^{-12} F/m) and ε'_r is the relative permittivity. The loss tangent, $\tan\delta$, is indicative of the efficient ability of the material to convert absorbed energy into heat and is also used to describe the dielectric response:

$$\tan\delta = \frac{\varepsilon''}{\varepsilon'} \qquad (2.30)$$

where the angle δ is the phase difference between the polarisation of the material and the alternating electric field. For optimum coupling, a balanced combination of moderate dielectric constant, ε', which allows for the adequate electromagnetic wave penetration and high loss (maximum loss factor, ε'', and tan δ) are required.

B. ii) Debye equations

Generally speaking, Debye equations are the basis for understanding the dielectric properties of materials.[145] Debye formulated the behaviour of permanent dipoles in liquids and also solutions of polar molecules in non-polar solvents. His approach basically considers the behaviour in alternating electric fields arising from the rotation of spherical dipoles in a viscous medium dominated by friction. Debye deduced the equation

$$\varepsilon^* = \varepsilon' - j\varepsilon'' = \varepsilon_\infty + \frac{\varepsilon_S - \varepsilon_\infty}{1 + j\omega\tau} \qquad (2.31)$$

where ω is the angular frequency, ε_s and ε_∞ are the dielectric constants at d.c. and very high frequencies, respectively. τ is the relaxation time that controls the build-up and decay of polarisation as the external electric field is applied or removed

$$\tau = \frac{\pi\eta D^3}{2kT} \qquad (2.32)$$

where η is viscosity, D is the molecular diameter, k is the Boltzmann constant and T is temperature. Separating the real and imaginary parts of the Equation 2.31, it is obtained that

$$\varepsilon' = \varepsilon_\infty + \frac{\varepsilon_s - \varepsilon_\infty}{1 + \omega^2\tau^2} \qquad (2.33)$$

$$\varepsilon'' = \frac{(\varepsilon_s - \varepsilon_\infty)\omega\tau}{1 + \omega^2\tau^2} \qquad (2.34)$$

The plot of Debye equation against $\omega\tau$ is shown in Figure 2-18. As illustrated, as the frequency is increased a point is reached at which the molecular polarisation starts to lag behind the alternating electric field hence contributing less to the total polarisation. This fall results in a reduction in the dielectric constant and a rise in the loss factor. This is when the energy is dissipated within the material. In solid dielectrics relaxation times are mostly longer than those proposed by Debye equations, therefore the notion of activation energy U_a is introduced which is the energy required by a dipole to position itself at a different orientation. The relationship between activation energy and relaxation time can be simply obtained from Equation 2.35:

$$\tau = \tau_0 e^{U_a/kT} \qquad (2.35)$$

where τ_0 is a temperature dependent constant. For most of dipolar solids activation energy is very large which leads to significantly small values for dielectric losses in such materials.

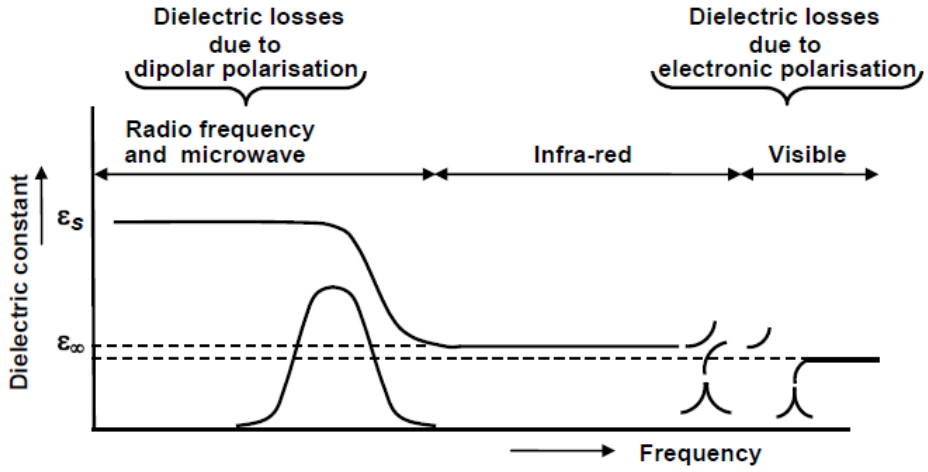

Figure 2-18. The plot of Debye equation against $\omega\tau$.[145]

iii) Magnetic loss

Magnetic losses play an important role in microwave heating of magnetic materials such as Fe_3O_4. Magnetic permeability (susceptibility) accounts for the losses of a material due to an alternating magnetic field. Similar to that of permittivity, permeability (μ') is the product of the permeability of the free space ($\mu_0=4\pi\times10^{-7}$ H/m) and relative permeability, μ_r:

$$\mu' = \mu_0\mu_r' \qquad (2.36)$$

Therefore, complex permittivity is written as

$$\mu^* = \mu' - j\mu'' \qquad (2.37)$$

where μ'' represents the magnetic loss factor as a result of the relaxation and resonance processes in an alternating magnetic field.

2.10.7 Penetration depth

Microwaves can penetrate into conducting materials up to a specific depth. This maximum depth is called penetration depth. The penetration of electric field is defined as the depth at which the magnitude of the field strength equals $1/e$ (=0.368) of its value at the surface. The penetration depth of high loss materials such as conductors can be calculated using Equation 2.38:

$$d = \sqrt{\frac{\rho}{\pi f \mu_0 \mu'}} \qquad (2.38)$$

where ρ is the resistivity of the material. As it clearly shows penetration depth depends on frequency of the electromagnetic field, resistivity and permeability of the material. For example, penetration depth is controlled by the permeability: the higher the permeability, the shorter the penetration depth. Table 2-3 summarises penetration depth of several materials at frequency of 2.45 GHz. Penetration depth ranges from micron to meters. For example, Fe has penetration depth of 3.2 microns while the penetration depth of alumina reaches 126 meters.

Table 2-3. Penetration depth and resistivity of a selected number of metallic materials.[141]

Material	Penetration depth (μm) at 2.45 GHz	Resistivity ($\times 10^{-8}\Omega m$)
Aluminium (Al)	1.7	2.709
Copper (Cu)	1.3	2.255
Iron (Fe)	3.2	9.87
Lead (Pb)	4.7	21.1
Nickel (Ni)	2.7	7.12
Tin (Sn)	3.5	11.5
Tantalum (Ta)	3.7	13.4
Tungsten (W)	2.4	5.39
Zinc (Zn)	2.5	6.01

2.11 Interaction of materials with microwave

Material interaction with microwaves falls broadly into three general categories. First group is transparent materials which are low dielectric loss or insulating materials. In the case of transparent materials microwaves pass through the material with little or no loss in intensity. Examples of this group of materials include quartz, glass and air. The second group includes opaque materials, usually conductors and sheet metals with free electrons, where microwaves are reflected by the material and do not penetrate. Third category includes materials that absorb microwaves based on their dielectric loss factor. It covers a wide range of materials from conductors to insulators, which is usually referred to as high dielectric loss materials or lossy dielectrics. These materials take up the energy produced by the microwave field and are heated up rapidly.

However, there is also a fourth group which is known as mixed absorbers. In industrial applications, this type of interaction would be associated with ceramics and polymer composites. Mixed absorbers take advantage of selective heating as the component of high dielectric loss absorb the microwaves, passing through to the component with low dielectric loss and hence retaining the energy.

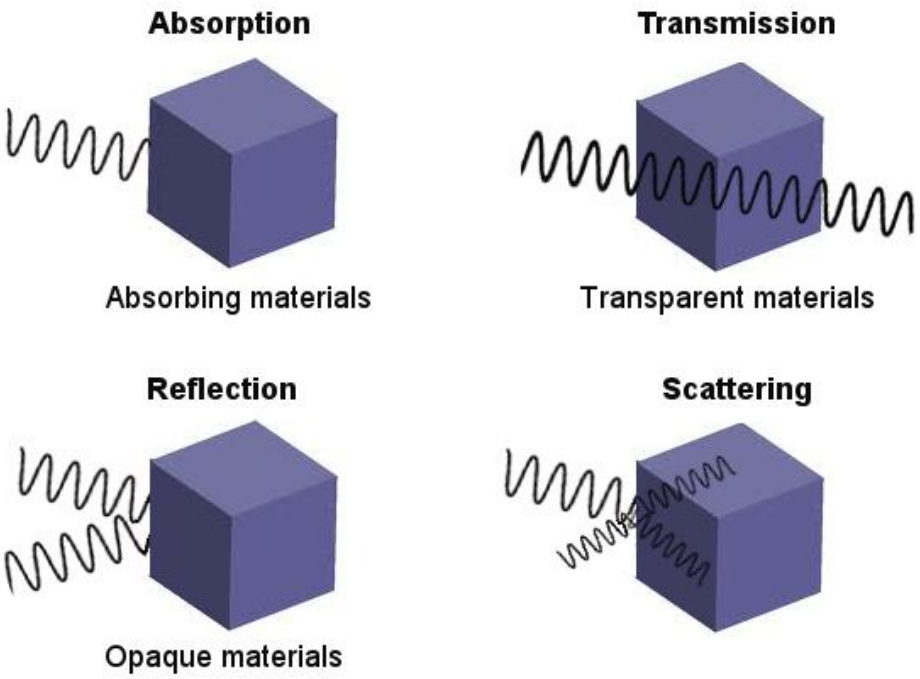

Figure 2-19. The interaction of different classes of materials with microwave is summarised in this picture. 4 classes of materials are categorised with respect to their properties.[141]

A common method to assist microwave heating of low loss materials is to increase the temperature with radiant heat up to a critical temperature where microwave absorption becomes more significant. This hybrid approach provides a more uniform temperature gradient as the external heat minimises the losses from the surface.[119]

2.11.1 Advantages and challenges of microwave heating

The major benefits of microwave processing can be simply summarised as the following:[146]

1) Volumetric uniform heating
2) Selective heating in composites
3) Better control on heating and cooling ranges

4) More efficient heating of thermal insulators such as ceramics which require longer processing times at high temperatures
5) Environmentally-friendly route for processing of materials
6) Cost savings due to the shorter time, lower temperatures, less energy consumption and reduced floor space
7) Enhanced properties of final product for example improved mechanical properties
8) Increased yields

However, it is important to mention the challenges of microwave heating too. One of the major drawbacks is that it is difficult to apply the method directly to process materials that absorb microwaves poorly. Another important issue that must be addressed is the difficulty in controlling accelerated/local heating (thermal runaway) leading to the formation of hot spots. Other problems such as inverted temperature profiles, arcing and the interaction of with plasmas are also present which need to be explored carefully before industrial exploitation of microwaves.[146]

2.11.2 Interaction of microwaves with Fe-based materials

The interaction of materials with microwaves depends upon the mechanism through which the material reacts to alternating electric and magnetic fields of electromagnetic radiation. The general assumption is that dielectric materials interact with microwaves in a different way than semiconductor materials and metals do. Dielectric loss is the dominant factor in microwave heating of dielectric materials such as pure oxides. Therefore, a large part of heating comes from the interaction of electric field of electromagnetic irradiation and magnetic losses play only a minor role. For conductive materials such as metals, it is generally the magnetic losses that are responsible for heating of metals using microwaves.

Most of the current theories concerning microwave interactions are based on the behaviour of the materials with electric field of microwave radiation. These theories only apply to dielectric materials and do not provide a comprehensive explanation of the behaviour of low dielectric loss materials such as metals. It is actually expected that due to small penetration depth of metals at common microwave frequencies they cannot be heated

by microwave heating. Bulk sheet metallic materials are extensively used as microwave guides since they have very small penetration depths and reflect the majority of incident microwaves. This is why it is prohibited to put metallic objects in domestic microwave ovens because it can cause arcing and result in equipment damage.

Fe, its oxides and ferrous alloys are used in an extensive range of applications and their use constitutes the largest percentage of metals used in the world. Walkiewicz et. al[147] reported successful microwave heating of metallic powders for the first time. In the 1990s, microwave was used in the synthesis of intermetallic alloys, carbides and nitrides.[148,149] Later, researchers at Penn State University[150] carried out a comprehensive study on microwave sintering of metals including ferrous alloys and concluded that microwave sintering not only provided a faster process at lower processing temperatures but the properties of final products was also improved significantly. This enhancement was attributed to the improved microstructures obtained by microwave sintering.

Cheng et. al.[150] showed that magnetic losses were responsible for heating of Fe powder using microwave heating. This observation agreed with the suggested theory that it is the eddy currents, generated as the result of the interaction of Fe with the magnetic field component, which contribute to the microwave heating of metals such as Fe. It was also observed that FeO and Fe_2O_3 displayed typical characteristics of metal oxides when they were exposed to microwave irradiation; they respond to the electric field of electromagnetic wave and dielectric losses are contributing factors to the heating of these oxides using microwaves. However, magnetite (Fe_3O_4), which is a well-known magnetic oxide of Fe, showed significantly improved heating rates when exposed to the magnetic field component.[150] It was clearly shown that magnetite, unlike other forms of iron oxide, responded to both electric and magnetic field component of microwave irradiation.

The processing of materials using microwaves has seen significant interest in the last few years. The majority of research is conducted using domestic or modified microwave ovens and a wide spectrum of materials have been synthesised most notably carbides, nitrides, complex oxides, phosphates and silicides.[142] However, attempts on microwave processing of iron oxides have been limited to microwave assisted hydrothermal techniques and microwave assisted plasma CVD processes.

Microwave assisted plasma CVD of iron oxides[151] which uses a gas feed of $Fe(CO)_5$ to synthesise a thin film of iron oxide has shown that Fe_3O_4 and γ-Fe_2O_3 nanoparticles with a hexagonal structure, typical of iron oxide, are achievable with a microwave power of 360 W. α-Fe_2O_3 was obtained at higher powers with a thin layer of carbon covering the spherical nanoparticles.

Microwave-assisted hydrothermal processing has dominated the research on preparation of iron oxides.[152,153] Although feasibility of the application of microwave heating in producing different particle shapes such as nanorings,[154] sheets and spheres[152] has been reported the exact role of microwave heating in altering the properties of iron oxide particles is not clear. From the processing point of view, it has been shown that the use of microwave irradiation would lead to shorter synthesis time, higher yields, better particle shape control and reduced chemical plant size.[152,154 ,155,156]

The overall results obtained from different processing techniques of iron oxides using microwave energy indicates important advantages such as faster, cleaner processes with higher yields. However, there seems to be a significant gap in the research related to the microwave assisted annealing of metallic Fe thin films to form iron oxide. It is expected that the conversion of iron into iron oxide using a microwave assisted process would be far simpler and it is envisaged that the oxidation of the iron could occur at either lower temperatures or faster times than are currently reported. It is also envisaged that the less demanding processing conditions associated with the microwave approach combined with the specific advantage of rapid heating and cooling would be beneficial for the fabrication of α-Fe_2O_3 thin films with the required nanostructure. This is a critical requirement for superior PEC performance.

Chapter 3

3 Experimental methodology

3.1 Sample preparation methods

3.1.1 Substrate cleaning

Microscopic soda glass and fluorine-doped tin oxide conductive glass (FTO) were used as the substrate for film deposition. The FTO substrate was supplied by Pilkington Group Ltd., UK, in two different types, TEC 8 and TEC 15 with sheet resistivity of 8 and 15 Ω/square, respectively. Before deposition, glass substrates were cut to 1×2 cm in size and cleaned according to the following procedure and then stored in ethanol.

1) Clean in ultrasonic bath for 15 minutes using distilled water
2) Rinse with distilled water for 10-15 times
3) Clean in ultrasonic bath for 15 minutes in isopropanol
4) Wash with distilled water
5) Clean in ultrasonic bath for 10 minutes using distilled water
6) Clean in ultrasonic bath for 15 minutes in acetone
7) Clean in ultrasonic bath for 15 minutes in absolute ethanol

3.1.2 APCVD

3.1.2.1 Precursor chemicals

Iron pentacarbonyl ($Fe(CO)_5$, 99.9%, metal purises, Sigma-Aldrich, Dorset, UK), tetraethoxysilane (TEOS, 98%, GC, Sigma-Aldrich, Dorset, UK), tetramethoxysilane

(TMOS, 98%, GC, Lancaster Synthesis, Morecambe, UK) and trimethyl orthoformate (TMOF, 98+%, Lancaster Synthesis, Morecambe, UK) were used as precursors as-received.

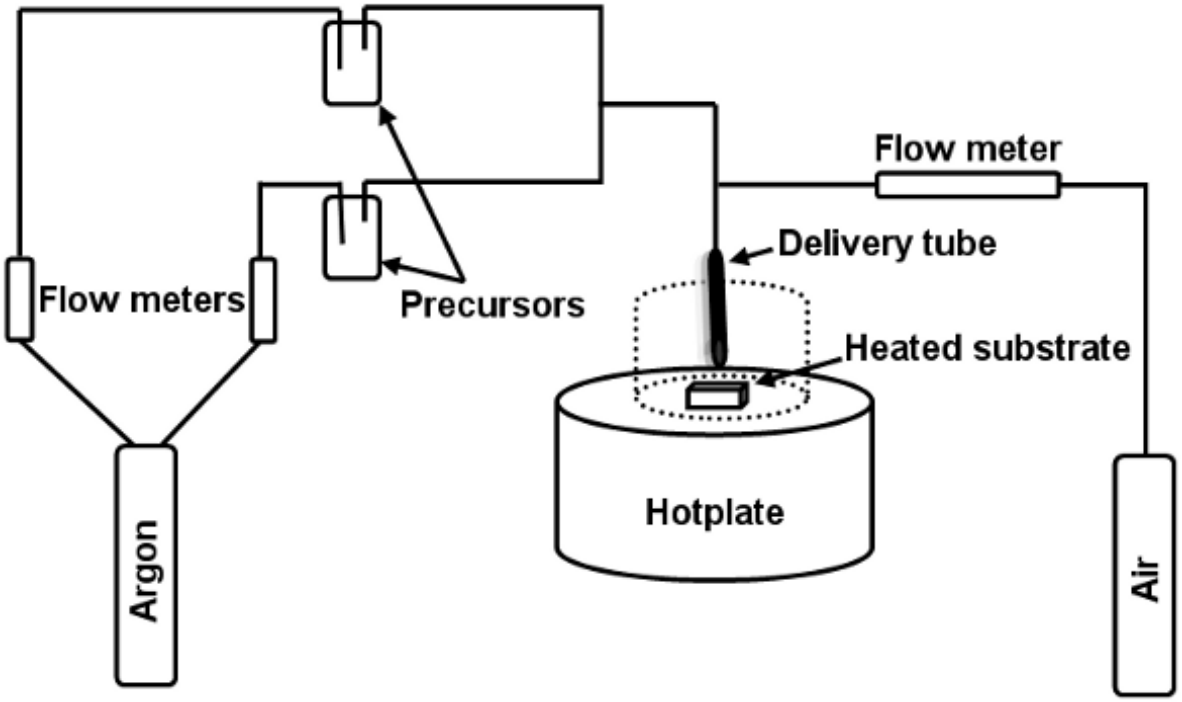

Figure 3-1. Schematic of the APCVD apparatus.

3.1.2.2 Deposition conditions – Iron pentacarbonyl as the source of Fe

A schematic of the deposition setup is shown in Figure 3-1. Films were deposited by APCVD where iron pentacarbonyl ($Fe(CO)_5$), tetraethoxysilane (TEOS), tetramethoxysilane (TMOS) and trimethyl orthoformate (TMOF) were used as precursors. In this deposition apparatus, Ar gas is bubbled into the precursors at different flow rates and then the aerosol of different precursors are mixed and directed towards a heated substrate using air as the mixing gas. The undoped sample which was prepared using only iron pentacarbonyl is referred to as PP or pure pentacarbonyl sample where doped samples are named after the doping agent used for their preparation, i.e. TEOS, TMOS, TMOF. TMOF was selected as the Si-free additive as it closely resembles the molecular structures of Si precursors used in this work (TMOS and TEOS).

Different deposition parameters such as time, temperature, diameter of the delivery tube, distance between the delivery tube and substrate, and flow rate of Ar and air were changed until the best conditions directed by film quality were achieved. Substrate temperature was measured by a K-type thermocouple and was maintained at about 375 °C during deposition. For optimised conditions Argon was used as the carrier gas and bubbled through 1 ml of each liquid at flow rates shown in Table 3-1 (The flow rates mentioned here are of the samples with the best PEC performance for each type of sample). Aerosols were then mixed with air at the flow rate of 1.7 L/min and the mixture was delivered to the substrate using a glass tube with an inner diameter of 10 mm positioned 20 mm above the heated substrate. The deposition time for all samples was maintained at 3 minutes. The temperature during deposition was measured by measuring the surface temperature of an FTO glass situated next to the substrate onto which the film was being deposited.

Table 3-1. Carrier gas (Ar) flow rate for different precursors.

Sample Name	Argon flow rate (ml/min)			
	$Fe(CO)_5$	TEOS	TMOS	TMOF
Pure Pentacarbonyl (PP)	17	-	-	-
TMOF	17	-	-	20
TMOS	17	-	2	-
TEOS	17	55	-	-

3.1.2.3 Deposition conditions – Ferrocene as the iron source

Ferrocene ($Fe(C_5H_5)_2$, 98%, Lancaster Synthesis, Morecambe, UK) and iron pentacarbonyl ($Fe(CO)_5$, 99.9%, metal purises, Sigma-Aldrich, Dorset, UK) were used as sources of iron. As ferrocene is in the form of powder at room temperature and its vapour pressure is not high enough to satisfy the requirements of a typical APCVD precursor, it was

heated to 160 °C using a hot oil bath. Then, the aerosol was brought into a chamber using argon as the carrier gas and directed towards the heated substrate using air. The delivery tube was positioned 20 mm above the substrate which was heated to 400 °C. The deposition conditions are shown in Table 3-2. It is worth mentioning that in order to make comparison between APCVD of iron pentacarbonyl and ferrocene the deposition conditions of iron pentacarbonyl were slightly altered to obtain films with similar thicknesses from the two different methods.

Table 3-2. Deposition conditions for two different samples. D is the diameter of the delivery tube and d is the distance between the delivery tube and FTO substrate.

Sample Name	Precursor	Flow rate		Temperature (°C)	Time (min)	d (mm)	D (mm)
		Ar (ml/min)	Air (L/min)				
Ferrocene (E18)	Ferrocene	150	2	400	18	20	10
Iron pentacarbonyl	Iron pentacarbonyl	20	2	400	5	20	10

3.1.3 AACVD

3.1.3.1 Precursor chemicals

Ferrocene ($Fe(C_5H_5)_2$, 98%, Lancaster Synthesis, Morecambe, UK) was used as a source of iron and toluene was used as the solvent.

3.1.3.2 Deposition conditions

In a typical deposition, 20 ml of a 0.1 M solution of ferrocene in toluene was used as the starting precursor. Air at a flow rate of 150 ml/min was used as the carrier gas, and the flow rate was controlled by a thermal mass flow controller (Bronkhorst UK Ltd., Suffolk, UK). Substrate slides (1cm×2cm) were placed inside the deposition chamber (reactor tube) and

then heated up to 450 ºC for 20 min before carrying out the deposition. The aerosols of the precursor solution were formed by keeping the round bottomed flask which was filled by the solution in a water bath above the piezoelectric modulator of an ultrasonic humidifier. The generated aerosol droplets of the precursor were transferred into the heated substrate by the carrier gas. The reactor was placed in a tube furnace. The deposition time was varied from 2 min to 1 hr but the best performance was obtained for the deposition time of 45 minutes. Figure 3-2 shows a picture of the AACVD set-up.

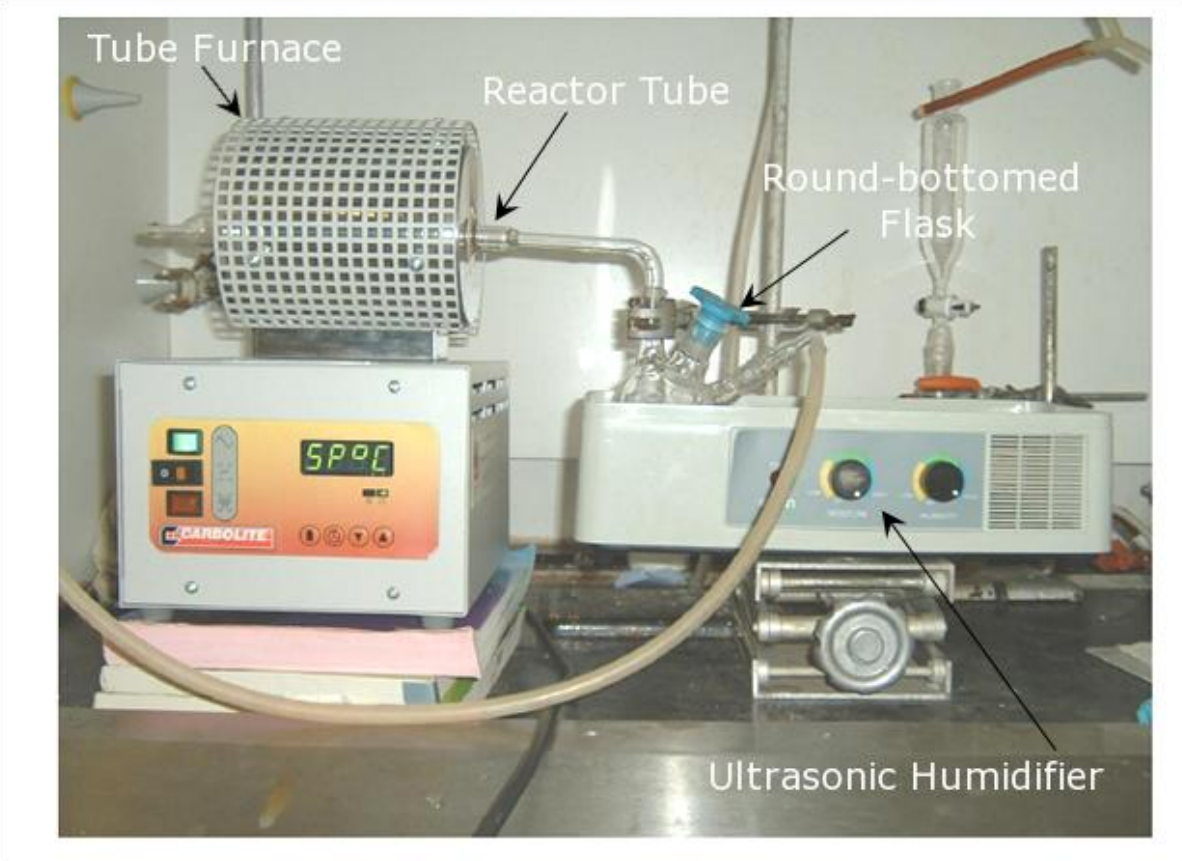

Figure 3-2. AACVD apparatus comprising of an ultrasonic humidifier and a tube furnace.

3.1.4 Electrochemical deposition

3.1.4.1 Cathodic electrodeposition of iron

The cathodic electrodeposition of Fe was conducted using the method reported by Cao et. al.[157] with some modification. The electrochemical solution consisted of 0.002 M $FeCl_3.6H_2O$ (reagent grade, SigmaAldrich, Dorset, UK) in absolute ethanol and stirred at 60

°C for 2 hours. The electrochemical deposition of Fe films was performed in a two-electrode configuration where FTO was used as a cathode and a Pt wire as an anode. An applied potential of 6.2 V for 50 seconds resulted in a black film of metallic Fe (thickness = 100-150 nm measured by cross-section SEM) on the FTO substrates. The current-time graph of a typical deposition of undoped sample is shown in Figure 3-3. The deposition of Fe film was confirmed by XRD. The films were then washed by deionised water and left in air to dry.

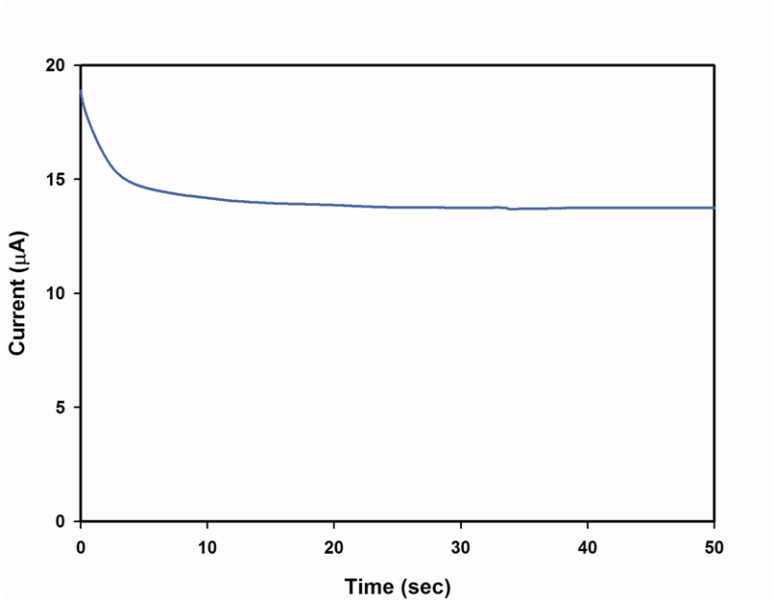

Figure 3-3. Current vs. time graph for electrodeposition of Fe.

In order to study the effects of Si doping on the properties and performance of photoelectrodes, Tetraethoxysilane (TEOS) was used as the source of Si. Solutions with different molar ratios of Si/(Fe+Si) (5%-40%) were prepared. A minimum concentration of Si/(Fe+Si) = 10% showed an appreciable improvement in photo-performance. Higher concentrations of TEOS (up to Si/(Fe+Si) = 40%) did not result in any further improvement in PEC performance. Hence all the results reported here are for the films prepared from the solutions with the molar ratio of Si/(Fe+Si) = 10% and that the dopant concentrations mentioned are for the electrochemical solutions. Doped Fe films were deposited from Si-containing solutions by applying 7 V for 50 seconds to achieve similar thicknesses to those of undoped Fe films.

3.1.5 Annealing procedures used

3.1.5.1 Conventional annealing

Thermal annealing of films were carried out using two different methods; conventional and microwave heating. Conventional annealing was carried out in a tube furnace (MTF-10-25-130, Carbolite, Hope Valley, UK); the sample was heated at the rate of 20 °C/min to the desired temperature. Both ends of the tube were kept open to allow for the flow of air. After annealing the furnace was turned off and the samples were left in the furnace to cool down. The temperature of the samples was measured using a K-type thermocouple.

3.1.5.2 Microwave-assisted annealing

Microwave-Assisted annealing was performed using a modified microwave oven (MC8087ARS multimode cavity, LG, Milton Keynes, UK) shown in Figure 3-5 capable of producing a tuneable continuous power output up to a maximum of 1000 W operating at 2.45 GHz frequency.

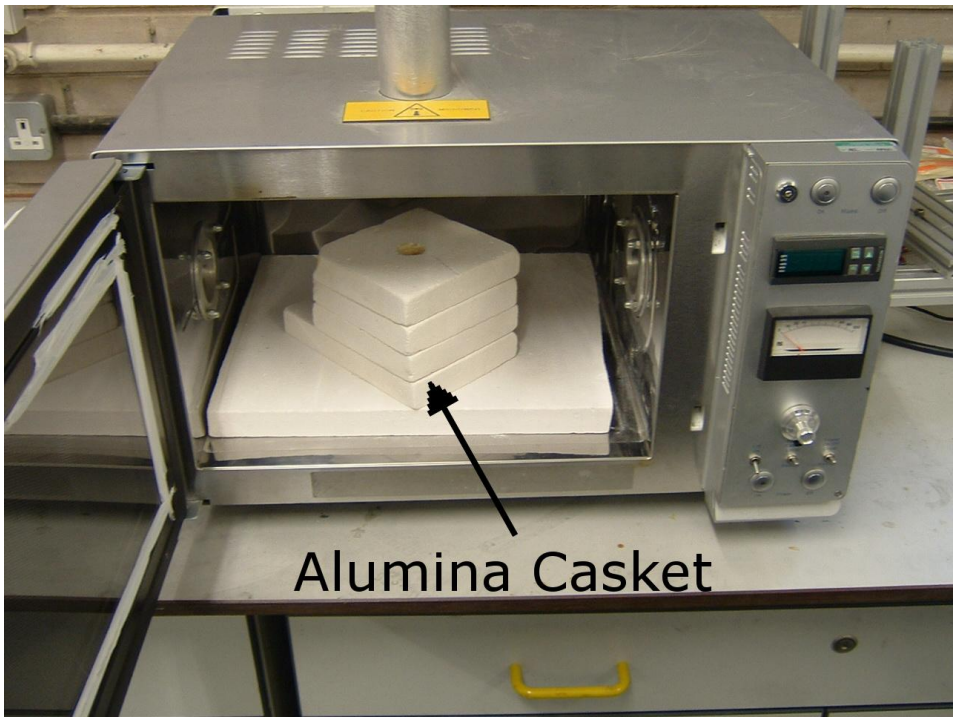

Figure 3-4. The microwave oven with the alumina casket positioned inside the oven.

Electrodeposited films were placed inside a high purity alumina casket to minimise the heat loss. SiC rods were used as secondary susceptors.[158] The top of the casket had a hole at the centre which allowed for the temperature measurement of the film using a thermal imaging camera (FLIR Thermovision A40, FLIR Systems, West Malling, UK) and temperature was recorded automatically (Figure 3-6) using ThermaCAM Researcher software.[159] Temperature calibration was performed using the boiling point of water and also melting point of V_2O_5 as described elsewhere.[160] Microwave power was manually increased so that the heating rate of 20 °C/min was maintained and the desired temperature was achieved.

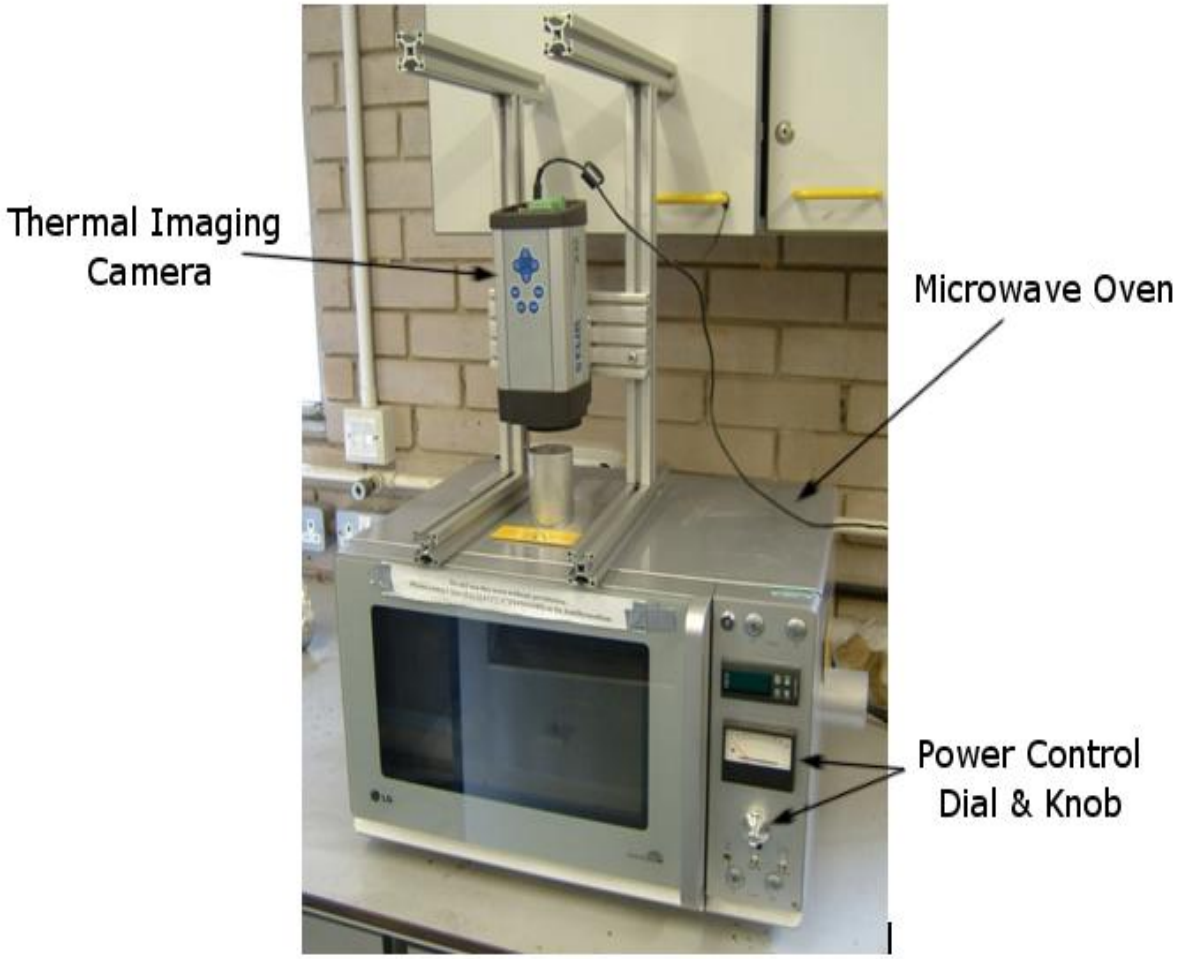

Figure 3-5. Picture of the microwave oven with the thermal imaging camera.

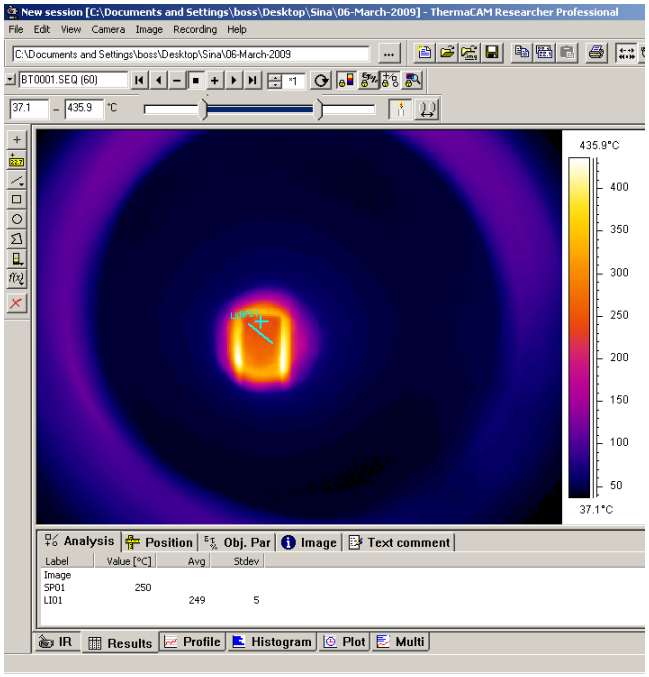

Figure 3-6. Screenshot of the ThermaCAM software analysing the readings taken by the thermal imaging camera showing the deposited film is being heated to 250 °C using microwave heating. It shows a relatively uniform temperature distribution across the surface of the film (249±5 °C). The difference in the temperature is mainly due to the thickness variations and the distance from the SiC susceptors.

3.2 Characterisation techniques used

3.2.1 XRD

X-ray diffraction (XRD) is a common method of examining the crystal structure of materials by exploiting the process of X-ray scattering from crystal planes. In a crystalline structure atoms are arranged in periodic crystal lattices with planar spacings *d*. When a crystalline material is irradiated by X-rays constructive interference of such rays will follow the Bragg condition (Equation 3-1):

$$n\lambda = 2d \sin\theta \qquad (3-1)$$

where λ is the wavelength of the X-rays, n is an integer and θ is the angle of incidence. The characteristic *d*-spacings of the crystal are identified by scanning the sample at a wide range

of incident angles. Then, the obtained XRD pattern is compared to the reference diffractograms in the database to identify the crystal structure of the material in question.

Figure 3-7. Picture of the Bruker D8 XRD system.

An important feature of XRD analysis is its ability to estimate the crystallite size in the material provided that certain criteria are met. The crystallite size (t) is obtained from so called Scherrer equation (Equation 3-2):

$$t = \frac{K\lambda}{B\cos\theta} \qquad (3-2)$$

where λ is the wavelength of the incident X-ray (in nm), K is a constant (here assumed to be 0.94[161]), B is the full-width-half-maximum (FWHM) value of the specific diffraction peak (in radians), and θ is the angle at which the peak is observed. The width of the peak is strongly affected by instrumental effects and stress in the film.[162] As shown in Equation 3-2, in highly

crystalline materials where crystallite size is large B must be small thus sharp peaks are observed. In other words, the less crystalline the material the broader the peaks.

The phase and crystallinity of deposited films on FTO and glass slides (soda glass) were characterised using a Bruker D8 (Figure 3-7) X-ray diffractometer (XRD) operating with monochromatic high-intensity Cu Kα (λ= 0.154184 nm) radiation using a PSD detector at an angular range of 2θ = 10° to 80°. The background was then removed from the XRD patterns and the XRD patterns were normalised to the major FTO substrate peak and smoothed using the diffractometer software.

3.2.2 XPS

X-ray photoelectron spectroscopy (XPS) is one of the most widely used surface characterisation methods. It is also known as electron spectroscopy for chemical analysis (ESCA). The basics of XPS are illustrated in Figure 3-8. The surface of the sample is placed in a vacuum environment and then irradiated with photons in the X-ray energy range. Following a direct transfer of energy from the irradiated photon to the electrons at the core level, photoelectrons are emitted. The emitted photoelectrons escape into the vacuum chamber and are then separated according to energy and counted.[163] The energy of the photoelectrons is a characteristic of the atomic and molecular environment from which they originated.[163] Similarly, the concentration of the emitting atom can be characterised by the number of photoelectrons.[163]

A basic XPS analysis of a surface will provide information on all the elements present (except H and He), both qualitatively and quantitatively. More sophisticated analysis would result in obtaining comprehensive information about the chemistry, electronic structure, organization, and morphology of a surface. In the outermost 10 nm of a surface, XPS can provide information such as identification of all elements (except H and He) present at concentrations >0.1 atomic %, semi-quantitative determination of the approximate elemental surface composition (error ≤ 10 %), and information about the molecular environment such as oxidation state.[163]

XPS spectra were recorded on a VG Scientific Escalab Mk I (Thermo VG Scientific, West Sussex, UK) instrument operating with an un-monochromatized Al Kα X-ray source

(1486.6 eV)(Figure 3-9). No etching was performed prior to analysis. It is extremely difficult to uniquely identify different oxidation states of Fe by XPS since the binding energies for Fe^{2+} and Fe^{3+} are very close to each other and in fact Fe^{2+} appears as a satellite peak of the main Fe^{3+} peak. However, it can be used to examine the presence of the Fe^{2+} qualitatively and it is a useful technique for identifying the presence of dopants.

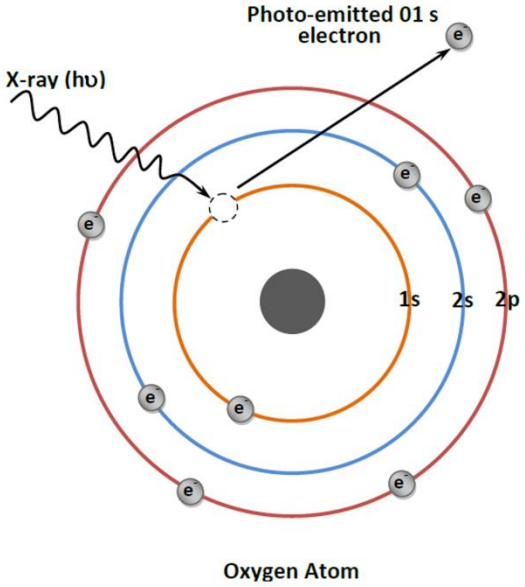

Figure 3-8. Basics of XPS and the corresponding energy transfer as the result of X-ray photons interacting with electrons in the material.

Figure 3-9. VG Scientific Escalab Mk I XPS instrument.

3.2.3 Raman spectroscopy

Raman spectroscopy is based on studying vibrational modes which are either not observed via IR or result in only weak IR absorption bands.[163] These vibrational modes are observed due to inelastic (Raman) scattering of a laser beam which interacts with phonons in the solid.[162] Interaction of a molecule with electromagnetic field would lead to the transfer of energy from the field to the molecule only if the Bohr's frequency condition is met (Equation 3-3):

$$\Delta E = h\nu = h\frac{c}{\lambda} = hc\bar{\nu} \qquad (3-3)$$

where $\bar{\nu}$ is wavenumber and ΔE is the energy difference between two quantised states.[164] If the energy difference between the incident and emitted radiation equals one quantum of vibrational energy the emitted photons are called Stokes photons.[163] However, if the molecule loses vibrational energy and upon re-emission the obtained photons possess higher energies than the exciting energy, these photons are called anti-Stokes photons.[165] The scattered irradiation involves two parts; firstly, Rayleigh scattering where the frequency remains the same as the incident beam and secondly, Raman scattering at which frequency is shifted by the value of the vibrational frequency of the molecule.[164] This Raman shift in the energy of the laser photons leads to the formation of Raman spectrum of specific material hence enabling Raman spectroscopy to be used as a method to identify different compounds.

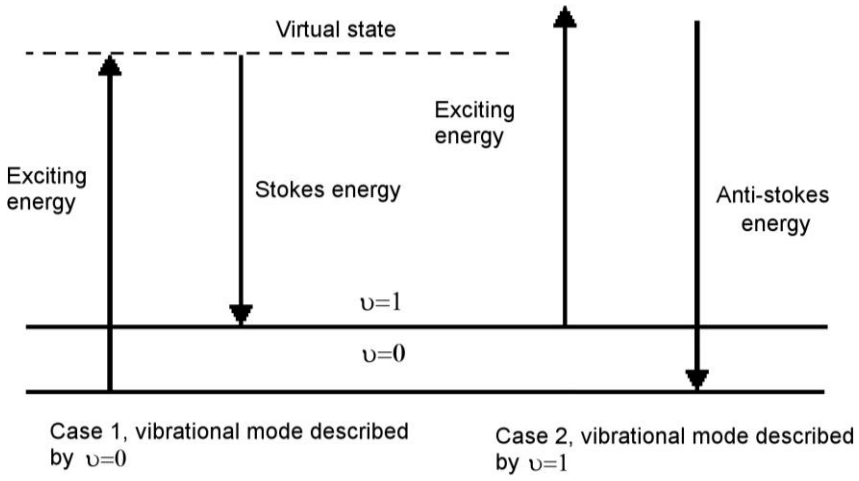

Figure 3-10. A description of the vibrational Raman effects based on energy level approach.

Figure 3-11. HORIBA Jobin Yvon LabRAM HR (with 632.8 nm He-Ne laser) Raman spectrophotometer.

Raman spectroscopy was performed using a HORIBA Jobin Yvon LabRAM HR (with 632.8 nm He-Ne laser) Raman spectrophotometer (Figure 3-11) (HORIBA Jobin Yvon Ltd., Middlesex, UK). The spectra were obtained in the range of 100 to 1600 cm^{-1}.

3.2.4 FEG-SEM

Surface nanostructure and the thickness of the films were studied using Leo 1530 VP (Carl Zeiss NTS Ltd., Cambridge, UK) field emission gun SEM (FEGSEM) at an accelerating voltage of 5 kV, and a working distance of 6 mm. The samples were investigated after PEC measurements. The samples were mounted on SEM specimen stubs using adhesive conductive carbon disc tapes (Agar Scientific, Essex, UK) and were coated by Au prior using a Polaron Emitech SC7640 sputter coater (Quorum Technologies Ltd, West Sussex, UK) to SEM experiments.

3.2.5 Focused ion beam SEM (FIB-SEM)

Focused ion beam SEM is a powerful tool to study the morphology and the thickness of thin films. FIB is a combination of ion scanning and ion machining methods. Therefore, it

allows for the precision cutting of the sample through its cross-section and imaging it using SEM.

Figure 3-12. FEI Nova 600 Nanolab FIB/SEM dual-beam system.

Nanostructure, surface morphology, and thickness of the films were studied using a FEI Nova 600 Nanolab FIB/SEM dual-beam system (FEI Company, Oregan, USA)(Figure 3-12). In order to protect the top-most layer of the thin films a thin layer of Pt was deposited using electron beam and then a thicker Pt layer was deposited over this layer. The thick Pt layer would provide a smooth and sharp image while it protects the thin films from destruction as a result of the bombardment of the surface by high energy ions.

3.2.6 AFM

Atomic force microscopy (AFM) operates on the basis of the physical finite interaction force between the tip and the sample surface. An AFM system consists of a cantilever, positioned parallel to the surface of the sample and has a sharp, force-sensing tip at its end interacting with the surface of the sample. As the interaction force between the tip and the surface changes, the cantilever is deflected. These deflections are then measured and

compiled as topographical information of the surface, which would eventually produce an image of the surface.[163]

Figure 3-13. Veeco dicaliber Veeco AFM system

AFM is carried out either in contact or tapping mode using a dicaliber Veeco AFM system (Veeco Instruments GmbH, Cambridge, UK) (Figure 3-13). Generally, tapping mode resulted in better images. Surface morphology and roughness of the samples were studied and compared using AFM. Surface roughness was measured using the software which analyses the digital images obtained and calculates the roughness as the ratio of measured surface area to the projected surface area. As expected, this value was dependant on measurement parameters such as resolution and degree of magnification of the images. In order to provide a comparative study all the measurement was done on the projected surface area of 5 μm × 5 μm, otherwise stated.

3.2.7 Inductively-coupled plasma mass spectrometry (ICP-MS)

Since one of the main objectives of this work was to study the effects of Si as a doping agent, it was important to confirm the presence of Si and to quantify the amounts of Si in the deposited iron oxide samples. ICP-MS is a powerful tool in elemental analysis of trace elements. It offers detection limits as low as parts per trillion (ppt) and it also enables

quantification of trace elements at high concentrations of parts per million (ppm) levels.[166] Approximate detection limits of different elements in ICP-MS method are shown in Figure 3-15.

Figure 3-14. Finnigan Elemental XR ICP-MS.

In a typical ICP-MS a diluted solution of the materials in question is fed into the apparatus. The solution is then used to form aerosols using a nebuliser. Finer droplets (1-2% of the solution) are separated from the larger droplets by means of a spray chamber.[166] The fine droplets are then injected to the plasma torch which is used to generate positively charged ions.[166] The resultant ions are then collected and analysed by a mass spectrometer. The signals read are then compared to those of the standard solutions and concentrations of specific elements are quantified.

Iron and silicon content of different films were quantified using a sector field high-resolution inductively coupled plasma mass spectrometer (SF-HR-ICPMS) apparatus (Finnigan Elemental XR, Thermo Scientific, West Sussex, UK) (Figure 3-14). Samples were prepared according to the following procedure. Films were deposited on FTO substrates and were then placed in 7 mg of concentrated HCl (36% w/w aqueous solution) for 8 h.

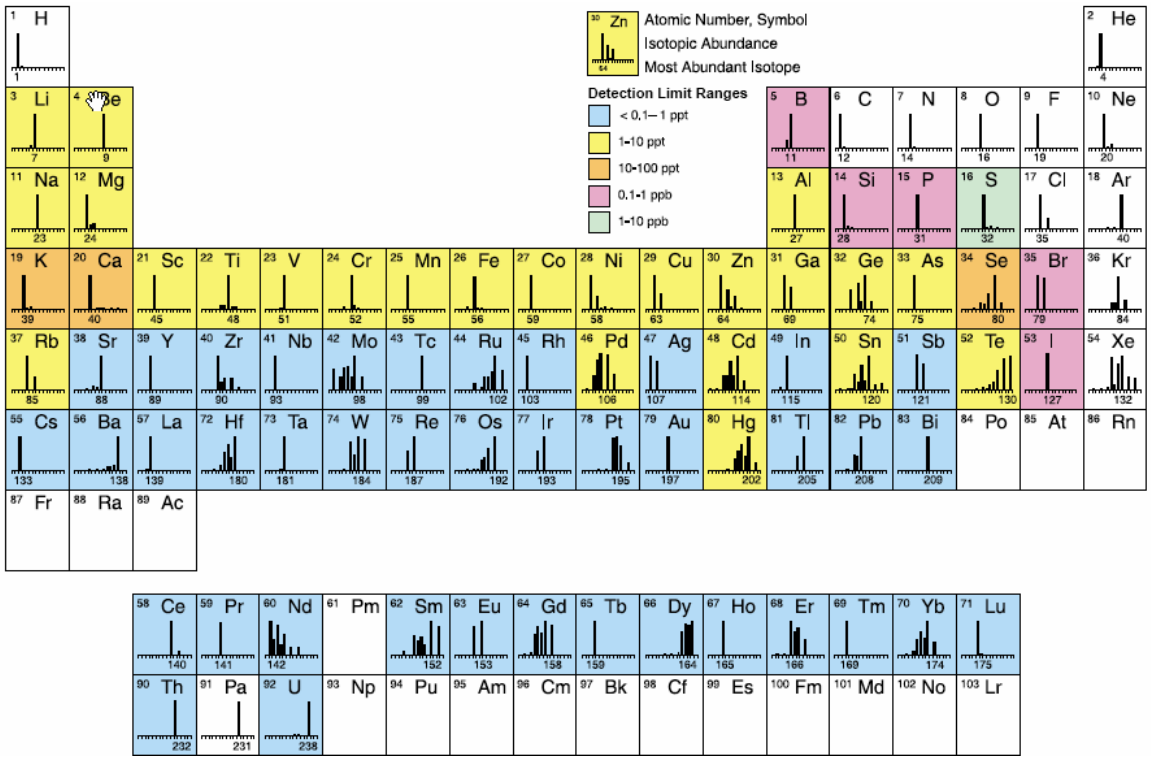

Figure 3-15. Detection limits of different elements in ICP-MS.[167]

Substrates were then removed from the sample tube, and the solution was diluted using 20 mg of deionised water prior to measurements. Standard stock solution of silicon and iron containing 100 ppb of each element in high purity 2% HNO_3 were prepared and were then diluted to obtain 10 different reference solutions of Si and Fe at different levels of concentration. Standard solutions of Fe and Si were prepared at different concentration levels; solutions of 1 ppm to 10 ppb for Fe and 100 ppb to 1 ppb for Si.

3.2.8 UV-vis spectroscopy

Electronic energy levels of electrons situated in the outer energy levels consists of optical transition energies in a range of about 1–6 eV, 200 nm to 3000 nm wavelength range.[168] This wavelength range is known as the optical range and also covers ultraviolate (UV), visible and infrared regions. When a solid material is illuminated by a light beam of intensity I_0 and the light beam crosses the sample, as a result of absorption, reflection and scattering of the beam by the sample, the intensity of the transmitted beam is reduced to I.[168] The beam intensity

attenuation dI after passing through the differential thickness dx of a material is formulated using Equation 3-4:

$$\mathrm{d}I = -\alpha I \, \mathrm{d}x \qquad (3-4)$$

where I is the beam intensity at a distance x into the material and α is the absorption coefficient of the material. Upon integration of Equation 3-4, the Beer-Lambert law is obtained (Equation 3-5) which relates the incoming light intensity to the thickness:

$$I = I_0 e^{-\alpha x} \qquad (3-5)$$

Experimental optical spectra are usually plotted showing the intensity of (absorbed, emitted, reflected, or scattered) radiation as a function of the photon energy (in eV) (or the wavelength (in nm) or the wavenumber (in cm^{-1})).[168]

$$E = \frac{1240}{\lambda} = 1.24 \times 10^{-4} \bar{\nu} \qquad (3-6)$$

Optical spectrophotometers function at different modes to measure different optical properties of materials, such as optical density (OD), absorbance (A), or transmittance (T). These parameters are calculated using the following equation, providing that the thickness of the sample is known:[168]

$$OD = \log \frac{I_0}{I} \qquad (3-7)$$

$$\alpha = \frac{(OD)}{x \log e} = \frac{2.303\,(OD)}{x} \qquad (3-8)$$

$$T = \frac{I}{I_0} = 10^{-OD} \qquad (3-9)$$

$$A = 1 - T = 1 - 10^{-OD} \qquad (3-10)$$

As can be understood by the above equations, for low optical densities, absorbance will be very close to optical density (A ≈ 1 − (1 − OD) = OD) so that the absorbance spectrum displays the same shape as the optical density.[168]

Optical absorption measurements were performed using a Lambda 35 Perkin-Elmer UV-vis spectrophotometer. A bare FTO substrate was used as the reference. The hematite films were scanned in the range of 400-700 nm with a slit size of 1 nm. Absorbance, transmittance and Tauc plots (See 2.1.1, p.16) were plotted for different samples to study the optical transitions and bandgap energies of deposited films.

Figure 3-16. Lambda 35 Perkin-Elmer UV-vis spectrophotometer.

3.2.9 Surface area measurements – dye adsorption studies

In order to obtain a better understanding of the surface area of the deposited films, dye adsorption studies were performed. Surface area of the films plays a significant role in the changes to the performance of photoelectrodes. Therefore, it is vital to investigate the extent of improvements in the surface area as a result of nanostructure formation. The challenge, however, is to select a suitable dye. To date, one group of dyes, namely azo dyes, have been reported to be suitable to study the surface area of iron oxide films and within the azo dyes, azo orange II has been suggested to be particularly good for hematite films.[169] Orange II (Figure 3-17) is a commercially available textile dye of the azo dye family which contain azo group (– N= N –) in their structure.

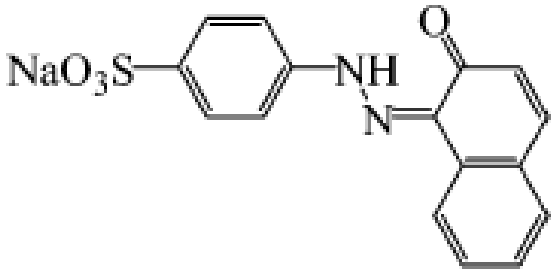

Figure 3-17. Molecular structure of azo Orange II.[170]

The dye adsorption studies were carried out as was reported in the literature.[99] Basically, the hematite electrodes were immersed in 1.5 mM solution of orange II dye in water of pH 3.5 for 15 minutes. The surface area of the electrode in contact with solution was maintained constantly at 0.1963 cm^2 by covering the electrode with a Kapton tape in which a circular hole was made using a conventional hole puncher. The immersed electrode was then put into a 0.5 ml 1M NaOH and the dye was desorbed. The concentration of the desorbed dye was then determined from the optical absorption at 450 nm. The roughness factor of the electrodes was then estimated by calculating the number of dye molecules assuming 0.4 nm^2 surface coverage of each dye molecule and surface area of 0.1963 cm^2 of hematite film exposed to the dye solution.

3.2.10 Photocurrent-potential performance

PEC performance of hematite electrodes was measured using a three-electrode configuration in 1 M NaOH electrolyte, Ag/AgCl/KCl(3M) as reference electrode, and a platinum wire as a counter electrode. The potential of the photoelectrode was controlled by a potentiostat (microAutoLab, type III, Windsor Scientific, Berkshire, UK) and is reported against the reversible hydrogen electrode (RHE). In the electrochemical cell light enters through a quartz window and travels about a 5 mm path length in the electrolyte before illuminating the photoelectrode. The Fe_2O_3 electrode was illuminated through electrolyte side and illumination area was 0.8 cm^2 unless stated otherwise. Two illumination sources were used. Initial measurements were carried out using a microscope illuminator equipped

with a 150 W halogen lamp. The distance between the light source and the electrode was maintained in such a way that the intensity of the light incident on electrode was at 1000 $W.m^{-2}$. The intensity of the light was measured using a PMA2144 Solar Light pyronometre (Solar Light Company Inc., PA, USA). The best samples were then re-measured using a solar simulator. The second illumination source was AM 1.5 class A solar simulator provided by Solar Light (Solar Light 16S – 300 solar simulator, Solar Light Company Inc., PA, USA).

3.2.11 IPCE and APCE

The incident photon to electron conversion efficiency (IPCE) was obtained by measuring the incident photon flux using a 75 W Xenon lamp connected to a monochromator (TMc300, Bentham Instruments Ltd., Berkshire, UK). The light was calibrated using a silicon photodiode. Photocurrent spectra were measured at a constant potential vs. Ag/AgCl using a combination of a lock-in amplifier (Bentham 485, Bentham Instruments Ltd., Berkshire, UK) and an in-house built potentiostat. Readings were collected at 5 nm intervals while the monochromated light was scanned from 320 to 650 nm. APCE was calculated using the data obtained from IPCE and UV-vis measurements.

3.2.12 Cyclic Voltammetery (CV) to determine flat-band potential and donor density

As outlined by Boschloo and Fitzmaurice[171] cyclic voltammetery can be used to calculate the flat band potentials of nanostructure electrodes in aqueous electrolyte. To do this it has to be ensured that the potential range is such that the electrode film is always under depletion conditions; i.e., the applied potential is more positive than the flat-band potential (V_{fb}). They showed that the current was an approximately linear function of the applied potential, in the directions of both the forward and the reverse scans. Furthermore, the current at a given potential is linearly dependent on the scan rate. If there are no peaks due to electrochemical reactions, it can be assumed that there is no faradic current and, therefore, the origin of this current must be capacitive.[171] The differential capacitance (C) is given by

$$C = \frac{dQ}{dV} = I\frac{dt}{dV} = \frac{I}{v} \qquad (3-11)$$

with Q the charge, V the potential, I the current, and v the scan rate used in recording of the CV. Therefore, if the current density is plotted against scan rate at different potentials the slope of these plots can be considered as the space charge layer capacitance at given potential (The capacitance of the nanostructured electrode can be calculated using the equation above). The data from the forward scans of the CVs are used to calculate the capacitance, which is presented in a Mott-Schottky plot. Linear relations are found at potentials close to V_{fb}. From the Mott-Schottky plots, donor density and flat-band potential can be calculated.

3.2.13 Electrochemical impedance spectroscopy

Electrochemical Impedance Spectroscopy (EIS) is a common technique for investigating the properties of electrochemical systems and has been used extensively to study different material systems such as batteries, fuel cells, and corrosion phenomena. A typical EIS experiment involves the application of a small amplitude sinusoidal signal (e.g. current) to the system and analysing the response. At an electrochemical interface such as semiconductor/electrolyte interface, the applied sinusoidal electric field is formulated as in Equation 3-12:[20]

$$U(t) = U_m \sin \omega t = U_m \exp(i\omega t) \qquad (3-12)$$

The corresponding current usually exhibits a phase shift (ϕ)

$$J(t) = J_m \sin(\omega t + \phi) = J_k \exp(i\omega t) \qquad (3-13)$$

The relation between complex values of potential and current are defined in Equation 3-15 where Z is called impedance:[20]

$$J_k = J_m \exp(i\phi) \qquad (3-14)$$

$$Z(\omega) = \frac{U_m}{J_m} \exp(i\phi) \qquad (3-15)$$

The impedance itself is a complex value which consists of a real (Z′) and an imaginary part (Z′′) as shown in Equation (3-16):

$$Z(\omega) = Z'(\omega) + iZ''(\omega) \qquad (3-16)$$

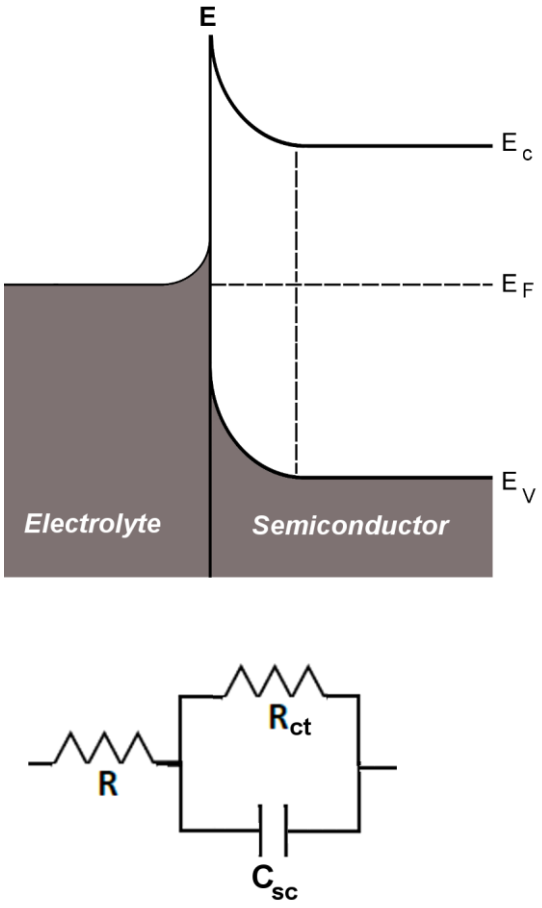

Figure 3-18. the schematic of the semiconductor/electrolyte interface and the equivalent electrical surface.

As shown in Figure 3-18, the solid/liquid interface can be simplified as an electric circuit comprising of a charge transfer resistance R_{ct}, a space charge capacity for semiconductor electrodes (C_{sc}) and a series resistance R corresponding to the resistance of the electrochemical system.[20] The plot of the real part of impedance against the imaginary part, known as the Nyquist Plot provides a quick overview of the system under study. By fitting the measured data to corresponding electric circuit it is possible to obtain quantitative data such as the capacitance of the space charge layer or the charge transfer resistance. By knowing the capacitance of the space charge layer, it is also possible to calculate the flat band potential and donor density of the semiconductor material using the Mott-Schottky plot.

Electrochemical impedance spectroscopic measurements were carried out in the dark to investigate the electrical properties of hematite films. The experiments were performed using

a computer-controlled potentiostat (AutoLab, PGSTAT12, Windsor Scientific, Berkshire, UK). The electrochemical cell was in the three-electrode configuration as mentioned in Section 3.2.10 (p.92). The superimposed a.c. signal was maintained at 20 mV, while the frequency range was between 120 KHz and 10 Hz at potentials from -0.8 to 0.2 V vs. $V_{Ag/AgCl}$ under dark conditions. A simple RC circuit was used as the fitting model to determine the capacitance (C) of the space charge layer at the hematite-electrolyte interface. The values for flat-band potential (V_{fb}) and donor density (N_D) were calculated using the Mott-Schottky relationship (Equation 3.17) and taking into account the intercept and the slope of the plot of $(A/C)^2$ vs. applied voltage:

$$\left(\frac{A}{C}\right)^2 = \frac{2}{eN_D\varepsilon_r\varepsilon_0}\left(\left|V - V_{fb}\right| - \frac{kT}{e}\right) \qquad (3.17)$$

where A is the surface area of the film (assumed to be as 1 cm^2), ε_r is the dielectric constant of hematite (taken as 12[172]), ε_0 is the permittivity of free space, T is the temperature and k is the Boltzmann's constant.

Chapter 4

4 Results and discussion

4.1 Introduction

This chapter discusses two distinct methodologies which were used to prepare hematite thin films; namely, high temperature preparation and microwave-assisted low temperature technique. The effects of different parameters on properties and performance of hematite photoelectrodes were investigated. The fabrication conditions were optimised in order to obtain best PEC performance.

4.2 High temperature preparation – APCVD and AACVD

4.2.1 APCVD – deposition parameters

Initial experiments were carried out using iron pentacarbonyl and TEOS as precursors in APCVD of hematite films. The first step was to find the best conditions such as the diameter of the delivery tube, carrier gas flow rate, deposition temperature and time. Visual examination of deposited films at different conditions was the first step in identifying the problems and carrying out further experiments to improve on the appearance of the films.

4.2.1.1 Delivery tube - The effect of the diameter and its distance from the substrate

Initially, a delivery tube with the diameter of 5 mm was used. The distance of the delivery tube from the substrate was kept constant at 20 mm. Argon gas was bubbled through iron pentacarbonyl and TEOS at flow rates of 11 and 20 ml/min, respectively. The aerosols were then mixed with air flowing at 2 L/min and directed towards the substrate. These conditions were set according to those used by Kay et. al.[99] The only difference was that in the work

conducted by Kay et. al.[99] was the diameter of the delivery tube (a 10 mm-wide tube was used in this work).

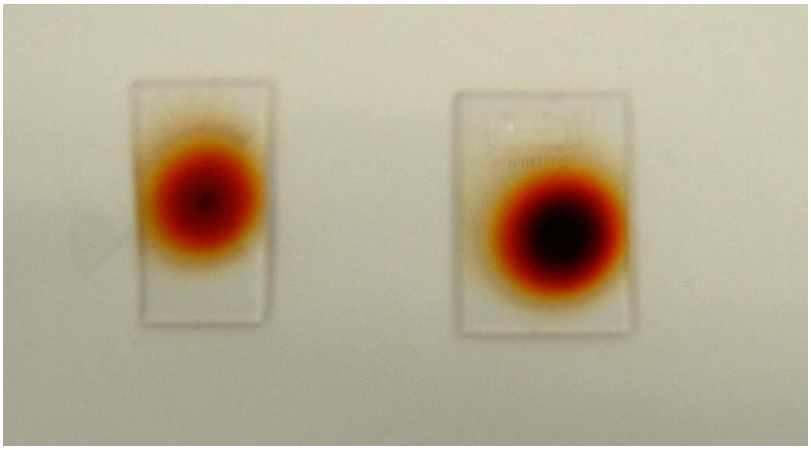

Figure 4-1. Hematite films deposited on glass substrates.

Films prepared using the above conditions did not show any photocurrent, they were hardly photoactive. Moreover, they were not homogenous in appearance. Substrate was covered with a circular film having a black area at the centre (Figure 4-1) and orange/red film surrounding it. Further examination of these types of films was carried out by SEM. As shown in Figure 4-2 and Figure 4-3, the black area had sharp plate-like features which were the result of high carbon content in the film. It was concluded that the high mixing flow would result in the delivery of large quantities of aerosol into the deposition chamber. However, the aerosol was not given enough time in the chamber and un-decomposed material reached the substrate. The deposition on the surface would result in high carbon content and formation of sharp carbon features on the surface. Another observation was that surface features were fairly large and the film was quite compact.

In order to decrease the black region and increase the porosity not only the mixing flow rate was reduced but also the distance between delivery tube and substrate was reduced to compensate for the lower flow rate so decomposed material could reach the substrate. However, despite improving the homogeneity of the film and a slight improvement in the photocurrent, a uniform film was not achieved.

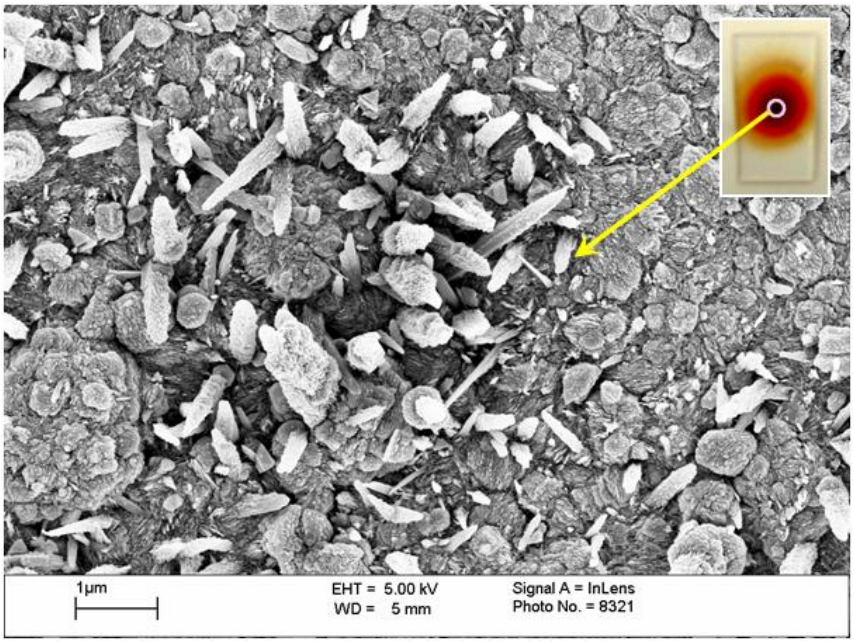

Figure 4-2. SEM picture of the surface of a hematite film at the centre of the film where black spots were seen (as shown by the circle at the top corner). The formation of long needle/plate-like structures is observed.

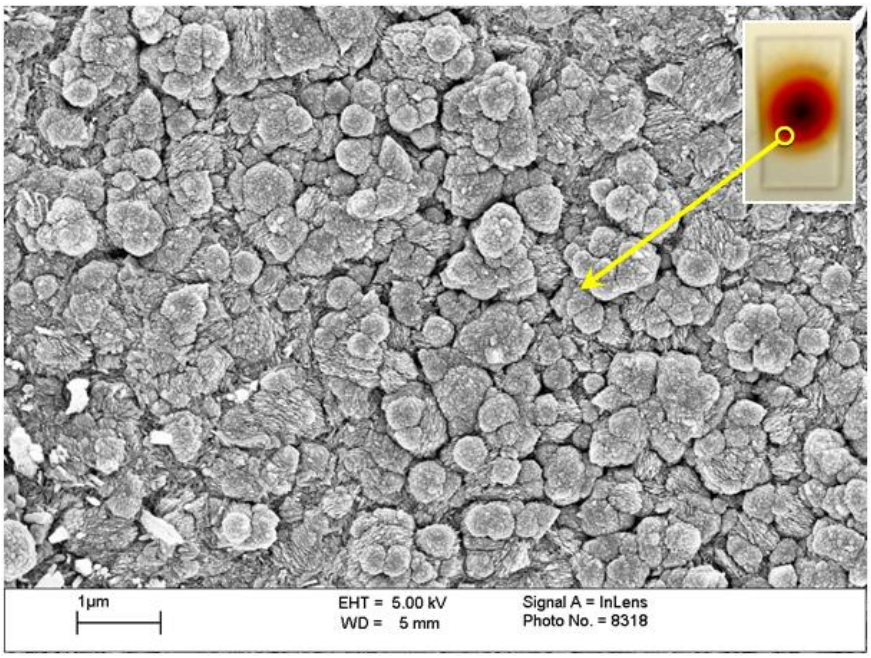

Figure 4-3. The surface morphology the red/brown area (as shown by the circle at the top corner) of the hematite film with black area at the centre.

The next step in modifying the deposition parameters was to utilise the geometry of the delivery tube, specifically the diameter. In order to achieve a better film the diameter of the delivery tube was increased to 10 mm while all other conditions were used as described above. Using a wider tube improved the appearance of the film to a large extent; films were made of circular fringes, the colour of the film maintained at orange/red and the black central area was removed.

The improved appearance was contributed to the fact that by using a wider tube the difference in the density of the aerosol inside the tube was decreased. In other words, the difference between the amount of material present at the centre of the tube and the areas close to the wall of the tube decreased. As a result, the amount of material delivered to the substrate was distributed more evenly throughout the whole area of the deposited film, which led to the formation of a more uniform film.

4.2.1.2 Carrier gas – Flow rate

The experiments were started by using Ar and air as the carrier gas while Ar was flowing at 10 and 20 ml/min for iron pentacarbonyl and TEOS, respectively, and air was used to mix the aerosols and directed them towards the substrate at the rate of 2 L/min (substrate temperature = 370 °C). However, the photocurrent of electrodes obtained at these conditions was far from the expected values. As the relative amounts of iron pentacarbonyl and TEOS was determined by the carrier gas flow rate, it was vital to obtain the best flow rate for each precursor. At first, the flow rate of TEOS was kept unchanged at 40 ml/min and Ar was bubbled through iron pentacarbonyl at flow rates ranging from 10-60 ml/min with a 5 ml/min increase for each deposition. The electrode photo-performance improved when the flow rate was increased from 10 to 20 ml/min (Figure 4-4). Photocurrents measured not only showed no improvements but dropped considerably at flow rates higher than 20 ml/min. Also, the change in the colour of the films was also visible from orange-red to red by increasing the flow rate.

Then, TEOS flow rate was changed from 20-100 ml/min with 10 ml/min steps while iron pentacarbonyl flow rate was kept constant at 20 ml/min. The reason behind the difference in the trend at which Ar was bubbled through two precursors was the difference in the vapour pressure of each precursor.

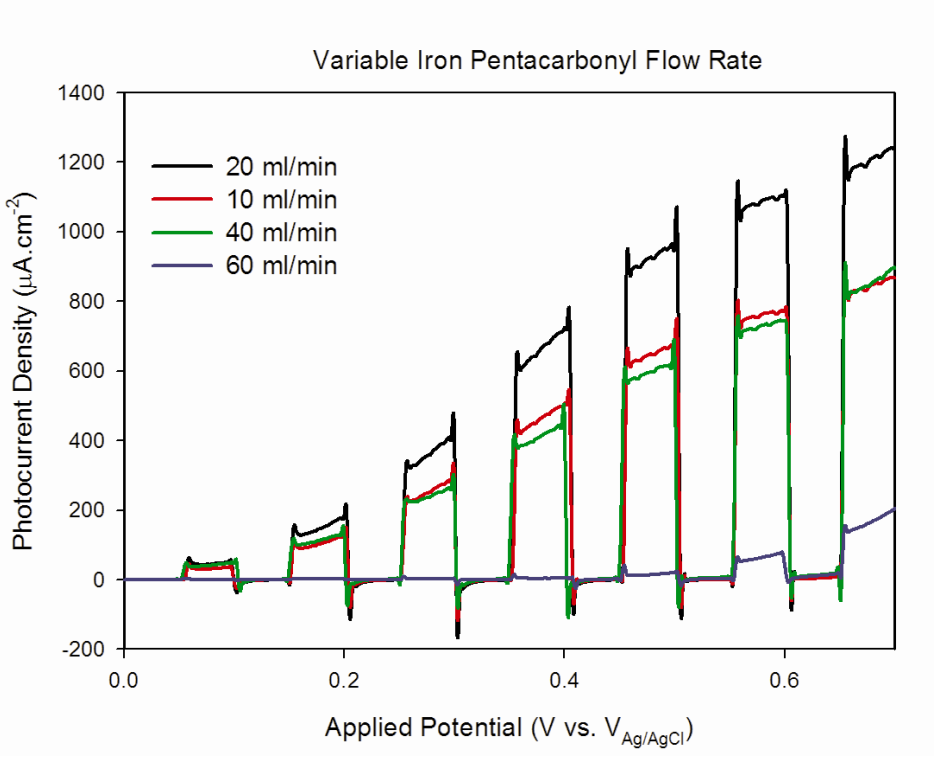

Figure 4-4. Photocurrent density vs. potential graphs of hematite films as a function of the flow rate of iron pentacarbonyl.

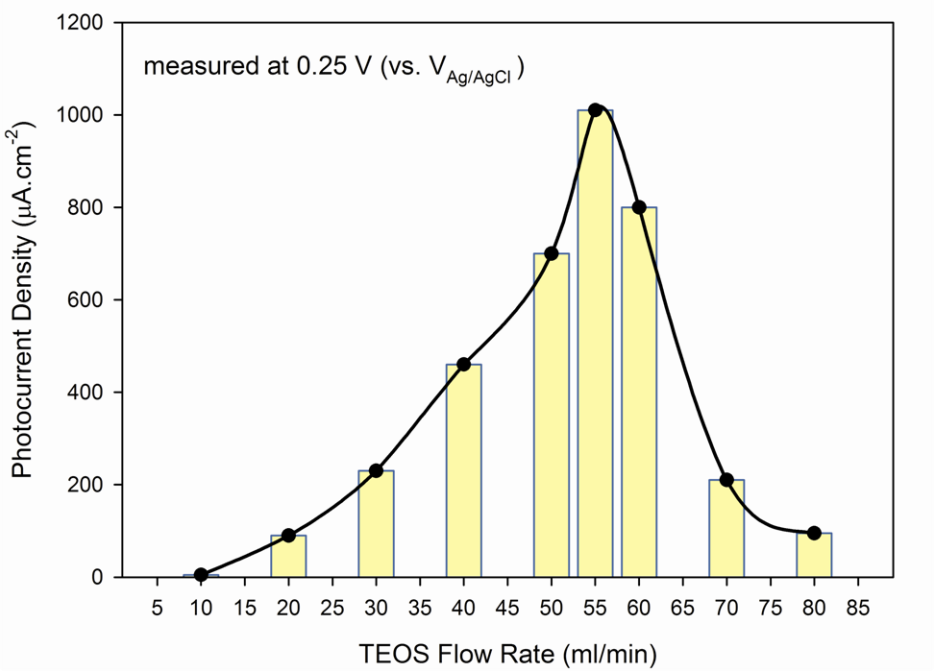

Figure 4-5. Photocurrent density of hematite films as a function of TEOS flow rate. The measurement potential for all samples was maintained at 0.25 V vs. $V_{Ag/AgCl}$.

The vapour pressure of $Fe(CO)_5$ is around 300 times more than that of TEOS; therefore, a small change in the iron pentacarbonyl flow rate would result in a large increase in the amount of aerosol in the final mixture. As shown in Figure 4-5, the flow rate at which the maximum photo-response is obtained is very narrow. The optimum TEOS flow rate was measured at 55 ml/min for the deposition temperature of 370 °C. The deposition time was maintained at 5 minutes for all the samples.

4.2.1.3 Deposition time and temperature

Improved photoelectrochemical performance was achieved when the deposition conditions were very different to the conditions used by Kay et. al.[99] It became clear that the deposition regime of this study was quite different to that of Kay et. al. It was concluded that, due to these differences and the fact that photocurrent obtained was very low, changing the temperature and studying its effect should be the next phase.

Figure 4-6. The APCVD deposition chamber.

In order to correlate the temperature shown by the hotplate display and the substrate temperature, a K-type thermocouple was used to measure the temperature of the surface of the substrate and hotplate. The difference was substantial. While the hotplate display showed 450 °C, the surface temperature of the hotplate and FTO substrate measured by the thermocouple were 380 and 320 °C, respectively. Increasing the temperature to 540 °C on the display increased the substrate temperature to 370 °C only. Unfortunately, it was the highest temperature that could be achieved by the ceramic hotplate available. Ceramic hotplate was then replaced by a metallic hotplate and the surface of the hotplate was covered by an insulating blanket to enable the hotplate to provide a high enough temperature by reducing the heat loss. The blanket was cut at the centre in order to accommodate a small metallic disc (diameter of 3 mm). The FTO substrate was then placed on top of the disc and, with this new configuration, it was possible to increase the temperature of the substrate surface up to 450 °C. It is worth mentioning that a glass cup with the height of 40 mm and diameter of 80 mm was used as the deposition chamber all the time. A hole was cut at the centre of the cup; therefore, the delivery tube could enter the chamber. As the deposition was carried out inside a fume cupboard, the cup was used to minimize the effect of the suction of the fume cupboard to insure that the aerosol reaches the substrate without any unwanted change in its path from the delivery tube to the substrate (Figure 4-6).

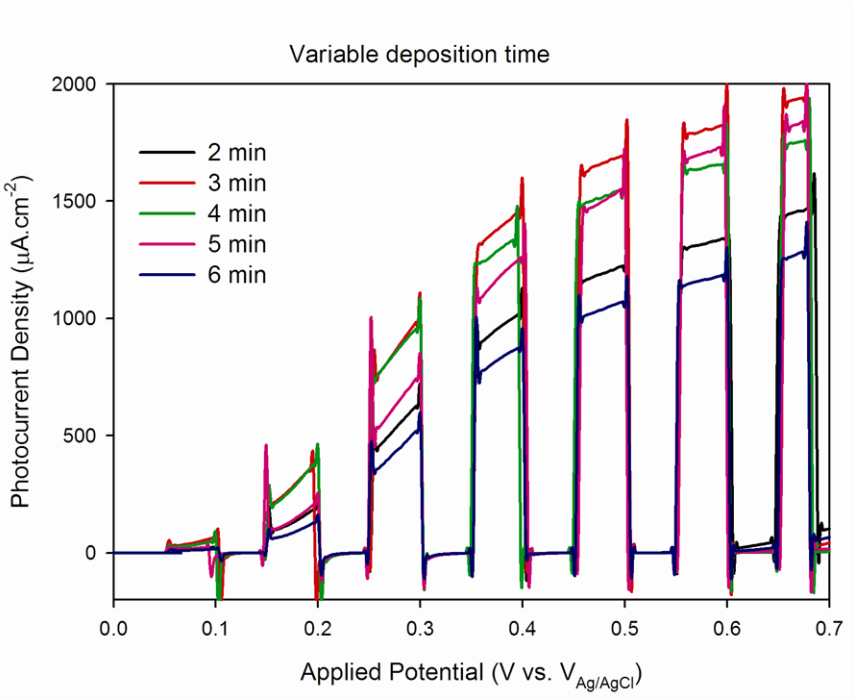

Figure 4-7. Photo-performance of hematite films as a function of deposition time.

To obtain the optimum temperature, Ar flow rate was kept constant at 20 and 55 ml/min for $Fe(CO)_5$ and TEOS, respectively, while the flow rate for air was maintained at 2 L/min. A glass tube with the diameter of 20 mm was used as the delivery tube positioning at 20 mm above the FTO substrate. Temperature was changed from 350 to 450 °C increasing at 10 °C steps. The best photo-performance was achieved at 370 °C.

4.2.1.4 Optimum conditions

Upon further refinements and more controlled conditions, it was observed that, the optimum deposition conditions were obtained when Ar was bubbled through $Fe(CO)_5$ and TEOS at flow rates of 17 and 55 ml/min, respectively. The aerosols were then mixed with air flowing at the rate of 1.7 L/min directing the mixed aerosol towards the FTO substrate. FTO substrate was situated 20 mm from the 10-mm-diametre delivery tube. The temperature of the substrate was kept at 370-375 °C. As mentioned before, the deposition conditions for other precursors (TMOS, TMOF and PP) were almost similar to these conditions (Table 3-1, p.74). The only difference was in the flow rate of Ar and deposition time which was changed to obtain the optimum conditions.

4.2.2 Structural characterisation

4.2.2.1.1 XRD

XRD results for films deposited in the presence and the absence of different Si precursors are shown in Figure 4-8. The common diffraction peaks of synthetic hematite correspond to (102), (104), (110), (113), (024), (116), (018), (214) and (300) reflections where the strongest peak occurs for (104) reflection. All the APCVD films show at least two major peaks of (104) and (110). TMOF shows two other peaks of (300) and (102) while these peaks are less intense in the XRD patterns of other samples. Crystallite size of different samples was estimated using the Scherrer equation; it was calculated that the crystallite size of all the samples was similar, ranging from ~ 30 nm to ~ 40 nm based on the (110) peak analysis.[173]

The dominant feature observed was the more intense (110) compared with (104) peak intensity in the deposited films except for TMOS. In the diffractograms of all films apart

from TMOS, the dominant hematite peak is (110) while in the XRD pattern of TMOS the (104) reflection is slightly stronger. It has previously been suggested that the (110) preferential orientation is the result of the presence of TEOS during APCVD.[174] However, XRD patterns for the hematite films shown in Figure 4-8 indicate the presence of the dominant (110) peak in this deposition regime when the films were formed on FTO substrates by APCVD regardless of the presence or the absence of Si-precursors.[173]

The presence of the more intense (110) reflection is very important. It is well-known that electrical properties of hematite are anisotropic. Especially, electrical properties along [100] plane differs substantially to the one orthogonal to it. (110) is the preferred orientation in hematite lattice with regards to conductivity as the conductivity along [100] plane is 4 times higher than that of normal to it. Therefore, it can be suggested that the existence of this preferential orientation could contribute to the performance of the films.[173]

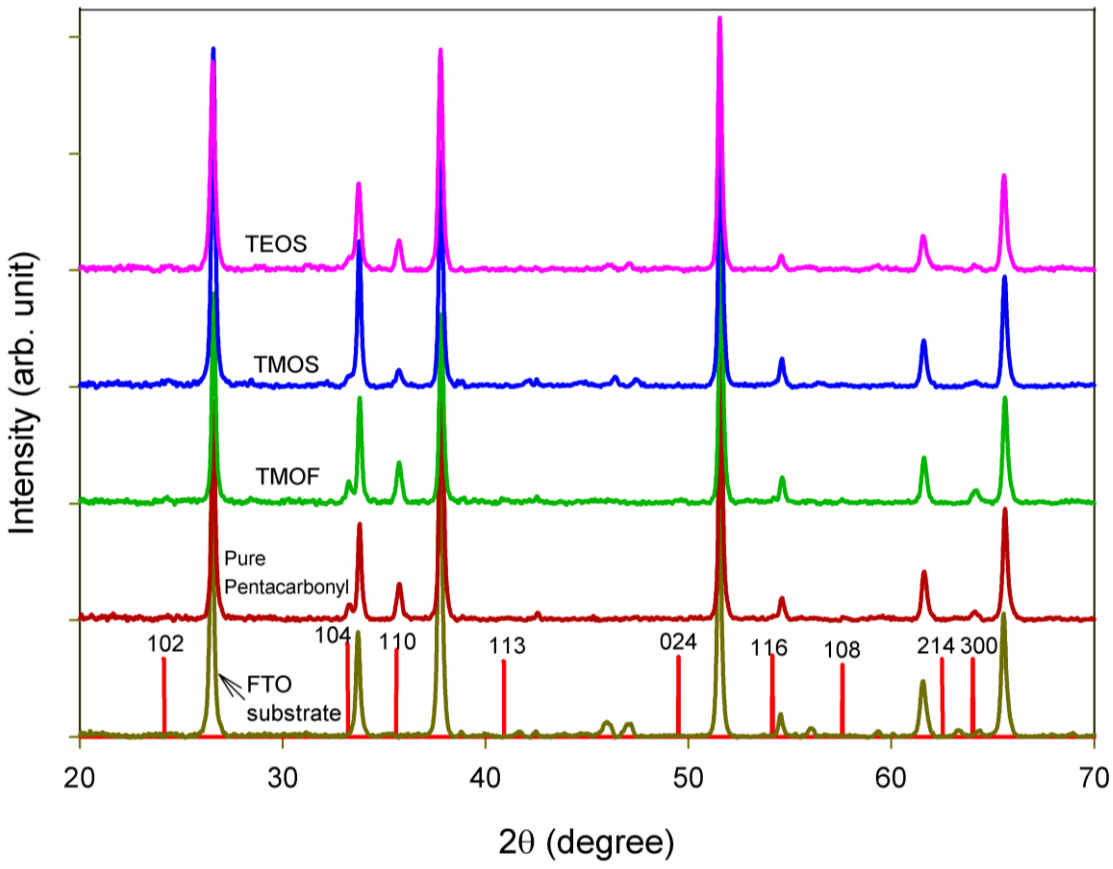

Figure 4-8. XRD patterns of α-Fe_2O_3 (hematite) films prepared using different precursors. Standard powder pattern of hematite is shown by lines with plane indices in hexagonal coordinates.[173]

- ***The effect of substrate in preferential orientation***

In order to determine whether the preferential orientation was due to the APCVD precursors or another factor such as substrate, the structural characteristics of doped and un-doped samples deposited on different substrates were investigated (Figure 4-9). The XRD patterns of pure pentacarbonyl and pentacarbonyl/TEOS deposited on microscope glass slides clearly show a different orientation to that of the films deposited on FTO substrates. In the TEOS sample, there is no evidence of the (110) reflection whereas the (104) reflection is predominant when the substrate is soda glass.[173]

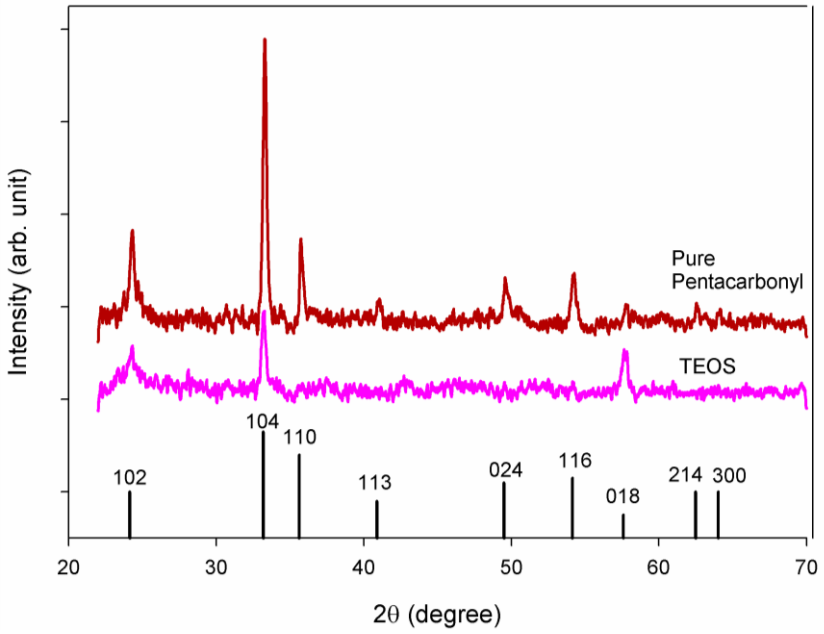

Figure 4-9. XRD patterns of pure pentacarbonyl and TEOS samples deposited on soda glass slide.[173]

In the case of the pure pentacarbonyl sample, the (104) reflection is still the dominant peak when the substrate is soda glass. This is a clear difference from the predominant (110) reflection observed in similar samples deposited on conductive FTO glass substrate (Figure 4-10). It suggests that substrate plays a major role in determining the orientation of films which has also been observed by other groups. For example, dominant (110) reflections were reported when un-doped hematite films were deposited on conductive ITO glasses using other preparation methods such as spray pyrolysis.[175,176] Therefore, it can be suggested that

silicon alone may not be responsible for the change in the peak intensities; it is the effect of FTO on the substrate along with the presence and decomposition of the second precursor, (e.g. TMOS, TEOS and TMOF) which results in the more dominant (110) reflections in hematite films.[173]

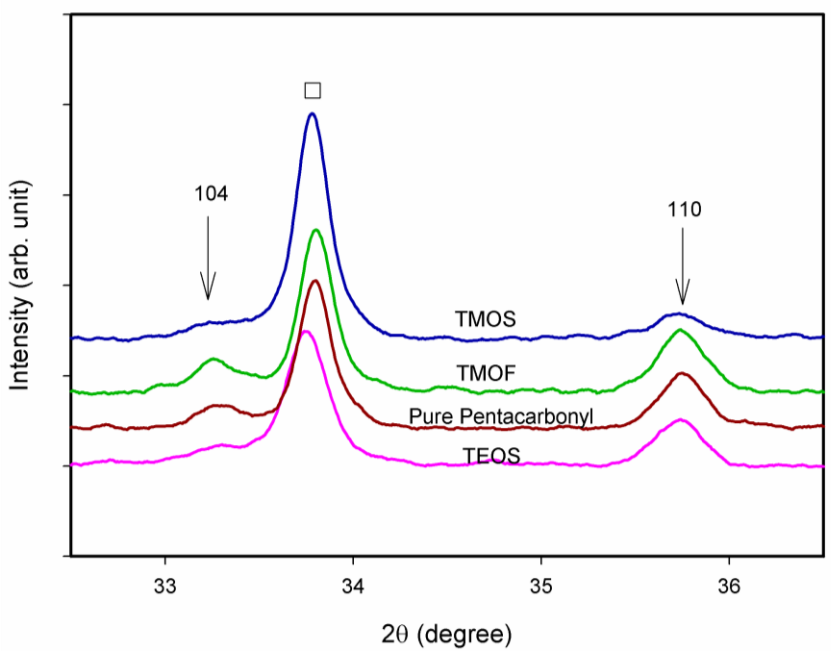

Figure 4-10. XRD pattern of different samples deposited on FTO glass. (110) and (104) reflections of hematite are marked with an arrow. The peak marked with □ belongs to SnO_2 in the FTO substrate.[173]

4.2.2.1.2 Presence of Fe^{2+} - XPS

XPS spectra of two different samples (pure pentacarbonyl and TEOS) are shown in Figure 4-11. If Si was incorporated as elemental Si, the binding energies of Si 2*s* and Si 2*p* (corresponding to the elemental Si) were expected to be observed at 99 and 150.7 eV, respectively.[177] Neither of the peaks was observed in the spectra obtained for both films. However, two peaks were observed at 102 and 154 eV in the spectra of the TEOS sample which are attributed to the Si 2*s* and Si 2*p* in SiO_2 structure. These results suggest that silicon is not present as elemental silicon in hematite films. Rather, silicon is incorporated into the hematite structure as Si^{4+} ions. However, due to the small amount of silicon present in the electrodes, the quality of the XPS spectra could not be improved. Therefore, it was difficult

to draw any further conclusions on the oxidation state of the silicon.[173] This is an area where further studies are required.

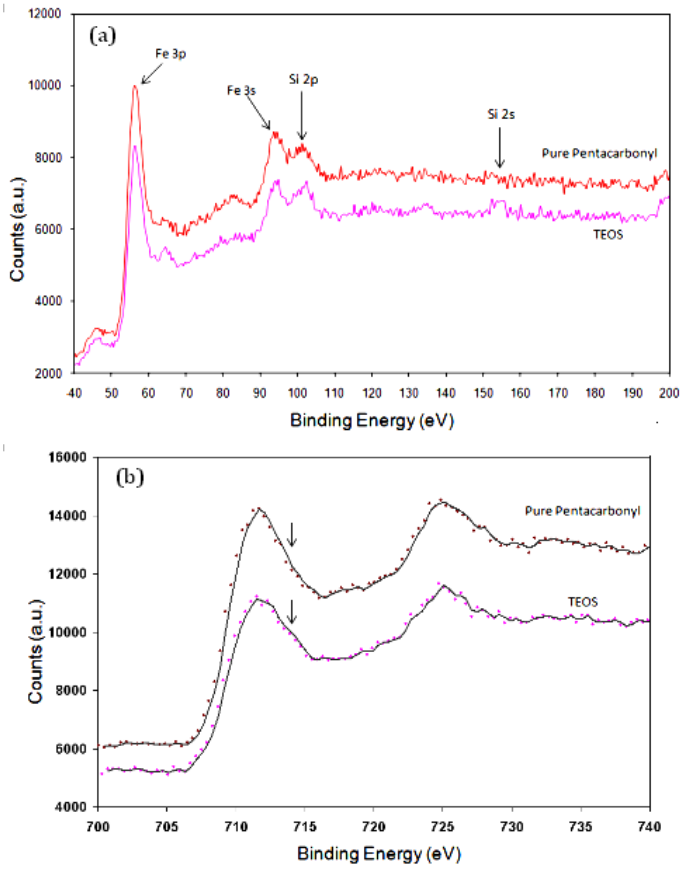

Figure 4-11. XPS spectra obtained for two different electrodes. (a) Binding energies of Fe^{3+} and Si^{4+} in the Fe_2O_3 and SiO_2 structures are marked, respectively. (b) XPS spectra of two samples at binding energies close to 715 eV. The expected position of the satellite peak (characteristic of Fe^{2+}) is marked with arrows.[173]

It has been suggested that doping can improve PEC performance of electrodes through enhancement of conductivity.[87] For example, it has been shown that addition of Ti^{4+} increased the conductivity of hematite.[95] The mechanism suggested was that titanium (Ti^{4+}) entered the hematite lattice substitutionally. This would lead to the formation Fe^{2+} sites in order to maintain the charge balance in the lattice. Fe^{2+} would act as donor centre with respect to the surrounding Fe^{3+} and can provide electrons to Fe^{3+} by thermal excitation[87]. Another explanation is that tetravalent ions may introduce electrons to the conduction band of the semiconductor and under the influence of a potential gradient the localised electrons

can produce electric current.[95] It has also been shown that tetravalent ions can enter the structure of hematite without inducing any changes in the oxidation states of Fe ions. In this mechanism the charge compensation is carried out by the formation of cation vacancies.[178,179,180]

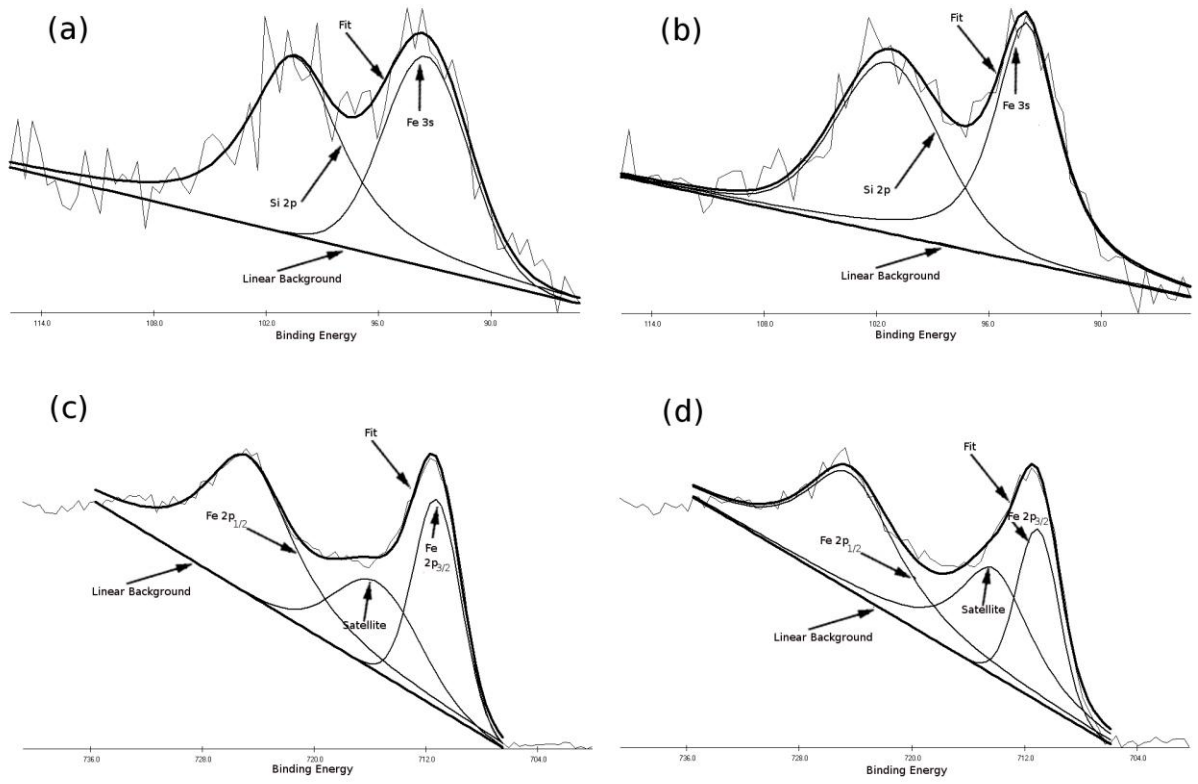

Figure 4-12. Curve fittings of XPS spectra using a linear background in two different regions of Si 2p (a and b) and Fe 2p (c and d). Figures (a) and (c) are spectra of pure pentacarbonyl sample and (b) and (d) are of TEOS sample.

In order to understand whether the incorporation of Si^{4+} introduced any changes in the oxidation states of iron different hematite films were examined using XPS. It is known that the binding energy for Fe^{3+} $2p_{3/2}$ is 711.2 in all iron oxides while Fe^{2+} shows the binding energy of approximately 709.7 eV in Fe_xO.[181,182,183] The presence of a satellite at ~715 eV is also regarded as the characteristic of Fe^{2+} while it has been shown that the presence of a satellite peak at ~718 eV is the characteristic of hematite structure. According to the results shown in Figure 4-11-(b), the binding energies of 711.5 eV and 711.6 eV were observed for TEOS and pure pentacarbonyl samples. Moreover, there is an apparent shoulder close to 713

eV which suggests that Fe^{2+} was present in the TEOS sample. This also provides an indirect evidence for the presence of Si^{4+} in the TEOS sample.[173] Figure 4-12 shows the results of curve fitting for pure pentacarbonyl and TEOS sample at two different regions of Si 2p and Fe 2p peaks. This was used to quantify the amount of Si^{4+} and Fe^{2+} which showed the presence of 1.3% Si and 4.7% Fe^{2+} in the TEOS sample. The apparent discrepancy in the Fe^{2+} can originate from the selection of the background as it will have significant implication in the quantification procedures. Another interesting feature of the XPS spectra is the presence of satellite peak in both samples and the changes in the binding energy of this peak. In the pure pentacarbonyl sample, this peak is at 715 eV which is close to the characteristic values of hematite while in the TEOS sample this peak occurs at 713 eV which is closer to the characteristics of Fe^{2+} in iron oxide structure.

4.2.2.1.3 Surface disorder - Raman spectroscopy

The Raman spectra of different samples are shown in Figure 4-13. The spectrum obtained for the pure pentacarbonyl sample is typical of hematite phase showing peaks at 221, 287, 406, 495 and 611 cm^{-1}. The main difference between the different samples is the presence of a forbidden peak at 660 cm^{-1} in the spectrum of the TMOS and TEOS samples. It is also observed that the intensity of this peak increased from sample TMOS to TEOS. As the intensity of the peak at 660 cm^{-1} increased, the PEC performance of the samples also improved.[173] It has been reported that this peak is a result of the breakdown of Raman symmetry selection rules induced by short-range order such as nano-dimensions or lattice defects.[92] It has also been attributed to magnetite (Fe_3O_4).[98]

Yu et. al.[184] have reported the appearance of forbidden modes in the Raman spectra of SnO_2 nanoparticles. It was attributed to a large amount of defects: vacancies of oxygen, vacancy clusters, and local lattice disorder at the interface and interior surface, which led to a significant lattice distortion and an evident space-symmetry reduction and the appearance of a group of new Raman peaks. In addition to the above defects, incorporation of silicon into the structure of hematite can also result in the formation of lattice disorder.[173]

Berry et. al.[178,179,180] have reported the mechanism through which tetravalent ions enter the structure of hematite. They have proposed a model which describes that these dopant ions adopt two distinct sites in the hematite structure; partially substituting at octahedral Fe

sites and occupying the vacant interstitial octahedral sites in α-Fe_2O_3.[179] In other words, two iron ions are replaced by three tetravalent ions and the charge neutrality is maintained through the formation of cation vacancies. It was also found that no change in the oxidation state of Fe occurred; the charge balance was achieved by the formation of different defect clusters as described above.[179]

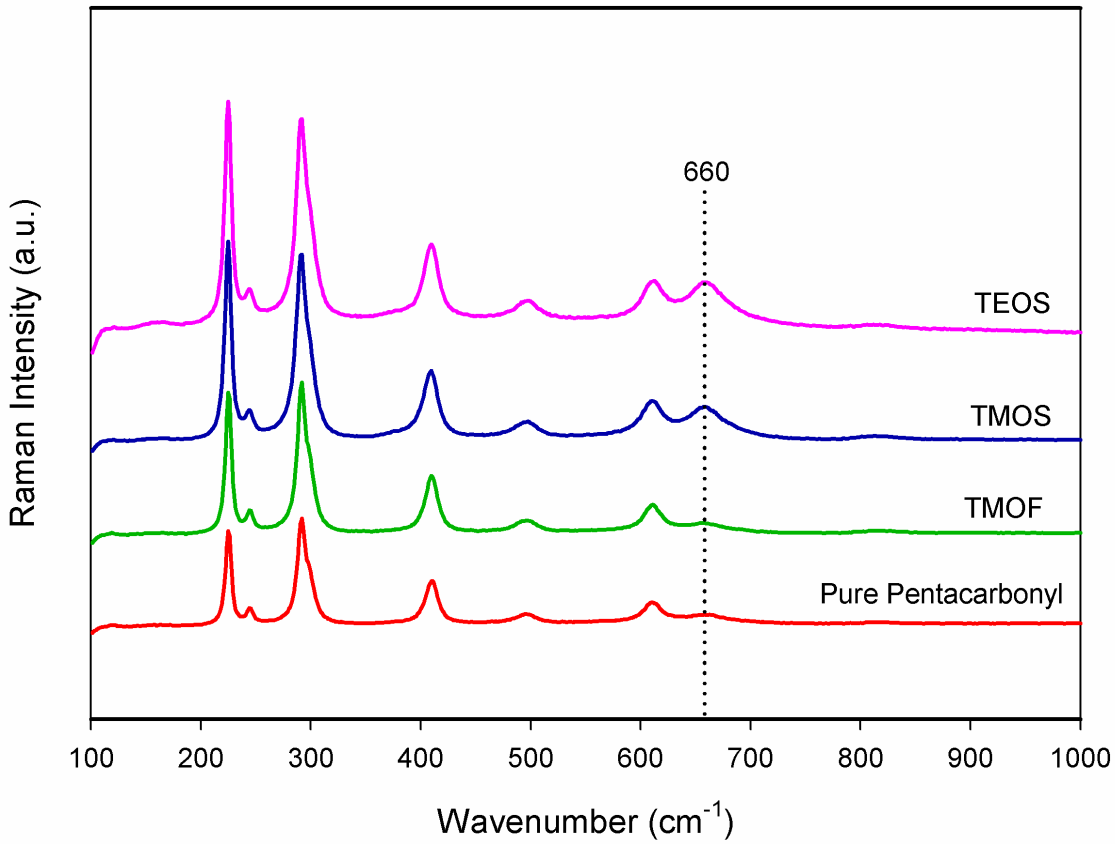

Figure 4-13. Raman spectra obtained for different samples. The position of 660 cm^{-1} is marked with a line.[173]

It is proposed that the peak at 660 cm^{-1} observed for TEOS and TMOS samples is the result of formation of lattice disorder in the structure of the doped hematite film as a result of Si incorporation and also changes in the nanostructure of the films. The lattice disorder can also be formed as the result of incorporation of silicon into the structure of hematite.[173]

Berry et. al.[178,179,180] have reported the mechanism through which tetravalent ions such as Ti^{4+} and Sn^{4+} enter the structure of hematite. They have proposed a model which describes that these dopant ions adopt two distinct sites in the hematite structure; partially substituting

at octahedral Fe sites and occupying the vacant interstitial octahedral sites in α-Fe_2O_3. They suggested that, in the parent hematite phase hematite, pairs of FeO_6 octahedra exist due to ordered octahedral vacancies. These octahedral are face-sharing and are formed by the chains of Fe-Fe-□-Fe-Fe-□- . After the addition of tetravalent ion M the chain is changed to Fe-Fe-□-M-□-M-□-M-□-Fe-Fe-□-. In other words, two iron ions are replaced by three tetravalent ions and the charge neutrality is maintained through the formation of cation vacancies.

It was also found that no change in the oxidation state of Fe occurred; the charge balance was achieved by the formation of different defect clusters as described above. It has also been observed that in a mixed compound of Fe_2O_3-Cr_2O_3 the symmetry breaking resulted in the appearance of this Raman peak.[185] Bersani et. al.[186] suggested that the non-perfect stoichiometry and also the presence of some metal ions which would replace iron were responsible for the formation of disorder and the appearance of this peak. Glasscock et. al.[96] also observed the existence of the peak at 660 cm^{-1} when the hematite films were doped with Ti and they attributed the existence of this peak to the disorder in the films.

Hematite structure becomes less stable as the particle size decreases. As the particle size increases, a defect spinel, Maghemite (gamma-Fe_2O_3) polymorph is formed. Although maghemite is not the thermodynamically-favoured phase it becomes more stable at smaller particle sizes due to a lower surface energy compared to the hcp polymorph. This is the results of the more open lattice structure, a lower number of broken bonds per unit surface and lower surface polarity (higher bond covalency) of spinel phase.[187] The difference between maghemite and hematite is extremely difficult to be identified by XRD if both phases coexist. Both two phases have the same diffraction pattern while they have different symmetry groups. Vibrational spectroscopy (FTIR and Raman) can be used to distinguish these two phases. However, due to the small particle size, the IR spectrum is largely affected by the morphology of the particles.

4.2.3 Si Content – EDX analysis

The simplest way of quantifying the amount of different elements in the hematite films is through EDX analysis. Figure 4-14 shows chemical mapping of specific elements in the film, namely, Fe, Oxygen (O), Sn, Si and Pt. As shown in this figure, elements such as Pt, Fe and

Sn can be easily identified at different parts of the cross section of the film. Pt is present at the top of the film as it was deposited prior to ion milling to protect the top surface of the hematite film. Sn is present in the FTO layer of the substrate. Oxygen is present throughout the hematite film and also substrate. However, it is almost impossible to detect any Si in the hematite film while it is clearly present in the glass layer under the FTO layer in the substrate. This clearly shows that the amount of Si present in the film, if any, is much lower than the detection limits of the EDX method which is relatively a bulk characterisation method.

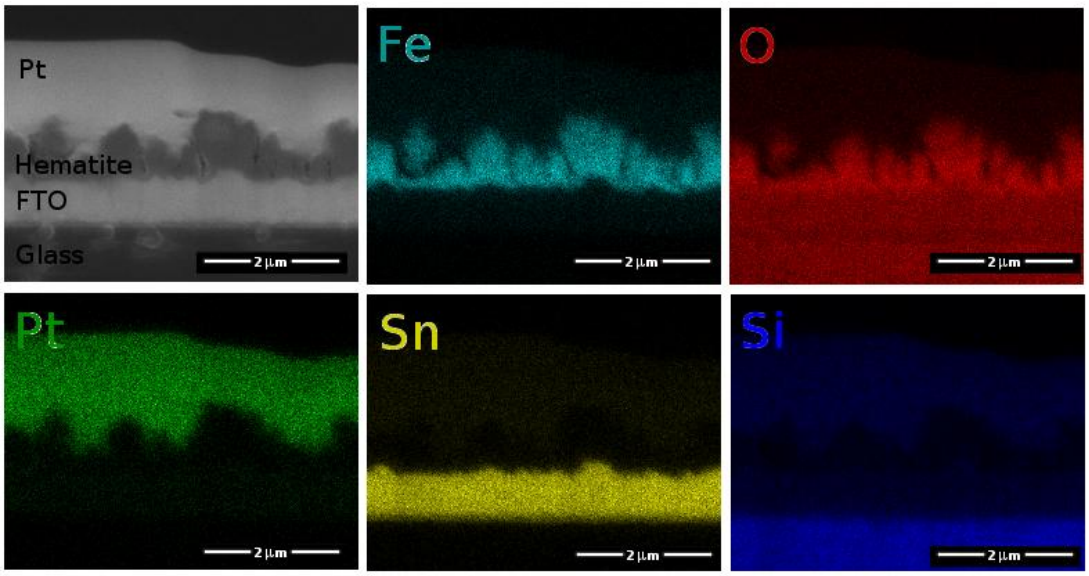

Figure 4-14. Elemental mapping of hematite films. Fe, Oxygen, Pt, Sn and Si have been investigated. The intensity of the colours is the indicator of the concentration of relative elements.

EDX line analysis of the hematite film across the thickness of the film was also carried out to quantify the amount of Si in the film. However, silicon was hardly detectable in the film due to the fact that the amount of silicon present in the films was far below the detection limits of EDX. Therefore, it is concluded that EDX was not a suitable method to quantify or even detect the presence of Si in the doped samples.

4.2.4 Si content – ICP-MS

In a previous study by Kay et. al.[99], the level of Si doping was calculated on the basis of the weight loss of the precursors. However, this technique does not account for the amount of silicon which is lost during the APCVD process. Precise measurement of the amount of silicon present in the hematite film is extremely difficult and challenging. In order to make some progress in this direction, ICP-MS measurements were carried out for the solutions prepared by digesting films in order to analyse the Si content in each hematite films.[173]

Different samples were characterised using this method. The samples selected were the films deposited with different argon flow rates for the silicon precursor, TEOS. Figure 4-15 illustrates the changes in the values of the Fe content in the films prepared at different TEOS flow rates. It was observed the best performing sample (TEOS Flow rate = 55 ml/min) exhibited the lowest Fe content while as the TEOS flow rate increased the Fe content was also increased. This suggests that the best performing samples were the thinnest among all the samples or had the highest porosity.

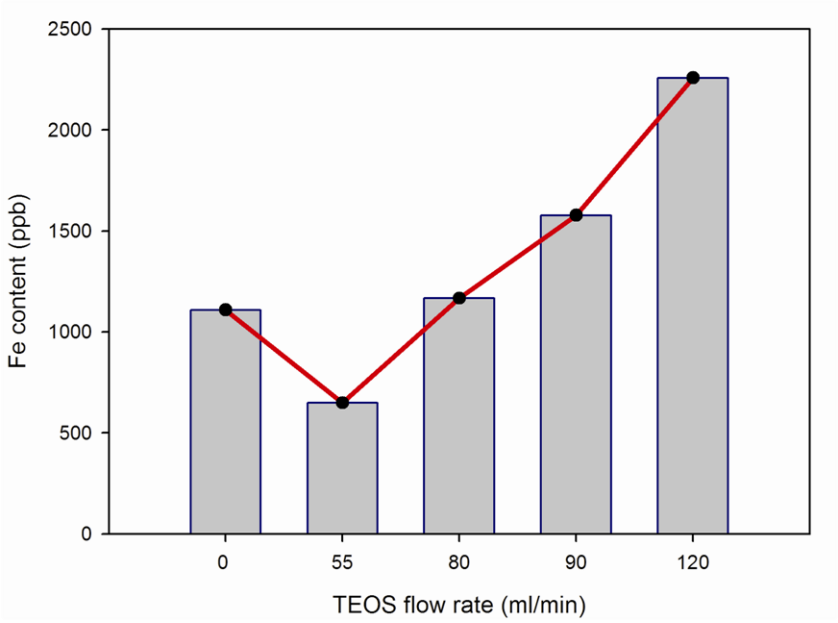

Figure 4-15. The changes in the Fe content of films as a result the changes in TEOS flow rate.

As shown in Figure 4-16, the pure pentacarbonyl samples which were prepared in the absence of TEOS had the lowest amount of silicon varying from 55 to 66 ppb. The existence

of relatively high amount of silicon in this sample could be due to the dissolution of silicon present at the glass surface (i.e. the back side of the FTO glass) during the sample preparation step or diffusion of Si into the hematite film from glass substrate during the APCVD process. Silicon content for the sample with the best PEC performance (which is corresponding to the Ar flow rate for TEOS = 55 ml/min) was measured in the range of 61-71 ppb which is slightly higher than that of pure pentacarbonyl sample. In order to prepare electrodes with higher levels of Si (called 'High TEOS') argon flow rate of the TEOS precursor was increased from 55 to 90 ml/min. The increase of the argon flow rate led to an increase in the amount of silicon detected from ~70 ppb to ~190 ppb.[173] This trend was consistent over a range of sample sets (Figure 4-16).

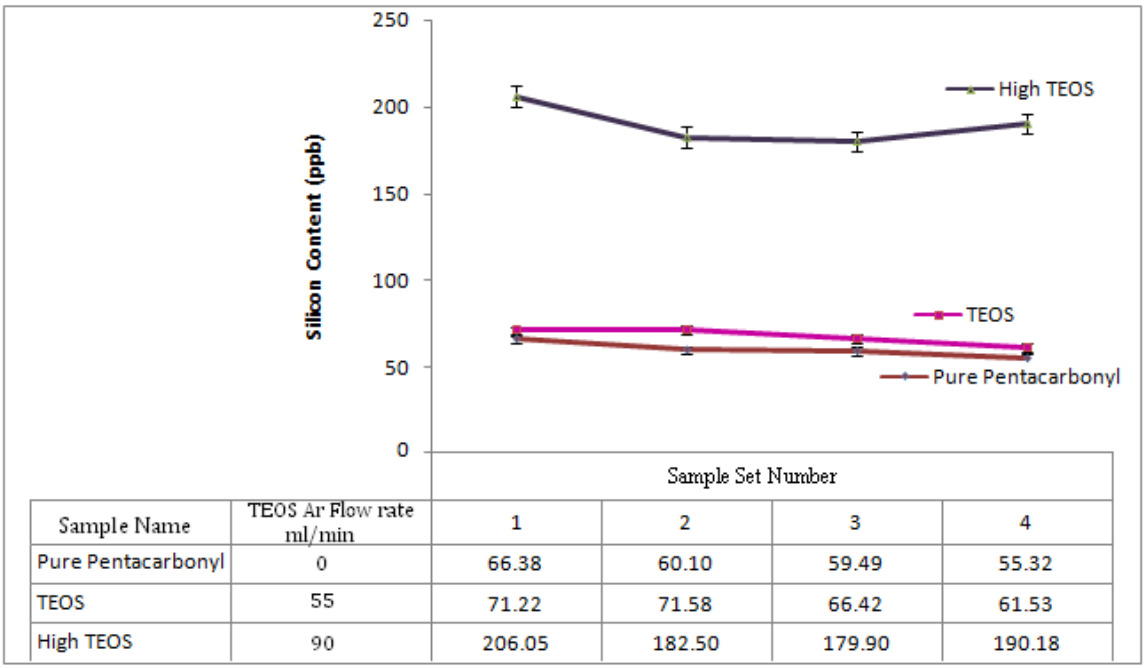

Sample Name	TEOS Ar Flow rate ml/min	1	2	3	4
Pure Pentacarbonyl	0	66.38	60.10	59.49	55.32
TEOS	55	71.22	71.58	66.42	61.53
High TEOS	90	206.05	182.50	179.90	190.18

Figure 4-16. The silicon content measured for three samples prepared by changing the argon flow rates for the TEOS precursor. The silicon content detected for 4 set of samples, each set prepared at increasing argon flow rate is shown in the table.[173]

A better explanation can be obtained if the ratio of the [Si]/[Fe] content is studied. As shown in Figure 4-17, this ratio increased as the TEOS flow rate was increased. The results clearly confirm the presence of silicon in the hematite films. They also confirm that the increase of argon flow rate leads to a higher amount of silicon in the hematite films.

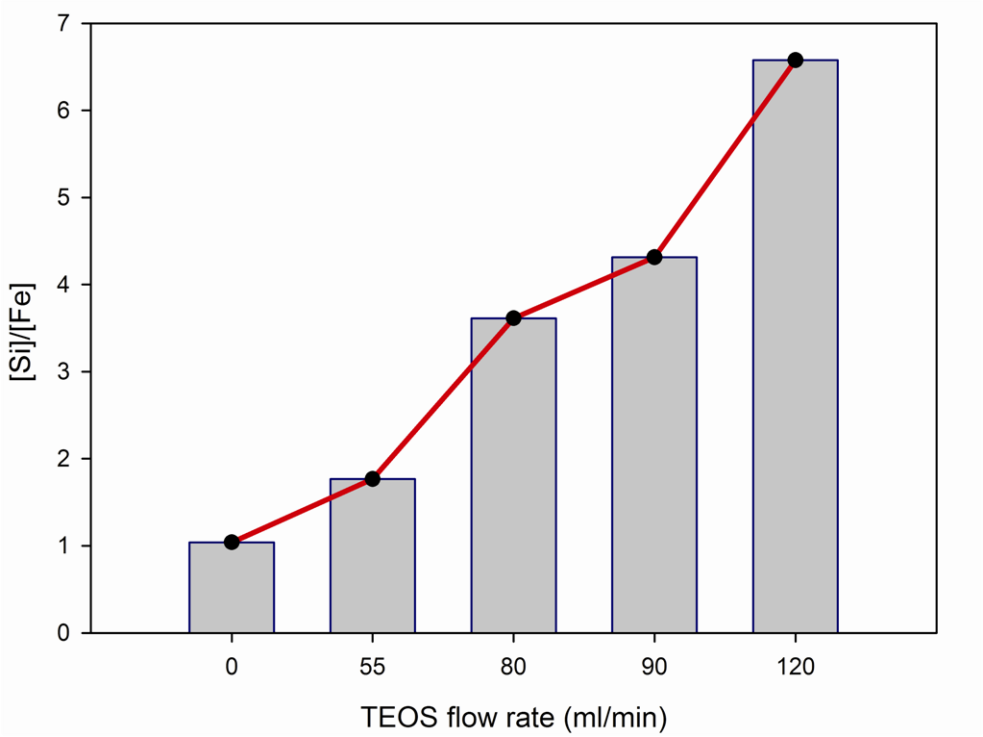

Figure 4-17. The changes in the [Si]/[Fe] ratio in film with different TEOS flow rates.

The determination of the exact amount of silicon in the hematite films using ICP-MS measurements was complicated by the fact that the films were made on FTO glass. Hence, it was difficult to prevent leaching Si into the digested solution from the back side and edges of the glass substrate. However, the qualitative analysis of the ICP-MS results indicates that generally the amount of Si in the hematite films could be adjusted by controlling the argon flow rate.[173]

4.2.5 Surface morphology and nanostructure (SEM)

SEM images of four types of hematite films showed a distinguishable difference in the surface morphology, in particular for the film made in the presence of Si-precursors. As shown in Figure 4-18, agglomerate/cluster structures in the pure pentacarbonyl and TMOF samples were present in two major sizes, 350±20 and 750±20 nm while the introduction of silicon into the electrodes resulted in a relatively uniform dispersion of approximately 350 nm±20 cluster/agglomerate structures.[173]

The tilted topography of each film at a much higher magnification is shown in Figure 4-19. As TMOF is introduced as the second precursor, although the formation of cluster/dendrite structure is initiated, it is still consisted of large particles whose sizes were distributed in a wide range. After the addition of silicon, the cluster/agglomerate nanostructure became finer; however, the particle size of the TMOS sample is larger than that of the TEOS sample.[173]

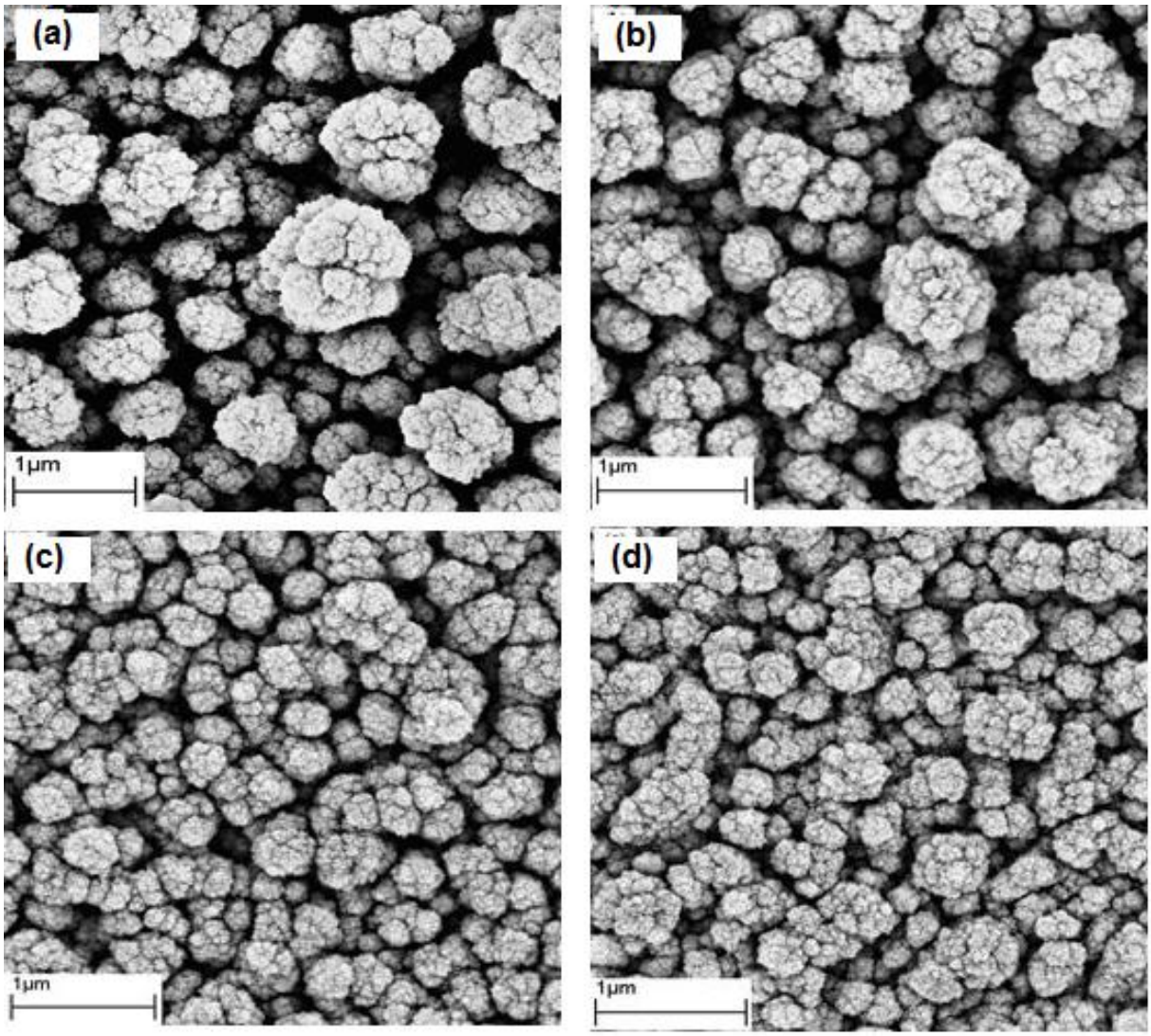

Figure 4-18. SEM pictures obtained for four types of hematite films; Pure pentacarbonyl (a), TMOF (b), TMOS (c), TEOS (d). Scale bars indicate 1 µm.[173]

In contrast to the nanostructure of the other three electrode types, the TEOS electrodes consisted of finer agglomerates/cluster nanostructures comprising of small individual particles uniformly distributed in size. Chu et. al.[188] investigated the relative stability of TEOS and TMOS in the gas phase. Their results showed a significant difference in the decomposition of TEOS and TMOS. The main difference was the formation of water during the decomposition of TEOS which accelerated further decomposition of TEOS *via* hydrolysis. Shimojo et. al.[189] and Takeguchi et. al.[190] studied the effect of water vapour on the deposition of iron oxide nanorods from iron pentacarbonyl by electron beam-induced deposition. They reported that addition of water facilitated the decomposition of iron pentacarbonyl, reduced the carbon content in nanorods, and induced the formation of crystalline iron oxide.[173]

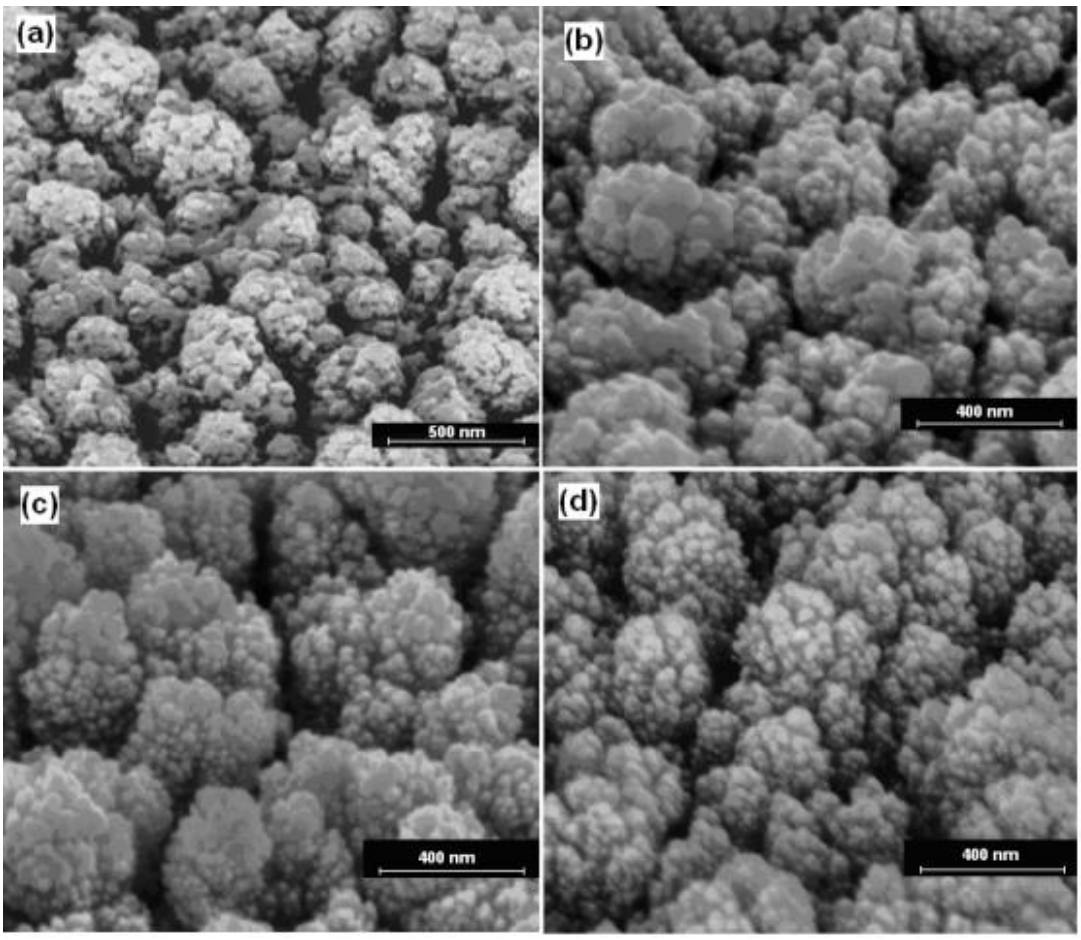

Figure 4-19. SEM pictures of four types of hematite electrodes prepared in this study. pure pentacarbonyl (a), TMOF (b), TMOS (c), and TEOS sample (d).[173]

Formation of small crystallites in the presence of TEOS compared to that of TMOS can be attributed to the effect of water formed during the decomposition of TEOS on the oxidation of iron pentacarbonyl. As water is introduced into the system by decomposition of TEOS, oxidation of iron pentacarbonyl accelerates rapidly and nucleation of iron oxide clusters increases. The increase in the nucleation sites results in a smaller crystallite size. However, in the case of TMOS in which the water formation is less favourable during the decomposition process, nucleation of iron oxide clusters takes place at a lower rate resulting in larger size crystallites. Smaller crystallite size along with less agglomeration could facilitate the separation of photo-generated charge carriers within the TEOS based hematite electrodes as the size of each particle in electrode structure becomes more compatible with the hole diffusion length of hematite.[85,99,173]

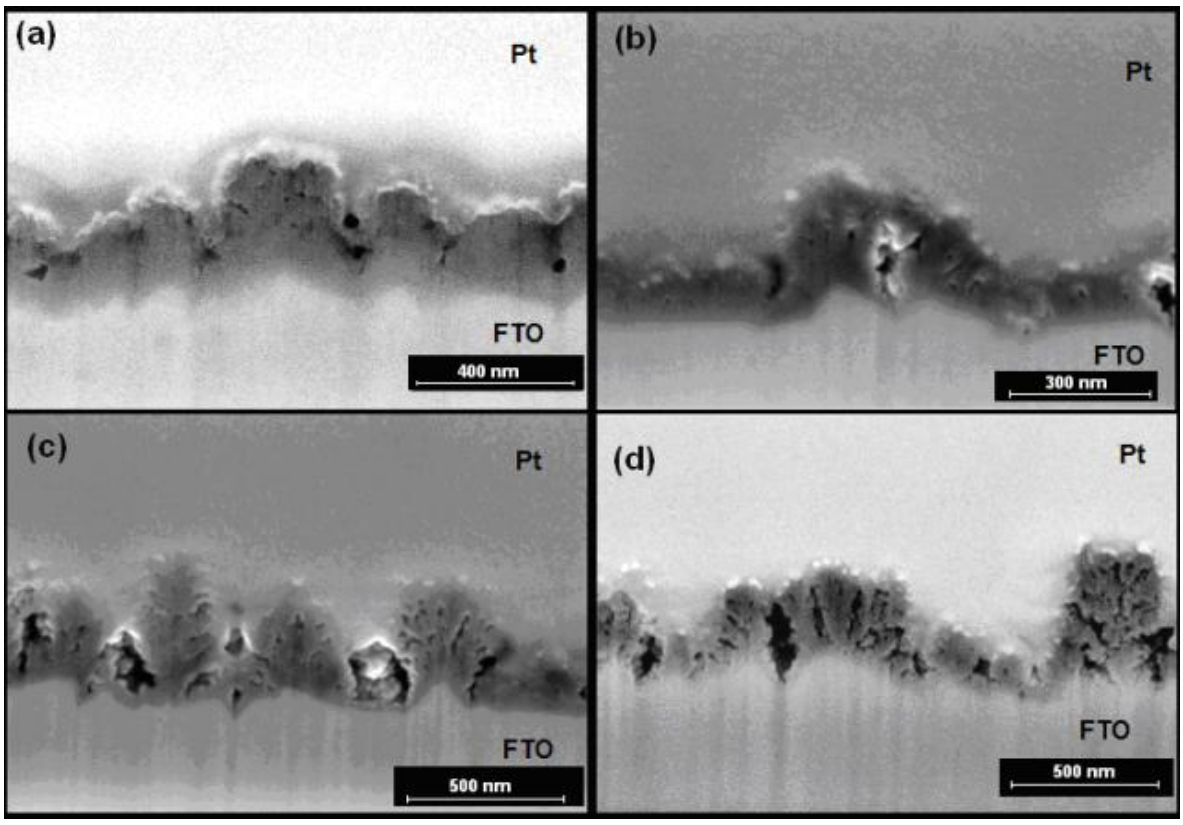

Figure 4-20. Cross sectional FIB/SEM images of four types of hematite electrodes prepared. Pure pentacarbonyl (a), TMOF (b), TMOS (c) and TEOS (d) . The deposited Pt layer and the FTO substrate are marked at each picture. Pictures are obtained at the tilt angle of 52°.[173]

The cross section and film thickness of hematite electrodes were studied by FIB/SEM. As shown in Figure 4-20, pure pentacarbonyl and TMOF films had maximum thicknesses of approximately 350 and 300 nm, respectively. The maximum thickness of both TEOS and TMOS films are in the order of 380-450 nm where the TMOS sample is generally thicker than TEOS. It is apparent that the growth of the hematite films on FTO glass follows the surface features of the substrate and almost conforms to the pattern of the FTO substrate. The difference in the cross sectional nanostructure of the each type of electrode is clearly visible in Figure 4-20. The film prepared by only iron pentacarbonyl precursor (with no additive agents) is more compact in nature and the lack of porosity agrees well with the tilted topography in Figure 4-18-(a). Porous structures are just beginning to appear for the hematite electrodes deposited in the presence of TMOF precursor. The porosity substantially increases for the thin films deposited with silicon precursors (TMOS and TEOS). The films deposited at the presence of TEOS precursor contain the highest porosity.[173]

4.2.6 Surface area measurements by dye adsorption

Hematite has the ability to react with Orange II due to the surface hydroxyl groups present at its surface and their intervention during chemisorptions of Orange II. Bandara et. al.[169] studied the dye absorption behaviour of hematite surfaces and concluded that Orange II was a suitable dye to study the surface area of hematite. They showed that a monolayer of the dye would form on the surface and calculated the surface coverage of 0.4 nm^2 for each orange II dye molecule at the surface of hematite.

The effect of the TEOS flow rate on the roughness factor of hematite films has been plotted in Figure 4-21. As shown, the general trend is decreasing; the increase in the TEOS flow rate hence Si content in the film (as shown by ICP-MS) resulted in the reduction of roughness factor of the films. This implies that the real surface area of the film decreased. However, this did not agree with the FIB-SEM observations for these samples where the increase in the porosity of the films was visible. This could be due to the fact that by increasing the TEOS flow rate, the surface of the hematite films contained more disorders. This could have strong implications of the chemical properties of the hematite surface and result in the less perfect coverage of the films by the monolayer of the dye.

Kay et. al.[99] reported roughness factor of 21±2 for their hematite samples but did not mention whether this value was for the undoped sample or doped. The highest roughness factor obtained in the present work (carried out for a minimum of 3 batches of samples) was 13±2 for undoped samples. The estimation of the surface roughness was performed by calculating the concentration of the desorbed dye solution (Orange II) from the absorption spectra. By knowing the surface coverage of the dye, it was possible to calculate the surface roughness of the films (See p.91). The introduction of TEOS into the deposition regime resulted in a significant increase, up to 50% for 10 ml/min TEOS flow rate, in the errors of the roughness factor measurements. This is an indirect confirmation of the huge changes in the surface properties of hematite electrode as a result of the TEOS introduction. At high TEOS flow rates the errors of the measurements reduced considerably while the roughness factor was also considerably low. Comparison of this information with Raman studies indicates that by increasing the TEOS flow rate the degree of surface disorder induced in the film increased substantially. These results suggest that dye adsorption studies for the measurement of roughness factor could be considered as a viable method for pure hematite surfaces but not suitable for doped hematite films.

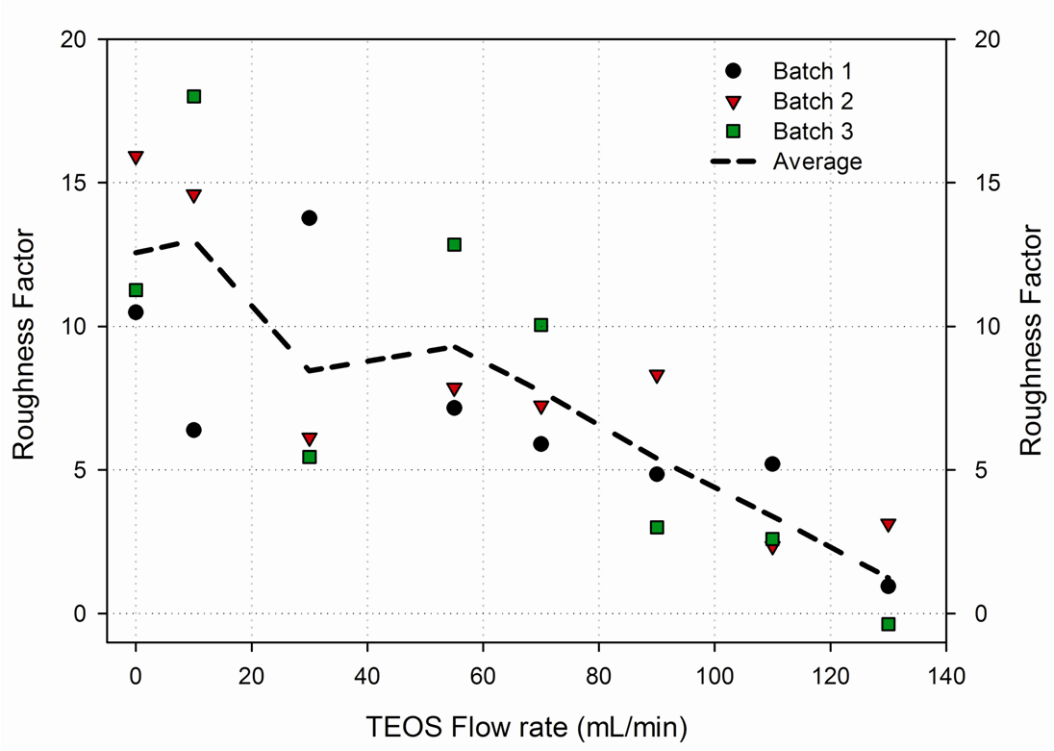

Figure 4-21. The graph shows the variation of the roughness factor of hematite films with respect to the changes in the TEOS flow rate.

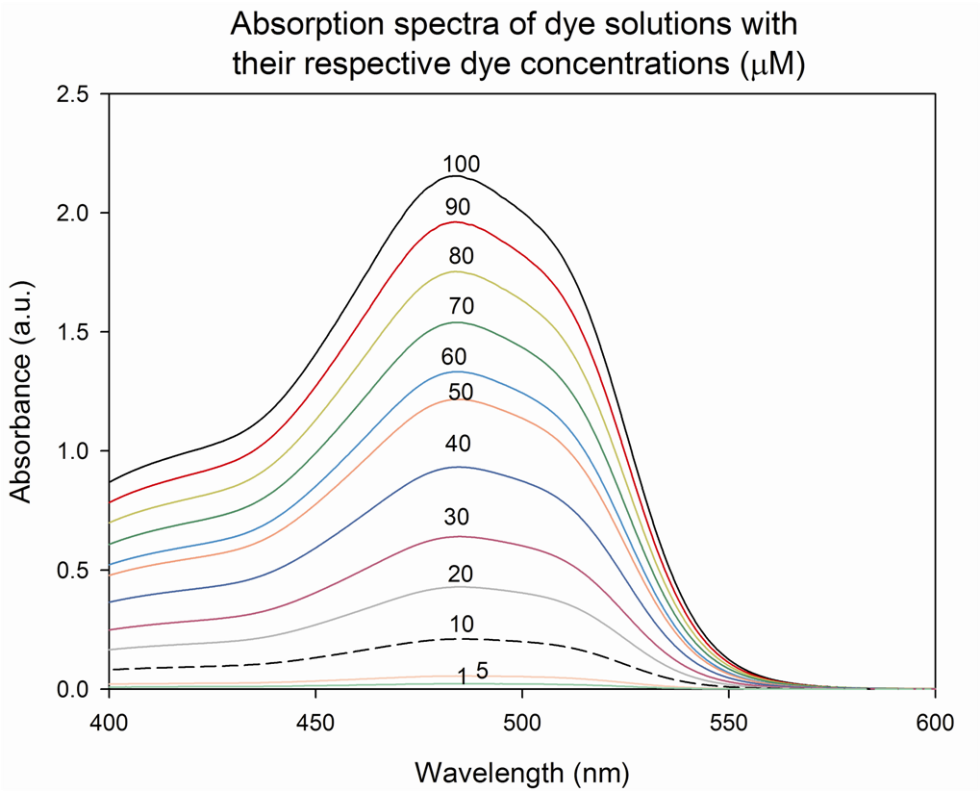

Figure 4-22. Optical absorption spectra of Orange II solution in water (pH=7).

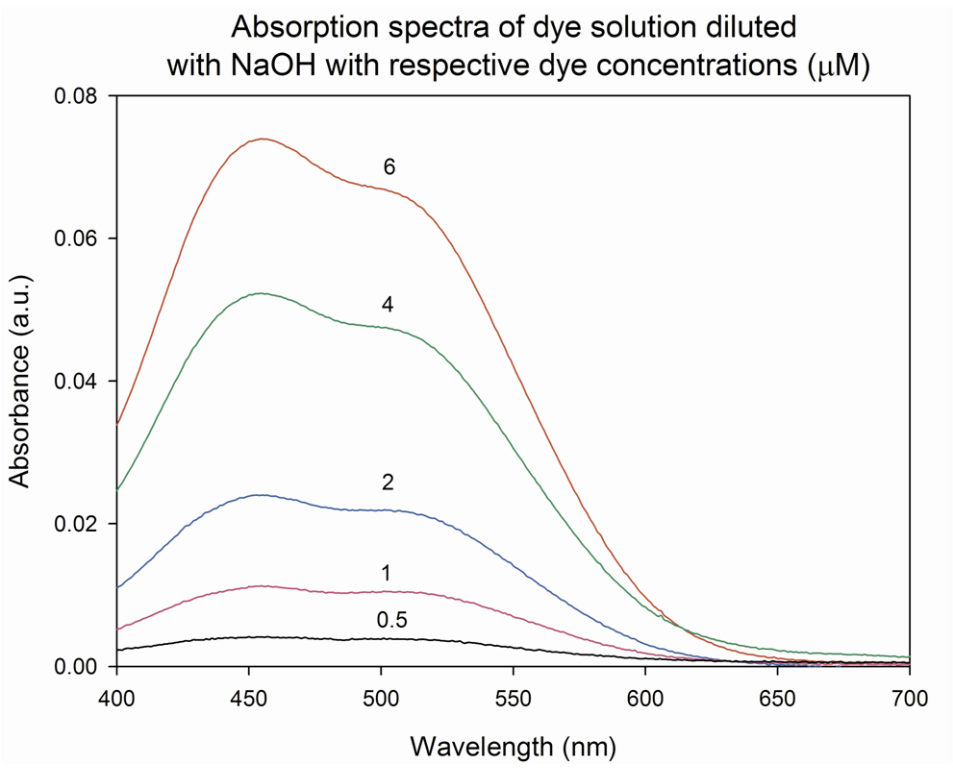

Figure 4-23. Optical absorption spectra of Orange II solutions in 1M NaOH.

It should be noted that the characteristics of absorption spectra of Orange II dye solution depends upon the solvent and the oxidising or reducing nature of the solution. As shown in Figure 4-22 and Figure 4-23, the absorption plot of the dye solution in alkali solution has two peaks with a maximum of the strongest peak at 450 nm. However, optical absorption behaviour of the dye changes as the pH changes. In aqueous solution (pH=7) the dye absorption spectra shows a maximum at 480 nm. Similar behaviour has also been observed by Yadav et. al.[170]

4.2.7 Bandgap - Optical properties

Optical properties of the films were studied by UV-vis spectroscopy. Absorption spectra of the films are shown in Figure 4-24. The light absorption is high at the short wavelength region of the spectra. As the wavelength increases the absorption is gradually decreased. As the spectra reach the characteristics of the optical absorption threshold for hematite (~ at 600 nm), the absorption drops rapidly and extends to the red region as a plateau.[173] The significant absorption beyond the α-Fe_2O_3 observed after this threshold could be the result of light scattering properties of nanoparticles at longer wavelengths which is a well-known phenomenon.[191,192]

The optical bandgap of hematite films can be estimated by calculating the intercept of the extrapolated linear fit to the experimental data of a plot of $(\alpha h\upsilon)^2$ versus incident photon energy ($h\upsilon$) near the absorption edge where α is the absorption coefficient of the electrode material.[24] The inset of Figure 4-24 shows $(\alpha h\upsilon)^2$ versus photon energy plots for each hematite electrode type. Indirect bandgap values measured are 2.05, 2.07, 2.08 and 2.12 eV for pure pentacarbonyl, TMOF, TMOS and TEOS electrodes, respectively, and closely match the values reported in the literature.[111] The bandgap values determined for pure pentacarbonyl, TMOF and TMOS are scattered around 2.0 eV whereas a slight enhancement in the bandgap was observed for the TEOS sample.[173]

The effect of the TEOS flow rate on optical properties of TEOS samples was also investigated. Three different types of samples prepared at different TEOS flow rates (30, 55, and 80 ml/min) were examined. As shown in Figure 4-25, as the TEOS flow rate was

increased in the sample deposition process a systematic increase in the indirect bandgap is observed.[173]

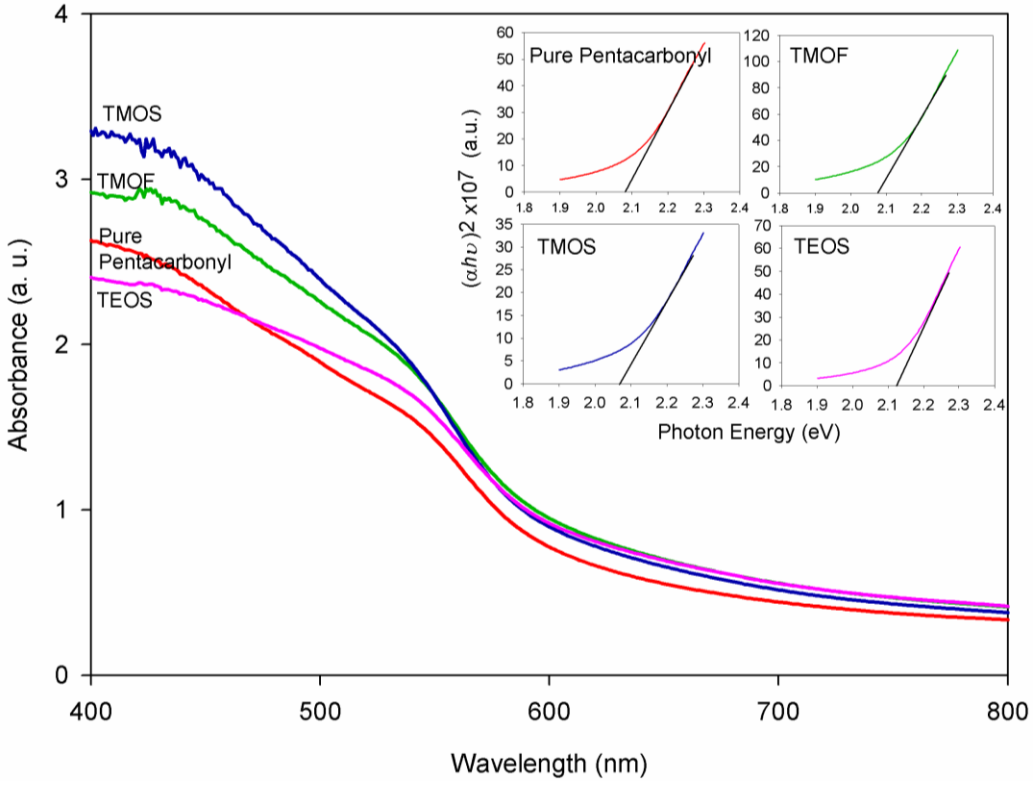

Figure 4-24. Absorption spectra of four types of hematite electrodes prepared in this study. TEOS in magenta, TMOS in blue, TMOF in green, and pure pentacarbonyl in brown. (Inset) $(\alpha h\upsilon)^2$ vs. wavelength plots for corresponding electrodes. The indirect bandgap was determined by extrapolation.[173]

This behaviour is in good agreement with the effect of particle size quantization on indirect bandgap of hematite.[193,194] Therefore, it suggests that the quantum size effect can be partly responsible for the increase of the bandgap of hematite as the increase in the TEOS flow rate would lead to decrease in the size of hematite particles.[173]

4.2.8 PEC performance

Current density-Potential (J-V) curves of different samples are shown in Figure 4-26. The electrodes made in the presence of Si precursors show negligible dark currents (<2 μA.cm^{-2})

up to 1.6 V_{RHE} whereas the dark current for other two electrodes (pure pentacarbonyl and TMOF) started to rise at potentials as low as 1.4 V_{RHE}. Pure pentacarbonyl electrodes showed a negligible photocurrent density of 1.5 $\mu A.cm^{-2}$ at 1.23 V_{RHE} whereas the samples prepared with TMOF had photocurrent densities slightly better than that (~ 6.3 $\mu A.cm^{-2}$ at the same bias).[173]

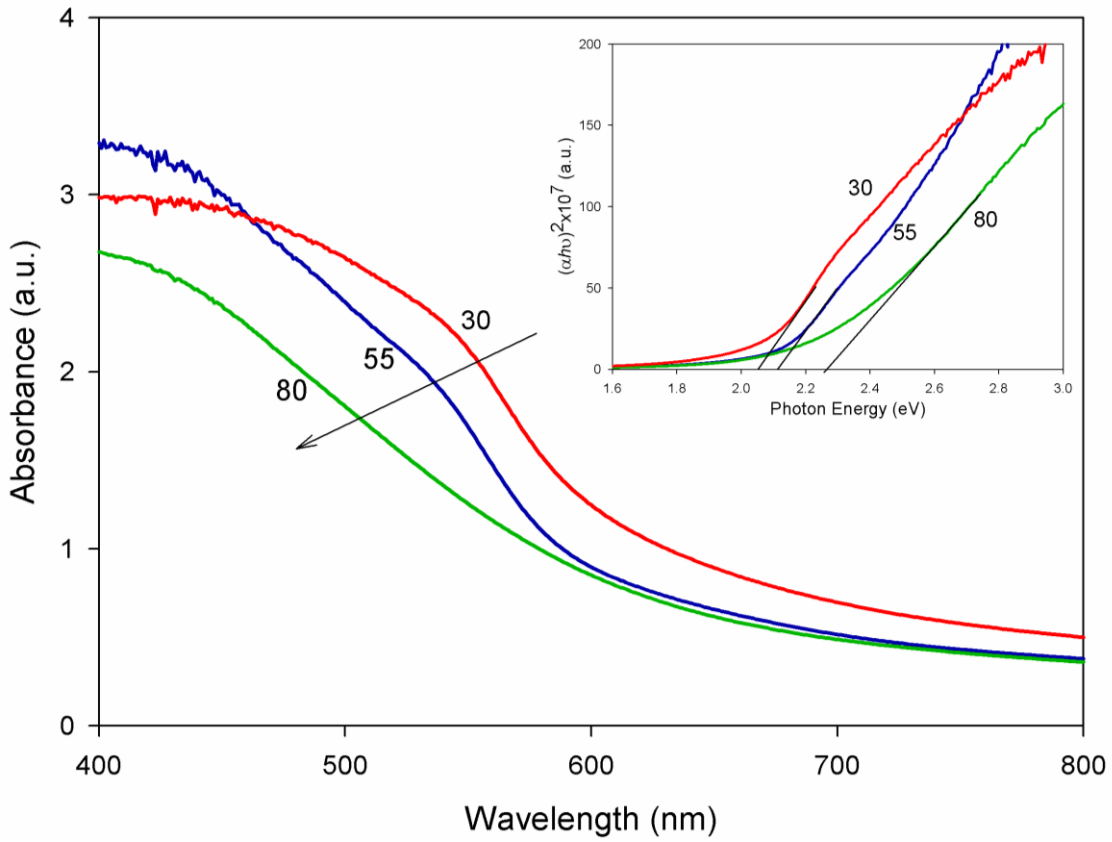

Figure 4-25. Absorption spectra of Si-doped hematite films with three different TEOS flow rates of 30, 55 and 80 ml/min. Inset shows the indirect bandgap measurements of the films.[173]

Comparing the cross sectional and topographical SEM images and XRD data of pure pentacarbonyl and TMOF electrodes, it is apparent that the porosity and surface morphology is slightly changed in the TMOF electrode. Although magnitude of the photocurrent enhancement in TMOF electrode compared to that of the pure pentacarbonyl electrode is small, this improvement can be attributed to the difference in the nanostructure. The best photocurrent performance was obtained when TEOS was used as the source of silicon, 1.67

mA.cm^{-2} at 1.23 V_{RHE} which is less than the previously reported highest performance for electrodes prepared by APCVD.[99,173]

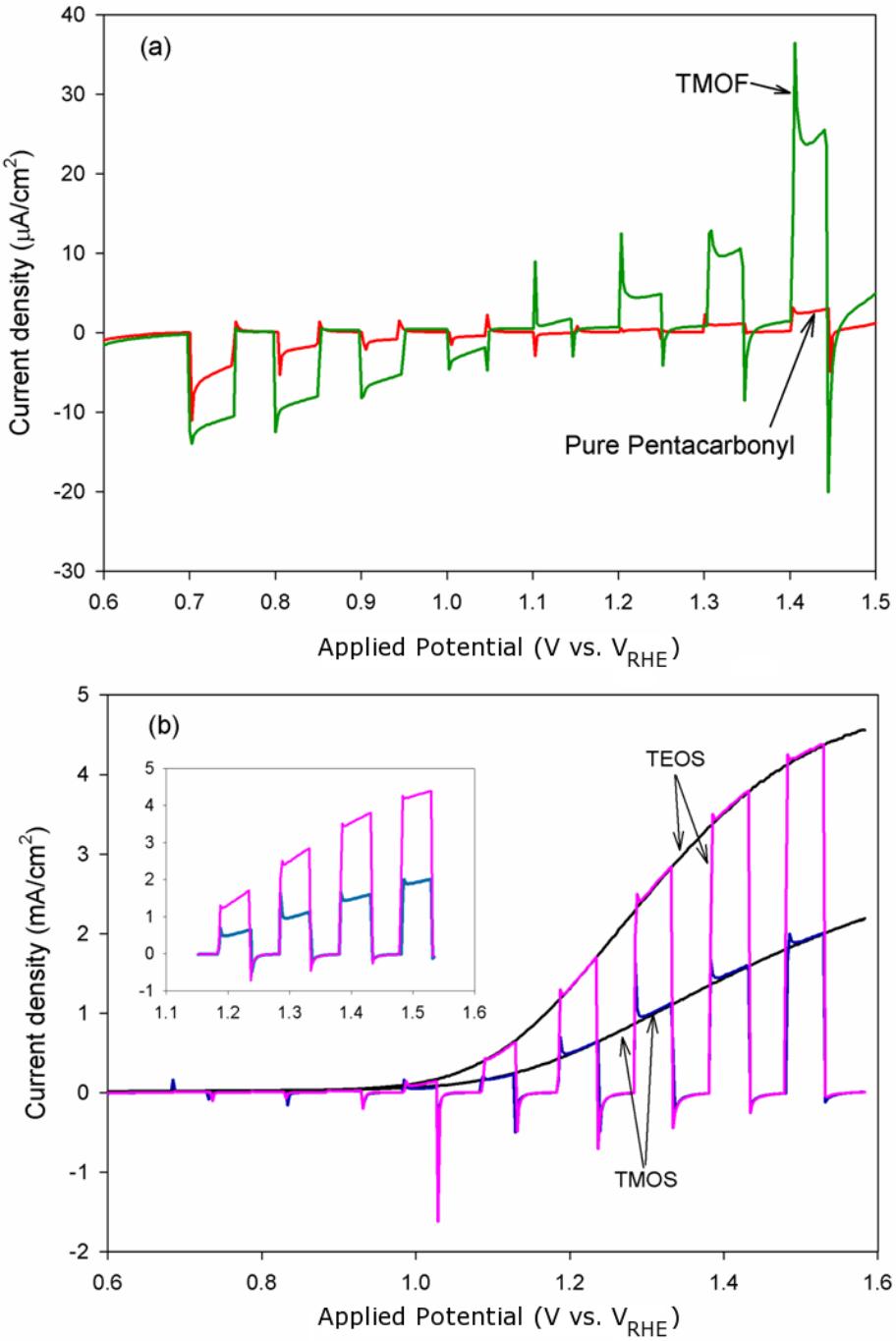

Figure 4-26. (a) Current density vs. applied potential (J-V) characteristics of pure pentacarbonyl and TMOF samples in 1M NaOH under AM 1.5 conditions. (b) Current density vs. applied potential (J-V) characteristics of TEOS and TMOS samples in 1M NaOH under AM 1.5 simulated light illumination. Inset shows the magnified J-V plot of the samples at the potential range of 1.1-1.6 V vs. V_{RHE}.[173]

The lower photocurrent achieved compared to the highest reported so far[99] may be attributed to the differences in the amount of Si present in these films, the precise control of which is rather difficult in the custom build APCVD set up. When TMOS was used as the Si source instead of TEOS, the photocurrent density decreased to 0.62 $mA.cm^{-2}$. It is worth mentioning that the vapour pressure of TEOS (<1 mmHg) is considerably lower than that of TMOS (173 mmHg). Therefore, obtaining the same level of Si as in the case of the TEOS electrode requires far better precise control over the amount of Si-containing agents reacting in the aerosol.[173]

It is apparent in SEM cross sectional images that the TEOS electrode consisted of fine nanostructures (compared to that of TMOS). As suggested by Kay et. al.[99] the formation of fine nanostructures with the particle sizes comparable to the hole diffusion length of hematite may be responsible for the superior photocurrent. Furthermore, the role of the primary particle size cannot be neglected; a larger primary particle size can still be partly responsible for the drop in the photocurrent output in the TMOS sample in comparison to that of in TEOS. The chopped photocurrent pulses for the TMOS electrode (see the inset of Figure 4-26-(b)) clearly shows relatively higher recombination at lower applied voltages in comparison to the case of TEOS supporting the proposed interpretation.[173]

4.2.9 Flat-band potential and donor density – EIS

The capacitance data (represented by Mott-Schottky plots) for 4 different types of hematite electrodes are given in Figure 4-27. The donor densities (uncorrected for the surface roughness factor) and flat-band potentials deduced from the capacitance measurements are given in Table 4-1 along with the photocurrent onset values read from the linear fit of the intercept of J^2-V plots.[173]

The introduction of organic additives (regardless of the presence or absence of Si) appears to shift the photocurrent onset towards the negative direction (Table 4-1). For example, hematite electrodes prepared using only iron pentacarbonyl alone showed photocurrent onset potential at around 0.12 $V_{Ag/AgCl}$. After the addition of TMOF, TMOS and TEOS the photocurrent onset potentials have moved to 0.07, -0.43 and -0.47 $V_{Ag/AgCl}$, respectively. It is clearly noticeable that, in particular the introduction of Si by the

incorporation of Si precursors in the APCVD process has significantly shifted the onset potentials towards the negative direction. It is assumed that specific adsorption of decomposition products of TMOS and TEOS may have played a role in this shift. As far as the photoanodic process is concerned this apparent shift has a significant advantage for PEC water splitting device fabrication, although the exact origin of this shift is yet unclear.[173]

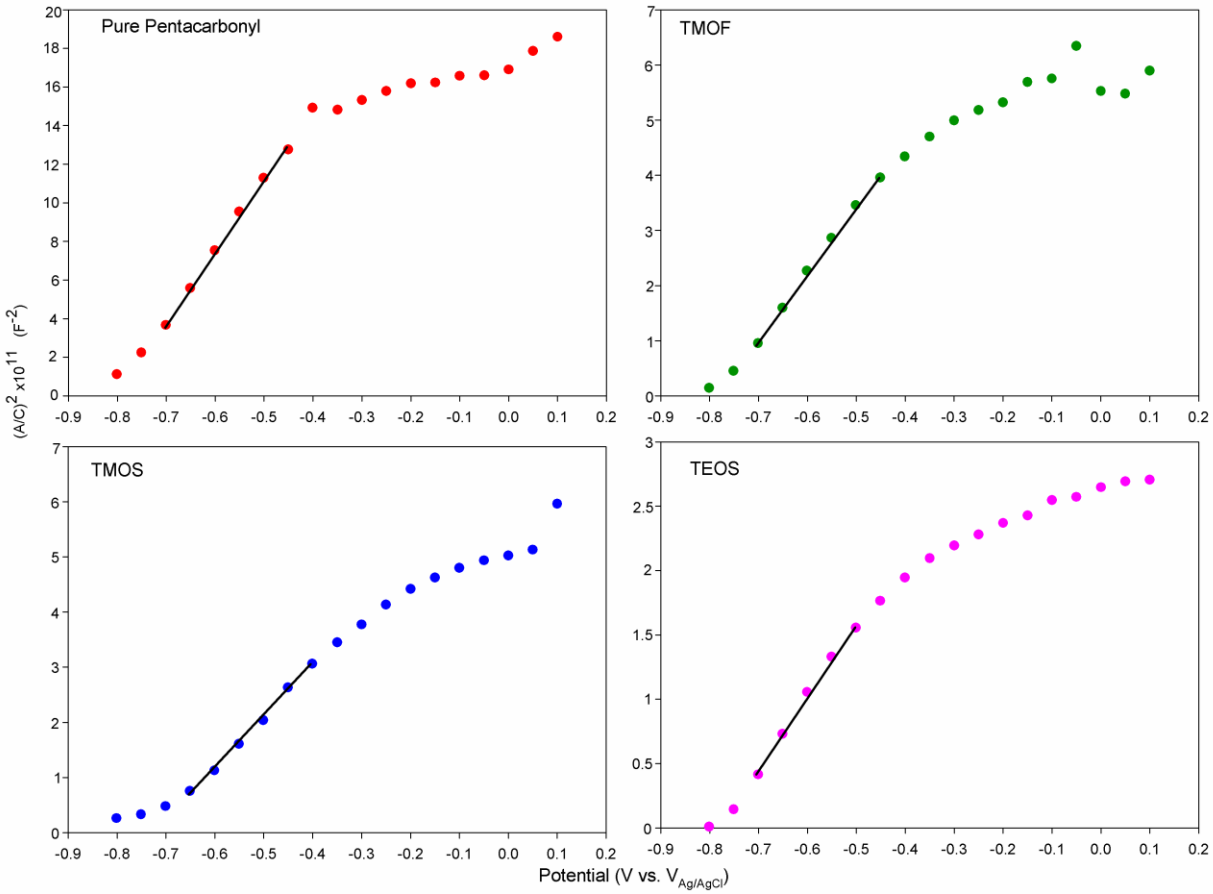

Figure 4-27. Mott-Schottky plots of four different hematite electrodes at the frequency of 100 kHz.[173]

It is apparent that at the potentials above -0.7 $V_{Ag/AgCl}$, all electrodes are in the depletion region. Therefore, the slopes of the linear region between -0.7 and -0.4 $V_{Ag/AgCl}$ of the Mott-Schottky plots were used in the estimation of donor density (uncorrected for the surface area) for each electrode (Table 4-1) change the linear plot of TEOS. Although the donor densities presented in Table 4-1 suggest that the concentration of charge carriers does not vary significantly between different samples, the true donor density for the samples made in

the presence of Si-precursors (in particular TEOS and TMOS samples) should be significantly smaller than the calculated values.[173]

As a rule of thumb if the surface area enhancement is about 100 times, the true donor density is in the order of 10^{21} m^{-3}. This value is at least three orders of magnitude smaller than the literature reported values for Fe_2O_3 electrodes.[96,195] Therefore, it seems that the recorded total capacitance should be somewhat higher than the true space charge layer capacitance. Although the estimated donor density (after considering the surface area enhancement of TEOS electrode) appeared to be less than the reported values, the estimated space charge widths for all four cases generally suggests that the depletion layer should be extended significantly into further interior of the TEOS and TMOS electrodes leading to a better harvesting of photo-generated charge carriers. Considering pattern of photocurrent performance obtained for 4 different types of Fe_2O_3 electrodes investigated in this study, this explanation agrees well.[173]

Table 4-1. Electrical and photoelectrochemical properties of four different types of hematite electrodes deduced from Mott-Schottky and J^2-V plots.[173]

Sample name	Donor density* (m^{-3})	Flat-band potential V_{fb} (V vs. $V_{Ag/AgCl}$)	Photocurrent onset potential, V_{onset} (V vs. $V_{Ag/AgCl}$)
Pure Pentacarbonyl	4.04×10^{24}	-0.80	0.12
TMOF	1.21×10^{25}	-0.78	0.07
TMOS	1.56×10^{25}	-0.72	-0.43
TEOS	2.52×10^{25}	-0.77	-0.47

* The donor density values were not corrected for the true surface area.

An important assumption of the depletion layer model at the semiconductor-electrolyte junction is that the semiconductor is not too heavily doped, hence the space charge layer capacitance (C_{sc}) is much smaller than the double layer capacitance (C_{dl}). Under this condition the observed total capacitance is very close to the C_{sc} (Equation 4.1):[173]

$$\frac{1}{C} = \left(\frac{1}{C_{sc}} + \frac{1}{C_{dl}}\right) \approx \frac{1}{C_{sc}} \qquad (4.1)$$

Therefore, the considering the relatively low surface area donor density obtained for pure pentacarbonyl and TMOF electrodes should reflect the true donor density values. For TMOS and TEOS electrodes the C_{sc} could be affected by two aspects. The first is the significant surface area enhancement. The second is the decrease of the width of the space charge layer induced by the dopants. The measured total capacitance for these two electrodes therefore, could be substantially influenced by the C_{dl}. Hence a true estimation of the extension of space charge layer and the donor density for TMOS and TEOS electrodes is difficult. A significant implication of this phenomenon is the frequency dispersion of capacitance measurements for nanostructured electrodes.[173]

In order to obtain a better understanding of the properties, such as flat-band potential, of hematite electrodes in electrolyte solution, the electrodes were investigated by cyclic voltammetry considering a capacitive behaviour at the hematite/electrolyte interface. Figure 4-28 and Figure 4-29 show CV and current-scan rate plots obtained for TEOS sample at different scan rates. The Mott-Schottky graphs obtained by this method are also shown in Figure 4-30.

By using this approach, the flat-band potential and donor density values calculated as -0.4836 V vs. $V_{Ag/AgCl}$ and 4.92×10^{24} m^{-3}. The flat-band potential obtained by this method is very close to the photocurrent onset potentials calculated from J^2-V graphs. However, it is much smaller than the values obtained from EIS measurements. As discussed earlier, the assumptions made for the calculations of flat-band potentials from EIS measurements could eventually result in significant degrees of errors and the information obtained from EIS must be treated very carefully.

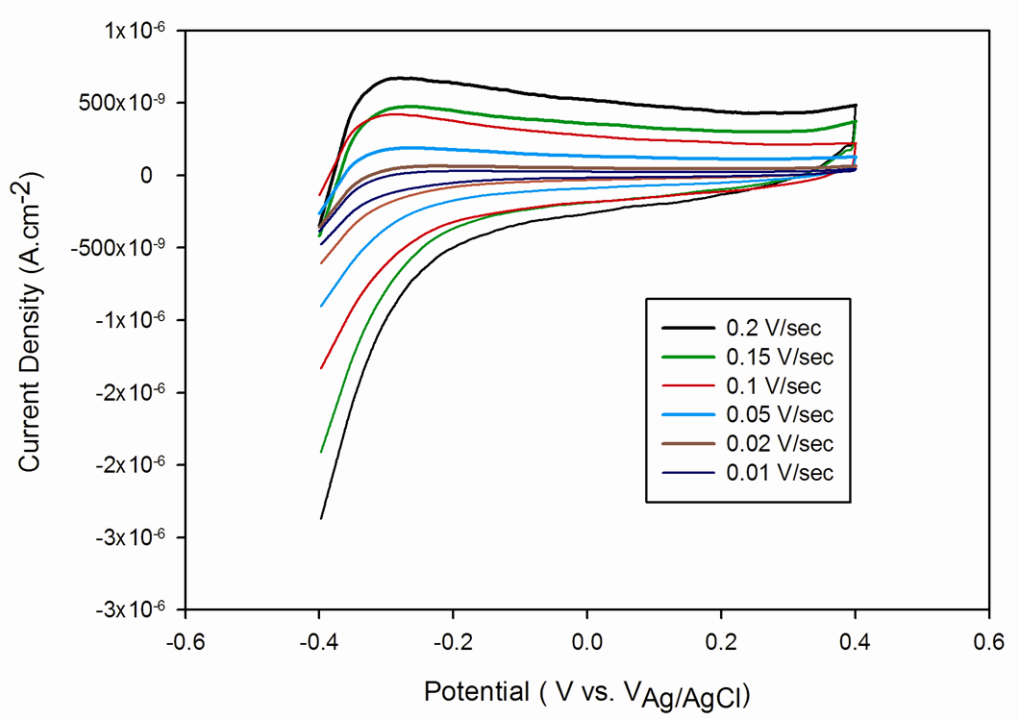

Figure 4-28. Cyclic voltammetery spectra of TEOS sample at different scan rates.

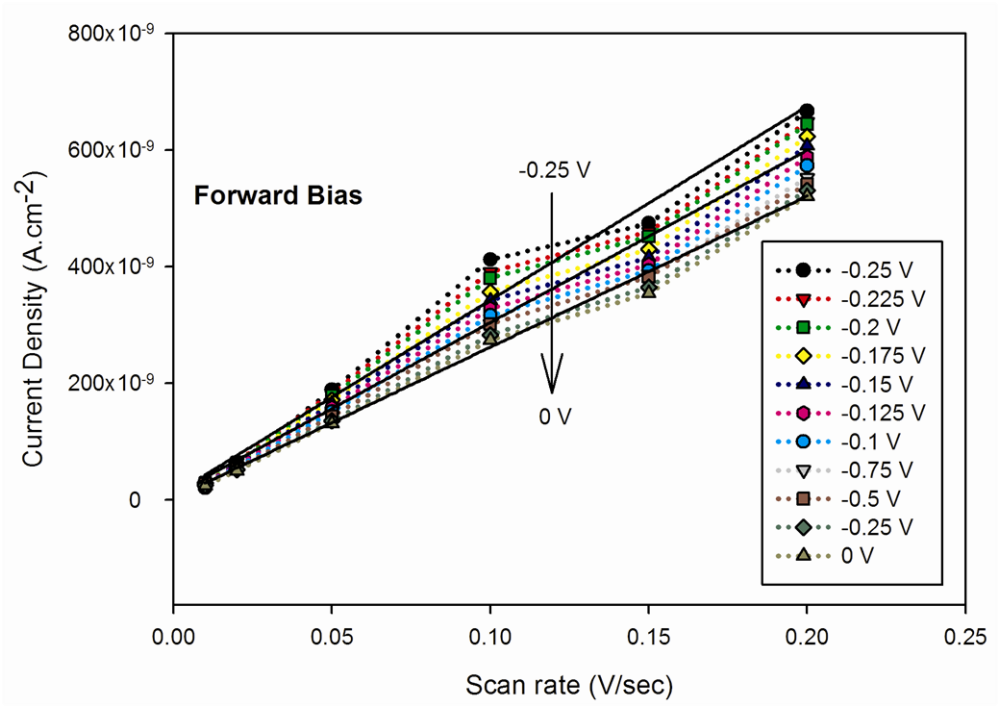

Figure 4-29. Current density vs. scan rates plots of TEOS sample at a range of potentials under forward bias. The slope of each plot equals capacitance. Three solid lines are the best linear fit for -0.25, -0.15 and -0.025 V.

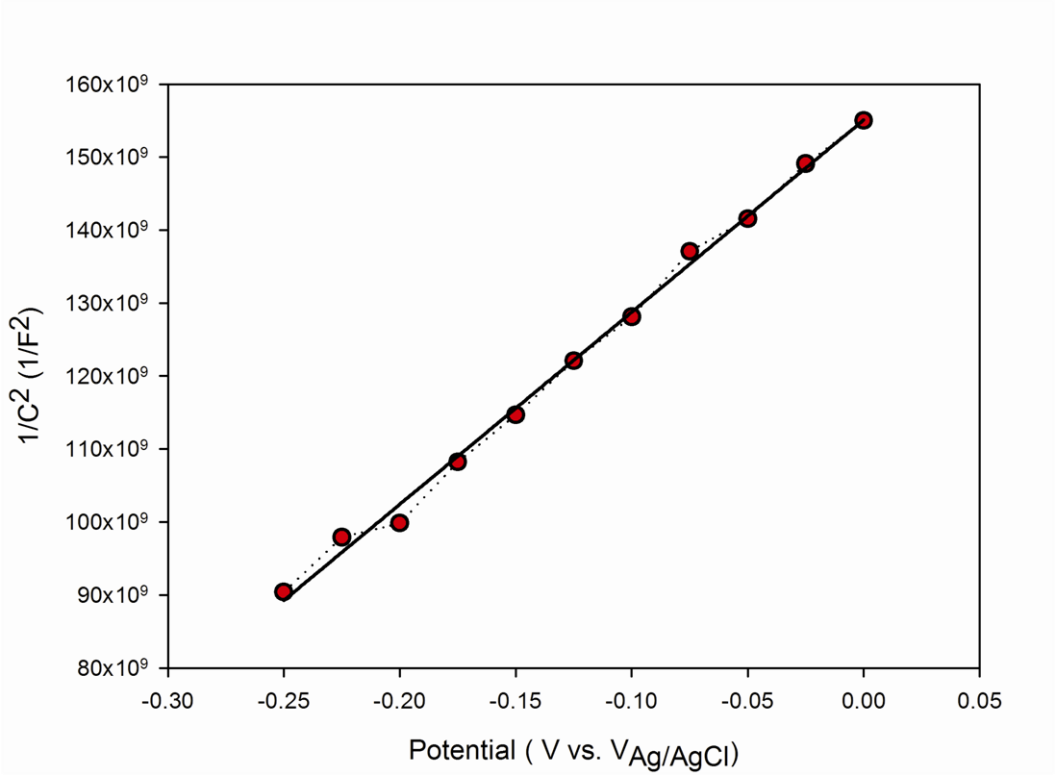

Figure 4-30. Mott-Schottky plot of TEOS sample obtained from CV method.

4.2.10 IPCE and APCE

Quantum efficiency of different types of samples was studied by both IPCE and APCE. As shown in Figure 4-31 and Figure 4-32, there is a significant difference in the IPCE and APCE spectra of doped and undoped samples. Figure 4-31-(a) depicts the IPCE of doped TEOS and TMOS samples showing a maximum of 34% and 17.3% at 350 nm, respectively (V = 0.23 V vs. $V_{Ag/AgCl}$). However, the maximum quantum efficiency at the same potential for both undoped samples occurred at 570 nm and 575 nm for TMOF and pure pentacarbonyl samples. It is clear that quantum efficiency for these samples is very low (less than 0.15%) which agrees well with their poor PEC performance. Similar trend is observed for all the samples in the case of their APCE (Figure 4-32-(a) and (b)). The expected theoretical values of the photocurrent at 0.23 V vs. $V_{Ag/AgCl}$ is calculated by the integration of the IPCE results over the wavelength range and considering the photon flux. This value equalled 1.3 $mA.cm^{-2}$ for TEOS sample and 0.67 for TMOS electrode (which is very close to the measured 0.63 $mA.cm^{-2}$). The value obtained for TEOS sample was smaller than the measured value (1.67 $mA.cm^{-2}$). Glasscock et al.[96] has also observed similar discrepancy

between theoretical and measured photocurrent densities of Si and Ti doped hematite electrodes. They attributed the problem to the nonlinearity of the photo-response of the electrodes. Apart from this, inherent errors in the measurement (e.g. the exact light intensity) and also multiplication of photocurrent obtained from electrodes with surface areas of smaller than 1 cm^2 (to achieve photocurrent density) can be an important source for this discrepancy.

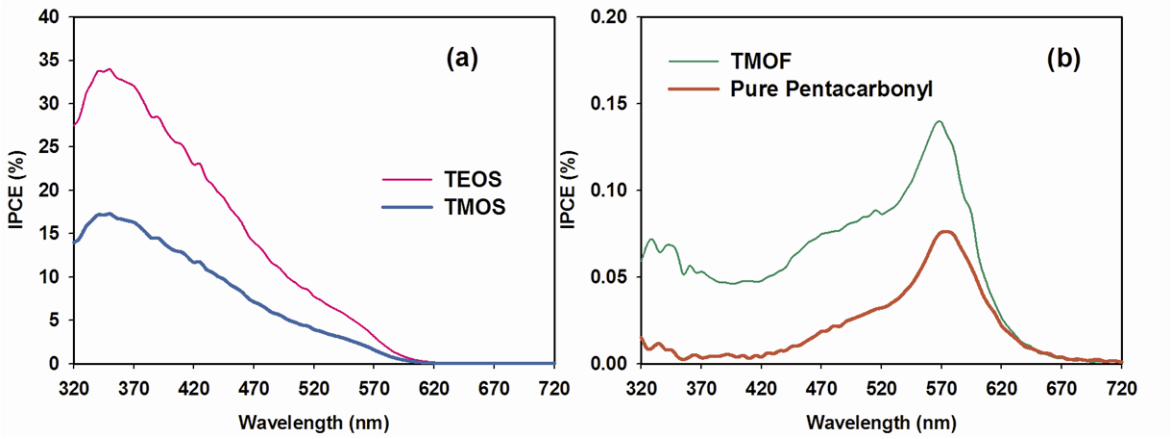

Figure 4-31. IPCE graphs of (a) TEOS and TMOS and (b) TMOF and pure pentacarbonyl samples. The measurement potential is 0.23 V vs. $V_{Ag/AgCl}$.

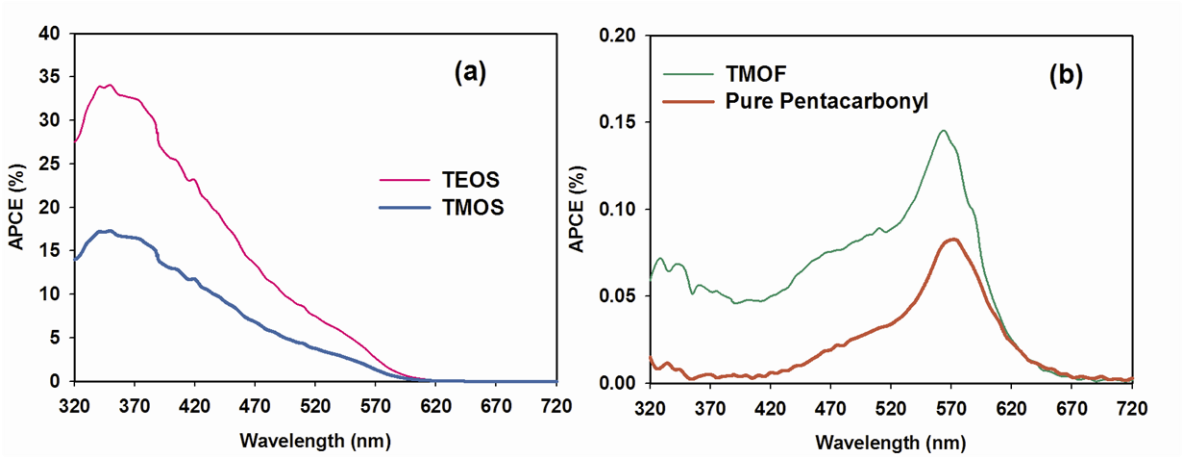

Figure 4-32. APCE graphs of (a) TEOS and TMOS and (b) TMOF and pure pentacarbonyl samples. The measurement potential is 0.23 V vs. $V_{Ag/AgCl}$.

The fundamental difference between quantum efficiency behaviour of the doped and undoped samples where the wavelength at which the maximum efficiency happened. In the

case of undoped samples, the maximum occurred at 350 nm which is far from the bandgap excitation wavelength. In contrary, maximum quantum efficiency of undoped samples appeared at wavelengths very close to the fundamental bandgap excitation (~570 nm). This clearly indicates substantial differences in the optical and electronic properties and charge generation and relaxation processes present in doped and undoped samples. This information provides good grounding for understanding of not only the unexpected poor photo-performance of undoped samples but also the reasons behind enhanced photocurrent densities observed for doped samples.

Iron oxides have three kinds of optical transitions: the ligand to metal charge-transfer transitions (LMCT), the ligand field transitions (d-d transitions) and the pair excitations.[196,197] The electronic spectra of iron oxides show Fe^{3+} ligand field transitions and multiple Fe^{3+} excitations in the visible and near-UV region.[197] It is agreed that the band gap at ~2.2 eV is due to Fe^{3+} d-d transitions and indirect in nature.[198] Higher lying direct transitions from the O_2-2p valence band orbitals to the conduction band happen above 3 eV(i.e. less than 400 nm).[198]

Few reports have been published regarding the carrier dynamics of iron oxides and the effects of defects and adsorbents on the carrier lifetime.[197,198,199,200] Unfortunately, there is only one study on the effects of doping on carrier relaxation of hematite which has concluded that carrier relaxation was insensitive to dopants.[199] These studies show that decay time of electrons for iron oxide nanoparticles is in the range of picoseconds while trapping is the predominant phenomena. The fast trapping of the excited electrons has been attributed to the existence of d-d states within the bandgap (mid-bandgap states) and not a consequence of the impurities or defects in most hematite nanoparticles.[197,199] Another important limiting factor is also known to be strong electron-phonon coupling which is greatly influenced by particle size and magnetic properties of samples.

Fan et. al.[197] observed an ultrafast relaxation and also subsequent slower relaxations upon excitation at 400 nm. Optical absorption around 400 nm originates mainly from the LMCT. They ascribed the ultrafast decay within 100-200 fs to an initial fast relaxation of hot electrons to the bottom of the conduction band. After the ultrafast decay, a fast and a slow decay process also occurred on several picoseconds and tens to hundreds of picoseconds time scales, respectively.[197] The fast decay is attributed to the relaxation of the hot electrons

at the bottom of conduction band via the efficient trapping into intrinsic low-lying electronic states through d-d hopping. The slow decay was then attributed to the slower relaxation of trapping electrons.[197]

Unfortunately, the time scales of the IPCE measurement are far from the ultra fast measurements used to study the carrier dynamics of iron oxides hence making it difficult to suggest any clear process for carrier relaxation and recombination in the samples. Moreover, there is no report on the effects of doping of hematite films and nanoparticles by tetravalent ions such as Si^{4+} and carrier relaxation processes. The observation from IPCE data is that the majority of the photo-performance of hematite electrodes originates from the quantum efficiency at wavelengths less than 400 nm. In this region, direct transitions from the O_2-2p valence band orbitals to the conduction band are responsible for optical absorption and relaxation processes are controlled by trapping in mid-bandgap states. However, it is suggested that the major difference between the doped and undoped samples is the degree in which the relaxations are altered by electron-phonon coupling. It is possible that the inclusion of Si^{4+} in the crystal structure of hematite alters the magnetic and dielectric properties of hematite films. This would probably further inhibit electron-phonon coupling in the doped samples hence rendering the relaxation processes slower and improving the photo-performance. However, further experiments are required to verify this. Another important aspect could also be due to the changes in the surface morphology of the samples and higher porosity of the doped samples. This would make the trapping sites more accessible to the adsorbates at the surface and increasing trap fillings. However, in order to evaluate any of these claims it is essential to investigate carrier dynamic properties of these films using ultrafast methods.

4.2.11 APCVD using ferrocene

As discussed earlier, Kay et. al.[99] reported crystalline Si-doped hematite films prepared by APCVD with efficiencies even higher than that of single crystals.[201] It was claimed that this outstanding performance was attributed to the fine dendritic nanostructure of the films as well as the doping effect of silicon. Although PEC performance of the Si-doped hematite electrodes prepared by APCVD was promising, un-doped electrodes performance was very poor (ca. photocurrent density <10 $\mu A.cm^{-2}$ at 1.23 V_{RHE}).[99]

Due to the specific requirements of APCVD method, i.e. precursor with high vapour pressure, the available iron precursors are limited. Ferrocene is a well-established iron source and has been widely studied in applications such as catalysts,[202] gas sensors,[203] antiknocking agents,[204] ferromagnetism[205] and carbon nanotubes.[206] It is stable at room temperature but becomes highly volatile at higher temperatures (vapour pressure of 30 mmHg at 150 °C [207]). Although its decomposition temperature has been reported above 400 °C,[208] Bernhauer et. al.[209] observed that the decomposition of ferrocene occurred at temperatures as low as 380 °C. Therefore, it offers a good alternative to iron pentacarbonyl for the deposition of hematite photoelectrodes *via* APCVD. In comparison with iron pentacarbonyl, Ferrocene is cheaper, less toxic and easier to handle.[210]

4.2.11.1 Initial experiments

The major problem in this method was the inconsistency in the uniformity of the films; incomplete coverage of the deposition area by the hematite film was a common problem. This problem was usually caused by the relatively large solid particles falling on the film and burning on the surface of the substrate. These particles were usually the result of the deposition of the aerosol inside the delivery tube, which were then pushed towards the substrate by the carrier gas. This problem was addressed by using a heating pad wrapped around the delivery tube to maintain a uniform temperature along the travel path of the aerosol.

The best PEC performance was achieved when APCVD of hematite electrodes using ferrocene was carried out by maintaining the temperature of ferrocene at 160 °C while argon was used as the carrier gas (flow rate 150 ml/min) to direct the aerosol outside the flask. The aerosol was then mixed with air flowing at 2 L/min and directed to the FTO substrate heated to 400 °C using a metallic hotplate. The temperature of the travel path of the aerosol was maintained at 150 °C using a heating pad wrapped around the glassware. A glass tube with the diameter of 10 mm was used as the delivery tube positioned 20 mm above the heated substrate. A glass cup was also used to minimise the effect of the suction of the fume cupboard. The optimum deposition time was found to be 18 minutes while shorter and longer deposition time resulted in poor PEC performance.

4.2.11.2 Structural characterisation (XRD)

Figure 4-33 illustrates the XRD pattern of hematite film prepared by APCVD of ferrocene (sample E18). As shown in this figure, four peaks of hematite are visible, (102), (104), (110) and (300) while all the other peaks correspond to the FTO substrate. This data suggests that the hematite film is reasonably crystalline. On the basis of analysis for (110) peak, mean crystallite size of this film is around 37 nm.

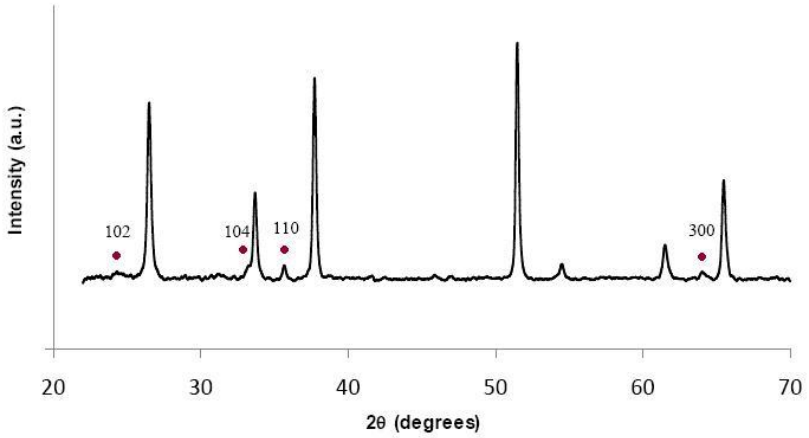

Figure 4-33. XRD pattern of hematite film prepared by APCVD of ferrocene.

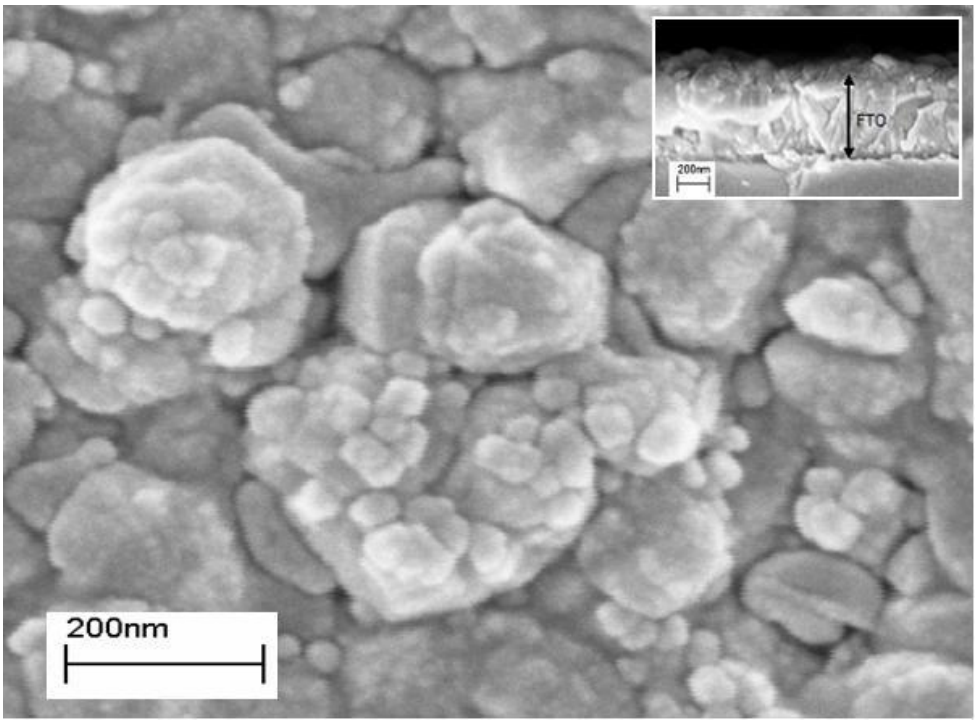

Figure 4-34. SEM pictures obtained for ferrocene APCVD sample. Inset shows the SEM cross section SEM of this sample.

4.2.11.3 Surface morphology (SEM)

Surface morphology and thickness of E18 sample was studied by SEM. As it is shown in the SEM pictures of the hematite film (Figure 4-34), it consists of two distinguished parts, small individual particles of approximately 70 nm and agglomerates of approximately 300 nm. The surface of the conductive FTO glass is covered with a very thin and relatively compact layer of hematite film. As shown in the inset of Figure 4-34, the thickness of the film varies between 100 to 150 nm.

4.2.11.4 Optical properties

Optical absorption spectrum of hematite film is illustrated in Figure 4-35. In order to measure the indirect bandgap of the hematite film, $(\alpha h\upsilon)^2$ was plotted against photon energy and indirect bandgap was calculated by extrapolating (Figure 4-36). Indirect bandgap is measured 2.08 eV which is in good agreement with the values previously reported for hematite. It also agrees well with the absorption edge measured using the absorbance plot (Figure 4-35). The absorption edge is measured to be around 592 nm which equals 2.09 eV.

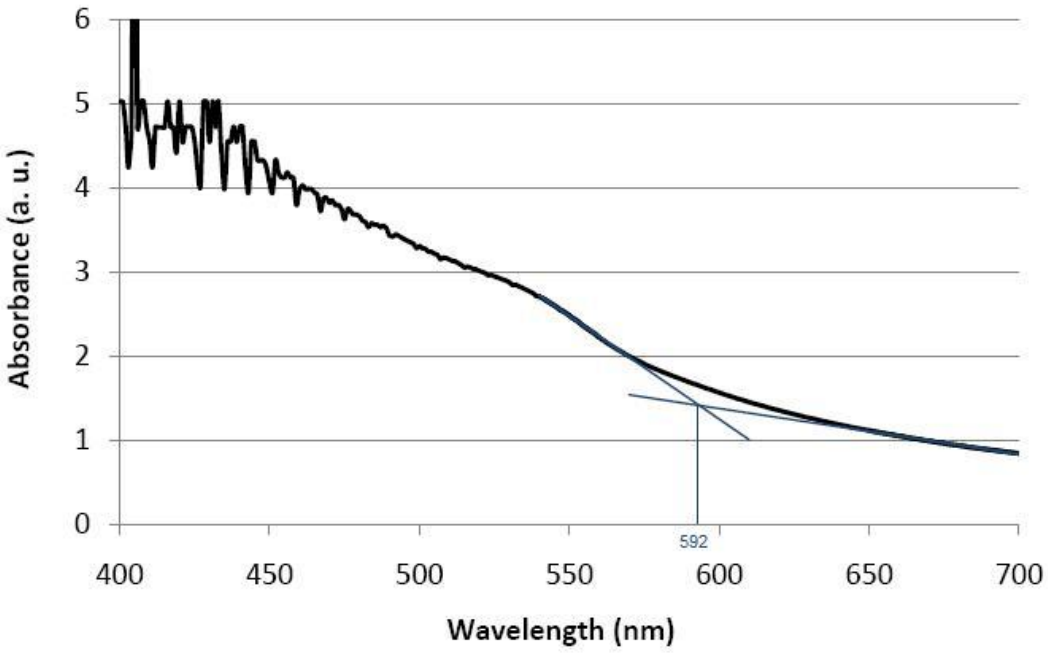

Figure 4-35. Optical absorption plot of the sample prepared by APCVD of ferrocene. The estimated light absorption edge is around 592 nm.

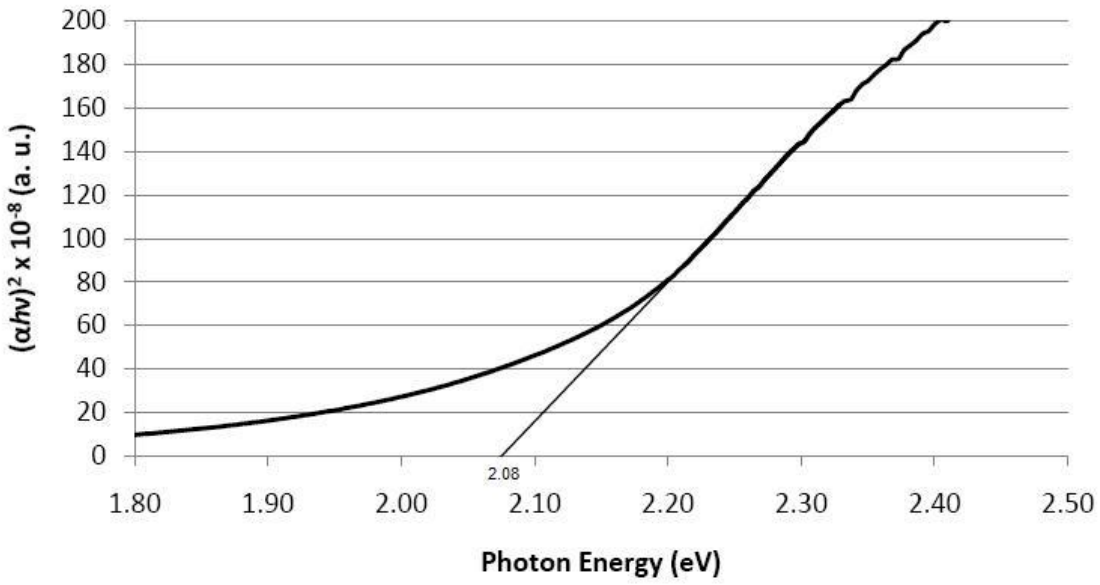

Figure 4-36. $(\alpha h\upsilon)^2$ vs. wavelength plot (Tauc plot) of ferrocene APCVD sample. Indirect bandgap was measured by extrapolation.

4.2.11.5 PEC performance

Photocurrent density- Voltage (J-V) curve of the hematite film is shown in Figure 4-37. Photocurrent density measured at 1.23 V vs. V_{RHE} is 540 μA.cm^{-2}. Dark current is almost negligible up to bias potential of as high as 1.7 V vs. V_{RHE}.

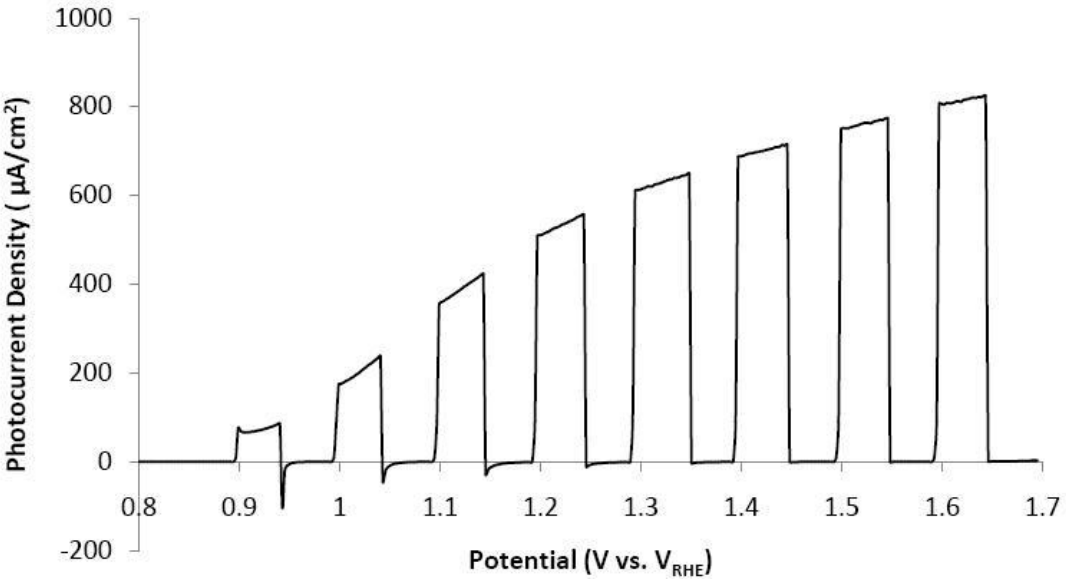

Figure 4-37. Photocurrent density vs. Potential (J-V) plot for ferrocene APCVD sample.

Although the results obtained from APCVD of ferrocene were promising, the complexity of the deposition setup and also difficulties in reproducing good films comparing to APCVD of iron pentacarbonyl were serious problems in this method. The important advantage, however, was that in this method no doping agent was used. The PEC performance of un-doped hematite films prepared by APCVD of ferrocene was superior to films prepared by APCVD of iron pentacarbonyl.

4.2.12 Comparison of APCVD of undoped hematite using ferrocene and Iron Pentacarbonyl

Figure 4-38 illustrates the XRD patterns of both samples. As illustrated, four peaks of hematite are identified in both samples; (102), (104), (110) and (300). All the other strong peaks correspond to SnO_2 in the FTO substrate. It confirms the formation of crystalline hematite films.[210]

Crystallite size of different samples was measured using the Scherrer equation. On the basis of the analysis of (110) peak, mean crystallite size of 37 and 20 nm was obtained for the ferrocene and iron pentacarbonyl samples, respectively.[210]

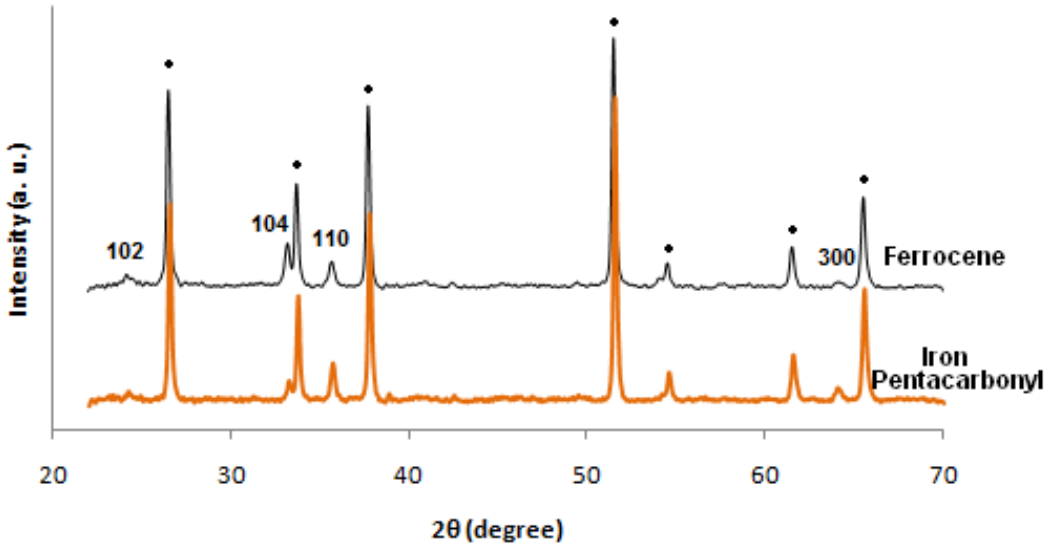

Figure 4-38. XRD pattern of the films prepared by ferrocene and iron pentacarbonyl. (102), (104), (110) and (300) reflections correspond to hematite. The peaks labelled with (•) correspond to the SnO_2 in the FTO substrate.[210]

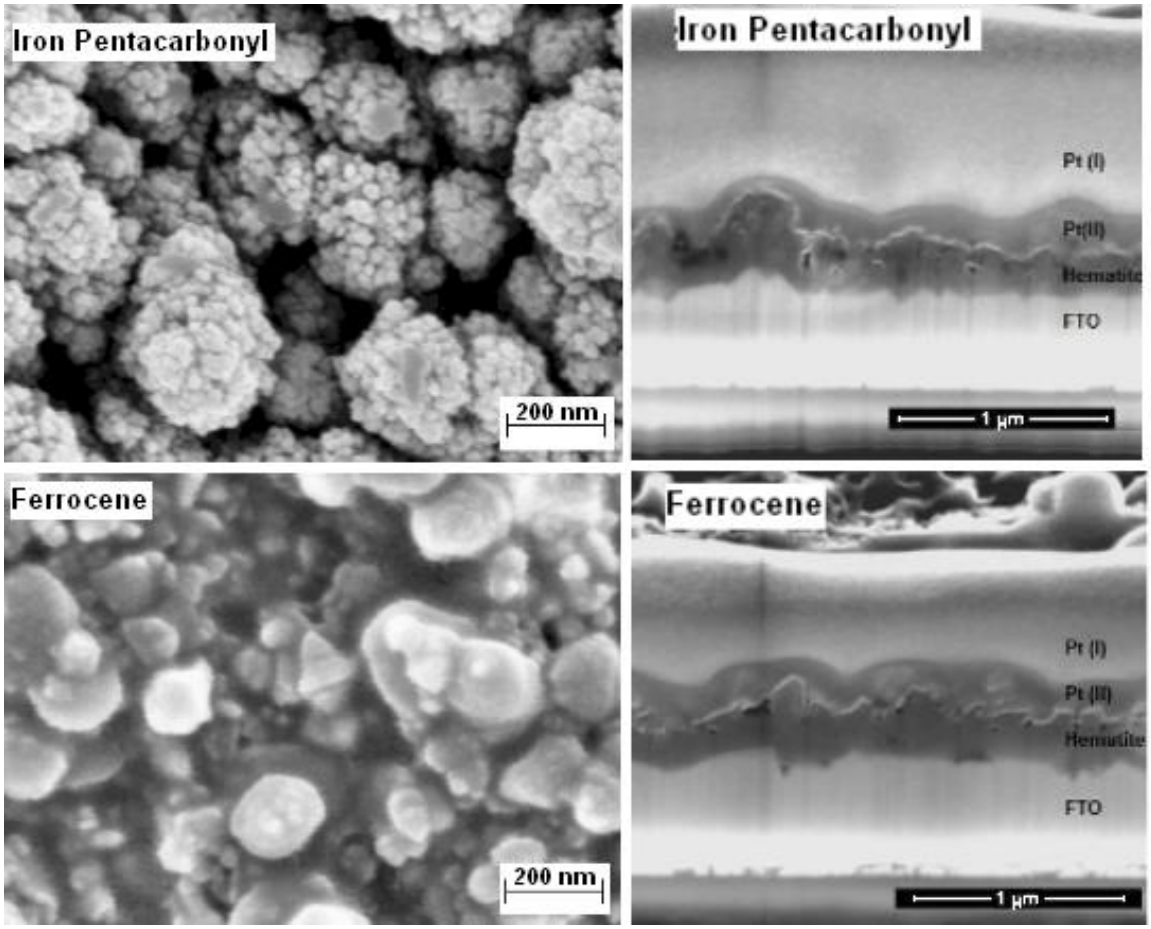

Figure 4-39. SEM micrographs of hematite films showing surface morphology and the thickness of the films prepared by iron pentacarbonyl and ferrocene. Pt (I) and Pt(II) are the platinum layers deposited by ion beam and electron beam, respectively.[210]

Surface morphology of the films was studied using SEM. As shown in Figure 4-39, the surface structure of the films prepared using ferrocene and iron pentacarbonyl is significantly different. The hematite films prepared by iron pentacarbonyl is made up of nanostructured agglomerate/clusters of around 200 nm in size which themselves consist of smaller particles of around 20 nm. The films prepared by ferrocene are almost free of the agglomerate/cluster features and comprise a nanostructure of bigger particles.[210]

Optical absorption spectra of two hematite films are illustrated in Figure 4-40-(a). It clearly shows that the absorbance of the ferrocene electrode is significantly larger than that of the iron pentacarbonyl sample at wavelengths lower than ~600 nm. As shown in Figure 4-39, the average thickness of each film is in the range of 300 nm. Therefore, the difference

in the optical absorbance (Figure 4-40-(a)) may not be due to the difference in the thickness of the films. The difference in the absorbance, however, can be attributed to the difference in the nanostructure, hence packing density of the films. SEM pictures confirm that while film thickness remains almost the same, films prepared by ferrocene are more compact than the iron pentacarbonyl sample which consist of a large number of voids and unfilled spaced within the nanostructure of the film.[210]

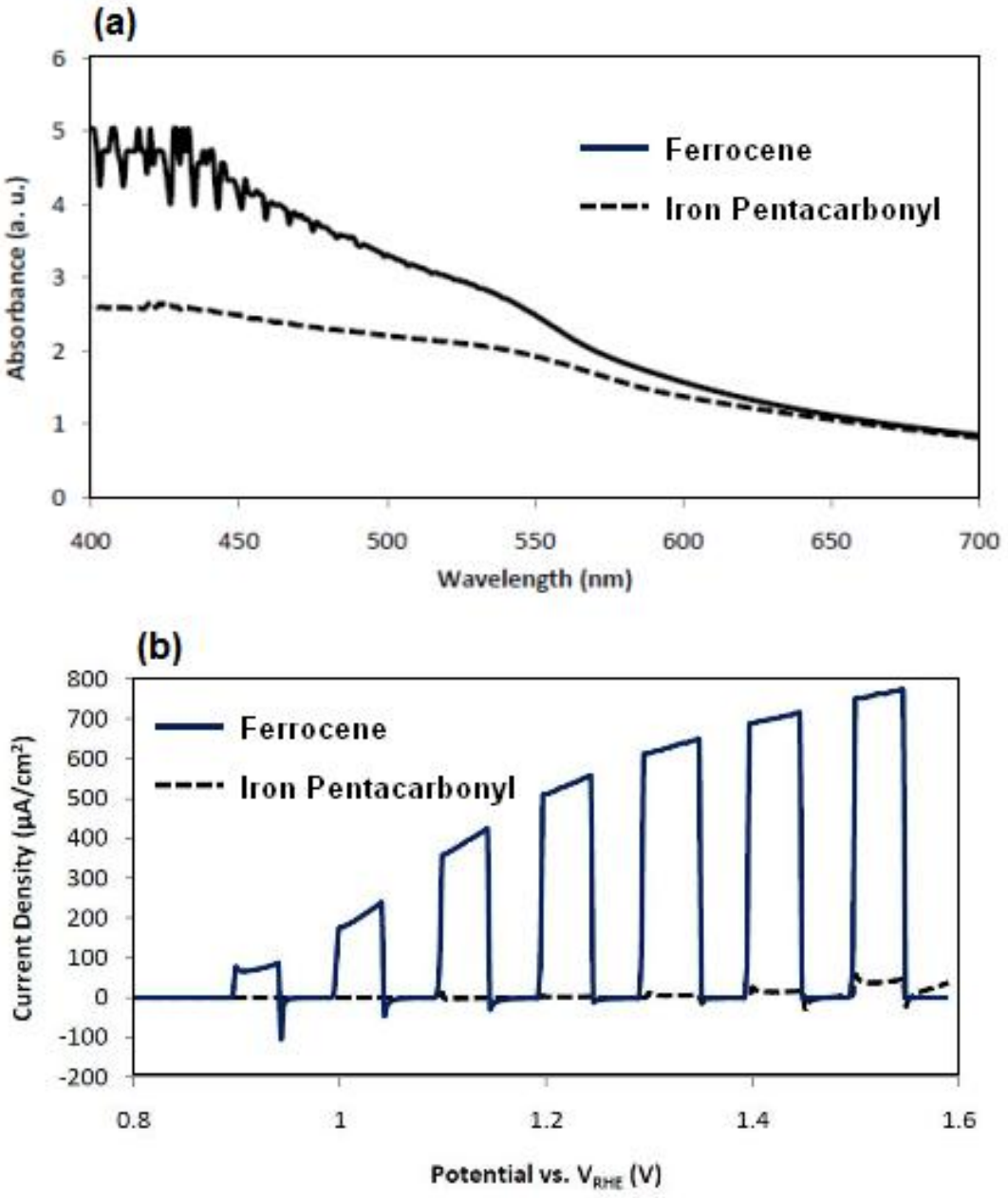

Figure 4-40. (a) Absorption spectra of Ferrocene and iron pentacarbonyl samples. (b) Photocurrent density vs. potential (J-V) plots of both samples.[210]

Photocurrent density-Voltage (J-V) curves of both types of films are shown in Figure 4-40-(b). Photocurrent density measured at 1.23 V vs. V_{RHE} for the ferrocene electrode is 540 $\mu A.cm^{-2}$ while it merely reaches 1.5 $\mu A.cm^{-2}$ for the iron pentacarbonyl electrode. The photocurrent density achieved in this work is far better than what has been previously reported for undoped hematite films prepared using APCVD.[99,210]

So far, iron pentacarbonyl has been the only iron precursor used to prepare hematite electrodes for PEC water splitting using APCVD. However, photocurrent densities obtained were less than 10 $\mu A.cm^{-2}$ at 1.23 V_{RHE}.[99] The results obtained for APCVD of ferrocene show that films prepared using ferrocene possess higher optical absorption which would lead to the higher charge generation and separation. Although high optical absorption is seemed to be partly responsible for improved PEC performance, further investigation is needed in order to understand the difference in the charge separation and quantum efficiency in each type of electrodes.[210]

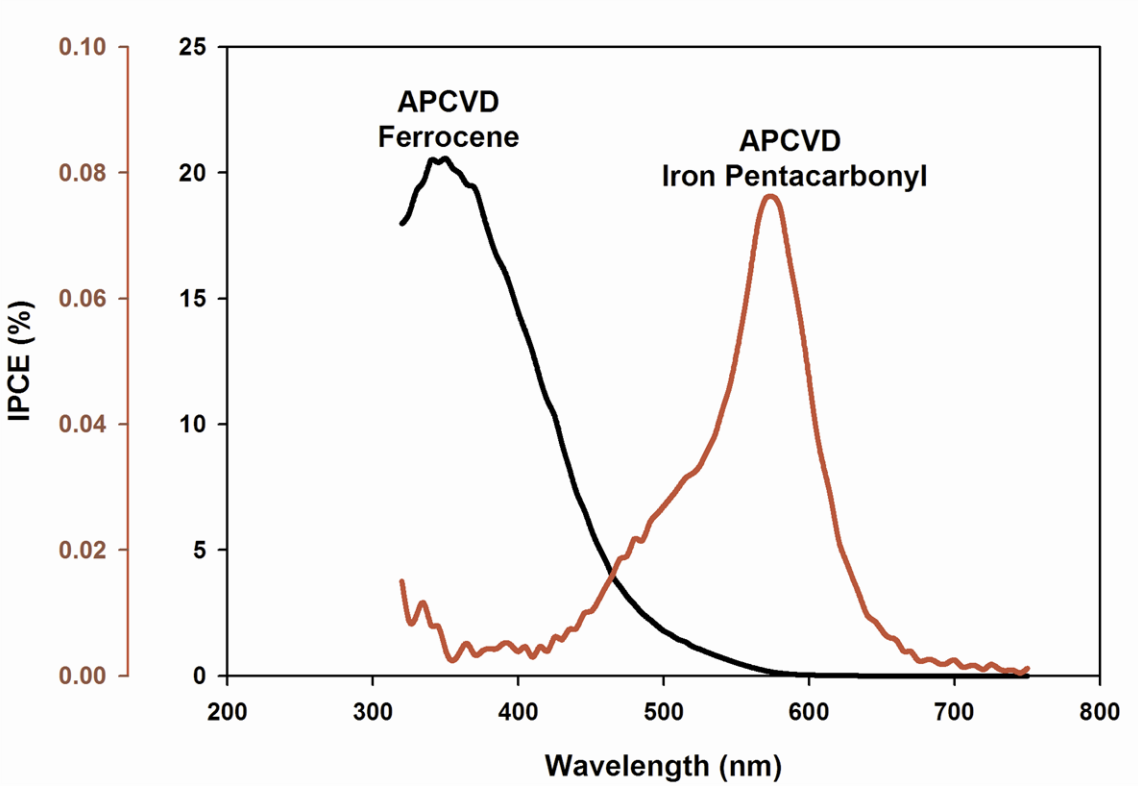

Figure 4-41. Quantum efficiency (IPCE) plots of hematite sample prepared by APCVD of ferrocene and iron pentacarbonyl. The measurement potential is 0.23 V vs. $V_{Ag/AgCl}$.

Figure 4-41 compares the external quantum efficiencies obtained for undoped hematite films prepared by APCVD of ferrocene and iron pentacarbonyl. As it clearly shows, undoped hematite film prepared by ferrocene as the precursor possess similar properties to the APCVD Si-doped sample (TEOS and TMOS) but at smaller IPCE values. The maximum IPCE occurs at 350 nm showing 20.5 % maximum efficiency. In contrast, undoped APCVD sample prepared by iron pentacarbonyl shows almost no quantum efficiency at this wavelength and obtaining a maximum of 0.08 % at 570 nm. As discussed before, this clearly shows different dynamics in carrier relaxation processes in two different films. It is suggested that it is not only higher optical absorption in ferrocene sample but also an improved charge separation and transport upon excitations at near UV region in ferrocene sample which is responsible for enhanced photo-performance. It is likely that electron-phonon processes and trapping by mid-bandgap states are significantly reduced in ferrocene sample as a result of smaller surface area and less inherent defects in this sample. Further work is needed in order to confirm this.

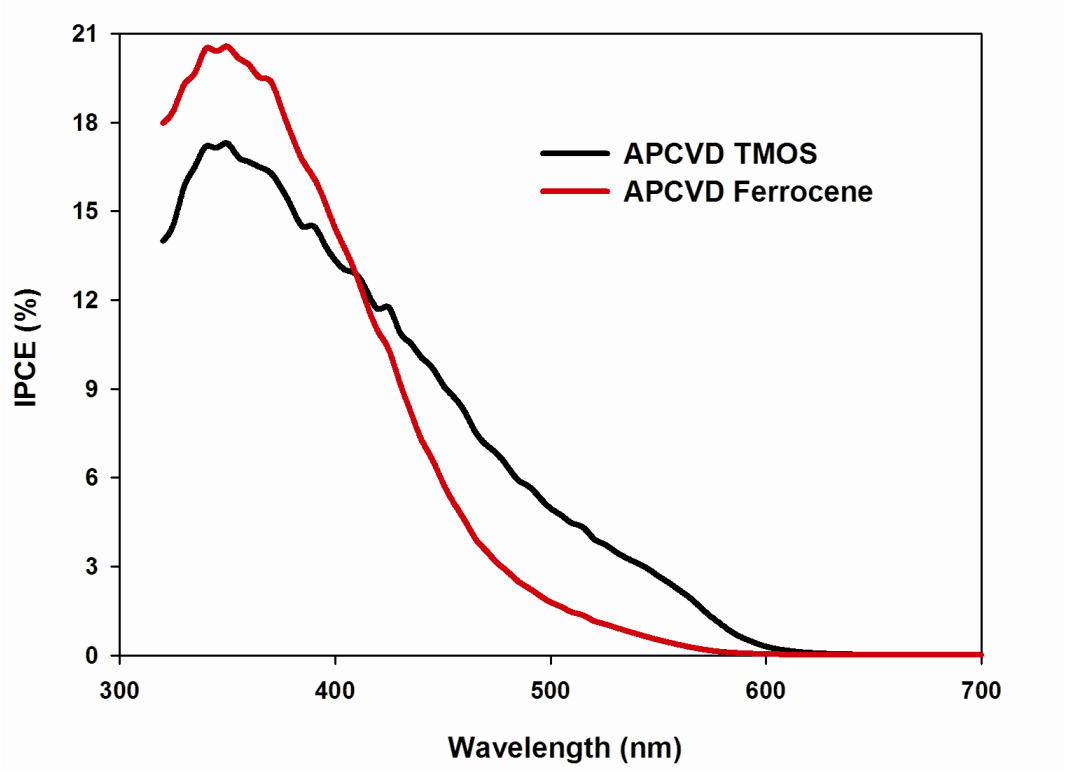

Figure 4-42. IPCE plots of TMOS and APCVD ferrocene. The measurement potential is 0.23 V vs. $V_{Ag/AgCl}$.

Another interesting feature of IPCE of hematite films obtained by APCVD of ferrocene can be seen by comparing its IPCE with that of the TMOS sample. Although both these samples show similar photocurrent densities at 0.23 V vs. $V_{Ag/AgCl}$ (540 and 630 $\mu A.cm^{-2}$ for ferrocene and TMOS samples, respectively) their IPCE action spectra is different. While ferrocene shows smaller photocurrent its maximum IPCE is greater by ~ 3%. The important feature however is the IPCE values at wavelengths bigger than 400 nm. The IPCEs of both samples are equal at 410 nm, 12.8 %. At longer wavelengths the IPCE of TMOS sample exceeds those of the ferrocene sample. The observed improved photocurrent density of TMOS sample originates from this difference. The light penetration depth decreases as the wavelength increases, therefore the light is absorbed at distances closer to the surface of the hematite film. The higher porosity of TMOS sample provide larger surface area which in turn results in better scavenging of photo-generated charge carriers at and near to the surface of the electrode. The improved quantum efficiency at wavelengths higher than 400 nm where most of the absorption is due to Fe^{3+} ligand field transitions and multiple Fe^{3+} excitations, indirectly indicates that carrier relaxation processes are slower and recombination occurs at smaller scales.

4.2.13 AACVD using ferrocene

4.2.13.1 Structural and PEC properties

J-V curve of best performing sample (deposition time 45 min) is shown in Figure 4-43. This sample showed the photocurrent density of 230 $\mu A.cm^{-2}$ at 1.23 V vs. V_{RHE} .

Figure 4-44 depicts the XRD pattern of the best AACVD sample. As shown in this figure, this film is a highly crystalline and oriented hematite film. The presence of 4 peaks of hematite is the representative of a highly crystalline film. (110) is the dominant peak in this XRD graph which along with strong peaks confirms the formation of strong preferential orientation inside the film. In addition to this, relative intensity of the peaks for hematite and FTO substrate shows that the thickness of the hematite films is considerably higher than that of tin oxide layer which is further confirmed with SEM.

Surface morphology of the best AACVD film was studied using SEM. As shown in Figure 4-45, the surface structure of hematite film consists of pyramid-like features whose

size ranges from around 500 nm to almost 2 µm, however, the majority of this surface features are about 1 µm. Thickness of the film is around 5 µm which indicates that the deposition occurred at the rate of 110 nm/min in this sample.

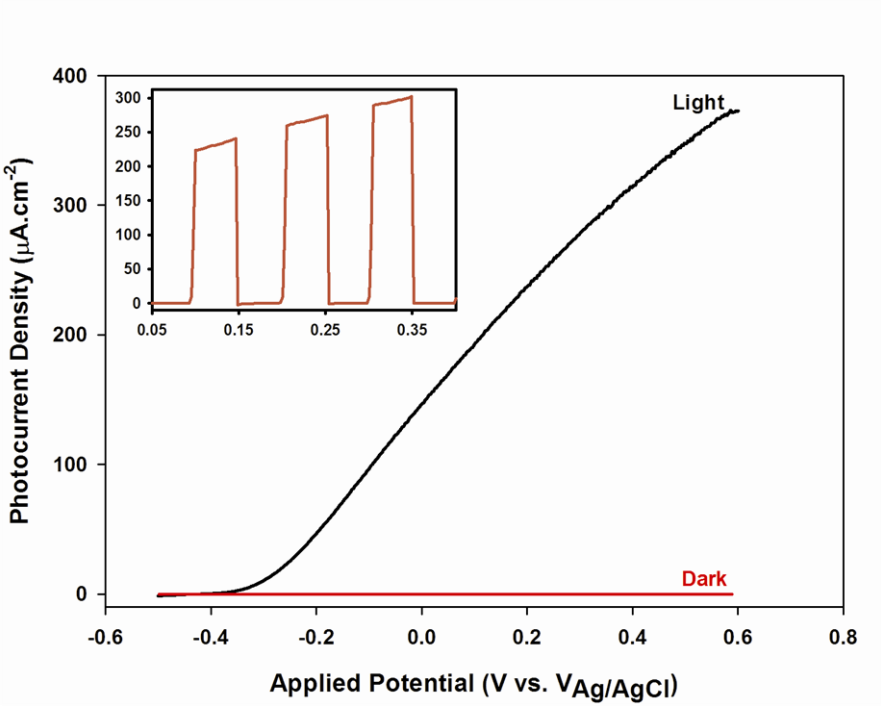

Figure 4-43. Photocurrent density vs. potential (J-V) plot of AACVD sample (deposition time 45 min).

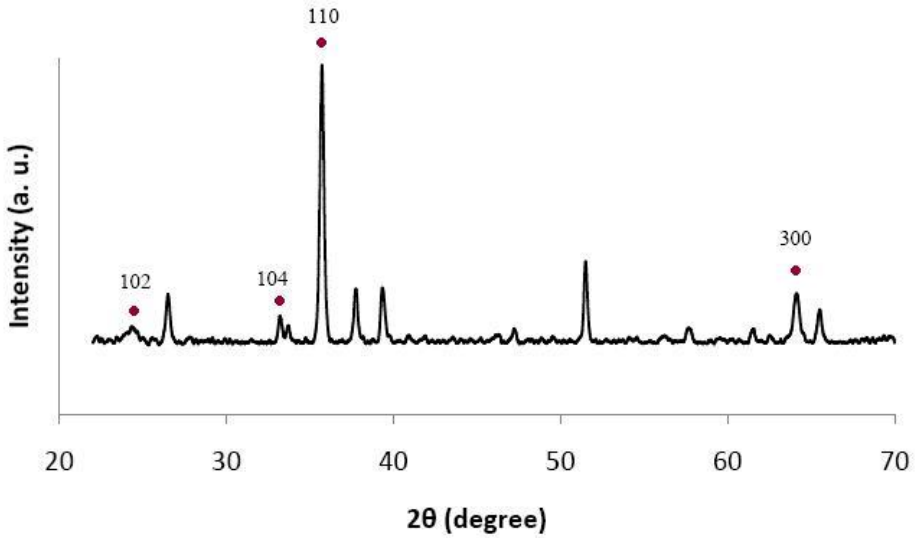

Figure 4-44. XRD graph of best performing AACVD sample. It shows strong preferential orientation at (110) reflection.

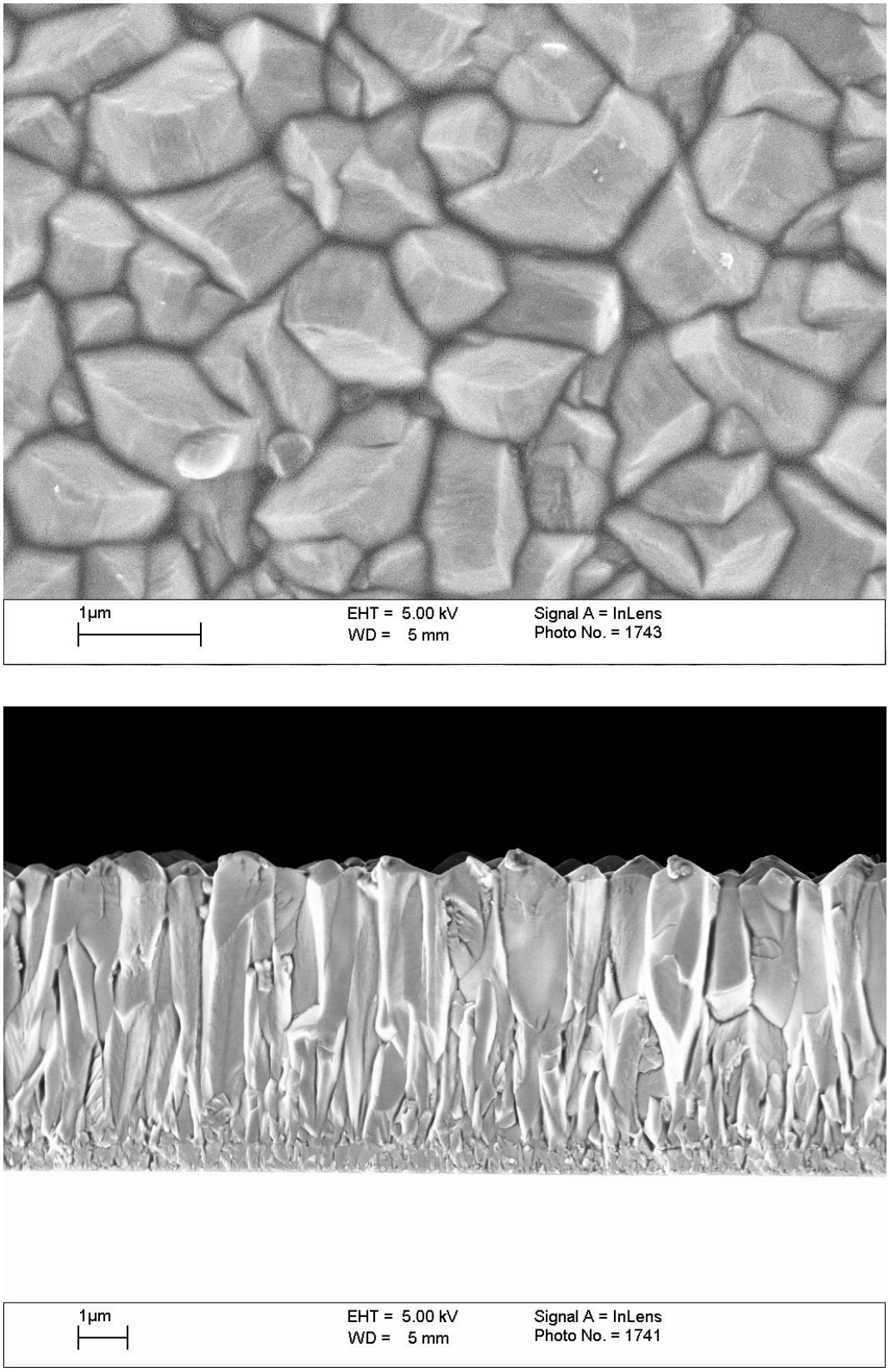

Figure 4-45. SEM picture of surface morphology and cross section (thickness) of the AACVD sample (deposition time 45 minutes).

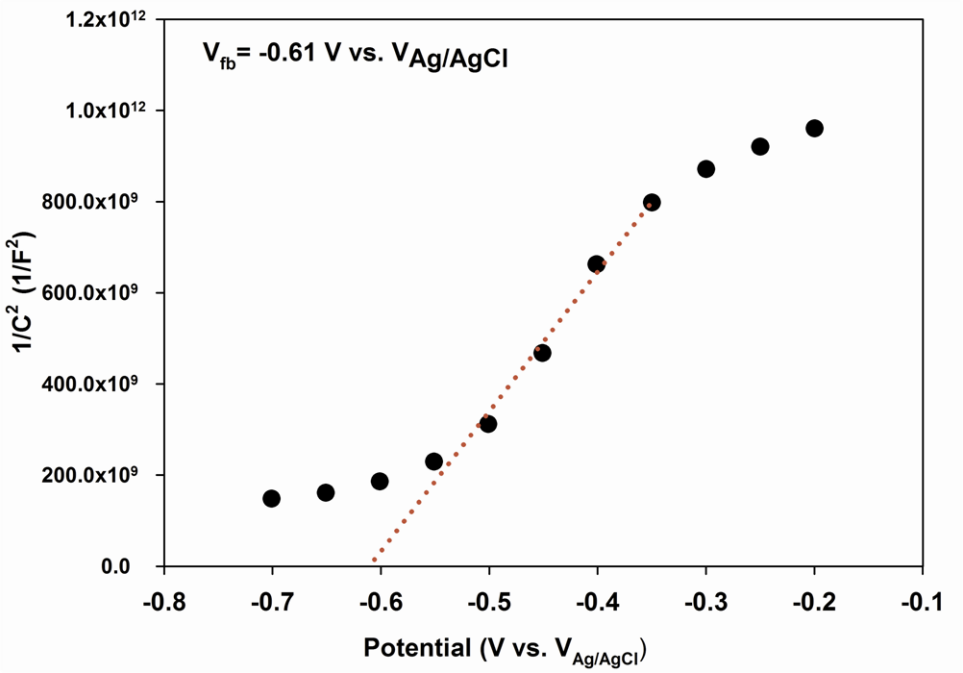

Figure 4-46. Mott-Schottky plot of ferrocene AACVD sample. Flat-band potential is obtained by extrapolation of the dotted line.

Considering the thickness of this sample and also the compactness of the film, it shows unexpected good photocurrent. Especially, the photocurrent onset of ~ -0.38 V vs. $V_{Ag/AgCl}$ is the best observed for hematite electrodes in this work. It is the closest onset potential to the typical flat-band potential of hematite electrodes. In fact, as will be discussed in the following, photocurrent onset potential of this sample closely matches the flat band potential measured.

The mismatch between the estimated flat band potential (-0.61 V vs. $V_{Ag/AgCl}$ from capacitance measurements, Figure 4-46) and steady-state photocurrent onset (-0.38 V vs. $V_{Ag/AgCl}$) thought to be originated from the recombination via surface states. This means even a higher bias (than the estimated value, i.e. the energy difference V_{FB} and H^+/H_2 level) is needed before photocurrent appears. Studying the reaction kinetics on the semiconductor/interface would provide useful information in this unclear area. In fact, understanding of surface kinetics would enable us to find alternative solutions to promote light-induced charge transfer reactions on hematite electrodes. For example, introduction of suitable surface catalysts such as Co could lead to charge transfer properties at the surface.

In order to study the kinetics of charge transfer and recombination at the surface of the hematite electrode a simple model was used which was first developed by Ponomarev and Peter.[211] The basis of this model is as follows: it can be considered that in an n-type semiconductor minority charge carriers (holes) generated upon illumination move to the surface where they can either transfer to the solution with the rate constant k_i or be captured by the surface states with the rate constant k_c. Captured holes can then be transferred to the solution with the rate constant k_{ct} or recombine with the electrons present in the conduction band with the rate constant k_{rec}.

Using this approach, Ponomarev and Peter[211] showed that the photoelectrochemical EIS (PEIS) plot would show two semicircles from which recombination and charge transfer rate constant could be calculated. The frequency corresponding to the maximum of the absolute value of the imaginary part of Z equals charge k_{ct} (charge transfer rate constant at the interface) and k_{rec} (recombination rate constant) can be calculated using the following equation (Equation 4.2):

$$\frac{Z_1}{Z_2} = 1 + \frac{k_{rec}}{k_{ct}} \qquad (4.2)$$

where Z_1 and Z_2 can be found in the semicircle at the lower frequency range. This single semicircle in the complex plane starts from Z_1, at low frequency and closes to Z_2, at higher frequency.[211]

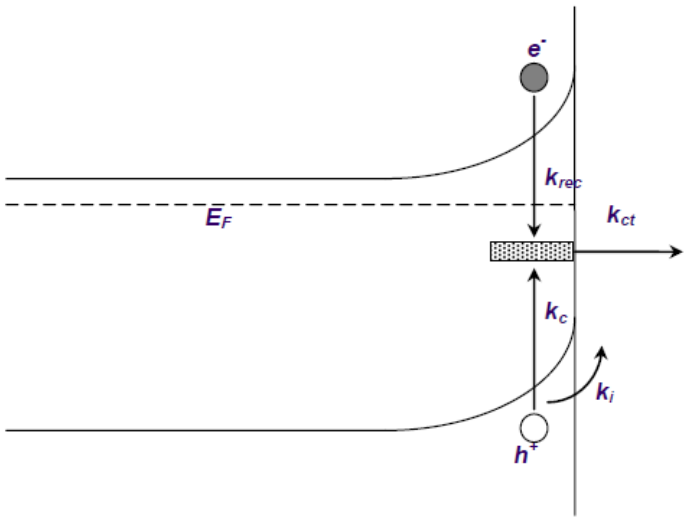

Figure 4-47. Schematic of the illuminated semiconductor/electrolyte interface.

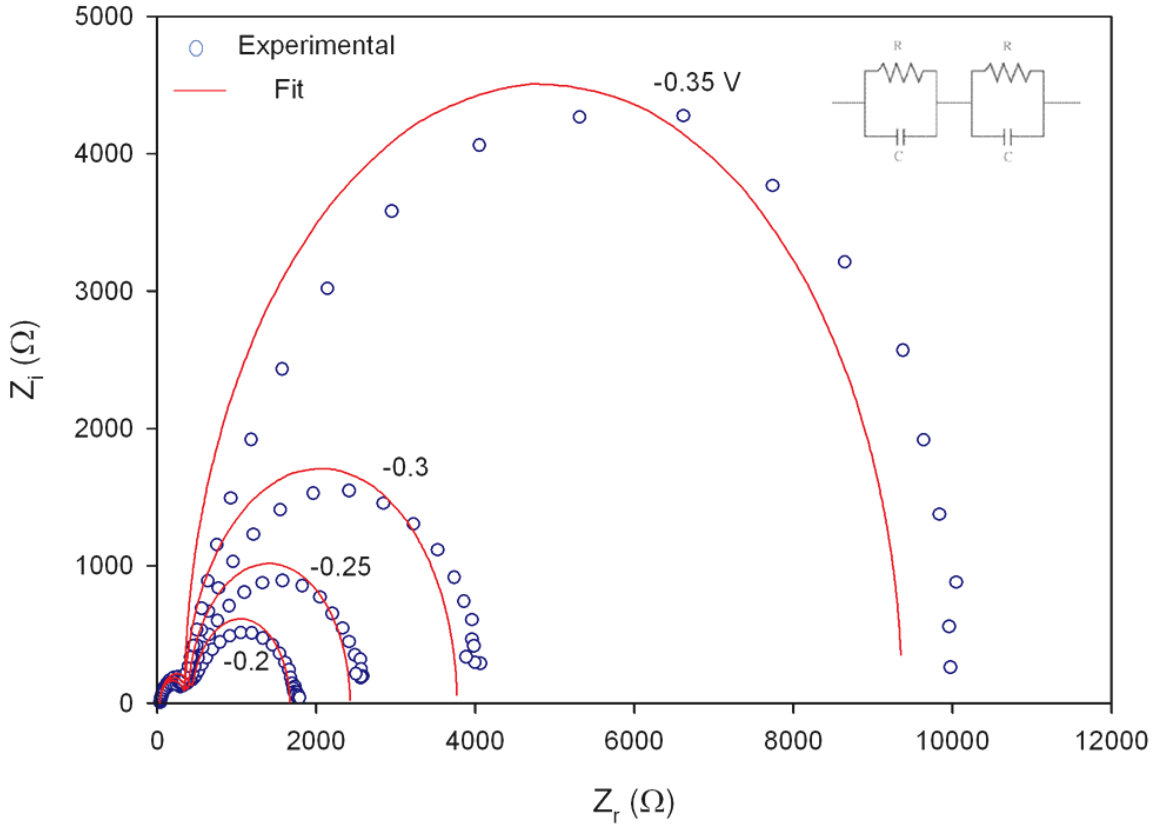

Figure 4-48. PEIS plots of ferrocene AACVD plot at different potential. The experimental data are fitted to the model circuit shown above.

PEIS measurement was performed under a wide frequency range and the experimental data fitted with the two-parallel-RC equivalent circuit proposed by the above model (Figure 4-48). The values for recombination and charge transfer rate constants were calculated and plotted against applied bias potential (Figure 4-49). As illustrated, both recombination and charge transfer rate constant increased by increasing forward bias. However, it was found that the degree at which charge transfer rate constant increased was higher than that of the recombination rate constant.

The plot of k_{ct}/k_{rec} shows a positive slope which illustrates this trend. The important issue of the aforementioned model is the potential range in which this model is applicable. As shown in Figure 4-48, the experimental results fitted the model only in the potential range of -0.35 to -0.2 V vs. $V_{Ag/AgCl}$.

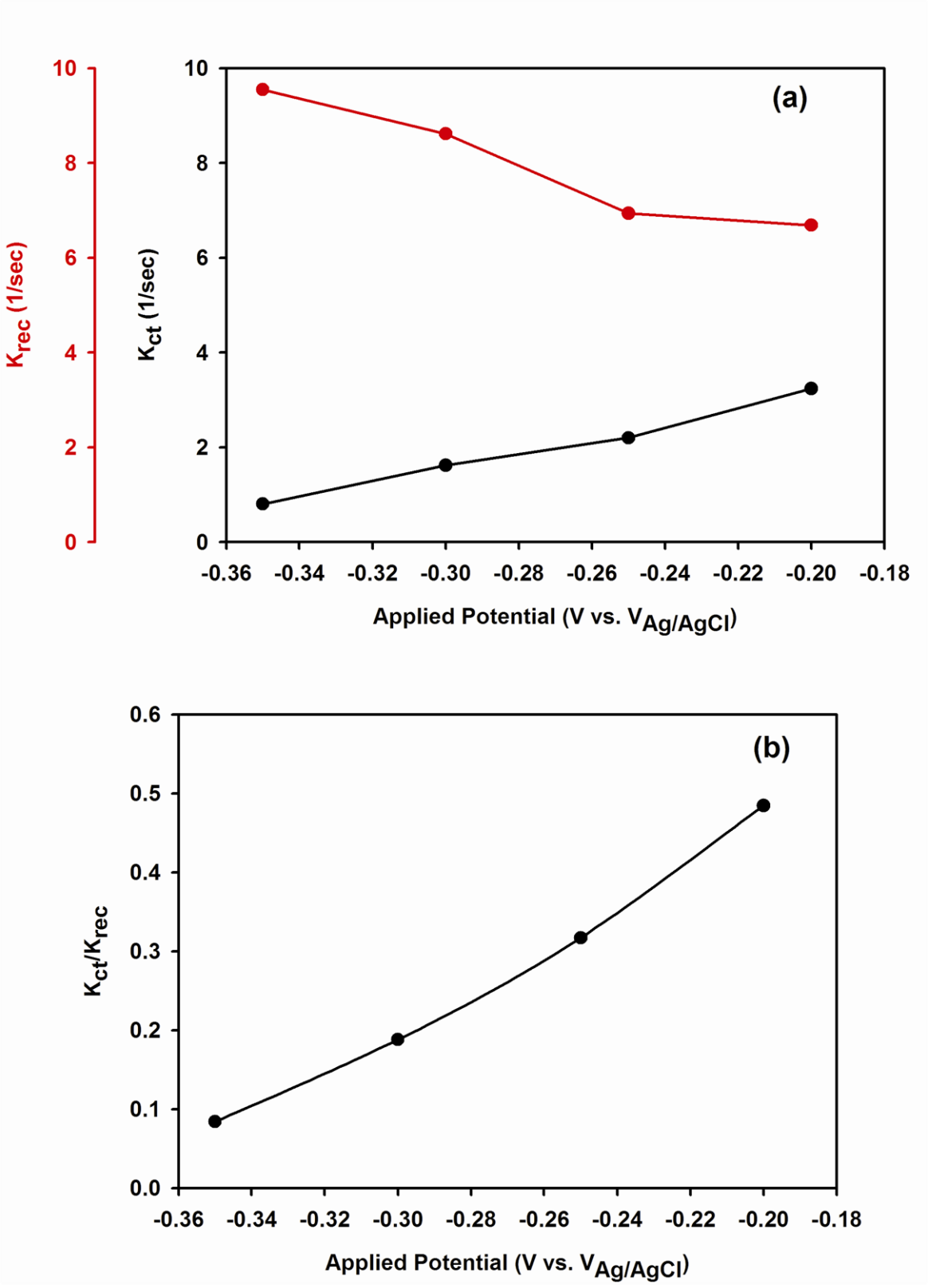

Figure 4-49. (a) Charge transfer and recombination rate constants of hematite electrode prepared by AACVD. (b) The ratio of charge transfer rate constant to recombination rate constant as a function of applied potential.

At potentials more positive than this range the charge transfer rate constant would increase significantly and equal the values of that of the recombination rate constant. This is when the photocurrent density obtained is quite reasonable and in the range of tens of $\mu A.cm^{-2}$. At potential lower than this range, the recombination pathways dominate the charge relaxation and transport processes so it becomes impossible to distinguish two semicircles from the impedance plot.

High recombination and very small charge transfer rate at negative bias potential attribute to the low photocurrent density and also unsuitable photocurrent onset at the negative region. A more comprehensive study is needed to identify the factors responsible for this behaviour. A higher gain in the photocurrent onset and shifting of the bandgap energetics of iron oxide is extremely important in achieving higher PEC water splitting efficiencies. The viability of this method for the films with more complex morphologies, such as those for the TEOS sample, is doubtful. In fact, the experimental data did not match the data forecasted from the model satisfactorily. This could be due to the large number of defects at the surface of such films. This would significantly alter the recombination processes at the surface of the electrode and bring more complications into the consideration. Therefore, it is suggested that this simple model is only used to obtain a qualitative understanding of the charge transfer and recombination rate constants for films with fairly smooth morphologies and small number of surface defects. A similar study is currently underway to modify the proposed model which is beyond the scope of this study. It is shown that a non-porous highly oriented micrometer-thick hematite films can be produced by AACVD using ferrocene as the precursor. Recombination and charge transfer rate constants at the surface of hematite photoelectrodes was investigated by PEIS taking into account a single trap model. It was found that as the applied voltage was increased both recombination and charge transfer rate constant increased, however, the degree at which charge transfer rate constant was increased exceeded that of the recombination rate constant which was in agreement with increasing of steady-state photocurrent density in the same potential region.

4.2.14 Growth mechanisms for APCVD and AACVD of thin films

It has been shown that surface morphology and nanostructure of the hematite films plays an important role in defining the PEC performance. APCVD and AACVD have provided

the capability to fabricate hematite films with different nanostructures. Tailoring the nanostructure and obtaining controlled morphology could be better achieved if the precursor decomposition and film growth mechanisms are understood. In this section, the difference in the growth mechanisms of different AACVD and APCVD deposited films are discussed.

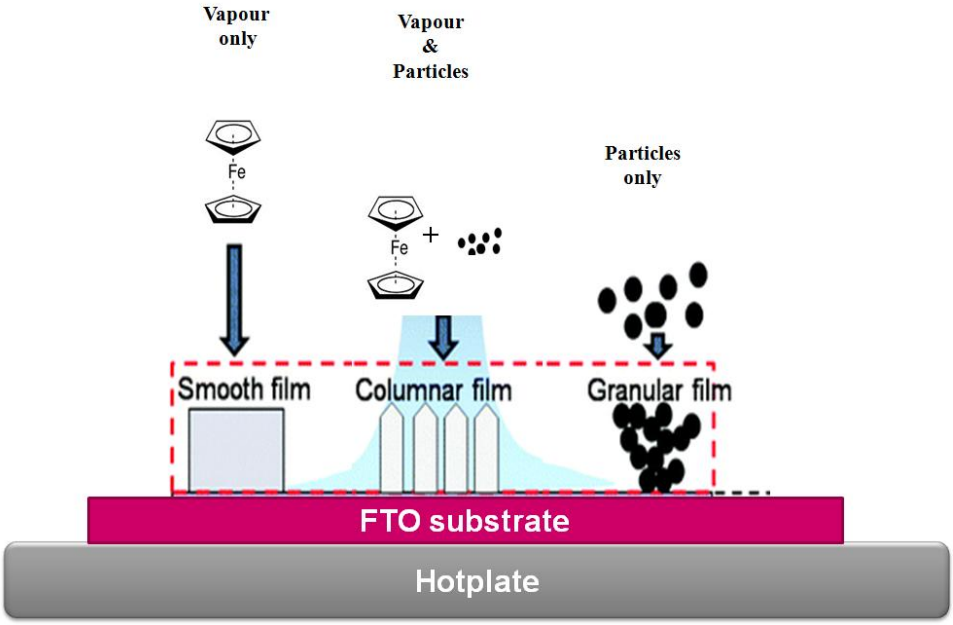

Figure 4-50. Schematic illustration of the deposition regimes in the AACVD of ferrocene. It is shown that different film morphologies will be obtained at different deposition conditions.[212]

Recently, An et. al.[212] have formulated the growth mechanisms of AACVD process and have proposed a general model to predict the morphology of oxide films produced by this method. The summary of their approach is as follows. Basically, in a typical AACVD process, the precursor is converted into the vapour phase which is the introduced to the reaction chamber. The vapour phase is then converted to the molecular form of the oxide as a result of the decomposition of the precursor. The molecular oxide is moved towards the surface of the substrate (boundary layer) by the convective flow.

Since the substrate is at a higher temperature than formed oxide and the vapour phase, the thermophoretic force is in a direction opposing the deposition. Therefore, one would

expect that no film would be formed on the substrate. However, as the thickness of the boundary layer is very small the thermophoretic velocity becomes much smaller than the diffusional velocity. Therefore, a very thin film is formed as a result of the diffusional deposition. From this point onwards, different morphologies can be obtained by carefully modifying the deposition conditions such as choice of the precursors, carrier gas flow, deposition time and the distance of the delivery tube to the substrate.

As shown in Figure 4-50, different regimes of vapour dominant, mixed vapour-particle and particle dominant could be achieved. The nature of each of these regimes, i.e. whether it is a particle dominant or mixed vapour-particle, is governed by various characteristic times: residence time (τ_{res}), reaction time of the precursor (τ_{rxn}), sintering time (τ_{sin}), and collision time (τ_{col}). For example, if the reaction time is significantly larger than the residence time, then the vapours will only react at the substrate leading to the formation of a dense film. When reaction time and residence time are comparable in magnitude a mixed vapour-particle regime is obtained leading to the formation of a columnar structure. Similarly, if sintering time is slow and a particle dominant regime is obtained, a granular morphology is formed.

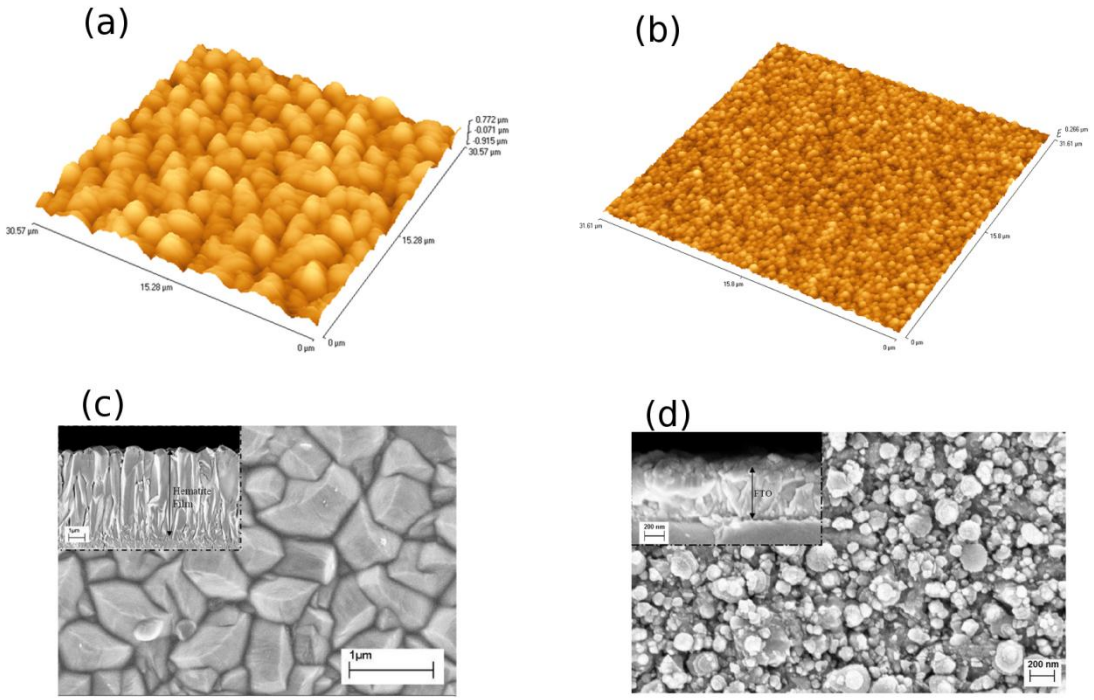

Figure 4-51. (a,c) AFM and SEM images of the samples prepared by AACVD and (b,d) APCVD of ferrocene.

A comparison of the surface morphology of two different films prepared by AACVD and APCVD of ferrocene is shown in Figure 4-51. During APCVD of ferrocene, there is no solvent involved; therefore, it is only the decomposition of ferrocene which controls the deposition regime. As shown in Figure 4-51-(b) and (d), a granular morphology is observed at the surface of the APCVD deposited sample.

This suggests that the reaction time of the ferrocene as precursor is much faster than the residence time, therefore, most of the vapour is converted into the particles before reaching the substrate. The porosity of the sample and the particle size of the granular structure is controlled by the collision and sintering times. Similar results are also observed for the APCVD deposited films using iron pentacarbonyl. The films are composed of small particles which form bigger agglomerates. Therefore, it can be concluded that the changes in the morphology of the doped samples (TEOS and TMOS) can be partly due to the induced changes in different timings of the deposition process upon introduction of Si-containing precursors.

Films deposited by AACVD of ferrocene exhibit completely different morphologies hence deposition and growth mechanisms to that of the APCVD method. Formation of dense columnar structures during AACVD is a clear indication of a vapour dominant and/or mixed vapour-particle deposition regime. The presence of toluene as the solvent resulted in the lowering of the reaction time to the values level to the residence time. Therefore, most of the deposition occurred when the precursor reached the substrate resulting in the formation of a dense compact film.

4.3 Low temperature preparation and microwave-assisted heating

4.3.1 PEC performance

In order to study the PEC performance, the microwave- and conventionally-annealed electrodes were scanned from -0.4 to 0.7 V vs. $V_{Ag/AgCl}$ applied potential and their photocurrent densities (J) was recorded at different potentials. The obtained J-V plots for undoped samples annealed using both conventional and microwave heating are shown in Figure 4-52.[213]

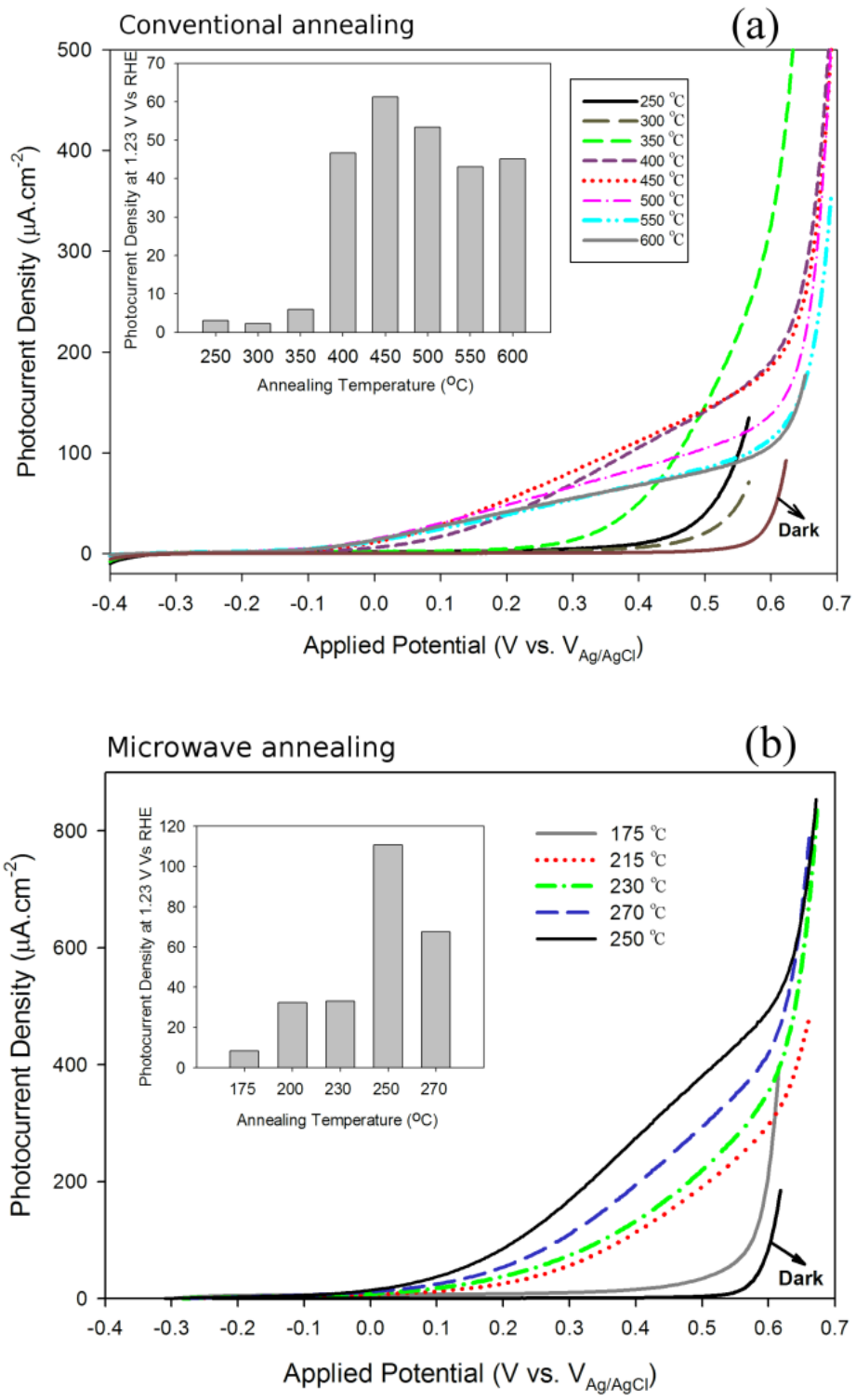

Figure 4-52. The graph showing photocurrent density vs. applied potential of the undoped samples annealed using (a) conventional and (b) microwave-assisted heating at different temperatures for the duration of 15 minutes. Inset shows the photocurrent density obtained at 1.23 V vs V_{RHE} as a function of annealing temperature for the samples.[213]

The insets in Figure 4-52 show the photocurrent density obtained for different undoped hematite electrodes at 1.23 V vs. V_{RHE} (0.23 V vs. $V_{Ag/AgCl}$) applied potential as a function of annealing temperature (all samples were annealed for 15 minutes at the relevant temperatures). As illustrated, in the case of conventional annealing, the photocurrent density reached its maximum value, 61 $\mu A.cm^{-2}$ at 0.23 V vs. $V_{Ag/AgCl}$, for the iron oxide films annealed at 450 °C for 15 min. Further annealing at higher temperatures resulted in the reduction of the photocurrent density to 45 $\mu A.cm^{-2}$ at 600 °C.[213]

The samples annealed at temperatures lower than 400 °C showed negligible photo-response at 0.23 V vs. $V_{Ag/AgCl}$. Dark current for all samples were fairly similar and remained negligible (<3 $\mu A.cm^{-2}$) for potentials up to 0.57 V vs. $V_{Ag/AgCl}$. As the applied potential exceeds 0.57 V vs. $V_{Ag/AgCl}$ the dark current also increases sharply. This can be attributed to the direct electrochemical oxygen evolution at the surface of iron oxide photoelectrodes at these high potentials.[213]

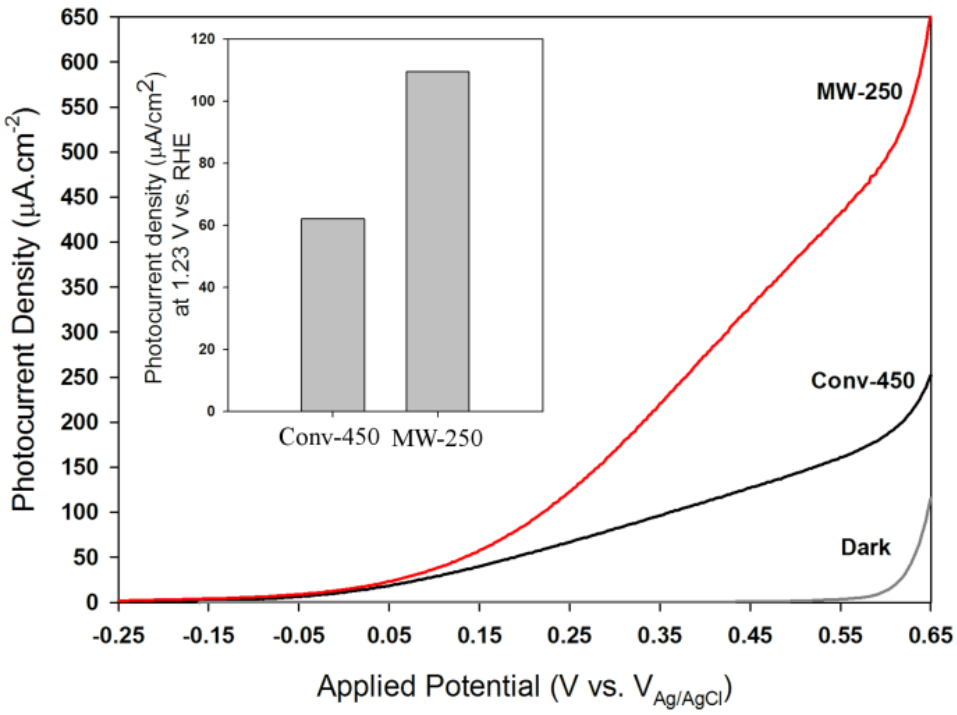

Figure 4-53. Graph showing the photocurrent density vs. applied potential for the undoped samples annealed at 450 °C using conventional heating (Conv-450) and 250 °C using microwave heating (MW-250). Both samples were annealed for 15 minutes. Inset shows the photocurrent density obtained at 1.23 V vs V_{RHE} as a function of annealing temperature for the samples.[213]

Photocurrent density obtained at different potentials for undoped samples annealed for 15 minutes by microwave irradiation is also shown in Figure 4-52-(b). The improvement in the PEC performance as a result of increase in the annealing temperature is evident. While the sample annealed at as low as 200 °C showed a small photocurrent density, about 30 $\mu A.cm^{-2}$ at 0.23 V vs. $V_{Ag/AgCl}$, the PEC performance of the sample annealed at 250 °C measured at the same potential was increased more than three-fold and reached 107 $\mu A.cm^{-2}$. It is important to note that the sample annealed using microwave-assisted heating at 250 °C produced photocurrent densities almost twice that of the sample annealed conventionally at 450 °C Figure 4-53.[213]

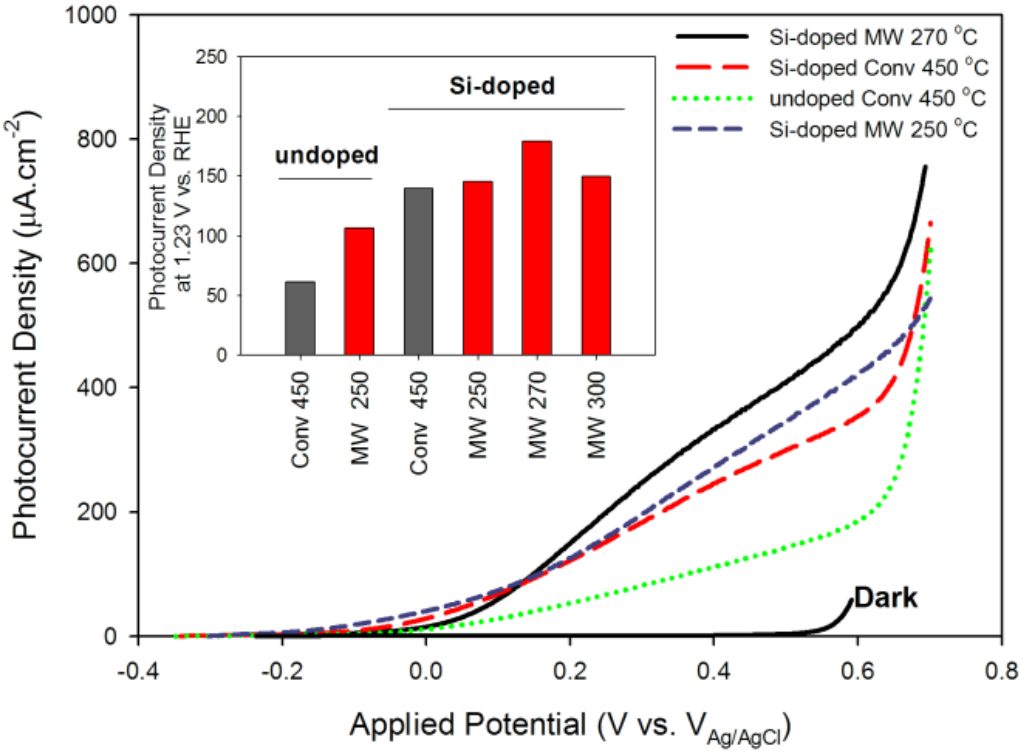

Figure 4-54. Photocurrent density-applied potential graph showing the PEC performance of Si-doped and undoped samples. Inset shows photocurrent densities obtained for different samples at 1.23 V vs. V_{RHE} annealed at corresponding temperatures using conventional and microwave heating.[213]

Figure 4-54 compares the PEC performance of undoped samples with the samples deposited with the addition of Si precursor (TEOS) during electrodeposition. The Si-doped samples outperformed the undoped photoelectrodes. For the samples annealed

conventionally at 450 °C for 15 minutes, photocurrent density at 0.23 V vs. $V_{Ag/AgCl}$ increased from 61 to 139 μA.cm^{-2} as the result of doping. A similar trend was observed for the samples annealed using microwave heating where the performance improved from 106 μA.cm^{-2} to 145 μA.cm^{-2} for the samples annealed at 250 °C for 15 minutes.[213]

Further slight increase in the microwave annealing temperature resulted in even higher photocurrents. The maximum photocurrent density achieved at 0.23 V vs. $V_{Ag/AgCl}$ (180 μA.cm^{-2}) was for the Si-doped sample microwave annealed at 270 °C for 15 minutes, Figure 4-54, which is almost 25% higher than the highest photocurrent obtained for Si-doped sample annealed conventionally. Thus the low temperature microwave annealed samples gave relatively superior performance compared to conventionally-annealed samples in general.[213]

4.3.2 Structural characterisation by XRD and Raman spectroscopy

The phase and crystallinity of the films as a function of annealing temperature was studied using XRD. As shown in Figure 4-56-(a) the as-deposited sample consists of only α-Fe. It is bcc Fe with the main reflection of (110). In the case of sample annealed conventionally, hematite (α-Fe_2O_3) peaks only appear in films annealed at 350 °C for 15 min. At lower temperature and longer times, for example 300 °C for 1 hour (Figure 4-55) although a very weak peak of iron oxide at (110) reflection was noticed the iron peak was still stronger than those of hematite, which showed iron was yet the dominant phase at 300 °C.[213]

As shown in Figure 4-56-(b), the intensity of α-Fe (110) peak decreased as the annealing temperature increased from 250 to 350 °C and this peak disappeared in the XRD pattern of the sample annealed at 450 °C for 15 minutes. On the other hand, the intensity of iron oxide peaks increases by increasing the annealing temperature. For example, as shown in Figure 4-56-(c), the (110) iron oxide peak became more intense as the annealing temperature is increased and a well-defined peak was recorded for the sample annealed at 450 °C for 15 min. This clearly indicated the formation of iron oxide and improvement in the crystallinity of the films. Reflections of (104) and (110) for α-Fe_2O_3 are clearly visible in the sample annealed at 400 °C for 15 min. Upon increasing the temperature, other peaks such as (012) and (116) start to appear confirming the formation of well-crystalline α-Fe_2O_3. Longer

annealing times did not result in significant improvement of the peak intensities and the number of visible peaks of iron oxide remained the same (Figure 4-57).[213]

Microwave annealing resulted in the oxidation of Fe at much lower temperatures than those of conventional heating. The samples annealed using microwave irradiation showed no visible Fe peak even at temperatures as low as 200 °C. As shown in Figure 4-59, the sample annealed at 200 °C for 15 min showed a weak but visible peak of (110) reflection of hematite. Increasing the annealing temperature from 200 to 250 °C resulted in the appearance of more peaks of hematite. At temperatures higher than 200 °C the intensity of (110) peak was increased (Inset of Figure 4-59). In order to further improve the crystallinity of the samples, they were annealed at longer times. Three peaks of hematite, (110), (104) and (012) reflections, were seen in the sample annealed at 250 °C for 1 hour using microwave irradiation (Figure 4-58).[213]

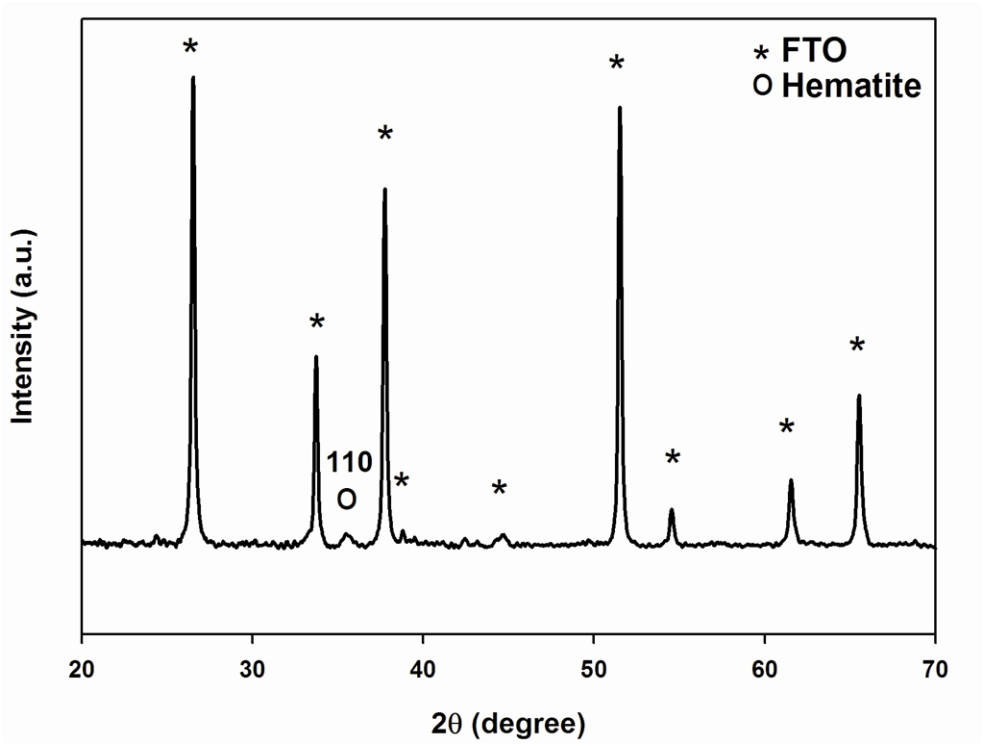

Figure 4-55. XRD pattern of the hematite film conventionally-annealed at 300 °C for 1 hour. The peaks of FTO substrate are labelled with an *. The (110) XRD reflection of hematite is also given and labelled by an o.

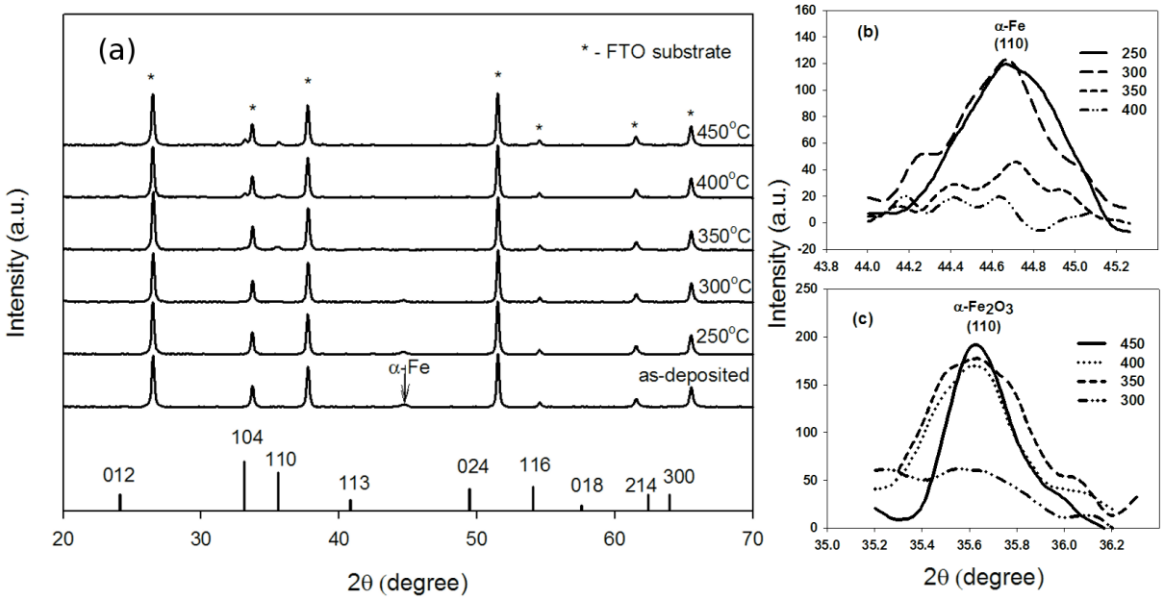

Figure 4-56. XRD diffractograms of the conventionally-annealed samples annealed for 15 minutes at the temperatures shown. (a) XRD pattern of annealed films at different annealing temperatures. The peak of Fe is shown with an arrow. The standard XRD reflections of hematite are also shown. (b) Graph shows (110) reflection of α-Fe confirming the disappearance of this peak as the temperature increased. (c) (110) reflection of hematite.[213]

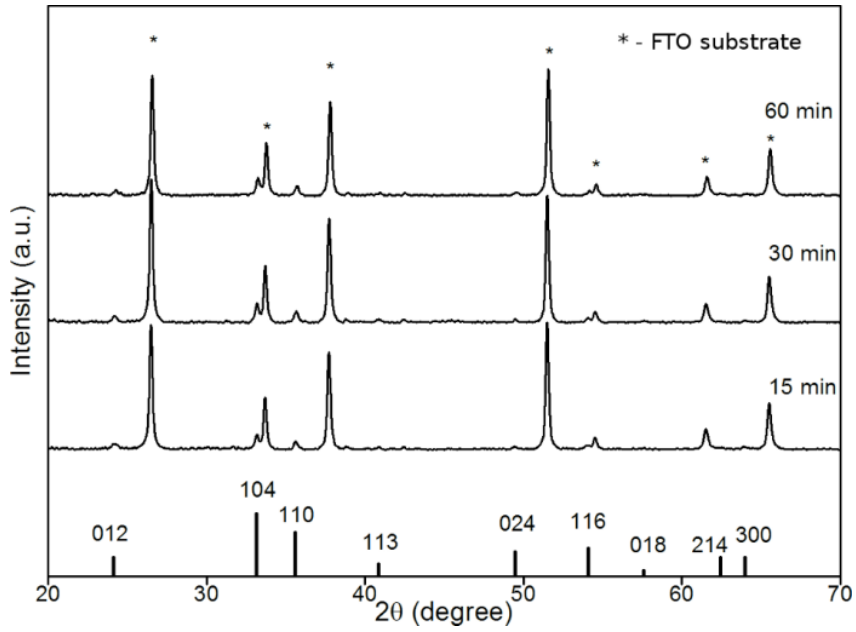

Figure 4-57. XRD diffractograms of the samples annealed using conventional heating at 450 °C temperature at different annealing times shown. The peaks of FTO substrate are labelled with an *. The standard XRD reflections of hematite are also given for ease of reference.[213]

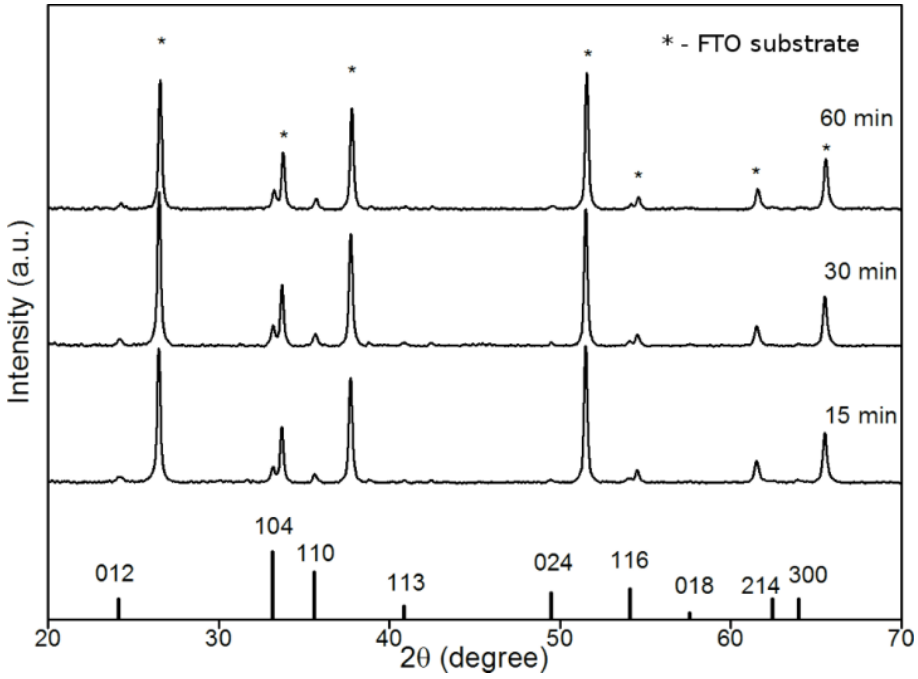

Figure 4-58. XRD diffractograms of the samples annealed using microwave assisted heating at 250 °C for different annealing times. The peaks of FTO substrate are indexed with an *. The standard XRD reflections of hematite are shown at the bottom.[213]

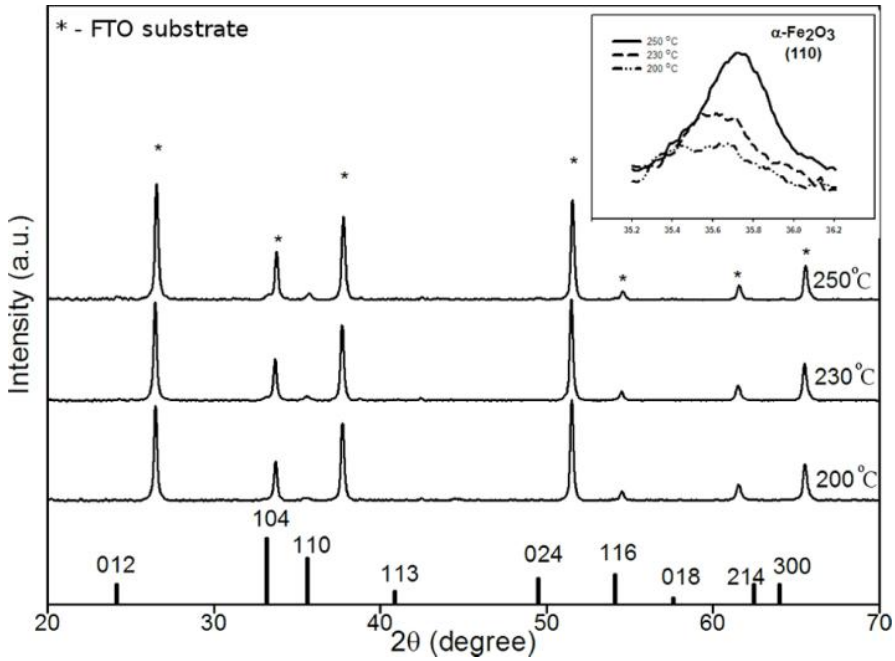

Figure 4-59. XRD diffractograms of the samples annealed using microwave assisted heating at temperatures shown for 15 minutes annealing times. The peaks of FTO substrate are labelled with an *. The standard XRD reflections of hematite are also given for ease of reference.[213]

Comparing the XRD graphs obtained for both conventional and microwave-assisted annealing situation, it can be concluded that the oxidation of iron and its conversion to iron oxide occurred at significantly lower temperatures when microwaves were used as the source of heating. The first signs of iron oxide formation in conventional annealing at short times were seen in the sample annealed at 350 °C for 15 minutes. However, similar behaviour was observed for the sample annealed using microwave assisted heating at 200 °C for only 15 minutes, corresponding to a 42% reduction in the annealing temperature for the initiation of the oxidation process.[213]

The structure and local symmetry of the annealed films were also probed using Raman spectroscopy. The Raman spectra of different samples are shown in Figure 4-60. The spectrum obtained for the as-deposited sample only shows a broad peak around 660 cm^{-1}. The peaks in the range of 600-700 cm^{-1} correspond to FeO_4 tetrahedra and the peak at 660 cm^{-1} has been attributed to either the IR silent A_1/A_{1g} mode of magnetite/maghemite[106] or disorder.[186,187] The presence of this peak (660 cm^{-1}) in this study is attributed to the non-hematite species at the surface of the as-deposited films and also the disorder as a result of a very small particle size in the as-deposited film and to the large number of small grains present in these samples.[213]

At the surface of the as-deposited Fe, it is likely that Fe interact with air and a thin layer of the Fe-O is formed at the surface, however, the presence of this layer cannot be identified by XRD due to its extremely small thickness. As the annealing temperature increased hematite was formed as a result of thermal oxidation. The first indication of formation of hematite is observed in the sample annealed conventionally at 350 °C for 15 minutes as typical Raman peaks of hematite at 221, 287, 406, 495 and 611 cm^{-1} start to appear.[213]

The significant difference between the different samples is the presence of a relatively strong peak at 660 cm^{-1} in the spectra of the sample annealed at low temperature and gradual reduction in the intensity of this peak relative to the hematite peaks as the temperature increased. It confirms that thermal oxidation progresses with increasing the temperature. The growth of particle size and formation of bigger grains as the result of increased annealing temperature leads to the reduction of the number of grains and also net structural disorder is reduced. This, along with the progress in the oxidation of Fe to α-Fe_2O_3, could contribute to the reduction of intensity of the peak at 660 cm^{-1}.[213]

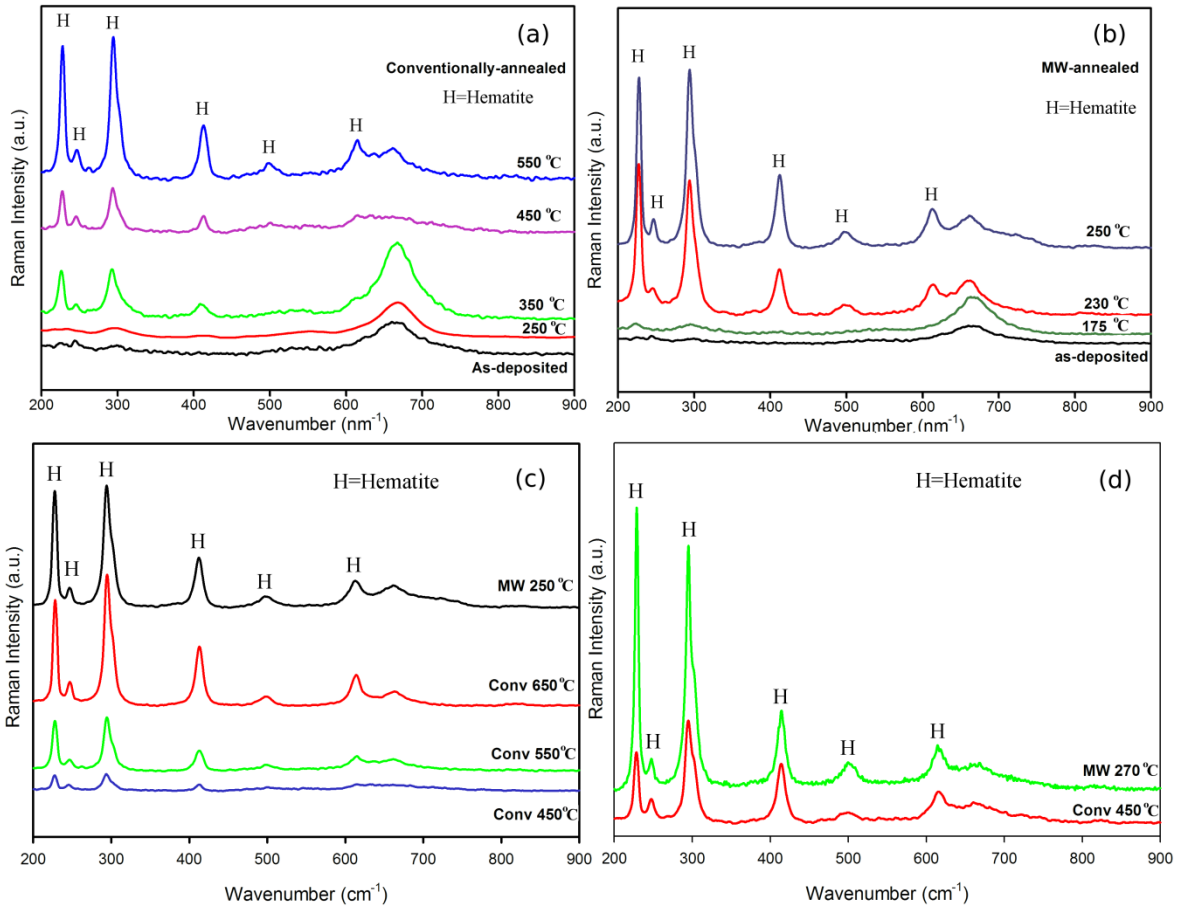

Figure 4-60. Raman spectra of electrodeposited films annealed using conventional (a) and MW-assisted heating (b) at the temperatures indicated. (c) illustrates the difference in the intensity of the Raman peaks for undoped samples and (d) compares the Raman spectra of the Si-doped samples annealing using microwave and conventional heating. Annealing time was maintained at 15 min for all samples.[213]

Similar trend is observed in terms of the samples annealed using microwaves. However, the oxidation process initiates at much lower temperatures. As shown in Figure 4-60-(b), there are strong peaks of hematite in the spectrum of the sample annealed at 230 °C using microwave heating. But the more interesting feature of the MW samples is that the intensity of the hematite peaks is significantly larger than the samples annealed conventionally (Figure 4-60-(c)) indicating that the local structure/polyhedral are well-developed in the microwave treated films. The intensities of Raman peaks of the microwave annealed samples at 250 °C become comparable with conventionally heated samples only when the temperature reaches 650 °C, indicating a significant reduction of around 400 °C for the annealing requirements.[213]

Figure 4-60-(d) compares Raman spectra of Si-doped samples. Both microwave and conventionally-annealed Si-doped samples show strong peaks of hematite, however, the intensity of the Raman peaks of the MW samples are higher than those of conventionally annealed samples. This agrees with the findings obtained for the undoped samples.[213] Such microwave assisted enhancements in reaction kinetics and microstructural developments of other systems are well documented in the literature.[148,214,215,216,217]

4.3.3 Surface morphology and particle size

The effect of annealing on the particle size and morphology of the films was studied using FEGSEM. Figure 4-61 shows the surface morphology of the samples annealed at different temperatures using both conventional and microwave-assisted annealing.

Figure 4-61-(a) shows the surface of the as-deposited iron which comprises particles of about 300 nm. Each of these individual particle clusters consisted of much smaller primary particles in the range of 20 to 30 nm. As the iron film is heated in the conventional furnace, these smaller nanoparticles dispersed in the surface dominate the morphology and oxidation characteristics of the films. As shown in Figure 4-61-(c), the majority of the particles are appeared to be converted to oxides at 350 °C. This is the temperature at which iron oxide peaks are first observed in XRD. It suggests that the dissociation of big particles to their constituent smaller nanoparticles could be correlated with the formation of α-Fe_2O_3 from Fe. At higher temperatures these oxide nanoparticles grow and sinter to each other forming larger particles. As shown in Figure 4-61-(d), a fairly continuous structure of joined big particles is formed at the surface as a result of growth and sintering of nanoparticles. Increasing the temperature to 500 °C seems to further sinter the bigger particles and reduce the porosity at the surface of the films.[213]

Microwave assisted annealing of electrodeposited films was found to require lower temperatures. As shown in Figure 4-61-(g) to Figure 4-61-(i), similar metal → oxide conversion mechanism is observed but it happens in a shorter temperate range. The collapse of big particles to smaller nanoparticles and the first signs of oxide formation were noted as morphological differences at temperatures as low as 200 °C, corroborating well with the XRD measurements of the annealed films (Figure 4-59). 230 °C resulted in the conversion of

most of the particles at the surface. At 250 °C, the nanoparticles begin to sinter together. However, the size of the joined particles in the microwave treated samples is much smaller compared to that of the samples annealed conventionally.[213]

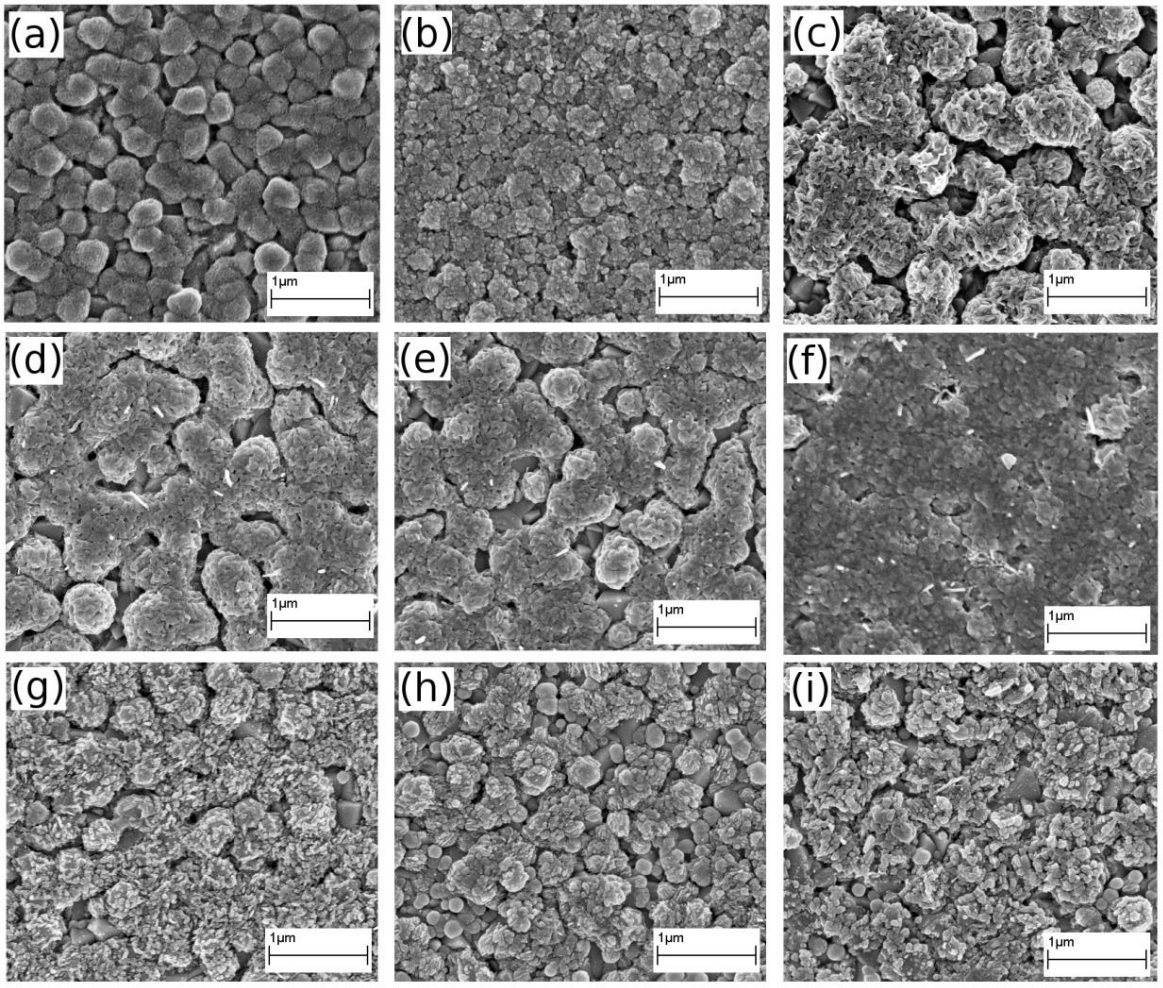

Figure 4-61. SEM photographs of different samples. a) as-deposited. b) Conv-300-15. c) Conv-350-15. d) Conv-400-15. e) Conv-450-15. f) Conv-500-15. g) MW-200-15. h) MW-230-15. i) MW-250-15. Note: Conv – xxx – yy = conventional heating - annealing temperature in °C – annealing time in minutes.[213]

Further heating for longer times led to higher degree of sintering of particles. Since this conversion and sintering occurs at much lower temperatures the final structure obtained from microwave assisted annealing contains finer features and possibly higher surface area. The differences in the size of the sintered oxide nanoparticles at the end of the annealing process both in the conventional heating and microwave assisted heating are shown in Figure

4-62. While the original size of the primary nanoparticles is almost maintained at 20-30 nm in the film annealed at 250 °C the size of the nanoparticles annealed at 450 °C in conventional heating increased to about > 80 nm.[213]

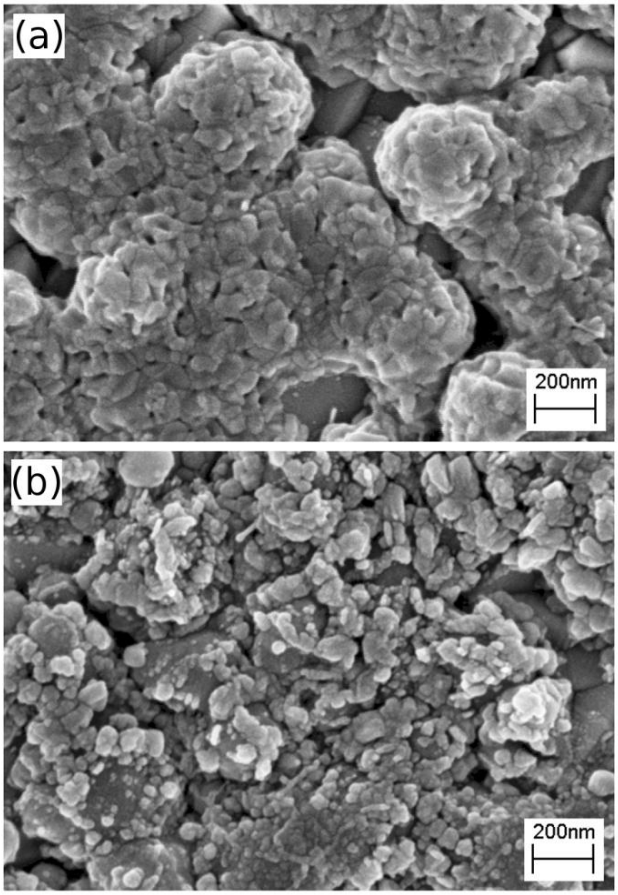

Figure 4-62. SEM images of the samples a) annealed conventionally at 450 °C and b) annealed using microwave heating at 250 °C. Annealing time is 15 min for both cases.[213]

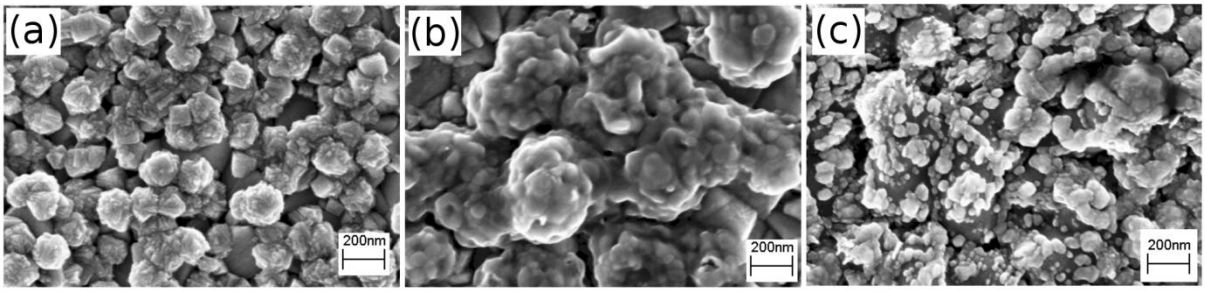

Figure 4-63. SEM images of (a) as-deposited (b) conventionally-annealed at 450 °C/15 min and (c) microwave annealed at 270 °C/15 min Si-doped films.[213]

Microwave annealing of Si-doped samples also resulted in α-Fe_2O_3 thin films with smaller morphological and microstructural features. As shown in Figure 4-63, while the as-deposited Si-doped samples include small nanoparticle aggregates of less than 200 nm in size, conventional heating at 450 °C for 15 minutes resulted in the oxidation of these samples and formation of big agglomerated particles. In contrary, microwave annealing resulted in a completely different surface morphology comprising of finer nanoparticles with minimum coalescence.[213]

Comparing SEM results and PEC performance, it is clearly shown that the increase in the particle size and coalescence of small particles at higher annealing temperatures resulted in a decrease of photocurrent density. Grain growth and increase in the particle size reduce the surface area, which could be responsible for the reduction in PEC performance. However, the loss in the PEC performance as a result of smaller surface area is compensated by the improvement in the oxidation and crystallinity. Therefore, it can be suggested that the PEC performance of these hematite films can be improved if high degrees of oxide formation and crystallinity are achieved while the size of the nanoparticles is preserved and growth is limited. The results presented here indicates that hematite electrodes obtained by microwave annealing show good degree of crystallinity while the retained nanostructure promotes the photocurrent densities achieved for microwave-annealed α-Fe_2O_3 films.[213]

4.3.4 IPCE measurements

In order to further investigate the difference between the PEC performance of the films annealed conventionally and using microwave irradiation, the incident photon to current conversion efficiency (IPCE) measurements were conducted at different wavelengths and at 0.23 V vs. $V_{Ag/AgCl}$. As shown in Figure 4-64, the IPCE of both types of samples are almost similar at wavelengths higher than 590 nm which is beyond the absorption threshold of hematite. However, at lower wavelengths there is a significant difference between the two types of samples.[213]

In the case of the undoped sample annealed in a conventional furnace at 450 °C for 15 minutes, the maximum efficiency of 5.1% is achieved at 355 nm. However, the sample annealed using microwaves showed the maximum efficiency of 8.2 % at 355 nm which

improved even further with Si-doping. The high efficiency values at short wavelengths are understood by the fact that the light penetration depth at short wavelengths is small and these high energy photons are absorbed in the vicinity of the surface of the film.[213]

The closer the photo-generated holes to the surface, the more efficient the collection of holes at the surface of the electrode as the holes have to diffuse through a shorter path to reach the surface of the film. As mentioned, the hole diffusion length in hematite is very small, therefore reducing the particle size could contribute to better hole diffusion and more efficient charge separation at the surface since the particle size is closer to the hole diffusion length. The difference in the IPCE of the two samples can be attributed to the difference in the observed particle size; as shown in Figure 4-62, microwave assisted annealing resulted in particles 4 times smaller than that of the films annealed using conventional heating.[213]

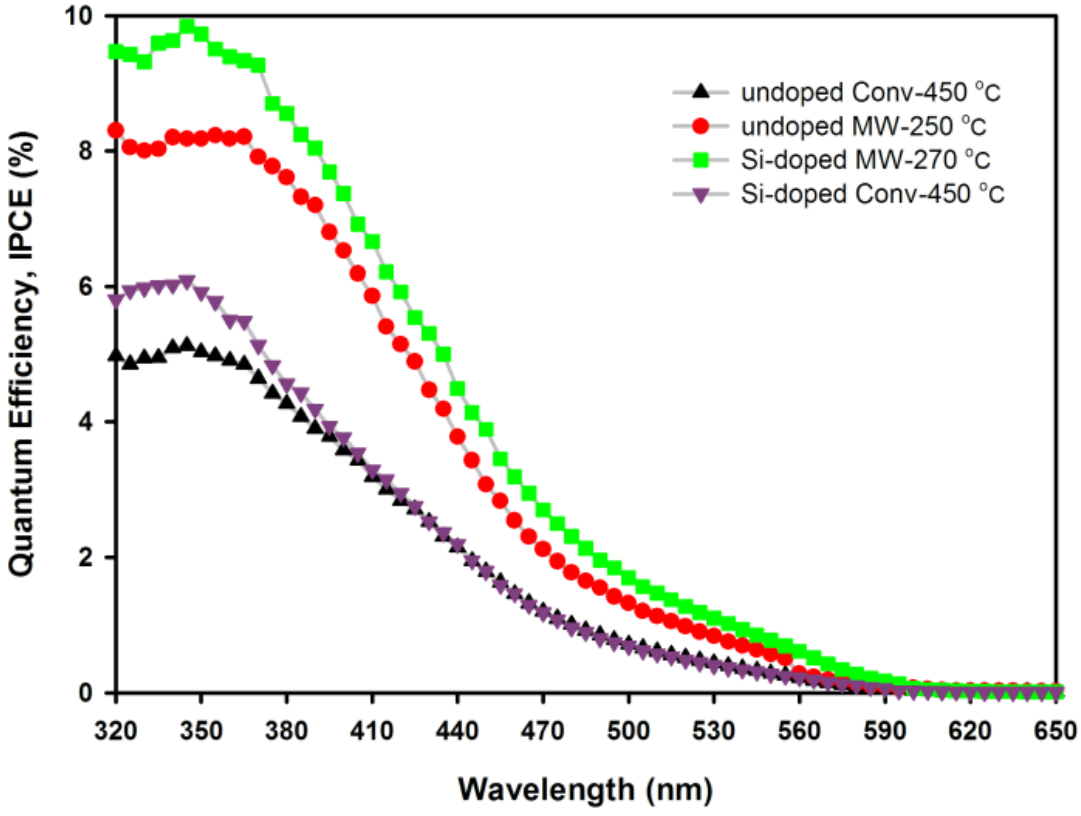

Figure 4-64. IPCE spectra as a function of wavelength at 0.23 V vs. $V_{Ag/AgCl}$ for undoped and Si-doped samples annealed using conventional and microwave assisted heating.[213]

Another interesting feature of the IPCE spectra is the fact that even the undoped sample annealed using microwaves showed higher quantum efficiency than that of Si-doped sample annealed conventionally. This could be attributed to the fine nanostructure at the surface of this type of film. The monochromated light of 355 nm has a very short penetration depth in the film. Therefore, the light is only absorbed in the first few nanometers of the top-most surface of the film. The holes generated at this area do not need to diffuse too far in order to reach the hematite/electrolyte interface. In other words, the depth in which the photo-generated holes are formed is comparable to the hole diffusion length in hematite. This would attribute to the high quantum efficiency at low wavelength regimes. Another important limiting factor is the size of the surface features of the hematite films. Finer nanostructure would also contribute to a better hole transport and hinder the recombination.

Higher annealing temperatures and longer annealing times would result in the growth of the fine grains of the hematite structure and consequently the collapse of the fine nanostructure. This would increase the charge recombination at the surface and also reduce the active surface area, leading to lower quantum efficiency. However, doping could compensate partly for these losses. It is expected that a sample with fine nanostructure and better charge transport properties, i.e. lower recombination, exhibits improved quantum efficiency and PEC performance. Here, it has been shown that such a hematite film could be prepared by annealing using a microwave method to retain the nanostructure and doping it with a Si-containing precursor (TEOS). The rapid heating of fine metallic particles in microwave environment could be due to the eddy currents generated in them and the associated joule heating.[132,133,148,149,218] This uniform local heating can facilitate faster bulk nucleation/oxidation.[213]

To evaluate the generic applicability of the microwave-assisted annealing method for oxidation of Fe films, further two types of Fe films, DC-sputtered Fe (thickness = 80 nm) and iron foil (thickness = 0.1 mm), were examined. The preliminary microstructure and PEC characterization results were very encouraging (See Appendix I). In fact, both sputtered Fe and Fe-foil were successfully converted to α-Fe_2O_3 at similar time-temperature profiles to electrodeposited samples; 250 °C for 15 minutes. Further optimization studies on the annealing temperature-time profiles for these types of samples are required in order to fabricate efficient hematite electrodes.[213]

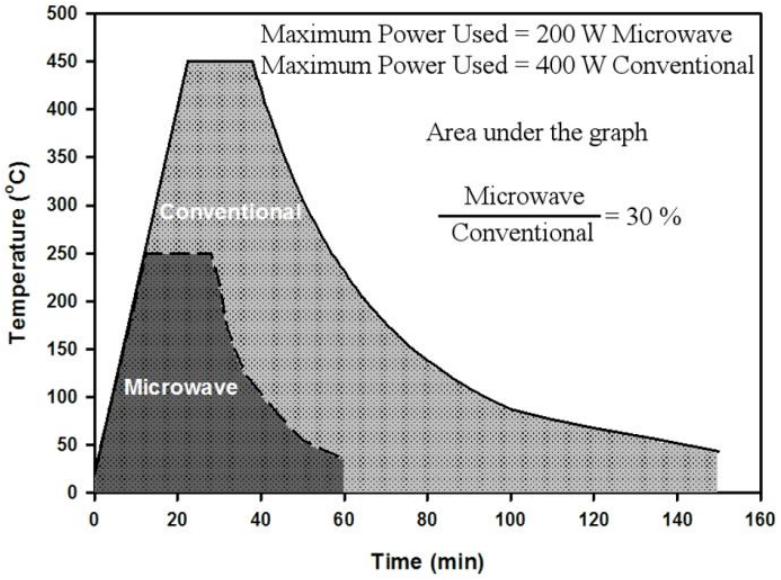

Figure 4-65. Time - Temperature profiles of the samples annealed at 450 and 250 °C for 15 minutes using conventional and microwave assisted annealing respectively. The maximum power used at the soaking temperature corresponding to each annealing technique is also mentioned.[213]

Another interesting prospect of the use of microwave heating is exemplified in Figure 4-65. It depicts the temperature-time profiles of both the annealing processes in a conventional furnace and in a microwave cavity for the undoped samples with best PEC performance. The area under the graph, roughly estimating the energy consumed during each annealing process, shows that microwave annealing requires only ~30% of the energy needed for the conventional method while operating at half the maximum power level. Moreover, the microwave method also produced hematite electrodes with almost twice the PEC performance of that of the conventionally-annealed electrodes.[213]

These results unambiguously confirmed that microwave annealing is a generic viable method for oxidising different types of metallic Fe films for solar-driven water splitting. The lower processing temperature requirements of the microwave process can open up the possibility of fabricating hematite thin films on conducting, flexible, plastic electronic substrates.

Chapter 5

5 Summary

Different preparation techniques for undoped and Si-doped iron oxide thin films using microwave-assisted and conventional preparation methods were investigated. The contributing factors in improving the photo-performance of hematite films were examined in detail. Two distinct strategies towards improving PEC performance of hematite photoelectrodes were examined; retaining a fine nanostructure and enhancing the photocatalytic behaviour through doping.

Un-doped and Si-doped nanocrystalline hematite electrodes were successfully prepared through APCVD. It was observed that the substrate played an important role in the formation of the (110) orientation in the films which is the favourable orientation with regards to electronic conduction. The best photocurrent density achieved was 1.67 $mA.cm^{-2}$ when TEOS was used as the silicon precursor. Although it is extremely difficult to quantify the level of silicon incorporation in the films, the qualitative results suggested an increasing trend in the amount of silicon in hematite films as the TEOS flow rate was increased. It can be concluded, from the XPS data, that Si is incorporated in the hematite structure as Si^{4+}. The XPS data also indicate the presence of Fe^{2+} in the doped samples which was regarded as the indirect confirmation of the existence of Si^{4+}. Based on Raman data it is envisaged that introduction of silicon induces lattice defects in the hematite structure. Based on the findings, it can be concluded that there is a combination of different factors (such as silicon incorporation into the hematite structure and formation of lattice defects, along with a nanostructure of small agglomerate/cluster enhancing hole transportation to the surface) contribute to the improvement of PEC performance in Si-doped hematite films.

The photocurrent density achieved for undoped hematite films prepared by APCVD using ferrocene was far better than what had been previously reported for undoped hematite films prepared using APCVD using other sources of Fe.[99] Films prepared using ferrocene

possessed higher optical absorption which led to the higher charge generation and separation. Based on the IPCE results, it is proposed that it is not only higher optical absorption but also an improved charge separation and transport upon excitations at near UV region in ferrocene sample which is responsible for the enhanced photo-performance. It is likely that electron-phonon processes and trapping by mid-bandgap states are significantly reduced in ferrocene sample as a result of smaller surface area and less inherent defects in this type of films.

It is also shown that a non-porous highly oriented micrometer-thick hematite films can be produced by AACVD using ferrocene as the precursor. Recombination and charge transfer rate constants at the surface of hematite photoelectrodes was investigated by PEIS taking into account a single trap model. It was found that as the applied voltage was increased both recombination and charge transfer rate constant increased, however, the degree at which charge transfer rate constant was increased exceeded that of the recombination rate constant which was in agreement with increasing of steady-state photocurrent density in the same potential region.

In addition, the feasibility of using microwave annealing for the fabrication of iron oxide thin films prepared by electrodeposition at low temperatures was investigated. It is demonstrated for the first time that significant enhancement of PEC performance could be achieved by using microwave-assisted annealing for the fabrication of α-Fe_2O_3 thin films. The process can also lead to significant energy savings (>60% when compared with conventional methods). Different types of Fe thin films were oxidized using both microwave and conventional heating techniques. The PEC performance of electrodeposited, undoped and Si-doped iron oxide samples showed that microwave-annealing resulted in superior structural and performance enhancements. The photocurrent densities obtained from microwave annealed samples are among the highest values reported for α-Fe_2O_3 photoelectrodes fabricated at low temperatures and short times; the highest photocurrent density at 0.55 V vs. $V_{Ag/AgCl}$, before the dark current onset, was 450 $\mu A.cm^{-2}$ for the Si-doped films annealed at 270 °C for 15 minutes using microwave irradiation (and 180 $\mu A.cm^{-2}$ at 0.23 V vs. $V_{Ag/AgCl}$) while conventional annealing at the same temperature resulted in samples with negligible (3 $\mu A.cm^{-2}$) photoactivity. In contrast, a 450 °C/15 min conventional heat treatment only resulted in a film with 25% lower photocurrent density than that of the microwave annealed sample.

The improved performance is attributed to the lower processing temperatures and rapidity of the microwave method that help to retain the nanostructure of the thin films whilst restricting the grain coalescence to a minimum. The lower processing temperature requirements of the microwave process can also open up the possibility of fabricating hematite thin films on conducting, flexible, plastic electronic substrates.

Chapter 6

6 Suggestions for future work

Losses due to bulk and surface recombination of photo-generated electron-hole pairs play a key role in determining the efficiency of hematite electrodes. The mismatch between the estimated flat band potential (from capacitance measurements) and steady-state photocurrent onset thought to be originated from the recombination via surface states. This means even a higher bias (than the estimated value, i.e. the energy difference V_{FB} and H^+/H_2 level) is needed before photocurrent appears. Studying the reaction kinetics on the semiconductor/electrolyte interface would provide useful information in this area. Photocurrent transient spectroscopy, intensity modulated photocurrent spectroscopy (IMPS) along with PEIS would give complementary information about the competition between surface recombination and electron transfer hence providing a better understanding of surface kinetics, which would allow for the development of more efficient hematite photoelectrodes.

It is believed that the photocatalytic properties of hematite are strongly affected by size, morphology, dopants, doping level, and surface area of particles and in turn films. Reports on the carrier dynamics of iron oxides and the effect of defects and adsorbents on the carrier lifetime are scarce. The time scales of the IPCE measurement are far from the ultra fast measurements used to study the carrier dynamics of iron oxides hence making it difficult to suggest any clear process for carrier relaxation and recombination. EPR spectroscopy and ultrafast time-resolved photocurrent experiments would provide useful information on the nature of different carrier relaxation processes and the effects of different parameters such as dopants and defects on carrier relaxation properties of photoelectrodes. A more detailed investigation on the nature of the defects and the exact doping levels could be carried out by using Mössbauer spectroscopy and high resolution magic-angle spinning NMR spectroscopy (HR-MAS NMR).

It is essential to develop a comprehensive understanding of how the microwave heating affects the oxidation kinetics of Fe and maintain the grain coalescence to minimum. Further work on the effects of microwave heating on preparation and performance of iron oxide

films has to be carried out using a hybrid microwave methodology in which both radiant heat and microwave energy are present. In order to elucidate the effects of microwave heating, the microwave power is varied while the conventional radiant heat is kept constant. These studies would provide important information on the fundamentals of microwave heating during annealing of hematite films. It would also provide a powerful tool for the further optimisation of microwave-assisted annealing hence enhancing the properties of the annealed films.

Control and development of unique and unobtainable nanostructures of functional materials could lead to major technological benefit. On the other hand, current processing methodologies of nanostructured functional materials often require energy intensive preparation techniques at high temperature regimes. The exploitation of microwave energy in processing of functional nanomaterials could pave the way for the development of cost-effective, environmentally-friendly processing pathways which could enhance the properties of functional nanomaterials through tuneable control and development of unusual nanostructures. Microwave energy can be exploited in two ways. First, during the preparation of functional materials (e.g. in an AACVD system) be developing a microwave-assisted deposition system in which microwaves replace the conventional source of heat such as hotplates. Secondly, microwave heating can be used as alternative to conventional heating for post deposition treatments of casted functional films (e.g. annealing the tape-casted films).

By harnessing the microwave energy it would be possible to lower the processing temperatures both during deposition and at post annealing steps. Initial steps can begin by investigating two specific classes of materials, namely oxide and nitrides. Of significant importance are iron oxide (α-Fe_2O_3/hematite), ferrites ($ZnFe_2O_4$, $CoFe_2O_4$ and $BiFeO_3$), tantalum oxide (Ta_2O_5) and tantalum nitride (TaN). The bandgap, electrical, chemical and catalytic properties of these materials hence their photo-performance are strongly affected by the particle size and composition.

Chapter 7

7 Bibliography

1- Bach, U. Solid-State Dye-Sensitised Mesoporous TiO_2 Solar Cells, PhD Thesis, École Polytechnique Federale de Lausanne, **2000**.

2- United Nations Development Programme, World Energy Assessment: Overview 2004 Update, **2004**.

3- World Energy Outlook 2008, International Energy Agency, OECD/IEA: France, **2008**.

4- Li, B.; Wang, L.; Kang, B.; Wang, P.; Qiu, Y.; *Sol. Energy Mater. Sol. Cells* **2006**, *90*, 549-573.

5- Li,Y.; Zhang; J. Z.; *Laser Photonics Rev.* **2010,** *4*, 517-528.

6- Ohi, J.; *J. Mater. Res.* **2005**, *20*, 3180-3187.

7- Sheppard, L. R.; Nowotny, J.; *Adv. Appl. Ceram.* **2007**, *106*, 9-20.

8- Wijayantha,K. G. U.; Auty, D. H.; Encyclopaedia of Materials: Science and Technology Updates, Elsevier: Oxford, **2005**, pp 1-5.

9- Armor, J. N.; *Catal. Lett.* **2005**, *101*, 131-135.

10- Bolton, J. R.; *Sol. Energy* **1996**, *57*, 37-50.

11- Fujishima, A.; Honda, K.; *Nature* **1972**, *238*, 37-38.

12- Somorjai, G. A.; Turner, J. E.; *Naturwiss.* **1984**, *71*, 575-577.

13- Nozik, A. J.; *Ann. Rev. Phys. Chem.* **1978**, *29*, 189-222.

14- Bak, T.; Nowotny, J.; Rekas, M.; Sorell, C. C.; *Int. J. of Hydrogen Energy* **2002**, *27*, 991-1022.

15- Anderman, M.; Kennedy, J. H.; Semiconductor electrodes: Iron oxide (Fe_2O_3)," In *Studies in Physical and Theoretical Chemistry*, Finklea, H. O., Ed.; Elsevier Science: Amsterdam, Netherlands, **1988**, pp 147-202.

16- Murphy, A. B.; Barnes, P. R. F.; Randeniya, L. K.; Plumb, I. C.; Grey, I. E.; Horne, M. D.; Glasscock, J. A.; *Int. J. of Hydrogen Energy* **2006**, *31*, 1999-2017.

17- Bard, A. J.; Fox, M. A.; *Acc. Chem. Res.* **1995**, *28*, 141-145.

18- Weber, M. F.; Dignam, M. J.; *J. Electrochem. Soc.* **1984**, *131*, 1258-1265.

19- Varghese, O. K.; Grimes, C. A.; *Sol. Energy Mater. Sol. Cells* **2008**, *92*, 374-384.

20- Memming, R.; Semiconductor Electrochemistry, WILEY-VCH Verlag GmbH:D-69469 Weinheim (Federal Republic of Germany), **2001**.

21- Nelson, J.; The Physics of Solar Cells, Imperial College Press: London, **2003**, pp 41-77.

22- Kao, K. C.; Dielectric Phenomena in Solids, Elsevier Academic Press: San Diego, **2004**.

23- Simons, J.; Andre, J. J.; Molecular Semiconductors, Photoelectrical Properties and Solar Cells, Springer-Verlag: Berlin Heinelberg, **1985**.

24- Hagfeldt, A.; Björksten, U.; Lindquist, S. –E.; *Sol. Energy Mater. Sol. Cells* **1992**, *27*, 293-304.

25- Rajeshwar, K.; In *Encyclopedia of Elctrochemistry*, Bard, A. J.; Stratmann, M.; Licht, S., Eds.; Wiley-VCH Verlag GmbH & Co., **2002**, Vol.6, pp 1-45.

26- Serpone, N.; Pelizzetti, E.; Photocatalysis Fundamentals and Applications, John Wiley and Sons, Inc.: USA, **1998**.

27- Tchikawa, H.; Faulkner, L. R.; In *Laboratory Techniques for Electroanalytical Chemistry*, Kissinger, P. T.; Heineman, W. R., Eds.; Marcel Dekker Inc.: New York, **1984**, pp 637-674.

28- Photocatalysis: Science and Technology, Kaneko, M.; Okura, I., Eds.; Kodansha Ltd.: Tokyo, Japan; Springer Verlog: Berlin, Germany, **2002**.

29- Butler, M. A.; *J. Appl. Phys.* **1977**, *48*, 1914-1920.

30- Akihiko Kudo, A.; Miseki, Y.; *Chem. Soc. Rev.* **2009**, *38*, 253-278.

31- Wang, H.; Turner, J. A.; *J. Electrochem. Soc.* **2010**, *157*, F173-F178.

32- Sato, N.; Electrochemistry at Metal and Semiconductor Electrodes, Elsevier Science B.V.: Amsterdam, Netherlands, **1998**.

33- Archer, M. D.; Nozik, A. J.; Nanostructured and Photoelectrochemical Systems for Solar Photon Conversion, Series on Photoconversion of Solar Energy Vol.3, Imperial College Press, **2009**.

34- Hagfeldt, A.; Lindquist, S. –E.; Gratzel, M.; *Sol. Energy Mater. Sol. Cells* **1994**, *32*, 245-257.

35- Lindquist, S. –E.; Hagfeldt, A.; Södergren, S.; Lindström, H.; In *Electrochemistry of Nanomaterials*, Hodes, G., Eds.; Wiley-VCH Verlag GmbH & Co., **2005**, pp 169-200.

36- Rensmo, H.; Lindström, H.; Södergren, S.; Willstedt, A. –K.; Solbrand, A.; Hagfeldt, A.; Lindquist, S. –E.; *J. Electrochem. Soc.* **1996**, *143*, 3173-3178.

37- Vanmaekelbergh, D.; de Jongh, P. E.; *J. Phys. Chem. B* **1999**, *103*, 747-750.

38- Södergren, S.; Hagfeldt, A.; Olssen, J.; Lindquist, S. –E.; *J. Phys. Chem.* **1994**, *98*, 5552-5556.

39- Bube, R.H.; Photoelectronic Properties of Semiconductors, Cambridge University Press, **1992**.

40- Fredlein, R. A.; Bard, A. J.; *J. Electrochem. Soc.* **1979**, *126*, 1892-1898.

41- Iwarchi, P.; Curran, J. S.; Gissler, W.; Memming, R.; *J. Electrochem. Soc.* **1981**, *128*, 2128-2133.

42- Dare-Edwards, M.P.; Goodenough, J.B.; Hamnett, A.; Trevellic, P.R.; *J. Chem. Soc. Faraday Trans. I* **1983**,*79*, 2027-2041.

43- Domen, K.; Naito, S.; Onishi, T.; Tamaru, K.; *Chem. Phys. Lett.* **1982**, *92*, 433-438.

44- Kim, H.; Laitinen, H. A.; *J. Electrochem. Soc.* **1975**, *122*, 53-58.

45- Kamat, P. V.; Dimitrijevic, N. M.; *Sol. Energy* **1990**, *44*, 83-98.

46- Kamat, P. V.; *J. Phys. Chem. C* **2007**, *111*, 2834-2860.

47- Reber, J. F.; Rusek, M.; *J. Phys. Chem.* **1986**, *90*, 824-834.

48- Cornell, R. M.; Schwertmann, U.; The Iron Oxides: Structure, Properties, Reactions, Occurrences and Uses, Wiley VCH Verlog GmbH & Co.: KGaA Weinheim, Germany, **2003**.

49-http://www.geocities.jp/ohba_lab_ob_page/Structure/Hematite_bond.JPG (accessed 30 November 2010).

50- Catti, M.; Valerio, G.; Dovesi, R.; *Phys. Rev. B* **1995**, *51*, 7441-7450.

51- Satsangi, V. R.; Kumari, S.; Singh, A. P.; Shrivastav, R.; Dass, S.; *Int. J. Hydrogen Energy* **2008**, *33*, 312-318.

52- Leygraf, C.; Hendewerk, M.; Somorjai, G. A.; *J. Solid State Chem.* **1983**, *48*, 357-367.

53- Hardee, K. H.; Bard, A. J.; *J. Electrochem. Soc.* **1976**, *123*, 1024-1026.

54- Hardee, K. H.; Bard, A. J.; *J. Electrochem. Soc.* **1977**, *124*, 215-224.

55- Cesar, I.; Kay, A.; Gonzalez Martinez, J. A., Grätzel, M.; *J. Am. Chem. Soc.* **2006**, *128*, 4582–4583.

56- Kodas, T. T.; Hampden-Smith, M. J.; Aerosol Processing of Materials, Wiley-VCH: Weinheim, Germany, **1999**.

57- Hitchman, M. L.; Jensen, K. F.; In *Chemical Vapour Deposition: Principles and Applications*, Hitchman, M. L.; Jensen, K. F., Eds.; Academic Press: London, **1993**, pp 1-26.

58- Wang, H. B.; Meng, G. Y.; Peng, D. K.; *Thin Solid Films* **2000**, *368*, 275-278.

59- Xu, C. Y.; Hampden-Smith, M. J.; Kodas, T. T.; *Chem. Mater.* **1995**, *7*, 1539-1546.

60- Palgrave, R. G.; Parkin, I. P.; *J. Am. Chem. Soc.* **2006**, *128*, 1587-1597.

61- Choy, K.-L.; In *Handbook of Nanostructured Materials and Nanotechnology*, Vol. 1: Synthesis and Processing, Nalwa, H. S., Ed.; Academic Press: San Diego, CA, **2000**, pp 533–577.

62- Lang, R. J.; *J. Acoust. Soc. Am.* **1962**, *34*, 6-8.

63- Renault, O.; Labeau, M.; *J. Electrochem. Soc.* **1999**, *146*, 3731-3735.

64- Rodes, C.; Smith, T.; Crouse, R.; Ramachandran, G.; *Aerosol Sci. Technol.* **1990**, *13*, 220-229.

65- Glerup, M.; Kanzow, H.; Almairac, R.; Castignolles, M.; Bernier, P.; *Chem. Phys. Lett.* **2003**, *377*, 293-298.

66- Spray, R. L.; Choi, K.-S.; *Chem. Mater.* **2009**, *21*, 3701-3709.

67- Markovac, V.; Cohen, M.; *J. Electrochem. Soc.* **1967**, *114*, 678-681.

68- Markovac, V.; Cohen, M.; *J. Electrochem. Soc.* **1967**, *114*, 674-678.

69- Leibenguth, J. L.; Cohen, M.; *J. Electrochem. Soc.* **1972**, *119*, 987-991.

70- Zotti, G.; Schiavon, G.; Zecchin, S.; Casalleto, U.; *J. Electrochem. Soc.* **1998**, *145*, 385-389.

71- Kulkurani, S. S.; Lokhande, C. D.; *Mater. Chem. Phys.* **2003**, *82*, 151-156.

72- Schrebler, R.; Bello, K.; Vera, F.; Cury, P.; Munoz, E.; del Rio, R.; Meier, H. G.; Cordova, R.; Dalchiele, E. A.; *Electrochem. Solid State Lett.* **2006**, *9*, C110-C113.

73- Hu, Y. –S.; Kleiman-Shwarsctein, A.; Forman, A. J.; Hazen, D.; Park, J. –N.; McFarland, E. W.; *Chem. Mater.* **2008**, *20*, 3803-3805.

74- Dong, W. T.; Zhu, C. S.; *J. Mater. Chem.* **2002**, *12*, 1676– 1683.

75- Ma, J.; Lian, J.; Duan, X.; Liu, X.; Zheng, W.; *J. Phys. Chem. C* **2010**, *114*, 10671-10676.

76- Hamada, S.; Matijivic, E.; *J. Colloid Interface Sci.* **1981**, *84*, 274–277.

77- Wang, X.; Chen, X. Y.; Gao, L. S.; Zheng, H. G.; Ji, M. R.; Tang, C. M.; Shen, T.; Zhang, Z. D.; *J. Mater. Chem.* **2004**, *14*, 905– 907.

78- An, Z. G.; Zhang, J. J.; Pan, S. L.; Yu, F.; *J. Phys. Chem. C* **2009**, *113*, 8092–8096.

79- Zeng, S. Y.; Tang, K. B.; Li, T. W.; Liang, Z. H.; Wang, D.; Wang, Y. K.; Zhou, W. W.; *J. Phys. Chem. C* **2007**, *111*, 10217– 10225.

80- Zhang, F. H.; Yang, H. Q.; Xie, X. L.; Li, L.; Zhang, L. H.; Yu, J.; Zhao, H.; Liu, B.; *Sens. Actuators B* **2009**, *141*, 381–389.

81- Almeida, T. P.; Fay, M.; Zhu, Y. Q.; Brown, P. D.; *J. Phys. Chem. C* **2009**, *113*, 18689–18698.

82- Pejova, B.; Najdoski, M.; Grozdanov, I.; Isahi, A.; *J. Mater. Sci. Mater. Elect.* **2000**, *11*, 405-409.

83- Quinn, R. K.; Nasby, R. D.; Baugham, R. J.; *Mater. Res. Bull.* **1976**, *11*, 1011-1017.

84- Kennedy, J. H.; Frese, Jr., K. W.; *J. Electrochem. Soc.* **1978**, *125*, 723-726.

85- Kennedy, J. H., Frese, Jr., K. W.; *J. Electrochem. Soc.* **1978**, *125*, 709-714.

86- Fujimori, A.; Saeki, M.; Kimizuka, N.; Taniguchi, M.; Suga, S.; *Phys. Rev. B* **1986**, *34*, 7318-7328.

87- Shinar, R.; Kennedy, J. H.; *Sol. Energy Mater.* **1982**, *6*, 323-335.

88- Merchant, P.; Collins, R.; Kershaw, R.; Dwight, K.; Wold, A.; *J. Solid State Chem.* **1979**, *27*, 307-315.

89- Khan, S. U. M.; Akikusa, J.; *J. Phys. Chem. B* **1999**, *103*, 7184-7189.

90- Beermann, N.; Vayssieres, L.; Lindquist, S. –E.; Hagfeldt, A.; *J. Electrochem. Soc.* **2000**, *147*, 2456-2461.

91- Lindgren, T.; Wang, H.; Beermann, N.; Vayssieres, L.; hagfeldt, A.; Lindquist, S. –E.; *Sol. Energy Mater. Sol. Cells* **2002**, *71*, 231-243.

92- Zoppi, A.; Lofrumento, C.; Castellucci, E. M.; Sciau, P.; *J. Raman Spectrosc.* **2008**, *39*, 40-46.

93- Rozenberg,G. K.; Dubrovinsky, L. S.; Pasternak, M. P.; Naaman, O.; Le Bihan, T.; Ahuja, R.; *Phys. Rev. B* **2002**, 65, 064112.

94- Kleiman-Shwarsctein, A.; Huda, M. N.; Walsh, A.; Yan, Y.; Stucky, G. D.; Hu, Y. -S.; Al-Jassim, M. M.; McFarland, E. W.; *Chem. Mater.* **2010**, *22*, 510–517.

95- Morin, F. J.; *Phys. Rev.* **1951**, *83*, 1005-1010.

96- Glasscock, J. A.; Barnes, P. R. F.; Plumb, I. C.; Savvides, N.; *J. Phys. Chem. C* **2007**, *111*, 16477-16488.

97- Sanchez, C.; Hendewerk, M.; Sieber, K. D.; Somorjai, G. A.; *J. Solid State Chem.* **1986**, *61*, 47-55.

98- Sartoretti, C. J.; Alexander, B. D.; Solarska, R.; Rutkowska, I. A.; Augustynski, J.; Cerny, R.; *J. Phys. Chem. B* **2005**, *109*, 13685-13692.

99- Kay, A.; Cesar, I.; Gratzel, M.; *J. Am. Chem. Soc.* **2006**, *128*, 15714-15721.

100- Duret, A.; Gratzel, M.; *J. Phys. Chem. B* **2005**, *109*, 17184-17191.

101- Kennedy, J. H.; Shinar, R.; Ziegler, J. P.; *J. Electrochem. Soc.* **1980**, *127*, 2307-2309.

102- Leygraf, C.; Hendewerk, M.; Somorjai, G. A.; *J. Catal.* **1982**, *78*, 341-351.

103- Houlihan, J. F.; Pannaparayil, T.; Burdette, H. L.; Madacsi, D. P.; Pollock, R. J.; *Mat. Res. Bull.* **1985**, *20*, 163-177.

104- Ingler, Jr., W. B.; Baltrus, J., P.; Khan, S. U. M.; *J. Am. Chem. Soc.* **2004**, *126*, 10238-10239.

105- Kleiman-Shwarsctein, A.; Hu, Y. –S.; Forman, A. J.; Stucky, G. D.; McFarland, E. W.; *J. Phys. Chem. C* **2008**, *112*, 15900-15907.

106- Kumari, S.; Singh, A. P.; Sonal; Deva, D.; Shrivastav, R.; Dass, S.; Satsangi, V. R.; *Int. J. Hydrogen Energy* **2010**, *35*, 3985-3990.

107- Aroutiounian, V. M.; Arakelyan, V. M.; Shahnazaryan, G. E.; Stepanyan, G. M.; Turner, J. A.; Khaselev, O.; *Int. J. of Hydrogen Energy* **2002,** *27*, 33–38.

108- Ingler Jr, W. B.; Khan S. U. M.; *Thin Solid Films* **2004**, *461*, 301–308.

109- Van de Krol, R.; Liang, Y.; Schoonman, J.; *J. Mater. Chem.* **2008**, *18*, 2311–2320.

110- Bjorksten, U.; Moser, J.; Gratzel, M.; *Chem. Mater.* **1994**, *6*, 858-863.

111- Vayssieres, L.; Sathe, C.; Butorin, S. M.; Shuh, D. K.; Nordgren, J.; Guo, J. H.; *Adv. Mater.* **2005**, *17*, 2320-2323.

112- Mohapatra, S. K.; John, S. E.; Banerjee, S.; Misra, M.; *Chem. Mater.* **2009**, *21*, 3048–3055.

113- Hahn, N. T.; Ye, H.; Flaherty, D. W.; Bard, A. J.; Mullins, C. B.; *ACS Nano* **2010**, *4*, 1977–1986.

114- LaTempa, T. J.; Feng, X.; Paulose, M.; Grimes, C. A.; *J. Phys. Chem. C* **2009**, *113*, 16293-16298.

115- Itoh, K.; Bockeris, J. O.; *J. Electrochem. Soc.*, **1984**, *131*, 1266-1271.

116- Sivula, K.; Le Formal, F.; Gratzel, M.; *Chem. Mater.* **2009**, *21*, 2862-2867.

117- Le Formal, F.; Gratzel, M.; Sivula, K.; *Adv. Funct. Mater.* **2010**, *20*, 1099-1107.

118- Stuerga, D.; In *Microwaves in Organic Synthesis*, 2nd Ed., Loupy, A., Ed.; WILEY-VCH Verlag GmbH & Co.: Weinhain, Germany, **2006**, pp 2-100.

119- Committee on Microwave Processing of Materials: An Emerging Industrial Technology, Commission on Engineering and Technical Systems, National Research Council, Microwave Processing of Materials, National Materials Advisory Board (NMAB), National Academy Press, Washington D.C., USA, **1994**, pp 1-100.

120- Bilecka I.; Djerdj I.; Niederberger M.; *Chem. Commun.* **2008**, 886-888.

121- Baghurst D. R.; Chippindale A. M.; Mingos M. P.; *Nature* **1988**, *332*, 311-312.

122- Wei, G.; Qin, W.; Han,W.; Yang, W.; Gao, F.; Jing, G.; Kim, R.; Zhang, D.; Zheng, K.; Wang, L.; Liu, L.; *J. Phys. Chem. C* **2009**, *113*, 19432–19438.

123- Reguera, E.; Díaz-Aguila, C.; Yee-Madeira, H.; *J. Mater. Sci.* **2005**, *40*, 5331-5334.

124- Wang, W. –W.; Zhu, Y. –J.; Yang, L. –X.; *Adv. Funct. Mater.* **2007**, *17*, 59–64.

125- Cirera, A.; Vila,`A.; Die´guez, A.; Cabot, A.; Cornet, A.; Morante, J. R.; *Sensor Actuat. B Chem.* **2000**, *64*, 65-69.

126- Murugan, A.V.; Samuel, V.; Ravi, V.; *Mater. Lett.* **2006**, *60*, 479-480.

127- Hart, J. N.; Menzies, D.; Cheng, Y.; Simon, G. P.; Spiccia, L.; *Sol. Energy Mat. Sol. Cells* **2007**, *91*, 6-16.

128- Chung, C.; Chung, T.; Yang, T.; *Ind. Eng. Chem. Res.* **2008**, *47*, 2301-2307.

129- Baldassari, S.; Komarneni, S.; Mariani, E.; Villa, C.; *Mater. Res. Bull.* **2005**, *40*, 2014-2020.

130- Gasgnier, M.; Loupy, A.; Petit, A.; Juliien, H.; *J. Alloy Compd.* **1994**, *204*, 165-172.

131- Baghurst, D. R.; Mingos, M. P.; *J. Chem. Soc. Chem. Commun.* **1988**, *12*, 829-830.

132- Landry, C. C.; Barron, A. R.; *Science* **1993**, *260*, 1653-1655.

133- Vaidhyanathan, B.; Ganguli, M.; Rao, K. J.; *Mater. Res. Bull.* **1995**, *30*, 1173-1177.

134- Katz, J. D.; *Annu. Rev. Mater. Sci.* **1992**, *22*, 153-170.

135- Berteaud, A. J.; Badot, J. C.; *J. Microwave Power* **1976**, *11*, 315-320.

136- Haas, P. A.; *Am. Ceram. Soc. Bull.* **1979**, *58*, 873.

137- Krage, M. K.; *Am. Ceram. Soc. Bull.* **1981**, *60*, 1232-1234.

138- MacDowell, J. F.; *Am. Ceram. Soc. Bull.* **1984**, *63*, 282-286.

139- Meredith, R.; Engineers' Hanbook of Industrial Microwave Heating, , Johns, A. T.; Warne, D.F., Eds.; IEE Power Series 25, The institute of Electrical Engineers: London, United Kingdom, **1998**.

140- Metaxas, A. C.; *Power Eng. J.* **1991**, *5*, 237-247.

141- Gupta, M.; Leong Eugene, W. W.; Microwaves and Metals, John Wiley & Sons (Asia) Pte Ltd.: Singapore, **2007**.

142- Rao, K. J.; Vaidhyanathan, B.; Ganguli, M.; Ramakrishnan, P. A.; *Chem. Mater.* **1999**, *11*, 882-895.

143- Wang, J.; Evidence for the Microwave Effect During Hybrid Sintering and Annealing of Ceramics, PhD Thesis, Loughborough University, **2005**.

144- Whittaker, A. G.; Mingos, D. M. P.; *J. Chem.. Soc. Dalton Trans.* **1995**, 2073-2079.

145- Metaxas, A. C.; Fundamentals of Electroheat: A Unified Approach, John Wiley & Sons Ltd.: Chichester, England, **1996**.

146- Clark, D. E.; Sutton, W. H.; *Annu. Rev. Mater. Sci.* **1996**, *26*, 299-331.

147- Walkiewicz, J. W.; Kazonich, G.; McGill, S. L.; *Miner. Metall. Proc.* **1988**, *5*, 39-42.

148- Vaidhyanathan, B.; Rao, K. J.; *Chem. Mater.* **1997**, *9*, 1196-1200.

149- Roy, R.; Agrawal, D. K.; Cheng, J.; Gedevanishvili, S.; *Nature* **1999**, *399*, 668-670.

150- Cheng, J.; Roy, R.; Agrawal, D.; *Mater. Res. Innov.* **2002**, *5*, 170-177.

151- Zajíčková, L.; Synek, P.; Jašek, O.; Eliáš, M.; David, B.; Buršík, J.; Pizurová, N.; Hanzlíková, R.; Lazar, L.; *Appl. Surf. Sci.* **2009**, *255*, 5421-5424.

152- Hu, X.; Jimmy, C. Y.; *Adv. Funct. Mater.* **2008**, *18*, 880-887.

153- Parsons, J. G.; Luna, C.; Botez, C. E.; Elizalde, J.; Gardea-Torresdey, J. L.; *J. Phys. Chem. Solids* **2009**, *70*, 555-560.

154- Hu., X.; Yu., J. C.; Gong, J.; Li, Q.; Li, G.; *Adv. Mater.* **2007**, *19*, 2324-2327.

155- Deshmukh, R. G.; Badadhe, S. S.; Mulla, I. S.; *Mater. Res. Bull.* **2009**, *44*, 1179-1182.

156- Hwang, J. –Y.; Shi, S.; Xu, Z.; Peterson, K. W.; *Chem. Eng. Comm.* **2006**, *193*, 1586-1591.

157- Cao, J.; Zhitomirsky, I.; Niewczas, M.; *Mater. Chem. Phys.* **2006**, *96*, 289–295.

158- Vaidhyanathan, B.; Annapoorani, K.; Binner, J. G. P.; Raghavendra, R.; Microwave Assisted Large Scale Sintering of Multilayer Electroceramic Devices, In *Ceramics Engineering and Science Proceedings*, Ohji, T.; Singh, M., Eds.; John Wiley & Sons: New Jersey, **2010**, Vol. 30, Issue.8, pp 11-18.

159- Wang, J.; Binner, J. G. P.; Vaidhyanathan, B.; Joomun, N.; Kilner, J.; Dimitrakis, G.; Cross, T. E.; *J. Am. Ceram. Soc.* **2006**, *89*, 1977-1984.

160- Binner, J. G. P.; Vaidhyanathan, B.; Wang. J.; A Comparitive Study of Temperature Measurements During Microwave Processing, 9th International Conference on Microwave and High Frequency Heating, Loughborough, UK, **2003**.

161- Durose, K.; Asher, S. E.; Jaegermann, W.; Levi, D.; McCandless, B. E.; Metzger, W.; Moutinho, H.; Paulson, P. D.; Perkins, C. L.; Sites, J. R.; Teeter, G.; Terheggen, M.; *Prog. Photovolt. Res. Appl.* **2004**, *12*, 177–217.

162- Glasscock, J. A.; Nanostructured Materials for Photoelectrochemical Hydrogen Production Using Sunlight, PhD Thesis, University of New South Wales, **2008**.

163- Ratner, B. D.; Castner, D. G.; Electron Spectroscopy for Chemical Analysis, In *Surface Analysis – The Principal Techniques*, 2nd Edition. John C. Vickerman, J. C.; Gilmore, I.S., Eds.; John Wiley & Sons, Ltd: Chichester, UK, **2009**, pp 47-112.

164- Ferraro, J. A.; Nakamoto, K.; Brown, C. W.; Introductory Raman spectroscopy, 2nd Edition, Elsevier Science: USA, **2003**.

165- Nafie, L. A.; Theory of Raman Spectroscopy, In *Handbook of Raman Spectroscopy: from the Research Laboratory to the Process Line*, Lewis, I. R.; Edwards, H. G. M., Eds.; Marcel Dekker Inc.: NewYork, USA, **2001**.

166- Thomas, R.; Practical Guide to ICP-MS, Marcel Dekker Inc.: NewYork, USA, **2004**.

167- http://minerals.cr.usgs.gov/icpms/images/detection_capabilities.gif (accessed 6 July 2010).

168- Garcìa Solé, J.; Bausá, L. E.; Jaque, D.; An Introduction to the Optical Spectroscopy of Inorganic Solids, John Wiley & Sons Ltd: Chichester, England, **2005**.

169- Bandara, J.; Mielczarski, J. A.; Kiwi, J.; *Langmuir* **1999**, *15*, 7670-7679.

170- Yadav, P.; Madhava Rao, B. S.; Batchelor, N. S.; O'Neil, P.; *J. Phys. Chem. A* **2005**, *109*, 2039-2042.

171- Boschloo, G.; Fitzmaurice, D.; *J. Phys. Chem. B* **1999**, *103*, 3093-3098.

172- CRC Handbook of Chemistry and Physics, 75th Edition, Lide, D. R.; Frederikse, H. P. R., Eds.;CRC Press Inc.: Boca Raton, USA, **1995**.

173- Saremi-Yarahmadi, S.; Wijayantha, K. G. U.; Tahir, A. A.; Vaidhyanathan, B.; *J. Phys. Chem. C* **2009**, *113*, 4768-4778. (http://dx.doi.org/10.1021/jp808453z).

174- Campbell, A. S.; Schwertmann, U.; Stanjek, H.; Friedl, J.; Kyek, A.; Campbell, P. A.; *Langmuir* **2002**, *18*, 7804-7809.

175- Desai, J. D.; Pathon, H. M.; Min, S. –K.; Jung, K. –D.; Joo, O. –S.; *Semicond. Sci. Technol.* **2005**, *20*, 705-709.

176- Desai, J. D.; Pathon, H. M.; Min, S. –K.; Jung, K. –D.; Joo, O. –S.; *Appl. Surf. Sci.* **2006**, *252*, 2251-2258.

177- NIST XPS database: http://srdata.nist.gov/XPS (Accessed July 20, 2008).

178- Berry, F. J.; Greaves, C.; McManus, J. G.; Mortimer, M.; Oates, G.; *J. Solid State Chem.* **1997**, *130*, 272-276.

179- Berry, F. J.; Greaves, C.; Helgason, Ö.; McManus, J. G.; Palmer, H. M.; Williams, R. T.; *J. Solid State Chem.* **2000**, *151*, 157-162.

180- Berry, F. J.; Bohorquez, A.; Moor, E. A.; *J. Phys. Chem. Solids* **2001**, *62*, 1277-1284.

181- Kuivila, C. S.; Butt, J. B.; Stair, P. C.; *Appl. Surf. Sci.* **1988**, *32*, 99-121.

182- Grosvenor, A. P.; Kobe, B. A.; Biesinger, M. C.; McIntyre, N. S. ; *Surf. Interface Anal.* **2004**, *36*, 1564-1574.

183- Yamashita, T.; Hayes, P.; *Appl. Surf. Sci.* **2008**, *254*, 2441-2449.

184- Yu, K. N.; Xiong, Y.; Liu, Y.; Xiong, C.; *Phys. Rev. B* **1997**, *55*, 2666-2671.

185- McCarty, K. F.; *Solid State Commun.* **1988**, *68*, 799-802.

186- Bersani, D.; Lottici, P. P.; Montenero, A.; *J. Raman Spectrosc.* **1999**, *30*, 355-360.

187- Chernyshova, I. V.; Hochella Jr., M. F.; Madden, A. S.; *Phys. Chem. Chem. Phys.* **2007**, *9*, 1736-1750.

188- Chu, J. C. S.; Breslin, J.; Wang, N. S.; Lin, M. C.; *Mater. Lett.* **1991**, *12*, 179-184.

189- Shimojo, M.; Takeguchi, M.; Mitsuishi, K.; Tanaka, M.; Furuya, K.; *Jpn. J. Appl. Phys.* **2007**, *46*, 6247-6249.

190- Takeguchi, M.; Shimojo, M.; Furuya, K.; *Jpn. J. Appl. Phys.* **2007**, *46*, 6183-6186.

191- Schaadt, D. M.; Feng, B.; Yu, E. T.; *Appl. Phys. Lett.* 2005, *86*, 063106.

192- Catchpole, K. R.; Polman, A.; *Opt. Express* **2008**, *16*, 21793-21800.

193- Pal, B.; Sharon, M.; *J. Chem. Technol. Biotechnol.* **1998**, *73*, 269-273.

194- Miller, E. L.; Paluselli, D.; Marsen, B.; Rocheleau, R. E.; *Thin Solid Films* **2004**, *466*, 307-313.

195- Liang, Y.; Enache, C. S.; Van der Krol, R.; *Int. J. Photoenergy* **2008**, Article Number: 739864.

196- Sherman, D. M.; Waite, T. D.; *Am. Mineral.* **1985**, *70*, 1262-1269.

197- Fan, H. M.; You, G. J.; Li, Y.; Zheng, Z.; Tan, H. R.; Shen, Z. X.; Tang, S. H.; Feng, Y. P.; *J. Phys. Chem. C* **2009**, *113*, 9928-9935.

198- Joly, A. G.; Williams, J. R.; Chambers, S. A.; Xiong, G.; Hess, W. P.; Laman, D. M.; *J. Appl. Phys.* **2006**, *99*, 053521.

199- Cherepy, N. J.; Liston, D. B.; Lovejoy, J. A.; Deng, H.; Zhang, J. Z.; *J. Phys. Chem. B* **1998**, *102*, 770-776.

200- Joly, A. G.; Xiong, G.; Wang, C.; McCready, D. E.; Beck, K. M.; Hess, W. P.; *Appl. Phys. Lett.* **2007**, *90*, 103504.

201- Sanchez, C.; Hendewerk, M.; Sieber, K. D.; Somorjai, G. A.; *J. Solid State Chem.* **1986,** *61*, 47-55.

202- Burri, D. R.; Shaikh, I. R.; Choi, K. M.; Park, S. E.; *Catal. Commun.* **2007**, *8*, 731-735.

203- Zhao, S. Y.; Ma, H. Y.; Chen, S. H.; Wang, C. T.; Li, D. G.; *J. Electrochem. Soc.* **2002**, *149*, H169-172.

204- Emel'yanov, V. E.; Simonenko, L. S.; Skvortsov, V. N.; *Chem. Technol. Fuels Oils* **2001**, *37*, 224-228.

205- Zhou, Y.; Zhang, Z.; Yue, Y.; *Mater. Lett.* **2005**, *59*, 3375-3377.

206- Nyamori, V. O.; Coville, N. J.; *Organometallics* **2007**, *26*, 4083-4085.

207- Andrews, J. T. S.; Westrum Jr., E. F.; *J. Organomet. Chem.* **1969**, *17*, 349-352.

208- Dyagikeva, L. M.; Mar'In, V. P.; Tsyganova, E. I.; Razuvaev, G. A.; *J. Organomet. Chem.* **1979**, *175*, 63-72.

209- Bernhauer, M.; Braun, M.; Huttinger, K. J.; *Carbon* **1994**, *32*, 1073-1085.

210- Saremi-Yarahmadi, S.; Tahir, A. A.; Vaidhyanathan, B.; Wijayantha, K. G. U.; *Mater. Letter.* **2009**, *63*, 523-526.

211- Ponomarev, E. A.; Peter, L. M.; *J. Electroanal. Chem.* **1995**, *397*, 45-52.

212- An, W. –J.; Thimsen, E.; Biswas, P.; *J. Phys. Chem. Lett.* **2010**, *1*, 249–253.

213- Saremi-Yarahmadi, S.; Vaidhyanathan, B.; Wijayantha, K. G. U.; *Int. J. Hydrogen Energy* **2010**, *35*, 10155-10165.

214- Vaidhyanathan, B.; Singh, A. P.; Agrawal, D. K.; Shrout, T. R.; Roy, R.; *J. Am. Ceram. Soc.* **2001**, *84*, 1197-1202.

215- Whittaker, A. G.; Mingos, D. M. P.; *J. Chem. Soc. Dalton Trans.* **1992**, 2751-2752.

216- Vaidhyanathan, B.; Binner, J. G. P.; *J. Mater. Sci.* **2006**, *41*, 5954-5957.

217- Vaidhyanathan, B.; Balaji, K.; Rao, K. J.; *Chem. Mater.* **1998**, *10*, 3400-3404.

218- Gadevanishvili, S.; Vaidhyanathan, B.; Agrawal, D. K.; Roy, R.; (The Penn State Research Foundation, USA), Microwave Processing Using Highly Absorbing Powdered Material Layers, US Patent 6,512,216 B2, January 28, **2003**.

Appendix I- Microwave annealing of DC-Sputtered Fe and Fe foil

DC-sputtered thin films of Fe and also commercial Fe foil (0.1 mm-thick Fe foil, Goodfellow Cambridge Ltd., UK) were annealed at 250 °C for 15 minutes. During DC-sputtering the deposition was conducted for 5 minutes at a power of 100 W, under Ar flow at a pressure of 3.5×10^{-3} mbar.

Figure 1 summarises the Raman results obtained for both of the samples annealed using microwave irradiation. As shown, both sputtered Fe and Fe-foil were successfully converted to α-Fe_2O_3 at similar time-temperature profiles to electrodeposited samples; 250 °C for 15 minutes. However, the degree of oxidation was smaller than that of the electrodeposited samples; the 660 cm^{-1} Raman peak is quite strong and there is only 3 peaks of hematite structure are present in the Raman spectra of both types of films.

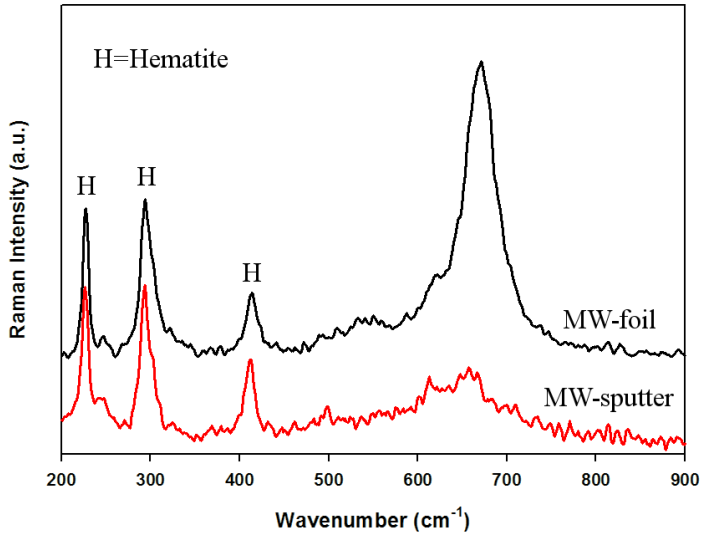

Figure 1. Raman spectra of Fe foil and sputtered Fe samples after microwave-assisted annealing 250 °C for 15 minutes.

The PEC performance of these electrodes was investigated and the J-V plots are shown in Figure 2. It is clear that the Fe foil sample has a large dark current and it shows typical ohmic characteristics of a metal electrode in contact with electrolyte at low applied potential. As the potential increases, square-shaped photocurrent pulses are observed which indicates the photoactivity of iron oxide layer formed on the surface of the Fe foil. The values of these

photocurrent densities are fairly small (~60 μA.cm^{-2} at 0.5 V vs. $V_{Ag/AgCl}$ compared to the dark current of ~580 μA.cm^{-2} at 0.5 V vs. $V_{Ag/AgCl}$).

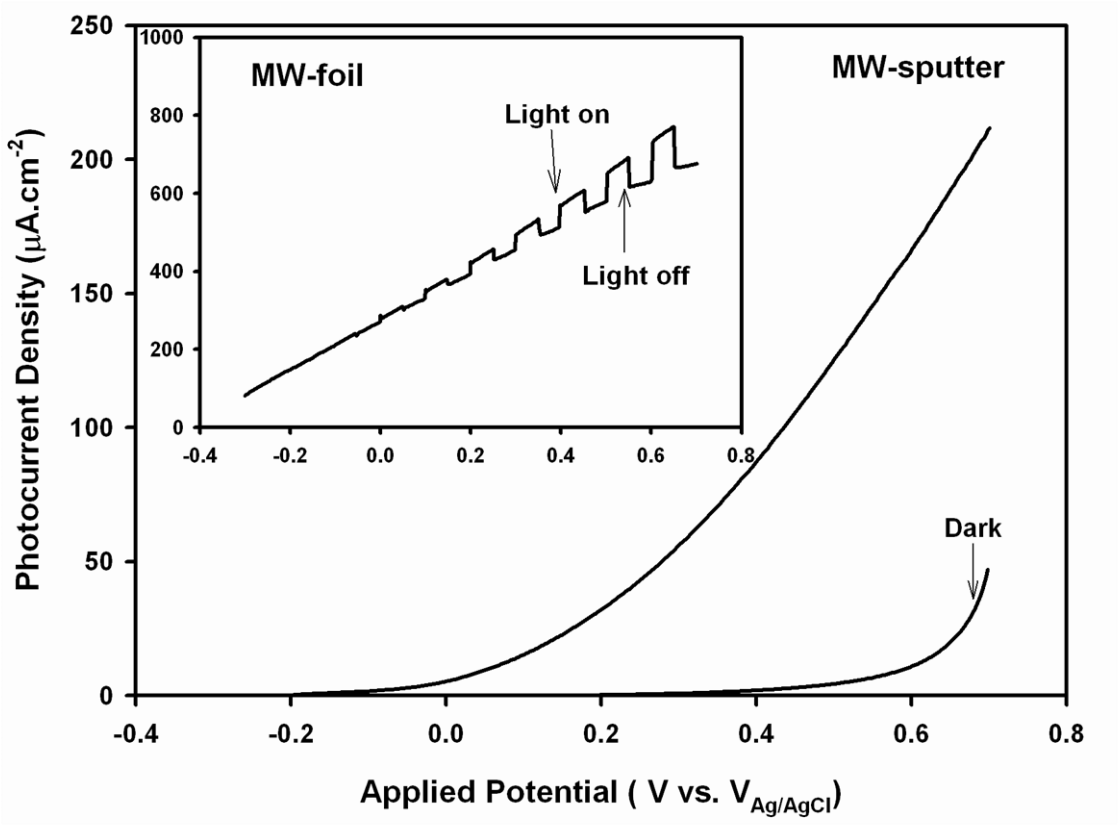

Figure 2. Photocurrent density - applied potential plots of Fe foil and sputtered Fe samples after microwave-assisted annealing at 250 °C for 15 minutes.

Based on photocurrent densities observed and the results from Raman spectroscopy) it can be concluded that it is only a thin layer of hematite formed at the surface of the Fe foil after microwave-assisted annealing. The results obtained for the sputtered Fe were more promising. This sample had negligible dark currents (<5 μA.cm^{-2}) even at applied potentials as high as 0.5 V vs. $V_{Ag/AgCl}$ while exhibiting photocurrent densities of 39 μA.cm^{-2} and 125 μA.cm-2 at 0.23 V and 0.5 V vs. $V_{Ag/AgCl}$, respectively. Further work is needed to optimise the annealing conditions for these types of samples and fabricate efficient hematite electrodes.

Appendix II: List of publications emanated from this study

1- Saremi-Yarahmadi, S.; Wijayantha, K. G. U.; Tahir, A. A.; Vaidhyanathan, B.; *J. Phys. Chem. C* **2009**, *113*, 4768-4778.

2- Saremi-Yarahmadi, S.; Tahir, A. A.; Vaidhyanathan, B.; Wijayantha, K. G. U.; *Mater. Letter.* **2009**, *63*, 523-526.

3- Saremi-Yarahmadi, S.; Vaidhyanathan, B.; Wijayantha, K. G. U.; *Int. J. Hydrogen Energy* **2010**, *35*, 10155-10165.